ABSTRACT

Title of dissertation: SUPERCONDUCTING NANOWIRE SINGLE-PHOTON DETECTORS FOR DARK MATTER DETECTION APPLICATIONS

Jamie Shawn Luskin, Doctor of Philosophy, 2024

Dissertation directed by: Dr. Matthew Shaw
NASA Jet Propulsion Laboratory

Superconducting Nanowire Single Photon Detectors (SNSPDs) are a leading detector technology for time-correlated single-photon counting from the UV to the near-infrared. Due to their unique combination of low energy thresholds and low intrinsic dark count rates, SNSPDs have become attractive as sensors for emerging low-mass dark matter (DM) detection experiments, where they offer the potential to fill existing technology gaps and enable the exploration of previously unconstrained parameter space. One developing DM detection concept, sensitive to MeV-scale DM electron recoils, uses *n*-type GaAs as a cryogenic scintillating target instrumented with a large-area SNSPD as the sensor for scintillation photons.

This thesis focuses on the development and characterization of SNSPDs with mm^2-scale active areas for DM applications in general, and specifically for the detection of scintillation light. This work demonstrates the coupling of *n*-type GaAs with SNSPDs, and the design of novel characterization experiments using optical and energy-tagged X-ray excitation to measure the effective light yield and photoluminescence timescales of cryogenic scintillators using SNSPDs. The isotropic nature of scintillation light and the large active

areas of the devices studied in this work introduce unique challenges for SNSPD design, nanofabrication, and performance. This thesis provides insights into the current state-of-the art, limitations, and approaches to scaling SNSPDs to cm^2-scale active areas for future work. The presented findings advance the status of SNSPDs for DM detection and other emerging High-Energy Physics applications.

SUPERCONDUCTING NANOWIRE SINGLE-PHOTON DETECTORS FOR DARK MATTER DETECTION APPLICATIONS

by

Jamie Shawn Luskin

Dissertation submitted to the Faculty of the Graduate School of the
University of Maryland, College Park in partial fulfillment
of the requirements for the degree of
Doctor of Philosophy
2024

Advisory Committee:
Professor Yanne Chembo, Chair
Dr. Matthew Shaw, Advisor
Professor Daniel Lathrop, Dean's Representative
Professor Jeanpierre Paglione
Professor Carlos A. Ríos Ocampo

© Copyright by
Jamie Shawn Luskin
2024

What we observe is not nature itself, but nature exposed to our method of questioning.

- Werner Heisenberg

DEDICATION

This thesis is dedicated to the memory of my grandfather

Dr. Jerome Lawrence Luskin,

The original Dr. Luskin and my greatest inspiration.

Acknowledgments

As I approach the end of my graduate career, I can't help but feel overwhelmed with gratitude for the people who have helped make this journey possible, both directly and indirectly. It wouldn't be right to start this section off any other way than to acknowledge my JPL advisor, Matt Shaw, for offering me the life-changing opportunity to work in our group. I can't thank you enough for your guidance, support, and kindness throughout the past 4.5 years. I also want to express my sincere appreciation to my UMD advisor, Yanne Chembo, for going above and beyond in providing invaluable guidance throughout this journey. And to the one and only Professor Maria Spiropulu - thank you for making me feel at home at Caltech and the INQNET labs, and for treating me like one of your own.

My sincerest gratitude extends to the brilliant JPL SNSPD group members. Andrew Mueller - thank you for being an exceptional office-mate, friend, and colleague and for listening to all of my rants (and taking them seriously no matter how inane or dramatic!). I am constantly amazed by your talents and inspired by the way you think. Ioana Craiciu - you are truly the best, and I appreciate all of your guidance and support during these last few chaotic months more than I can ever express. Professor Boris Korzh - you have had such a profound impact on the way I approach measurements and science. Jason Allmaras - thank you for being an incredible resource any time, any place, no matter what goes wrong. I deeply admire and look up to your technical skills, work ethic, and the way you reason through problems. To the rest of the group- Emma Wollman, Sahil Patel, Emanuel Knehr, Sasha Sypkens, Bruce Bumble, Andrew Beyer, Fiona Fleming, Jasen Zion and former members Ekkehart Schmidt and Gregor Taylor - your contributions and support have been instrumental to my professional development and it is a pleasure to work with you all.

A sincere thank you goes out to my collaborators at Fermilab Cristian Peña, Si Xie, and Christina Wang for guiding many of the experiments in this thesis, and at LBNL, Maurice Garcia-Sciveres and Steve Derenzo for the insightful and lively discussions.

Dr. J - I don't know that I will ever find the words to convey the impact that you and your class have had on me, but I would not have ended up on this trajectory without you and your philosophy will always be my foundation. The next (long-overdue) pitcher is on me!

Keric Morinaga - thank you for sharing your love of yoga with me and for building the most incredible and supportive community at the Touchstone gyms. Your lessons and philosophy have played a pivotal role in keeping me mentally grounded throughout this process.

A pleasant surprise during this PhD was getting to meet so many wonderful people at Caltech. I am sincerely thankful to Sam Davis, Iraj Umesh, Preeti Bhat, and all of the INQNET group members for welcoming me and supporting me. Tracy Sheffer - you leave us all feeling so taken care of, and we simply could not do what we do without you! Rahaf Youssef - I immensely appreciate your intellect, brilliant insights, kindness, and friendship throughout the past few years. Claire Ellison, Tommy Sievert, Ray Wynne, and Damian Wilson - thank you for being the infinite source of joy that you are for everyone around you. Lautaro Narvaez - thank you for patiently helping me with anything I've ever brought to you. There is truly no problem you can't solve and your expertise in electronics is truly wizard-level. Thank you to the Hutzler group members for being the best neighbors in Downs-Lauritsen and delightful humans to interact with. A tremendous thank you goes out to the illustrious and incomparable Jason Trevor. Thank you for everything that you do to keep so many groups running and for teaching me all things high-energy physics and beyond. You are an absolute legend, one of my favorite people, and the closest thing to a superhero I've ever met.

I would like to thank my family for their support throughout my entire (long!) education. I am so fortunate to have all of you in my corner. To my late grandfathers, Jerome Luskin and Nunzio Brusca - you are profoundly missed and will always be a guiding light

for me. I am also eternally grateful for the incredible Leal family for their love and support during those early years of studying like a maniac.

A posthumous thank you is extended to my late great-uncle, Dr. Burton Kleinman, who has always been an immense inspiration to me. I deeply admire how your work transcended the boundaries between mathematics, physics, and chemistry (and I hope I inherited some of those Kleinman genes!). There is a near-unity probability that we had a lot in common and I'll always wish that we could chat about things.

Finally, to my incredible wife, Elaina - I could not have done any of this without your unconditional support. Thank you for believing in me, helping me grow, and for being the best partner in the universe.

Table of Contents

Foreword ii

Dedication iii

ACKNOWLEDGEMENTS iv

1 Dark Matter 1
- 1.1 Introduction . . . 1
- 1.2 Evidence for Dark Matter . . . 2
  - 1.2.1 Galactic Rotation Curves . . . 2
  - 1.2.2 Cosmological scale . . . 3
  - 1.2.3 Gravitational Evidence . . . 6
- 1.3 Dark Matter Candidates . . . 9
  - 1.3.1 Classes of Dark Matter Candidates . . . 10
  - 1.3.2 WIMP Dark Matter . . . 11
  - 1.3.3 Axions and Axion-Like Particles (ALPs) . . . 13
  - 1.3.4 Dark Photons . . . 16
  - 1.3.5 sub-GeV Dark Matter . . . 17
    - DM-electron scattering . . . 18
    - DM-electron absorption . . . 19
- 1.4 DM Detection Strategies . . . 21
  - 1.4.1 Direct Detection of sub-GeV Dark Matter . . . 22
  - 1.4.2 *n*-type GaAs as a Cryogenic Scintillating Target . . . 23
  - 1.4.3 DM Detection concept using *n*-type GaAs . . . 26
  - 1.4.4 Sensor Classes for *n*-type GaAs and Low Mass DM Targets . . . 28

2 Superconducting Nanowire Single Photon Detectors 32
- 2.1 Introduction . . . 32
- 2.2 Device Operation Principles . . . 33
- 2.3 Detection Metrics . . . 35
  - 2.3.1 Detection Efficiency . . . 36

2.3.2 Dark Count Rate . . . 37
2.3.3 Timing Resolution . . . 38
2.4 Design Tradeoffs for Large-area SNSPDs . . . 39
2.4.1 Active Area vs Timing Performance . . . 39
2.4.2 Array Size vs Readout Complexity . . . 40
2.5 Large-active area SNSPDs . . . 40
2.5.1 Materials . . . 41
2.5.2 Device architecture . . . 42
Nanowire vs Microwire Detectors . . . 43
2.6 SNSPDs for Dark Matter Detection and HEP Applications . . . 43

3 Large Active Area SNSPD Design and Characterization 46
3.1 Background . . . 46
3.2 Generation 1 Microwire Arrays . . . 49
3.2.1 Detector Design . . . 49
3.2.2 Materials . . . 49
3.2.3 Detector Characterization . . . 50
Cryogenic set-up and Readout . . . 50
Optical Characterization . . . 51
Efficiency Measurements . . . 55
T_c Measurement . . . 57
Timing Resolution Characterization . . . 59
3.3 Generation 2 Microwire Arrays . . . 62
3.3.1 Detector Design . . . 65
3.3.2 T_c Measurement . . . 67
3.3.3 Optical Characterization . . . 68
3.3.4 Timing Resolution Characterization . . . 70

4 Backgrounds in Microwire Arrays 77
4.1 Extrinsic Background Mitigation . . . 78
4.1.1 Filtering . . . 78
Dark Packaging . . . 78
4.2 Intrinsic Backgrounds in Microwire Arrays . . . 81
4.3 Scaling with Active Area . . . 81
4.4 Temperature Dependence of Dark Counts . . . 83

5 Optically-excited Scintillation Measurements 87
5.1 Overview of systems measured . . . 88
5.1.1 GaAs Specifications and Analysis . . . 89
5.2 Detector and Sample Information . . . 89
5.2.1 System A . . . 89
Device packaging and Hybridization . . . 90
5.2.2 System B . . . 90

Device packaging and Hybridization 90
5.3 Calibration of SNSPDs for Scintillation Light 91
5.4 Scintillation timescale measurements 94
5.4.1 Measurement setup 96
5.4.2 Results and exponential fitting 97
5.5 Effective Light-yield Measurements 98
5.5.1 Measurement Setups 99
5.5.2 System A effective light yield 100
5.5.3 System B Effective Light Yield 100
5.6 Future work towards Absolute Light Yield Measurements 101

6 X-ray Excited Scintillation Measurements 103
6.1 Compton Scattering 105
6.2 X-ray Source 107
6.3 Calibration of HPGe Detectors 108
6.4 Timescale Measurements 111
6.4.1 Background Measurements of GaAs-SNSPD System 113
6.4.2 CAEN Digitizer Readout 114
6.4.3 Source Effect on GaAs-SNSPD System 115
6.5 Compton Scattering Analysis and Challenges 119
6.5.1 Poisson Statistics and Mean Photon Number Fitting 122
6.5.2 Understanding the Observed Distribution 124
6.5.3 Understanding System Losses and Secondary X-ray Generation . . 128

7 Designs and Challenges of Improved Microwire Arrays 132
7.1 Optical Stack Design for Microwire Arrays 133
7.1.1 Rigorous Coupled Wave Analysis 136
7.1.2 Angled-Incidence RCWA Simulations 136
7.1.3 DBR Optical Stack Design for Broad-Angle Efficiency 138
Angular Distribution of Light from GaAs 140
DBR Design 148
7.2 Fabrication Challenges and Steps Forward 149

8 Microwire Arrays in Other Experiments 155
8.1 Detection of High Energy Particles with Large Area SNSPDs 155
8.1.1 Detector Design and Measurement Infrastructure 156
8.1.2 Results 156
8.2 Broadband Reflector Experiment for Axion Detection 158
8.2.1 Detection Concept and Experiment Design 158
8.2.2 RCWA Efficiency Simulations 160
8.2.3 Future Work 162

9 Conclusions 164

9.1 Summary 164
9.2 Future Work and Outlook 165

A Procedure for IV Curve Analysis with DC Coupled Cryogenic Amplifiers 166

B *n*-type GaAs Sample Information 171
B.1 Sample A - More Information 171
B.2 Sample B - More Information 172

C Publications 174

Bibliography 175

Chapter 1: Dark Matter

1.1 Introduction

Elucidating the particle nature of dark matter (DM) is one of the largest unsolved problems in fundamental physics. Though DM has evaded direct detection to date, indirect probes of its gravitational interactions with celestial bodies at multiple scales indicate that it comprises nearly 80% of the matter in the Universe and is necessary to explain large-scale structure formation.

The most mature and large-scale experimental DM search programs have focused on the Weakly Interacting Massive Particle (WIMP) paradigm. Due to a lack of conclusive detection signal, new theoretical frameworks have emerged in recent years, and there is now strong motivation to explore a broader set of candidate particles experimentally. Hidden sector DM candidates are neutral under Standard Model (SM) forces and charged under new forces that can weakly couple to ordinary matter via portal interactions. The range of potential mass of hidden sector DM is broader than that of the WIMP DM. Importantly, the mass range below a GeV, the so-called *sub-GeV* DM contains theoretically well-motivated targets that are either below the noise floor or not accessible in WIMP search experimental programs and thus require the development of novel experimental approaches. Increasing the sensitivity of direct detection experiments to lower masses of DM requires the development of new target materials sensitive to proposed interactions and new low-noise sensors with low-energy thresholds. As these technologies develop, sub-GeV DM can be explored

substantially with smaller-scale table-top direct detection pilot experiments.

This chapter serves as a brief introduction to DM. Section 1.2 briefly summarizes the experimental evidence for DM, Section 1.3 presents an overview of relevant DM candidate particles, and Section 1.4 introduces DM detection strategies to motivate the work contained in this PhD thesis.

1.2 Evidence for Dark Matter

Evidence for the existence of DM has steadily increased over the last several decades. Observational support includes its gravitational effects, such as galaxy rotation curves, gravitational lensing, and the large-scale structure of the universe, all of which cannot be accounted for by visible matter alone. Further evidence comes from cosmological observations consistent with predictions from the Lambda cold dark matter model (ΛCDM), which serves as the standard model of Big Bang cosmology.

1.2.1 Galactic Rotation Curves

The earliest evidence for a cold, non-luminous matter pervading the Universe came from the study of galactic rotation curves. These were first measured in the Coma Cluster by Franz Zwicky in the 1930s [1] and later in the 1970s by V. Rubin [2] in the Andromeda galaxy and others [3]. Obtaining a rotation curve entails measuring the rotational velocity of galaxy or galaxy clusters via Doppler shifts and subsequently plotting this quantity with respect to the distance from the center of the galaxy.

The rotational velocity of a galaxy can be expressed using Newtonian mechanics as

$$v_{rot}(r) = \sqrt{\frac{GM(r)}{r}}, \tag{1.1}$$

where M is the enclosed mass, r is the radial distance from the galactic center, and G is the gravitational constant. Assuming that visible matter comprises the entirety of the mass distribution, v_{rot} should decrease as $\frac{1}{\sqrt{r^2}}$ for distances beyond the visible galactic disc. In practice, the measured v_{rot} curves flatten at large r (see figure 1.1), implying a constant mass distribution that can't be explained by visible matter alone.

Measured galactic rotation curves are all consistent with a spherically symmetric mass distribution that increases linearly with r [4]. On the contrary, the visible mass, constituted by stars and gases which can absorb and emit light, is concentrated in the inner disk. Zwicky, in addition to pioneering these early measurement techniques, coined the term "dunkle materie" (dark matter) to refer to the non-luminous component of the mass distribution.

Other proposed explanations for this discrepancy include modifications to gravity including Modified Newtonian Gravity [5]; however, these lack consistency with phenomena at other scales [6] that are explained in the following sections.

1.2.2 Cosmological scale

The Cosmic Microwave Background (CMB) is the background radiation in the Universe comprised of the photons that first decoupled from matter shortly after the Big Bang. It was initially believed to be isotropic until faint (μK-scale) anisotropies in temperature and polarization were discovered in the early 1990s. The origins of these anisotropies are understood to be from the matter-energy density of the early universe. Namely, it is hypothesized that oscillations in the baryon-photon fluid under the influence of the gravitational potential due to local wells and peaks of cold dark matter produced the temperature anisotropies, which now manifest in the CMB power spectrum as acoustic peaks [9].

The CMB has a blackbody spectrum with a temperature of 2.73 K, peaked at $\lambda =$

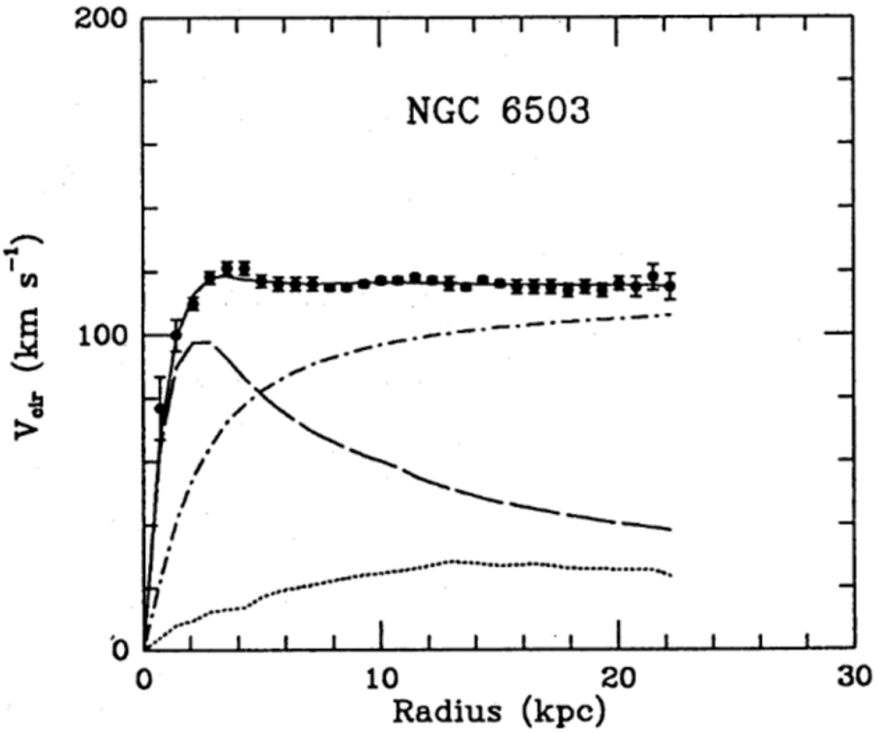


Figure 1.1: Rotation curve measured for the galaxy NGC 6503 (black dots) and fit to DM-halo model shown with the solid black line. The dashed black line is the Keplerian prediction based on visible matter. The dotted-dash is the DM-halo rotation curve that is required to explain the flatness of the curve at large r. Figure adapted from ref. [7]

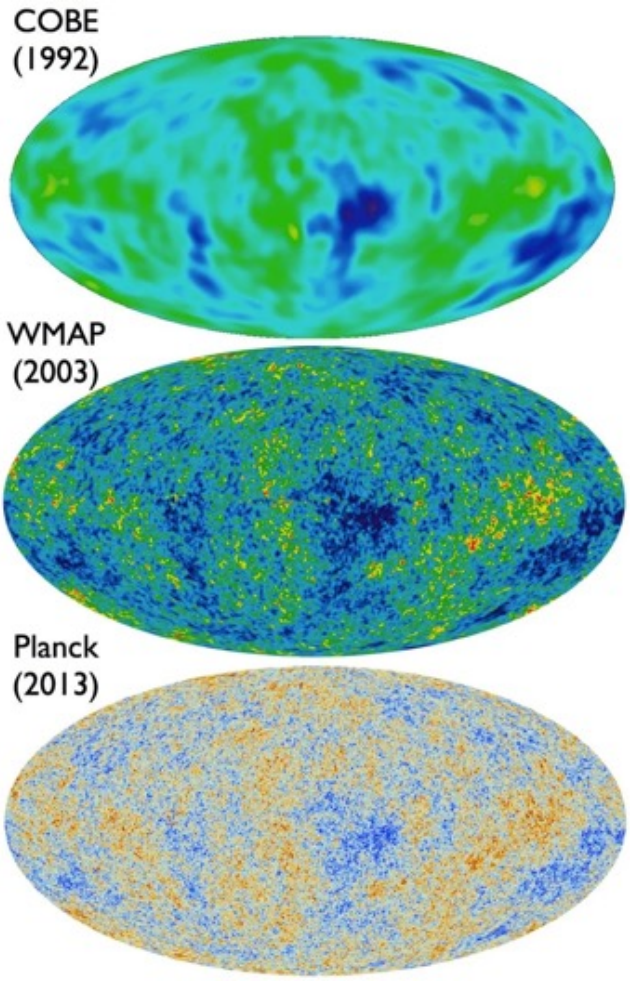


Figure 1.2: The CMB map as seen by NASA's COBE (top)and WMAP (middle) missions and ESA's Planck mission (bottom). Figure adapted from [8].

1.06 mm. Atmospheric water molecules absorb this wavelength of light, making it amenable to study via ground and space-based missions (see figure 1.2 for examples). Missions such as COBE [10], WMAP [11], and Planck [12] have directly measured the temperature anisotropies. The power spectrum of these temperature fluctuations offers a means to validate cosmological models that make predictions about this spectrum.

Lambda-Cold Dark Matter (ΛCDM), a mathematical model of the Big Bang serving as the cosmological standard model, contains three main components describing the baryonic matter, dark matter, and dark energy contents of the Universe. As shown in figure 1.3, the ΛCDM model prediction fits the CMB anisotropy data with high statistical significance. This alignment reinforces the robustness and accuracy of the ΛCDM model and the importance of dark matter in our understanding of the Universe and its evolution.

The baryonic and non-baryonic matter densities extracted from the 2018 Planck collaboration are $\Omega_b h^2 = 0.0224$ and $\Omega_{\mathrm{DM}} h^2 = 0.120$, where h is the dimensionless Hubble constant [12]. The ratio between dark matter and baryonic matter densities is given by $\Omega_{\mathrm{DM}}/\Omega_b \approx 0.120/0.0224 \approx 5.4$, indicating that dark matter is approximately five times more abundant than ordinary matter.

1.2.3 Gravitational Evidence

Gravitational lensing measurements have also provided a compelling set of evidence for the existence of dark matter. Gravitational lensing is a phenomenon whereby a massive celestial body causes significant perturbations in the space-time metric such that light is bent from a distant source as it travels toward an observer. Most lines of sight that are accessible are in the weak gravitational lensing regime, where distortions can't be measured from a single source. In composite lensed images, mass distributions can be reconstructed through correlations in the observed ellipticity of the distorted objects. In these measure-

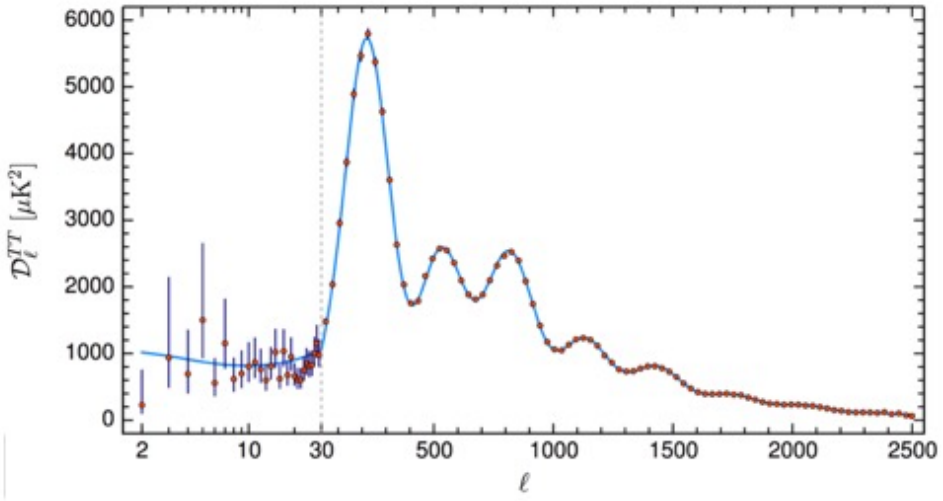


Figure 1.3: Temperature power spectrum of CMB measured by Plank mission – red dots , and the λCDM model prediction is shown in blue. Figure taken from ref. [12]

ments, the reconstructed mass causing the lensing phenomenon exceeds the visible mass of the object by a factor of tens to hundreds, pointing to the presence of dark matter.

A well-known example is the bullet cluster [13], which was formed through the collision of two galaxy clusters roughly 3.8 billion years ago. The Hubble space telescope was used to obtain weak gravitational lensing measurements, from which the mass distribution was derived. The luminous mass distribution was also extracted from X-ray spectra of the cluster measured by the Chandra x-ray observatory. The mass reconstructed from lensing is a factor of 200 more abundant than the luminous mass extracted from the spectroscopic measurements. As shown in figure 1.4, there is a clear offset between the visible center of mass and the center of mass reconstructed from weak gravitational lensing. This offset arises because dark matter only interacts conventionally through gravity and not via traditional electromagnetic forces. Consequently, during the collision, dark matter passed through largely unaffected, while the visible matter, which interacts electromagnetically, experienced drag and slowed down, leading to the observed separation between the two.



Figure 1.4: Composite image taken from ref. [13]of the galaxy cluster 1E 0657- 56, also known as the “Bullet Cluster.” Pink depicts the hot gas measured by Chandra X-ray observatory and includes most of the normal baryonic matter - Blue depicts the concentration of mass determined by weak gravitational lensing

1.3 Dark Matter Candidates

It has has been conclusively shown that none of the particles in the Standard Model can account for the properties of dark matter, as they either interact too strongly with light or do not have the necessary mass and behavior. DM thus requires extensions beyond the Standard Model of particle physics, which describes the known fundamental particles and forces. This has led to the development of numerous theoretically well-motivated dark matter candidate particles. Constraints on these candidates are typically calculated one model at a time, but it is possible that dark matter is composed of multiple species of particles. This collection of particles is often referred to as the *dark sector*. The dark sector may involve complex interactions, similar to the visible sector, but these would be extremely weak or invisible to current detection methods, making them difficult to study directly.

There are specific properties that dark matter models must satisfy based on observational evidence. First, dark matter does not emit light, meaning any viable candidate must have an extremely weak or vanishing electric charge and electric or magnetic dipole moments. As a result, dark matter cannot radiate energy electromagnetically or thermalize through photon emission, making it approximately dissipationless. Additionally, dark matter is known to be collisionless—if collisions occurred, dark matter halo profiles would be spherical, but observations show that DM halos are clustered, with prolate shapes in their centers and triaxial structures toward their outskirts [14]. Finally, dark matter is non-relativistic (or 'cold'), as indicated by the formation of large-scale cosmic structures [15, 16].

Dark matter candidates are discussed extensively in reviews [17–20]. The following sections contain first an overview of the general classes of DM candidates, WIMP dark matter for context regarding the previous work in the community, and finally sub-GeV

dark matter for its relevance to the context of the work contained in this PhD thesis.

1.3.1 Classes of Dark Matter Candidates

The search for DM has expanded beyond Weakly Interacting Massive Particles (WIMPs) and now includes a wide range of alternative candidates. These candidates can be broadly classified into two categories: *wavelike* (or ultralight) and *particle-like* dark matter. The classification depends on the de Broglie wavelength, λ_{dB}, which is given by:

$$\lambda_{\mathrm{dB}} = \frac{h}{p}$$

where h is Planck's constant, and p is the momentum of the particle. This wavelength provides insight into whether the particle behaves more like a classical particle or exhibits wave-like properties. Wave-like behavior occurs when the de Broglie wavelength is comparable to or larger than the characteristic scale of the system, for example the the average inter-particle separation in a galaxy like the Milky Way. Particle-like behavior is exhibited when the de Broglie wavelength is much smaller than the relevant physical scales, causing the dark matter to behave classically with trajectories similar to standard particles. These two classes differ fundamentally in their mass, behavior, and detection strategies.

In general, wavelike dark matter consists of particles with extremely low masses. These candidates include bosonic fields such as scalars or pseudoscalars [21]. Axions are a prominent example, originally introduced to resolve the strong CP problem in quantum chromo-dynamics (QCD) [22]. Their mass range is typically $10^{-22}\,\mathrm{eV}$ to $10^{-5}\,\mathrm{eV}$, and they are promising dark matter candidates due to their ability to form a coherent oscillating field. Axions can be detected through haloscope experiments like ADMX [23], where they convert into photons in the presence of strong magnetic fields. Other novel detection techniques involve nuclear magnetic resonance (NMR) [24] and condensed matter

systems [25]. Dark Photons are another example of wave-like dark matter, arising from a hidden $U(1)$ gauge symmetry [26, 27]. With masses less than 1 eV, dark photons can oscillate with ordinary photons, leading to observable signatures. Detection methods often involve photon mixing experiments, such as cavity searches or precise atomic clock measurements.

Particle-like dark matter candidates arise in extensions of the Standard Model and can range from keV to solar mass scales. Sterile Neutrinos [28] are one such candidate, with masses in the range of keV to MeV. Unlike active neutrinos, sterile neutrinos do not interact via the weak force, making them challenging to detect. Additionally, models proposing a Dark Sector suggest the existence of dark baryons, analogous to protons and neutrons but confined to a dark sector. This dark sector may involve its own set of forces and particles, weakly interacting with Standard Model particles. Detection could arise from, missing energy signatures in collider experiments, dark sector particles decaying into visible matter, or direction detection searches [29–31].

1.3.2 WIMP Dark Matter

Of the possible DM candidates, the (particle-like) Weakly Interacting Massive Particle (WIMP) paradigm has been the most tested experimentally over the past several decades. Broadly, a WIMP is a proposed fundamental particle which interacts via gravity and another force(s) that is non-vanishing in strength at the weak-scale or below, with a mass range from a few GeV$/c^2$ to several TeV$/c^2$.

The primary WIMP production mechanism is thermal freeze out. In the early hot and dense Universe, WIMPs interacted more frequently with ordinary matter due to the high temperature. As the Universe expanded and cooled, the interactions between WIMPs and other particles became less frequent due to lower particle densities. Eventually the expan-

sion rate of the universe exceeded the annihilation rate of the dark matter, resulting in a reduced number of WIMPs and leaving a stable relic density.

Through observational evidence from cosmological surveys and insights from particle physics experiments, the relic abundance of DM has been determined with high precision. Any DM theory must account for this precise relic abundance in order to be considered viable. The relic density of WIMP DM can be obtained from the Boltzman equation and expressed as:

$$\Omega_\chi \approx \frac{3 \times 10^{-27}\,\mathrm{cm}^3\,\mathrm{s}^{-1}}{\langle \sigma_A v \rangle} \tag{1.2}$$

where $\langle \sigma_A v \rangle$ is the thermally averaged annihilation cross section for DM and h is the dimensionless Hubble parameter. A particle with electroweak-scale interactions naturally leads to a relic abundance that is consistent with the relic abundance derived from cosmological constraints. This has been referred to as the "WIMP miracle".

WIMP experiments are generally designed to detect nuclear recoils caused by interactions between WIMPs and atomic nuclei. The interaction cross-section for WIMPs with nuclei is typically larger than that with electrons. Thus, the recoil energy deposited in a nucleus from a WIMP collision is generally more significant than the energy deposited in an electron collision.

Targets designed to probe WIMP interactions include noble liquids such as xenon and argon. The LZ experiment is one of the largest-scale WIMP searches. The characteristic nuclear recoil energy in liquid xenon is on the order of 10 keV, which is comparable to the recoil energy from radiogenic backgrounds. Because of this, one of the primary design considerations in WIMP experiments is the minimization of radiogenic backgrounds.

Another challenge facing WIMP experiments is the the intrinsic scaling of the interac-

tion rate. The number of WIMP interactions, n_{DM}, is given by the relation:

$$n_{\mathrm{DM}} = \frac{\rho_{\mathrm{DM}}}{M_{\mathrm{DM}}} \tag{1.3}$$

where ρ_{DM} is the dark matter density and M_{DM} is the mass of the dark matter particle. As M_{DM} increases, n_{DM} decreases, making the interaction rate lower. For this reason, WIMP experiments need to have extremely large target volumes to significantly probe the parameter space. For example, the latest iteration of the LZ experiment features a target mass of 7 tons of liquid xenon.

1.3.3 Axions and Axion-Like Particles (ALPs)

The concept of axions emerged in the 1970s as a solution to the strong CP problem in quantum chromodynamics (QCD). The strong CP problem refers to the apparent absence of a significant violation of the CP symmetry (combined Charge Conjugation and Parity) in strong interactions, despite the fact that the QCD Lagrangian allows for a potential CP-violating term:

$$\mathscr{L}_{\mathrm{QCD}} = \frac{\theta}{32\pi^2} G_{\mu\nu}\tilde{G}^{\mu\nu} \tag{1.4}$$

where $G_{\mu\nu}$ is the gluon field strength tensor, and $\tilde{G}^{\mu\nu}$ is the axion field strength tensor. The parameter θ is expected to be a small number, but its value is not constrained by theory, and large values would induce strong CP-violation effects that are not observed experimentally.

In 1977, Peccei and Quinn proposed a solution to this problem by introducing a new symmetry (Peccei-Quinn symmetry) that spontaneously breaks, leading to what became known as the *axion*. The axion is a light scalar particle that provides a dynamic mechanism

to relax the value of the θ-term to near zero, effectively solving the strong CP problem.

Axion-like particles (ALPs) are generalizations of the axion. These are hypothetical light scalar particles that do not necessarily arise from the Peccei-Quinn mechanism but share similar properties, such as interactions with photons and other particles.

The axion field $a(x)$ can be described by the following Lagrangian density:

$$\mathscr{L}_{\text{axion}} = \frac{1}{2}\partial_\mu a\, \partial^\mu a - \frac{1}{2}m_a^2 a^2 + g_{a\gamma\gamma} a F_{\mu\nu}\tilde{F}^{\mu\nu} \tag{1.5}$$

Here, m_a is the axion mass, $F_{\mu\nu}$ is the electromagnetic field strength tensor, and $\tilde{F}^{\mu\nu}$ is its dual. The coupling constant $g_{a\gamma\gamma}$ describes the interaction strength of the axion with two photons. This term allows axions to couple to photons and can lead to observable effects, such as axion-photon conversion in external magnetic fields.

Axion-like particles have similar interactions, but their Lagrangian can also include interactions with other particles, depending on their origin:

$$\mathscr{L}_{\text{ALP}} = \frac{1}{2}\partial_\mu a\, \partial^\mu a - \frac{1}{2}m_a^2 a^2 + g_{a\gamma\gamma} a F_{\mu\nu}\tilde{F}^{\mu\nu} + g_{a\psi\psi} a \bar{\psi}\psi \tag{1.6}$$

where ψ represents a fermion field, and the second term introduces the possible interaction of ALPs with fermions.

RF resonant-cavity experiments, such as ADMX and HAYSTAC (Haloscope At Yale Sensitive To Axion CDM), aim to detect axion dark matter by exploiting axion-photon conversion in a strong magnetic field. The axion signal is expected to manifest as a narrow-band electromagnetic wave at a frequency determined by the axion mass, resonantly enhanced by a tunable microwave cavity. ADMX and HAYSTAC focus on axion masses in the range $\sim$ 1–40 μeV, corresponding to frequencies in the GHz range. HAYSTAC has probed masses in the region of $\sim$ 4–20 μeV, complementing ADMX at slightly higher frequencies. These experiments contribute to systematically excluding portions of the viable

axion parameter space.

Resonant-cavity experiments face several limitations that constrain their ability to explore the full axion parameter space. These setups are inherently narrow-band, sensitive to a small range of axion masses at a time. Scanning a broader range requires precise tuning of the cavity frequency, which is time and resource intensive. Additionally, the resonant frequency of a cavity is determined by its dimensions, making it challenging to probe very small axion masses ($< 1\,\mu$eV) due to the prohibitively large cavity sizes required, or very large axion masses ($> 40\,\mu$eV), where resonant enhancement becomes inefficient. Noise further limits sensitivity, with thermal noise dominating at lower frequencies and quantum noise at higher frequencies, though the HAYSTAC collaboration has made significant progress in overcoming the latter through quantum squeezing techniques. Finally, the weak axion-photon coupling strength ($g_{a\gamma\gamma}$) necessitates long integration times to detect potential signals, adding to the challenges.

Despite significant progress by experiments like ADMX [23, 32–36] and HAYSTAC [37, 38], large regions of the axion mass parameter space remain unexplored. The low-mass range ($< 1\,\mu$eV) and high-mass range ($> 40\,\mu$eV) are particularly challenging due to the constraints of cavity design and sensitivity. Exploring these regions will require innovative approaches and new technologies, as resonant-cavity designs are fundamentally limited in their scalability. Developing broadband haloscopes is essential to overcome these challenges, enabling simultaneous searches over wide mass ranges and reducing the time required to explore the uncharted axion landscape. The Broadband Reflector Experiment for Axion Detection (BREAD) collaboration introduces an innovative approach to search for axion and dark photon dark matter across a wide range of masses, spanning approximately μeV to eV, without requiring tuning. The experiment utilizes a cylindrical dish resonator designed to fit within solenoidal magnets. In this setup, axions (in the presence of the magnetic field) or dark photons interact with the metallic surface of the dish, converting into

photons independent of their mass. These photons are subsequently directed by a parabolic focusing reflector onto a highly sensitive single-photon counting detector.

For the pilot dark photon experiment within the BREAD program, the large-area microwire arrays developed and characterized in this thesis are currently being integrated as the single-photon detector. Chapter 8 describes the characterization and integration of these sensors into the experiment and plans for the future.

1.3.4 Dark Photons

Dark photons are hypothetical particles that are introduced as the gauge bosons (force carriers) of a new U(1) symmetry associated with DM interactions. The idea behind dark photons is that they could mediate interactions between dark matter particles and possibly visible matter, but with a very weak coupling to the standard model particles. This idea is motivated by the dark sector in theoretical physics, which posits the existence of a hidden sector of particles that interact very weakly with ordinary matter.

In its theoretical framework, a dark photon can mix with the standard photon, leading to the possibility of dark matter-photon interactions. This interaction is particularly interesting for explaining anomalies observed in certain experiments, such as the *g-2 anomaly* in the muon magnetic moment, and for providing a candidate for dark matter.

The Lagrangian for the dark photon can be written as:

$$\mathscr{L}_{\gamma'} = -\frac{1}{4}F_{\mu\nu}F^{\mu\nu} - \frac{1}{4}F'_{\mu\nu}F'^{\mu\nu} + \frac{\varepsilon}{2}F_{\mu\nu}F'^{\mu\nu} + m_{\gamma'}^2 A'_\mu A'^\mu \tag{1.7}$$

where $F_{\mu\nu}$ is the field strength tensor for the standard photon, $F'_{\mu\nu}$ is the field strength tensor for the dark photon, and ε is a small parameter that represents the mixing between the standard photon and the dark photon. The term $m_{\gamma'}^2$ corresponds to the mass of the dark photon, and the mixing term enables the possibility for photon-dark photon oscillations.

The interaction between the dark photon and standard model particles is typically modeled as a kinetic mixing term:

$$\mathscr{L}_{\text{int}} = \varepsilon F_{\mu\nu} F'^{\mu\nu} \tag{1.8}$$

This term leads to weak couplings between ordinary matter (via the electromagnetic interaction) and dark matter (via the dark photon).

1.3.5 sub-GeV Dark Matter

The absence of a DM signal in existing WIMP direct detection experiments and the lack of supporting non-Standard Model physics in collider experiments have led to interest in the development of other candidates for DM. The lack of sizable interaction between DM and ordinary matter motivate the hypothesis that dark matter is neutral under all standard model forces but interacts through new forces that to-date have been undiscovered. This is referred to as hidden sector DM. In several frameworks, the sub-GeV scale arises naturally and via production mechanisms beyond the standard freeze-out. Each mechanism implies targets in the DM parameter space that are accessible experimentally. The DM relic density can be accounted for by mechanisms that describe portal interactions between hidden sector forces and ordinary, for example via an exchange of a dark photon. Importantly, the parameter space for these models is unexplored experimentally and also, in part, beyond the scope of astrophysical bounds.

The higher mass region of the hidden sector parameter space is well-probed by WIMP search experiments (few GeV to 100 TeV). The lower region of the hidden sector DM parameter space below a few GeV is not well-probed by WIMP search experiments and requires new detection strategies. This is referred to as sub-GeV dark matter.

One of the challenges in probing light dark matter via traditional nuclear recoil methods

lies in the kinematics; for lighter masses of DM, the total kinetic energy transferred to the nucleus during a recoil is suppressed. Low nuclear recoil energies are a challenge to detect and necessitate sensors with drastically reduced energy thresholds and background rates.

Another avenue to search for DM is through interaction with electrons in target materials as opposed to nuclei. This is more kinematically favorable, as a higher fraction of kinetic energy can be transferred from a light DM particle to an electron via inelastic scattering processes, for example. Due to the inverse relationship between interaction rate and the DM mass shown in Equation 1.3, interactions can be probed with smaller target volumes and exposure for lighter dark matter masses. For this reason, pilot programs for sub-GeV DM searches are able to utilize table-top sized experiments.

The measurable signatures of hidden sector DM are dictated by the type of new force coupling the DM to ordinary matter. As are described in benchmark models [39], a new force can be mediated by scalar of vector bosons which couple to leptons or hadrons. The bench-marked coupling models are described in detail in this reference for hidden sector DM in general, and also the low-mass (sub-GeV) parameter space for hidden sector dark matter .

For concreteness, sub-GeV DM that interacts with electrons through a dark-photon mediator is described in the following section.

DM-electron scattering

Using the notation in reference [40], a DM particle χ can couple to the standard model via a $U(1)$ gauge boson $A^{'}$ (dark photon). A' kinetically mixes with the SM $U(1)$ field via the following interaction:

$$\mathscr{L} \supset \frac{\varepsilon}{2\cos\theta} F_Y^{\mu\nu} F_{\mu\nu}^{'} \tag{1.9}$$

where θ is the mixing angle, ε is the coupling strength, and $F_Y^{\mu\nu}$ and $F_{\mu\nu}^{'}$ are the field

strengths.

The scattering cross-section can be written as

$$\sigma_e = \frac{16\pi\mu_{\chi e}^2\alpha\varepsilon^2\alpha_D}{(m_{A'}^2+\alpha^2m_e^2)^2} \approx \begin{cases} \dfrac{16\pi\mu_{\chi e}^2\alpha\varepsilon^2\alpha_D}{m_{A'}^4}, & m_{A'} \gg \alpha m_e \\ \dfrac{16\pi\mu_{\chi e}^2\alpha\varepsilon^2\alpha_D}{(\alpha m_e^4)}, & m_{A'} \ll \alpha m_e \end{cases} \tag{1.10}$$

where $\mu_{\chi e}$ is the DM-electron reduced mass and $\alpha = g_D^2$ (the $U(1)_D$ coupling.

The corresponding form factor can be written as

$$F_{DM}(q) = \frac{m_{A'}^2+\alpha^2m_e^2}{m_{A'}^2+q^2} \approx \begin{cases} 1, & m_{A'} \gg \alpha m_e \\ \dfrac{\alpha^2m_e^2}{q^2}, & m_{A'} \ll \alpha m_e \end{cases} \tag{1.11}$$

where q is the DM-electron momentum transfer. The DM form factor describes how the interaction between dark matter particles and ordinary matter varies with the momentum transfer in a scattering event which which is essential for calculating event rates in dark matter detection experiments and understanding the interaction mechanisms. In a DM-electron scattering interaction, the DM can transfer at most its kinetic energy $1/2m_{A'}v^2$, where $v = 10^{-3}c$ is the galactic DM velocity and c is the speed of light. The parameter space for both regimes is shown in figure 1.6.

DM-electron absorption

Dark matter (DM) candidates such as axion-like particles (ALPs) and dark photons can interact with ordinary matter via absorption, especially through interactions with bound electrons. The absorption of dark photons A' can be modeled as the absorption of a non-relativistic particle with mass m with coupling ε to electrons [26, 27]. In absorption other DM transfers its entire rest mass energy $m_{A'}c^2$.

The absorption of dark photons or axion-like particles occurs when these particles interact with electrons bound in atoms. The process is commonly referred to as the axio-electric effect for axions and axion-like particles. This interaction leads to the absorption of the dark-matter particle, which transfers its energy to an electron, causing it to be ejected from its atomic orbit. For a dark photon, this effect arises due to kinetic mixing with the photon field, while for axions, the interaction is based on the axion's coupling to the electromagnetic field.

For dark photons, the absorption cross section can be expressed as:

$$\sigma_{\gamma'}(E) = \frac{\varepsilon^2}{m_{\gamma'}^4} \left(\frac{E^2}{\Delta E^2 + E^2} \right) \tag{1.12}$$

where ε is the kinetic mixing parameter, $m_{\gamma'}$ is the mass of the dark photon, E is the energy of the incoming dark photon, and ΔE is the energy width of the absorption process, typically related to the material's band gap or the electron binding energy.

For axion-like particles (ALPs), the absorption cross section is given by:

$$\sigma_a(E) = \frac{g_{a\gamma\gamma}^2}{m_a^4} \left(\frac{E^2}{\Delta E^2 + E^2} \right) \tag{1.13}$$

where $g_{a\gamma\gamma}$ is the axion-photon coupling constant, m_a is the mass of the ALP, and the other terms are analogous to those for dark photons.

Current direct detection experiments such as XENON100 [41–43], CDMSlite [44], and SuperCDMS [45–47] are sensitive to these types of interactions, especially with electron recoil events. The cross section can be probed by observing the energy deposited by dark-matter particles in the form of electron recoils, allowing for the constraining of the coupling constants (ε for dark photons, $g_{a\gamma\gamma}$ for ALPs) in regions of parameter space that were previously unexplored.

However, the sensitivity of these experiments to lower mass range for dark-matter parti-

cles, especially below a few MeV, remains poorly probed. This region is difficult to explore due to the relatively low recoil energies associated with light dark-matter candidates, which are often below the detection thresholds of existing experiments. Moreover, many direct detection experiments have better sensitivity at higher masses (e.g., GeV-scale DM), leaving a significant gap in their ability to probe lighter candidates such as dark photons or ALPs with small masses.

To overcome these limitations, future experiments are under development with the goal of lowering the energy thresholds and increasing the sensitivity of detectors. These next-generation experiments aim to probe the unexplored regions of parameter space where dark photons and axions may exist. Theoretical studies have already begun to investigate the potential for detecting bosonic DM absorption in materials with lower energy thresholds, such as semiconductors and superconducting materials. These materials probe potentially weakly coupled interactions of low-mass dark photons and axions, and thus could enable the detection of these particles in new mass ranges [48, 49].

1.4 DM Detection Strategies

As shown schematically in figure 1.5, there are the three general categories of experiments that provide complementary insight into the nature of dark matter. Indirect dark matter detection strategies focus on the measurement of the products of dark matter interactions (i.e. gravitationally) rather than the dark matter itself. Accelerator experiment aim to produce dark matter directly or via decays of heavier new particles. Direct DM detection experiments aim to directly measure the collisions between dark matter and a target material in terrestrial apparatuses. Importantly, the verification of an excess as a dark matter signal would require concurrent study and verification between all of the above channels as well as consistency with expected daily and annual modulation of the signal [50, 51].

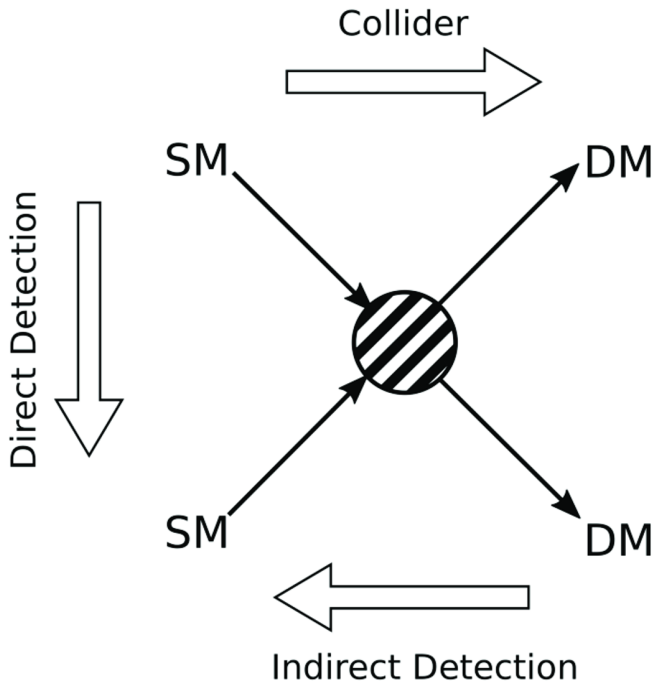


Figure 1.5: Schematic showing the possible channels of dark matter detection. Indirect DM detection involves searching for the standard model (SM) products of dark matter interactions and constraining annihilation cross sections. Collider searches seek to produce DM through high-energy collisions. Direct Detection probe interactions of DM with a target material through a measurable signal of the energy deposition.

Direct detection experiments search for DM interactions with nuclei or electrons in target materials. Large-scale, mature experiments have placed exclusions on much of the DM parameter space above 1 GeV. With the theoretical developments and evidence from collider experiments that DM might have a lighter mass (>GeV) than once previously thought, it is important to devise novel detection strategies to explore the sub-GeV DM parameter space.

1.4.1 Direct Detection of sub-GeV Dark Matter

Many new experiments spanning a diversity of fields from atomic [52] and molecular [53] physics to condensed matter physics [54], [55], [56], [57] have been proposed to probe sub-GeV DM via both electron and nuclear recoils. Figure 1.6 shows the approxi-

mate mass range of sub-GeV regime, along with some of the proposed experiments that are under development.

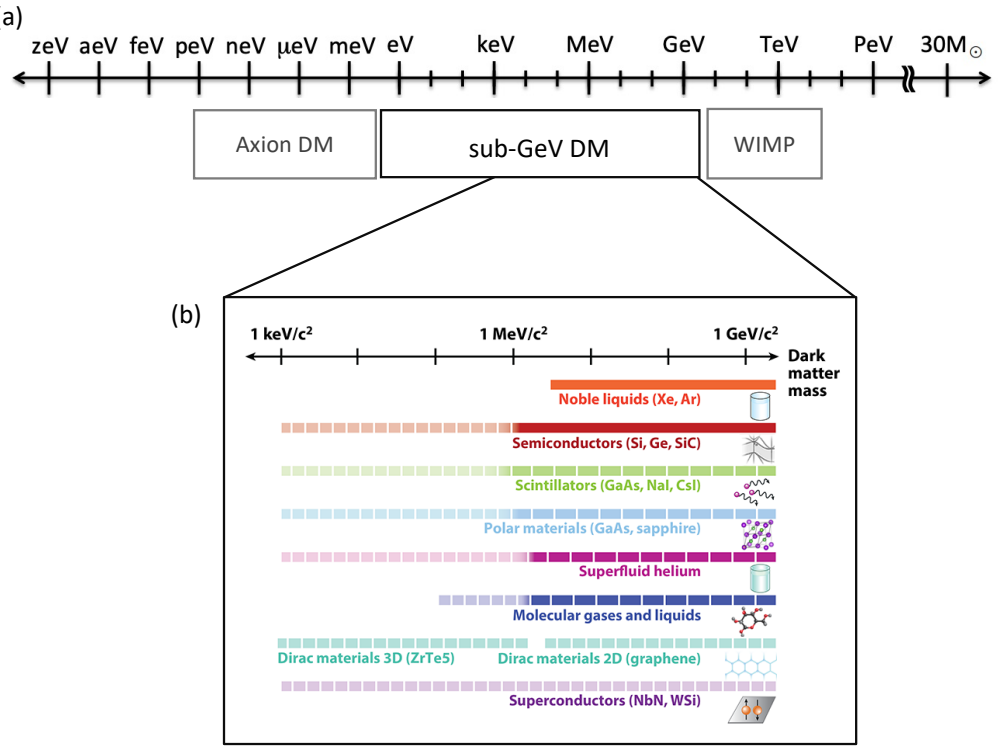


Figure 1.6: (a) Parameter space of dark matter (DM) mass showing the sub-GeV regime between WIMP and axion DM predictions. (b) Experiment proposals for sub-GeV dark matter searches. Materials in use are indicated by solid lines, while those under consideration for the near-term and long-term are shown by solid-dashed and light-dashed lines, respectively. The horizontal scale indicates the mass-sensitivity range. Figure adapted from ref. [58].

1.4.2 *n*-type GaAs as a Cryogenic Scintillating Target

Scintillators are a widely adapted experimental target for direct dark matter searches [59]. In direct DM searches, when dark matter particles interact with electrons in a scintillating material, they deposit energy, causing the material to emit photons through radiative de-

Acceptor	Energy Level	Wavelength
Shallow defects	1.44 eV	861 nm
Ionized boron on arsenic site	1.33 eV	930 nm
$Si_{Ga}V_{Ga}$ complex	1.16 eV	1069 nm
$Si_{Ga}V_{Ga}Si_{Ga}$ complex	0.93 eV	1333 nm

Table 1.1: Radiative acceptors in *n*-type GaAs and their associated energy levels and wavelengths.

cays. These photons are then detected by sensitive detectors, providing a measurable signal that can be analyzed to infer the presence of dark matter. As a novel cryogenic scintillator, *n*-type Gallium Arsenide (GaAs) features a band gap of 1.52 eV and desirable properties as a target for the MeV/c^2 mass range, which falls within the poorly explored sub-GeV regime [60]. An *n*-type GaAs target coupled to a single photon detector is the system of interest that this work will focus on. *N*-type GaAs doped with silicon (Si) and boron (B) was first proposed as a cryogenic scintillator for the detection of sub-GeV DM via electron recoils due to its high luminosity and the commercial availability of large, high-purity crystals[61–63]. Scintillation photons are emitted from *n*-type GaAs via the following process:

(1) Electronic excitation leaves one or more holes in the valence band

(2) Acceptors trap the valence band holes

(3) The acceptor holes recombine radiatively with delocalized donor band electrons and scintillation photons are emitted

The emission wavelengths are thus dependent on acceptor energy levels. Known acceptors and their associated energy level/corresponding scintillation wavelength are listed in table 1.1 [64]. Scintillation in the 930 nm band is the most dominant. Figure 1.7 adapted from ref [62]shows the x-ray excited luminescence spectra of *n*-type GaAs doped with silicon and boron measured with silicon and InGaAs CCDs at 10K, where the contributions from these different radiative decay processes can be seen. The relative intensities of

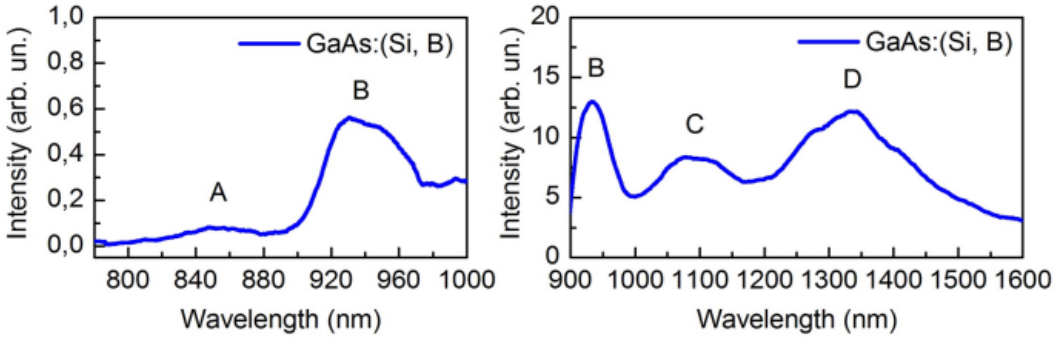


Figure 1.7: X-ray excited luminesence spectra of *n*-type GaAs doped with silicon and boron measured with a silicon CCD (left) and an InGaAs CCD (right) showing the near-infrared emission bands. Figure adapted from ref.[62].

the emission bands depend on the dopant and free carrier concentrations, as do the decay timescales.

One of the most desirable features of *n*-type GaAs compared to other cryogenic scintillators is its lack of afterglow [60], the emission of scintillation photons at long time scales after a particle interaction has occurred. In order to avoid these afterglow effects in GaAs, the samples must be doped above the so called Mott transition [65]. In cooling the crystals from room temperature to below 1 K, some of the free carriers bind to individual silicon atoms at an energy level 2.3 meV below the conduction band, and repulsion then forces the additional electrons into the next higher available energy level, which is in the conduction band. Electrons in the conduction band remain highly mobile down to 0 K, and they serve two purposes: (1) annihilation of any meta-stable radiative states that would result in unwanted afterglow, and (2) efficient combination with electron holes to maximize the prompt scintillation light (the desired signal).

To demonstrate this, figure 1.8 adapted from reference [63] shows the intensity of the scintillation light emitted from a GaAs sample at 10K of sample before, during, and after

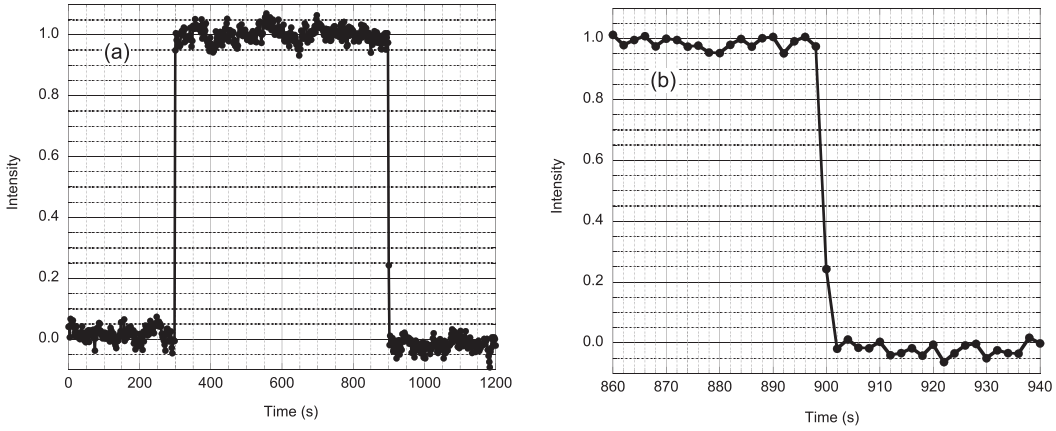


Figure 1.8: Figure adapted from ref [63] showing (a) the normalized intensity of emitted scintillation light before, during, and after irradiation with 50 keVp X-ray beam and (b) an inset showing the time during which the shutter closed. Of note is the sharp return to a baseline around 0 intensity after irradiation.

a 600 second exposure to the 50 keVp X-ray beam. The scintillation intensity is cleanly correlated with the opening and closing of the excitation beam shutter with no lingering emission after irradiation, as shown by the return to a baseline around 0 intensity.

1.4.3 DM Detection concept using *n*-type GaAs

In the detection concept that is the focus of this work, photons are emitted from *n*-type GaAs after excitation by DM-electron scattering or absorption of DM by an electron and subsequent radiative recombination. The near-infrared scintillation photons are then detected by an SNSPD. The signal associated with a DM – electron interaction depends on the mass of the DM particle and the interaction. In a DM-electron scattering event, for the case that the DM particle is heavier than an electron (the case relevant for *n*-type GaAs as a target material), the maximum energy transferred is the kinetic energy of the DM. Given a galactic DM velocity $v_\chi = 10^{-3}$ c, where c is the speed of light, a $10\,\mathrm{MeV/c^2}$ DM particle transfers

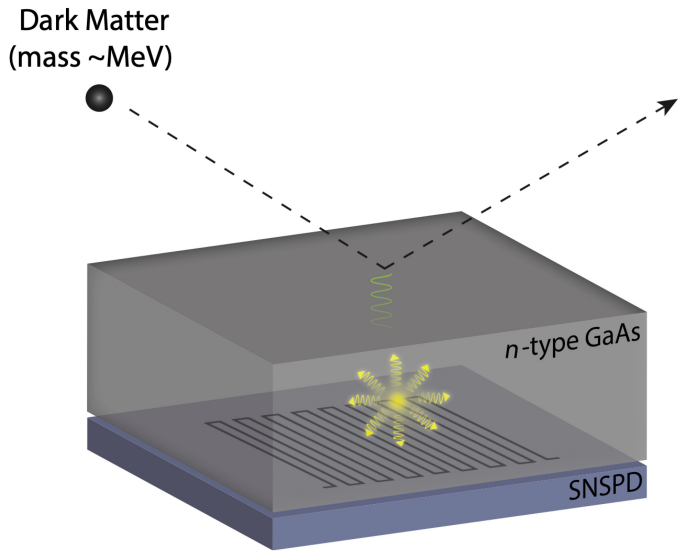


Figure 1.9: Schematic depiction of the detection concept: a DM particle scatters off (or absorbs onto) an electron in *n*-type GaAs, exciting it to a higher-energy level; scintillation photons are emitted through radiative recombination processes; these are subsequently detected by the SNSPD array

$$E_e \leq \frac{1}{2} m_\chi v_\chi^2 \lesssim \frac{1}{2} (10\,\mathrm{MeV})^2 \left(10^{-3} c\right)^2 \lesssim 5\,\mathrm{eV}\ [39]. \tag{1.14}$$

A 5 eV energy deposit into *n*-type GaAs leads to the emission of 3–4 scintillation photons given its 1.52 eV band-gap.

In a DM-electron absorption event, the DM transfers all of its rest mass to the electron. The energy transferred to an electron is thus given by simply the DM mass [39]:

$$E_e \approx m_\chi c_\chi^2 \approx m_\chi. \tag{1.15}$$

In principle, using *n*-type GaAs as a target, bosonic DM (dark photons, scalars, and axion-like particles) can be probed via absorption onto electrons in *n*-type GaAs for DM masses down to 1 eV [48].

Figure 1.10 shows projections for GaAs as a scintillating target for dark photon absorption with sensitivity down to one or more photons.

Figure 1.11 shows projected sensitivities of the dark matter - electron scattering cross section as a function of dark matter mass for GaAs targets, given exposures of 1g-month to 10kg-years for two different form factors.

1.4.4 Sensor Classes for *n*-type GaAs and Low Mass DM Targets

The sensor requirements for the scintillation photons emitted from *n*-type GaAs are high sensitivity in the near-infrared, low dark count rate, and cryogenic operation. Given this, superconducting devices are natural candidate to develop detection concept. It should be noted that the development of SNSPDs for this detection concept will extend to many other experiments in the dark matter detection landscape in the future.

SNSPDs are typically operated at sub-kelvin cryogenic temperatures and have been

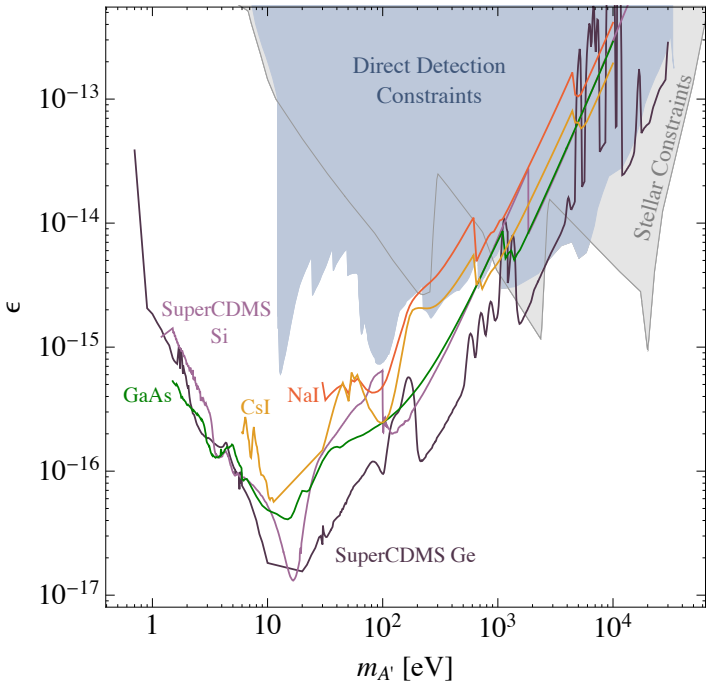


Figure 1.10: Constraints (shaded regions) and projected sensitivities (solid colored lines) for dark photon dark matter. The yellow, orange, and green solid lines show projected sensitivities for hypothetical experiments with the scintillating targets CsI, NaI, and GaAs, assuming an exposure of 10 kg-years. Figure adapted from ref. [48].

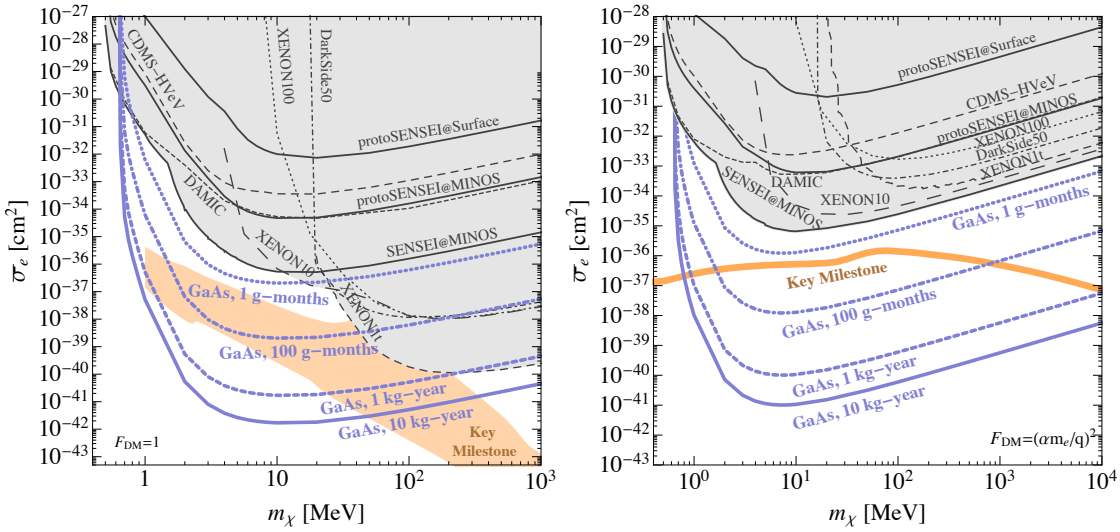


Figure 1.11: Projected sensitivities (blue lines) to dark-matter-electron scattering mediated by a heavy mediator (**left**) or light mediator (**right**) of a GaAs target assuming for different exposures (1g-month, 100g-month, 1 kg-year, 10 kg-year). We assume zero background events for events with one or more photons, a radiative efficiency of 1, and a photon detection efficiency of 1. Existing constraints are shown in gray from SENSEI, DAMIC at SNOLAB, XENON10, XENON100, XENON1T, DarkSide-50, and CDMS-HVeV [66–75]. Orange regions labelled "Key Milestone" are from [76].

demonstrated with near-unity system detection efficiency in the NIR and ultra-low dark count rates. The main challenge with SNSPDs in the context of instrumenting large-scale scintillating targets is scaling the active area of SNSPDs to the cm^2-regime while preserving these detection metrics to the greatest extent possible.

As an alternative sensor, TES-based technologies are under development to instrument *n*-type GaAs. TES are somewhat maturely developed for nuclear recoil DM experiments. In large collaborations such as SuperCDMS [45], large-area cryogenic detectors, with a total area of 45 cm^2, utilizing TES-based athermal phonon sensors have achieved 4 eV energy sensitivity [45]. Given that $\sigma_E \propto \sqrt{A}$, where A is the total instrumented area, resolutions of 600 meV in 1 cm^2 detectors are feasible given the current state-of-the-art. Extending athermal phonon sensors to lower mass electron recoil DM searches will entail design features such as lowering the critical temperature (T_c) of the TES and optimizing sensor geometry

to improve athermal phonon collection efficiency. This would enable further enhancements in sensitivity and expand the instrumented active area per channel beyond $1\,\mathrm{cm}^2$.

In GaAs, both phonons and NIR photons are produced after excitation. The TESSERACT collaboration is developing both nuclear recoil and electron recoil experiments with the approach of exploring multiple target materials and developing multiple detection strategies. One of the developing ER experiments involves *n*-type GaAs instrumented with TES-based athermal phonon sensors. The prototype design includes a $1\,\mathrm{cm}^3$ GaAs target instrumented with athermal phonon sensors on its surface, and inside an optical cavity with a $1\,\mathrm{cm}^3$ x 1 mm thick Ge crystal that serves as an infrared photon collector [77]. TES readout offers the possibility to use the same detector to measure both scintillation and phonons in coincidence which can give background discrimination capabilities. The main challenge to TES readout for low energy threshold DM experiments is the low energy excess (LEE), the observed increase in event rates or signals at low energy thresholds that are not accounted for by known backgrounds or expected detector noise. Nearly all experiments instrumented with phonon sensors with sufficiently low energy thresholds see a this steeply rising event rate [78–81]. Efforts to understand the origin of [82] and mitigate the LEE are ongoing.

Chapter 2: Superconducting Nanowire Single Photon Detectors

2.1 Introduction

Since their first demonstration by Golt'sman et al. in 2001 [83], superconducting nanowire single photon detectors (SNSPDs) have emerged as detector for time correlated single photon counting from the UV to the near-infrared. Specialized devices have shown detection efficiency of 98% at 1550 nm [84], timing jitter as low as 2.7 ps [85], intrinsic dark count rates of 6×10^{-6} counts per second [86], and energy thresholds as low as 42.8 meV (wavelength 29 μm) [87]. Many of these demonstrations have involved detectors that are optimized for one performance metric at the expense of others. As a relatively new detector technology, one of the challenges for SNSPDs is to realize devices that perform well across multiple metrics. This continues to develop as our understanding of the fundamental device physics and intrinsic trade-offs becomes more complete.

SNSPDs have made their way into a wide variety of applications, including quantum optics [88], [89] quantum information science [90–95], imaging [96, 97] and free-space laser communication [98]. Most of these demonstrations involve fiber-coupled light incident on a small, circular active area. Driven by imaging [96] and astronomy[99] applications, the active areas of SNSPDs have grown steadily over the past several years from the order of the cross section of a single-mode optical fiber core (10s of μm^2) to arrays with active areas in the mm^2 regime [100]. Large-scale arrays up to kilopixel [101] and now megapixel-scales [102] have been developed using row-column [103] or ther-

mal row-column multiplexing techniques[104] that provide spatial resolution, and time-of-flight readout bus multiplexing for large scale cameras [102].

Recent developments in nanofabrication, device characterization, and modeling of fundamental device physics have pushed forward the performance of SNSPDs in their historical strengths as single photon detectors, revealing novel applications in fundamental physics. The project described in this paper will focus on the development of SNSPDs for dark matter searches using cryogenic scintillating targets. With sufficient research and development of the technology, these SNSPDs have the ability to provide new capabilities for low-mass dark matter searches and across many areas of High Energy Physics.

2.2 Device Operation Principles

SNSPDs are constructed from current-carrying nanoscale wires. Typical devices have wire widths from 10s to 100s of nm and thicknesses of 2-10 nm. A common technique to achieve high optical coupling efficiency and absorption is to meander the nanowire over the active area with a high fill factor. SNSPDs are usually operated from 1–4 K depending on the superconducting materials used (WSi, MoSi, NbTiN, NbN, etc.) with a DC bias current applied through a bias tee. In parallel with the nanowire is the readout arm which consists of a load impedance, usually the input to a readout amplifier. The readout portion can be DC or AC coupled. A schematic of the photon detection mechanism in SNSPDs is shown in figure 1. The detection cycle begins with the nanowire in the current-carrying superconducting state. When a photon is absorbed in the cross section of the nanowire, it triggers a cascade of events that ultimately leads to a detection signal. Qualitatively, this cascade can be understood as follows: absorption of a photon leads to the formation of electron-hole pairs, which through a down-conversion process transfer their energy into a hot-spot of excited quasi-particles and high energy phonons. The evolution of this hot-spot leads to the

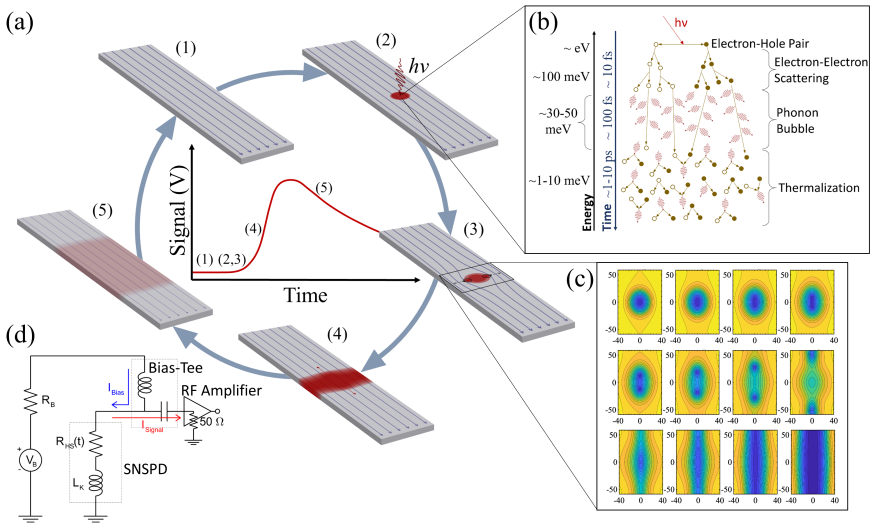


Figure 2.1: (a) Schematic depiction of the SNSPD photon detection mechanism reproduced from [105]. The device begins in the current-carrying superconducting state (1) until a photon is absorbed (2) which generates a hot-spot of excited quasi-particles and high-energy phonons through a down-conversion process depicted in (b). The evolution of this hot-spot destabilizes the superconducting state and leads to the formation of vortices, which are depicted in (c). Current flow causes the vortices to move (3), and they dissipate energy, causing the formation of a normal domain across the entire cross-section of the nanowire. The normal domain propagates along the length of the wire (4), which increases the impedance of the device. This change in impedance diverts current from the nanowire to the readout circuitry, leading to a voltage transient (center). Once current is diverted to the readout, the nanowire cools, recovers to the superconducting state, and current returns to the device. (d) A typical SNSPD is operated using a bias-tee with the DC port carrying the bias current and the RF port coupled to a low-noise amplifier.

instability of the superconducting state, and vortices form. The dissipative vortex evolution leads to the formation and growth of a normal domain which spreads along the length of the nanowire, increasing the impedance of the device, until the nanowire transitions fully into the normal state. At this time, the bias current gets diverted into the readout electronics. The nanowire then cools and recovers to its superconducting state, and its impedance decreases until the bias current returns fully to the device. In typical SNSPDs, the photon absorption and hot-spot formation phase typically occurs on a picosecond timescale, and the recovery phase timescale which is set by the kinetic inductance of the nanowire, is on the order of nanoseconds[105].

Traditional SNSPDs are comprised of nanowires with widths $\mathcal{O}(100\,\text{nm})$ meandered over the photoactive area and are fabricated using electron-beam lithography (EBL) to achieve the required resolution and optimal performance. Recent advances in the preparation of thin superconducting films have enabled the fabrication of a novel class of single-photon detectors with wire widths of several micrometers. Microwire devices offer many advantages over traditional nanoscale devices for applications such as dark matter searches where large active areas area required, as they are amenable to fabrication via optical lithography - a more scalable fabrication process than electron beam lithography which is used to fabricate traditional devices [106].

2.3 Detection Metrics

This section reviews some of the detection metrics of SNSPDs, following ref [107] and the current state-of-the-art for each metric.

2.3.1 Detection Efficiency

The system detection efficiency (SDE) is the probability of registering an electrical output signal produced by a photon once the photon has entered into the the photon detection system. The SDE can be thought of as being comprised of multiple components:

$$SDE = \eta_{coupling} \cdot \eta_{absorb} \cdot \eta_{internal} \cdot \eta_{trigger}, \tag{2.1}$$

where $\eta_{coupling}$ is the efficiency of the delivery of light to the active area of the device, η_{absorb} is the probability that a photon incident on the detector's active area gets absorbed into the material, $\eta_{internal}$ is the probability that an absorbed photon results in an observable output pulse, and $\eta_{trigger}$ is the efficiency of the readout electronics in registering the output signal as a detection event.

While conceptually useful, it is often difficult to accurately measure each separate component of SDE. Instead, it is conventionally measured by using the following relation:

$$SDE = \frac{R_{light} - R_{dark}}{R_{incident}}, \tag{2.2}$$

where R_{light} is the recorded count rate when the device is under illumination, R_{dark} is the count rate recorded when the device is not under illumination (background count rate), and $R_{incident}$ is the incident rate of photons delivered to the detector.

The current state-of-the-art result for the highest SDE is 98% for the TE polarization (electric field parallel with the nanowire grating) at 1550 nm in a MoSi SNSPD developed by the NIST group [84]. This was achieved using an optical stack with distributed Bragg reflector (DBR) mirrors and a 50-μm diameter active area.

2.3.2 Dark Count Rate

A dark count in a photodetector is defined as an output pulse that registers as a detection event in the absence of an incident photon. The dark count rate (DCR) can be expressed as:

$$DCR = R_{intrinsic} + R_{background} + R_{electronic}. \tag{2.3}$$

The intrinsic dark counts, $R_{intrinsic}$, in SNSPDs result from spontaneous resistive state formation. At the temperatures at which SNSPDs operate (1–4 K), it has been shown that the primary phenomenon underlying intrinsic dark counts is thermally activated vortex-anti-vortex pair unbinding [108] or vortex entry and crossing from the nanowire's edge. This effect is exacerbated by geometric factors [109, 110], such as constrictions in the nanowire width or sharp bends at the ends of meanders, where it is observed that dark count rates increase [110]. In these regions, increased current density from current crowding [111–114] lowers the barrier for both vortex entry and vortex-anti-vortex unbinding.

Background counts, $R_{background}$, primarily result from spurious photons reaching the detector's active area, originating from black-body radiation outside or within the cryostat. Spurious photons can also arise from Cherenkov radiation in materials surrounding the detector or from transition radiation from charged particles passing through boundaries between media with different dielectric properties. The background count rate in a given system, $R_{background}$, can be reduced through appropriate shielding around the detector, the implementation of light-tight packaging, the use of mid-IR absorbing paint on areas surrounding the detector in the cryostat, and spectral filtering to attenuate the black-body radiation reaching the detector. This is a particularly important consideration for rare-event search applications such as dark matter detection.

The electronic noise component, $R_{electronic}$, arises from electronic noise which causes

the readout electronics to register a detection click that did not originate from the detector itself. This can be mitigated by using low-noise cryogenic amplifiers, or if the waveforms of an SNSPD are measured on an oscilloscope, pulse shape discrimination between an actual SNSPD output pulse and a detection event caused by electronic noise can be implemented.

The current record for the lowest DCR observed in an SNSPD was measured to be 6×10^{-6} cps in a WSi SNSPD with an active area of 400 µmby 400 µm, measured at 300 mK [115].

Chapter 4 of this thesis details the study of the dark count rates in large-area microwire arrays and efforts.

2.3.3 Timing Resolution

Because SNSPDs are used for time-correlated single-photon counting, timing resolution is an important detection metric. The timing resolution is typically characterized by the instrument response function (IRF), which is measured by comparing the detector response to a reference. Typically, the full width at half max (FWHM) of the IRF is taken to be the timing jitter of the device. The measured IRF has contributions from intrinsic and extrinsic IRFs. Extrinsic contributions from electrical and amplifier noise can broaden the IRF [116, 117], and a lot of work has been done in the SNSPD community to engineer low-noise cryogenic amplifiers and readout to minimize this. Intrinsic contributions include contributions from the stochastic nature of energy down-conversion in the superconductor after photon absorption and those from geometric jitter, geometric inhomogeneities, and constrictions in the device. These dominate in large-scale meander arrays. Chapter 3 details these effects and presents jitter measurements in large-area microwire arrays.

Sub-3-ps jitter has been demonstrated in specialized 5-μm-long niobium nitride (NbN) devices that were designed to minimize intrinsic (down-conversion) and geometric jit-

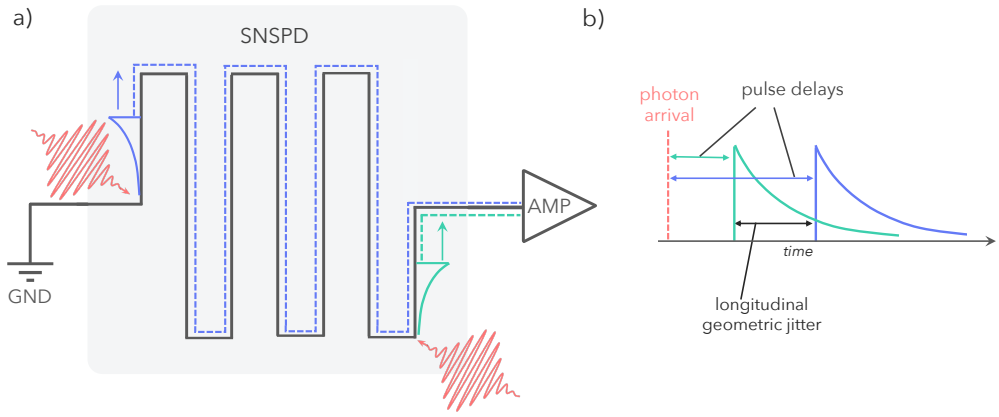


Figure 2.2: The origin of longitudinal geometric jitter is shown in (a), where the microwave signals associated with photon detection events along different segments of the nanowire have different lengths to travel. This leads to different delay times relative to the photon arrival, shown in (b).

ter [85].

2.4 Design Tradeoffs for Large-area SNSPDs

2.4.1 Active Area vs Timing Performance

There is an intrinsic trade-off between the active area and timing performance in SNSPDs. Increasing the active area of an individual pixel also increases the length of the nanowire, which in turn increases the kinetic inductance. The recovery timescale in SNSPDs is governed by the relationship $T_r = \frac{L_k}{R_L}$, where L_k is the kinetic inductance and R_L is the load resistance. Because of this direct proportionality, the recovery timescale (T_r) will be slower in SNSPDs with longer wire lengths, which will also limit the maximum count rate achievable by the detector. Additionally, longer nanowires have greater longitudinal geometric jitter, which arises from propagation delays due to detection events at varying locations along the nanowire's length. The origin and effect of longitudinal geometric jitter on delay times in the onset of the SNSPD detection pulse are shown in figure 2.2. This effect can be

mitigated using differential readout, in which both ends of the nanowire are connected to readout circuits. In this configuration, when a photon is absorbed at a particular position in the nanowire, the counter-propagating positive and negative voltages pulses counter propagate, and the arrival times of the signals at the two ends are which are slightly offset from each-other can be analyzed such that the propagation delay effects are canceled out.

Larger SNSPD pixel areas have more bends and a greater probability of constrictions occurring along the nanowire length. Constrictions have the effect of locally increasing current density and causing suppressed I_{switch} . This prevents operation at higher I_{bias}, at which the jitter performance is better due to enhanced signal-to-noise ratio (SNR).

2.4.2 Array Size vs Readout Complexity

One way to alleviate the constraints described in the previous subsection, where larger SNSPDs have the intrinsic trade-off of lower timing resolution, and a reduced maximum count rate (slower recovery time), is to design an SNSPD array in which multiple pixels operate in parallel. Direct readout of individual pixels increases thermal load in the cryostat and readout complexity. Given this, the mm^2-scale arrays studied in this work have been designed in linear array formats. These arrays, with pixel counts of 4, 8, and 16, are feasible for direct readout. The direct, single-ended readout scheme employed in this work has been scaled to 64-pixel arrays [118]; however, in the pursuit of cm^2-scale devices with thousands of pixels, this approach isn't scalable. Multiplexing techniques reduce the number of coax lines required to bias and readout arrays.

2.5 Large-active area SNSPDs

In recent years, the active areas of SNSPDs have steadily increased from the scale of a single-mode optical fiber diameter ($\sim 100\,\mu m^2$) to the mm^2 regime [119]. As new applica-

tions for SNSPDs that leverage these large active areas emerge, there is a growing interest in exploring novel materials and device architectures. For applications in high energy physics such as dark matter (DM) searches, it is necessary to realize SNSPDs with larger active areas than the current state-of-the-art, by at least an order of magnitude. Scaling devices beyond the mm^2 regime remains an open question that presents many challenges in terms of design, fabrication, and readout.

2.5.1 Materials

The question of which materials are best for large-active area SNSPD fabrication remains an open topic in the community. For scaling to mm^2 active areas and beyond with large pixels sizes, it is an open question which approach to take as far as the material selection. The challenge is to yield a thin-film superconductor with high material homogeneity over a large active area. WSi and MoSi are promising materials for large active-area detectors since the films are amorphous and are, thus, expected to be very homogeneous over large areas compared to polycrystalline superconductors such as NbN or NbTiN. Producing a thin-film superconductor with a large area is generally easier with an amorphous material than with a polycrystalline one. Amorphous superconductors lack the grain boundaries present in polycrystalline materials, which can interrupt superconducting pathways and create weak links between grains. This uniformity makes amorphous films less prone to structural defects over large areas, which is beneficial for achieving consistent superconducting properties across the entire film. In polycrystalline films, grain boundaries introduce stress and dislocations that are amplified over large areas. Amorphous films, being structurally homogeneous, have fewer internal stresses and are more resilient over larger areas. Additionally, amorphous films are easier to deposit over large areas because their lack of well-defined crystal structure makes them less sensitive to the surface on which

they're deposited. This allows for more flexibility in deposition conditions and substrates, making it simpler to produce large, uniform films without needing the precise conditions required for well-formed crystal growth in polycrystalline films. The substrate versatility of amorphous superconductors was shown with MoSi in reference, wherein MoSi deposited on a passivated GaAs surface was observed to have the same critical temperature as MoSi deposited on silicon, and the detection metrics of the devices fabricated from both of these were very similar [120].

2.5.2 Device architecture

In traditional devices, nanowires are often patterned in a meander geometry to enhance optical absorption. This design allows the nanowire to cover a larger area by folding back and forth in a continuous, closely packed pattern, thereby increasing the likelihood that an incoming photon will interact with the detector.

The fundamental unit enabling superconducting meanders is the hairpin bend, which consists of a single 180° turn connecting two wire segments. However, one of the main factors limiting the performance of meander-based SNSPDs is the current crowding effect, particularly in the bending regions [111, 112]. In SNSPDs, current crowding occurs when the super-current density increases at sharp bends, corners, or discontinuities in the nanowire. This localized increase in current density can surpass the superconductor's switching current, I_{switch}, causing the SNSPD to transition to the normal state prematurely. As a result, the performance of the detector is degraded.

Additionally, the higher current density in the bends lowers the energy barrier for vortex entry, which is a primary cause of dark counts in SNSPDs. Thermally activated vortices can lead to an increase in dark count rate, further degrading performance by decreasing the signal-to-noise ratio [113]. The impact of current crowding becomes more pronounced in

meanders with higher fill factors.

To mitigate these effects, several strategies can be employed. One approach is to use bend thickening techniques, which help reduce the localized current density in the bending regions [113, 114]. Additionally, the design of the bends can be optimized to minimize current crowding and the associated enhancement of dark counts. Specifically, sharper bends with smaller inner radii tend to degrade performance, while rounded bends with smoother transitions are more effective [109, 111]. Another technique to improve current crowding effects involves helium ion irradiation of the straight segments of the meander [121].

Nanowire vs Microwire Detectors

In 2020, single photon sensitivity in micrometer-wide superconducting wires was first demonstrated in small microstrip devices [122]. Near-IR photons were detected in a device made from a 3.3 nm-thick MoSi film with 2 μm-wide wires. This led to increased interest in developing microwire devices with non-trivial active areas and an exploration of new materials. Near-IR photon sensitivity in wires as wide as 4 μm and with active areas as large as 1 mm^2 have since been reported [123], with similar results seen in NbN devices[124].

2.6 SNSPDs for Dark Matter Detection and HEP Applications

SNSPDs are the single-photon detector of choice for quantum information science and technology applications. However, their unique combination of high timing resolution, low dark count rates, and a response over a broad range of wavelengths makes the technology attractive for HEP applications. In particular, SNSPDs can be used in low-mass DM experiments where the primary sensor requirements are (1) (vanishingly) low intrinsic dark count rates, (2) a high photon detection efficiency and (3) low energy thresholds for infrared single photon detection. For these metrics, SNSPDs are the highest performing detectors

available in separate demonstrations. To mature the technology for DM detection, it is necessary to combine these performance metrics into one device and understand the inherent trade-offs. This is a central focus of the work contained within this thesis. Additionally, it is important to investigate the fundamental limits of the aforementioned detection metrics for SNSPDs.

There are now multiple pilot and proof-of-concept phase low mass dark matter detection experiments using SNSPDs in the detection scheme. The development of large-active area SNSPDs to instrument *n*-type GaAs targets is one of the primary focuses of the work contained in this thesis. Light A' Multilayer Periodic Optical SNSPD Target (LAMPOST) is a dark photon search targeting DM in the eV mass range, via coherent absorption in a multilayer dielectric haloscope [115]. The layered dielectric target is designed to capture the conversion of dark photons to regular photons which are then focused onto an SNSPD. In this detection concept, the sensitivity is ultimately governed by the limits of the SNSPD and in principle as the energy thresholds of SNSPDs are lowered, versions of this experiment that probe lower mass dark photon DM can be implemented to constrain more of the parameter space at lower masses. Of interest to this future direction are mid-infrared SNSPDs whose current status and challenges are summarized in the next section.

The Broadband Reflector Experiment for Axion Detection (BREAD) experiment features a cylindrical metal barrel to convert dark matter into photons and parabolic reflectors to focus signal photons onto a photosensor [125, 126]. This science program contains two pilot experiments. GIGABread is the RF pilot axion and dark photon experiment targeting DM in the tens of GHz regime and focuses them onto a coaxial horn antenna. INFRABread is the program's pilot dark photon search at IR frequencies. The detectors developed and characterized in this thesis are being deployed as the photo sensors for this pilot experiment. More on the current status of this implementation is described in chapter 8.

In addition to their use in low mass DM searches, the mm^2-scale arrays from this work

are also large enough to be potentially interesting technology for broader HEP applications. One of the 8 pixel 2 mm x 2mm SNSPD arrays of this work was deployed in the Fermilab Test Beam Facility and exposed to various high energy particles [127]. The results are described in Chapter 8 and are a promising step towards developing SNSPD sensors optimized for high energy particle detection and identification for future accelerator-based experiments.

Chapter 3: Large Active Area SNSPD Design and Characterization

This chapter details the design and performance characterization of large active-area SNSPDs. The primary application of these arrays is their hybridization with *n*-type GaAs,which is described in chapter 5 and 6. The work presented here aims to optimize the performance of SNSPDs and understand the limitations.

The SNSPDs used for measurements in this chapter were fabricated by Ekkehart Schmidt, Sahil Patel, and Emanuel Knehr in the Microdevices Laboratory (MDL) clean room at JPL. All measurement setups described in this chapter were constructed as a part of this thesis research, and all of the described measurements were performed and analyzed independently as a part of this thesis research.

3.1 Background

The context of the large active area arrays studied in this chapter can be understood in thinking about scaling the dark matter detection concept using *n*-type GaAs targets. Referring back to figure 1.11 where the projected sensitivities of GaAs to DM-electron scattering were plotted, we consider the requirements for instrumenting the quoted target masses of 1 g , 1 kg , and 10 kg with SNSPD sensors. It is as assumed that the GaAs material is homogeneous and the SNSPDs are evenly distributed across the target area.

For a 1 g target mass of GaAs with a thickness of 0.5 cm and an SNSPD pixel size of 1 mm^2, approximately 38 SNSPD pixels would be required to instrument the target,

resulting in a total active area of about 1 cm^2. For a larger 1 kg target mass, the GaAs thickness is increased to 10 cm, and the SNSPD module is defined, where each SNSPD module has a size of 1 cm^2 with 100 pixels per module. This configuration would require roughly 1,900 pixels to fully cover the target, resulting in an active area of about 10 cm^2. Finally, for the largest quoted target mass of 10 kg with the same GaAs thickness of 10 cm, the SNSPD module size is further increased to 2 cm^2, with 100 pixels per module. This results in the need for around 4,700 pixels to cover the target, which equates to a total active area of about 100 cm^2.

These calculations are based on the assumption that the GaAs material is homogeneous and that the SNSPDs are evenly distributed across the target area. Additionally, the pixel sizes are fixed at 1 mm^2, 1 cm^2, and 2 cm^2 for each of the respective module sizes, ensuring that the required photon detection capacity is met as the target mass increases. The scaling of the SNSPD array and active area is directly related to the target mass and the geometry of the GaAs material, which are both crucial for optimizing the performance of the detector system.

With this scaling in mind, one of the key challenges is efficiently fabricating a large number of pixels. Optical lithography is a promising solution for this issue, as it allows for the efficient patterning of the large pixel arrays. Over the past few years, the yield of photolithography-fabricated devices has significantly improved, making it a feasible option for producing high-performance SNSPDs at larger scales.

Another challenge lies in the scalable readout of these many pixels. With an increase in the number of pixels, the complexity of the readout system also grows, which increases the heat load, and the complexity of cryo-coolers required for operation. To address this, multiplexing techniques can be employed to reduce the number of coaxial lines required for biasing and reading out the array. The discussion of multiplexing techniques is left to the conclusion chapter, as their potential applications for next-generation microwire arrays

will be explored in future work.

In general, scintillation light is emitted when atoms and molecules are excited by radiation, such as gamma or particle radiation. These transitions are inherently isotropic because they depend on the intrinsic properties of the energy states rather than external directional factors. Given the isotropic nature and random polarization of scintillation light, efficient collection requires a sensor with the following properties:

1. Large active area
2. High system detection efficiency over the range of scintillation wavelengths
3. High system detection efficiency over a broad range of incident angles
4. Polarization insensitivity

To meet the requirement for a large active area, linear arrays with micron-scale wire widths were chosen as the device architecture. This design facilitated the realization of mm^2-scale SNSPDs while ensuring scalability to cm^2-scale devices and beyond. SNSPDs with micron-scale wire widths have the advantage that it is easier to cover larger active areas, and the larger feature sizes and are more compatible with optical lithography processes for scalable fabrication. In contrast, traditional SNSPDs comprised of nanowires with widths nm-scale widths meandered over the photoactive area are fabricated using electron-beam lithography (EBL) to achieve the required resolution and optimal performance.

To date, SNSPD development has primarily focused on applications involving fiber-coupled light that is normally incident. Challenges and approaches to improving system detection efficiency across a broad range of incident angles using optical stacks with DBR back-reflectors are discussed in Chapter 7. Polarization-insensitive designs have been

Table 3.1: Properties of the films used for detector nanofabrication

Name	Substrate	Film	Stoichiometry (W:Si)	Thickness	Sheet Resistance	ρ_{300}	T_C	Fabrication
Film1	Si	WSi	52:48 ±10 %	2.2 nm	1000 Ω	220 μΩ cm	2.6 K	e-beam lithography
Film2	SiO_2	WSi	70:30 ±1 %	5.1 nm	570 Ω	177 μΩ cm	3.25 K	e-beam lithography
Film3	SiO_2	WSi	42:58 ±1 %	4.7 nm	750 Ω	320 μΩ cm	1.9 K	e-beam lithography
Film4	SiO_2	MoSi	unknown	2 nm	1180 Ω	236 μΩ cm	3.4 K	photolithography

demonstrated for normally incident, fiber-coupled light [128] and can be adapted for scenarios involving a broader range of incident angles. Additionally, as discussed in Chapter 7, optical stacks optimized for polarization-averaged light can be designed.

3.2 Generation 1 Microwire Arrays

The first generation of microwire arrays fabricated at JPL are described in ref. [119]. This work investigated 8-pixel SNSPD arrays made from amorphous superconducting thin films including WSi of 3 different stoichiometries and MoSi using both electron beam and photolithography.

3.2.1 Detector Design

The 8-pixel SNSPD array features meander geometry, 1 μm-wide wires, 25% fill factor, and a total active area of 1 mm^2 was fabricated from each material for comparison. Optical and SEM images of the SNSPD active areas are shown in figure 3.1.

3.2.2 Materials

The films studied and fabricated into devices are summarized in table 3.1.

Film 1 was co-sputtered from tungsten and silicon targets using the procedures outlined in Ref. [123]. Films 2, 3 and 4 were deposited onto an oxidized Si(100) substrate with a 240 nm-thick thermal oxide. Film 2 was sputtered from a $W_{50}Si_{50}$ target in an Ar atmosphere at a pressure of 5 mTorr and a sputter power of 130 W. Film 3 was sputtered from a

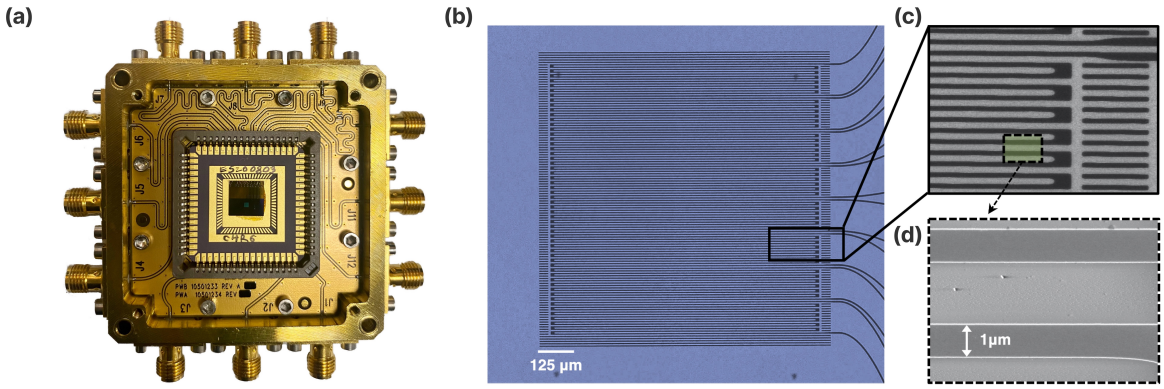


Figure 3.1: (a) A photograph of a mm^2 array in detector packaging (b) Optical image of the detector chip, (c) scanning electron micrograph of the meander, and (d) SEM showing zoomed in view of a micron-wide wire made with photolithography.

$W_{30}Si_{70}$ target in an Ar atmosphere at a pressure of 5 mTorr and a sputter power of 130 W. Film 4 was made by co-sputtering process from Mo and Si targets in an argon atmosphere at a pressure of 2.5 mTorr. The Mo target was DC biased with a current of 130 mA, while 73 W of RF power was applied to the Si target.

3.2.3 Detector Characterization

Cryogenic set-up and Readout

All SNSPDs and composite *n*-type GaAs / SNSPD systems were characterized using a temperature-controlled 880 mK stage of a He^4 sorption fridge. Each of the arrays was individually biased and measured using a DC coupled cryogenic amplifier designed to be compatible with the 1 µs recovery time of the WSi arrays. A schematic of the readout is shown in figure 3.2.

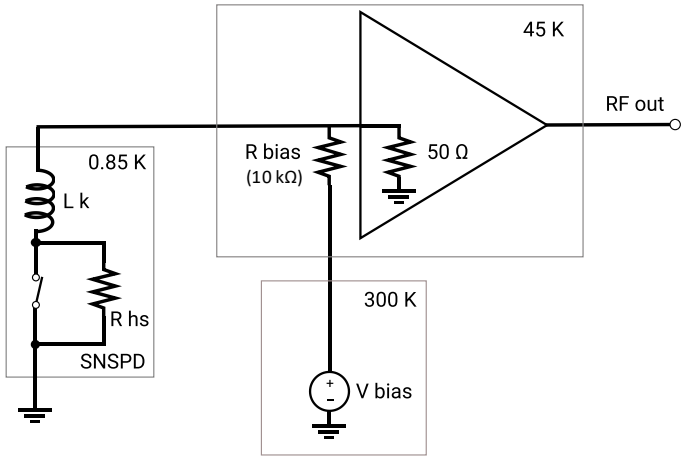


Figure 3.2: Readout scheme featuring DC-coupled cryogenic amplifiers at 40K stage.

Optical Characterization

The Photon count rate (PCR) versus bias current (I_B) was measured at 1064 nm for all devices. A plateau in the PCR curve indicates saturated internal detection efficiency (IDE) , meaning that all photons absorbed in the nanowire lead to a detection event. It is desirable for this plateau to be as long as possible in a device for the target wavelength so that I_B can be chosen in a regime with low background counts (maximizing SNR) and so that fluctuations in I_B don't lead to a fluctuation in the IDE. As shown in figure 3.3, all devices fabricated yielded functional detectors, with the longest plateaus seen for films 1 and 3. This result shows that SNSPDs can be made using photolithography as a scalable (towards cm^2-scale active area) fabrication technique. The film 3 array had the best yield, and a device from that wafer was selected for further characterization and integration into scintillation measurements described in chapter 5. Shown in figure 3.4, the photo-response at 1064 nm and dark count rate of the film 3 array was characterized across all pixels.

Single photon detection is seen in all pixels of the array, and saturated internal detection

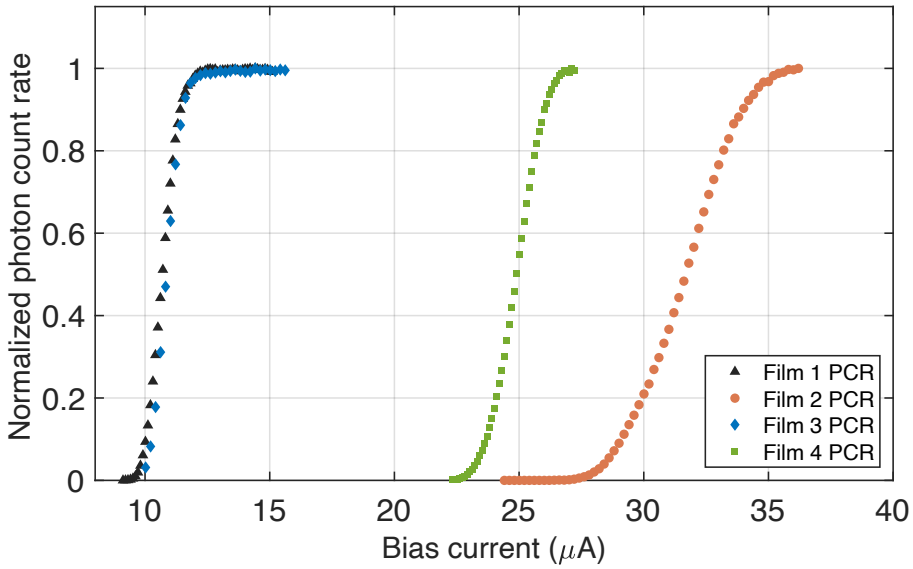


Figure 3.3: Photon count rate (PCR) versus bias current (I_B), normalized on the saturation plateau. The characterization wavelength is 1064 nm.

efficiency in 6/8 pixels. The long plateaus seen in the photon count rate curves in figure 8 for pixels 1–2, 4, and 6–8 are desirable for device operation, as the photon count rate is stable to drifts in current or temperature. Long plateaus also allow the device to be operated at a bias current with low dark counts to optimize SNR.

The bottom plot of figure 3.4 shows the photoresponse at 1064 nm of a single pixel of the array along with the dark count rate shown in light blue measured with a lid to block background photons. The dark count rate with this lid is about 10^{-2} cps at bias currents optimal for operation that are well within the plateau in the PCR curve. In figure 3.5, (a) shows the mm^2 array mounted at the 1K stage of the sorption in the packaging that was used for all measurements in this section, (b) is the lid used for dark count rate measurements, and (c) is the lid used for measurements where optical access was needed (PCR curves, jitter, and efficiency measurements).

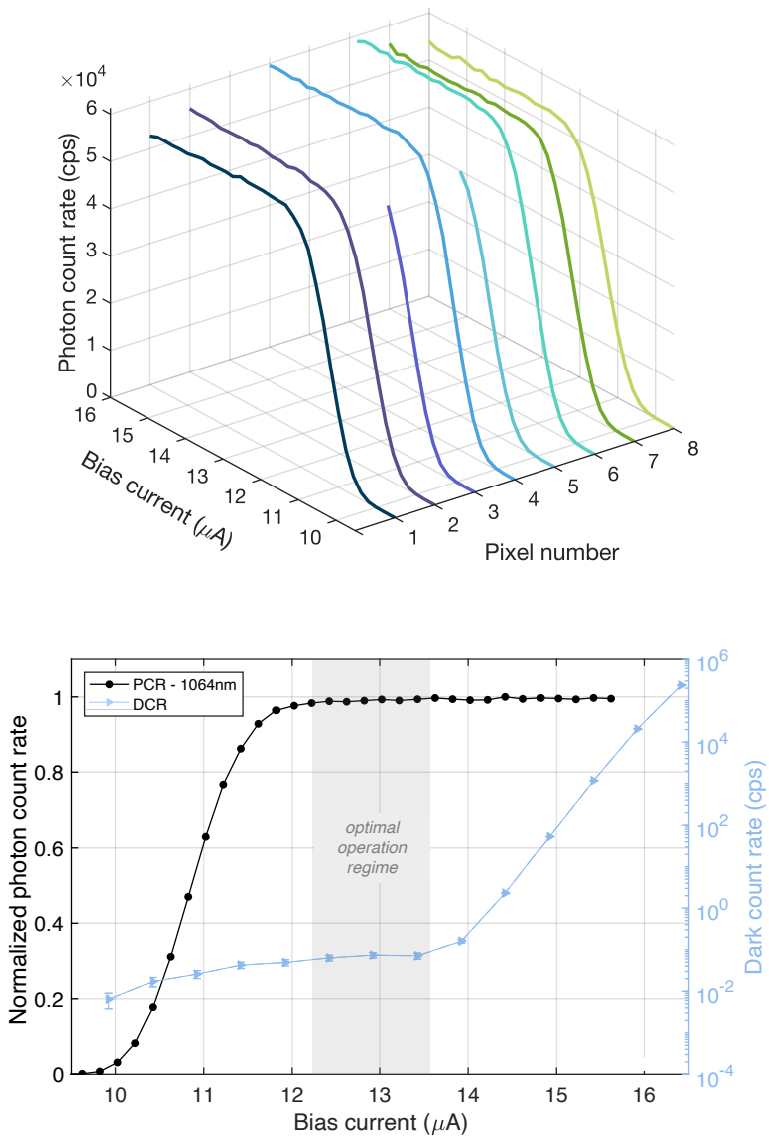


Figure 3.4: (Left) Photon count rate for each pixel of the SNSPD array as a function of bias current. All pixels exhibit single photon sensitivity and all pixels except 3 and 5 have long plateaus. (Right) Normalized photon count rate from pixel 1 of the array with dark count care. The shaded gray area shows the optical operation regime, with the photon count rate on the plateau, and a low dark count rate.

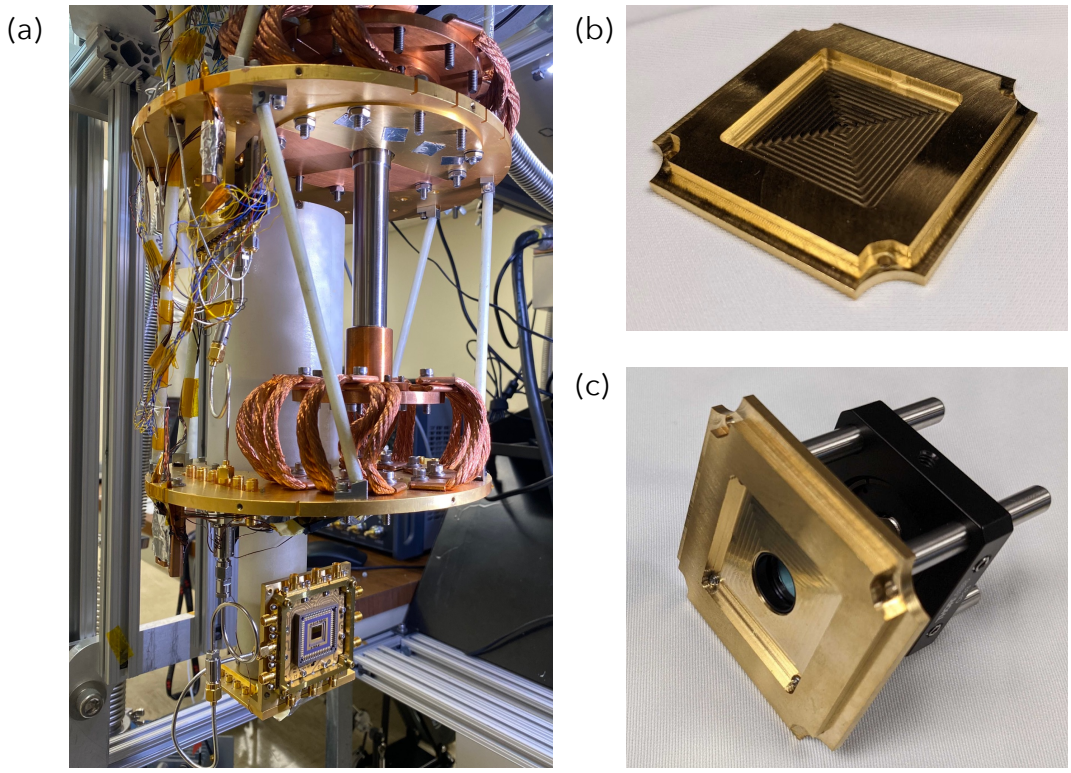


Figure 3.5: (a) a packaged film 3 array mounted onto the 1K stage of the open sorption fridge. (b) shows the lids for dark count measurements and (c) is the lid with optical access with a threaded hole to mount filter stacks.

Efficiency Measurements

The system detection efficiency of an array (SDE_a) is defined as the fraction of photons incident on the detector that are counted by the readout electronics as detection events. The relationship between this and the individual pixel system detection efficiency (SDE_p is $SDE_a = \Sigma SDE_p$).

The efficiency of the Film 3 device was characterized using the biasing and readout scheme depicted in figure 3.2 according to a procedure similar to those of references [128, 129]. The efficiency measurement setup is shown in figure 3.6. 1064 nm photons from a mode-locked fiber laser were sent into a fiber beam splitter. A power meter (PM 1) was connected to one output of a 90:10 fiber beam splitter (BS) to monitor power fluctuations in the laser. Light from the signal output of the beam-splitter was collimated and directed through three attenuator wheels consisting of various neutral density (ND) filters, and then coupled into a single fiber patch cable via a collimator. The attenuation factor corresponding to each ND filter was measured at $\lambda = 1064$ nm using a calibrated power meter (PM 2). Linearity was verified with combinations of different ND filters at high power measured by PM 2. These calibrations are shown in appendix c.

After calibration, the light was attenuated down to the single-photon level and a known quantity of 1064 nm photons was delivered into the cryostat to illuminate the SNSPD. The transmission of this SMF-28 fiber at 1064 nm was also calibrated. On the lid of the SNSPD, the collimated beam passes through an aspheric lens with a nominal focal length of 15 mm. Losses through these optics were calibrated, and the lens was placed out of focus to increase the spot size illuminating the detector, to approximately 500 µm. The logic behind this selection of spot size is outlined as follows:

A Gaussian beam has an intensity profile given by

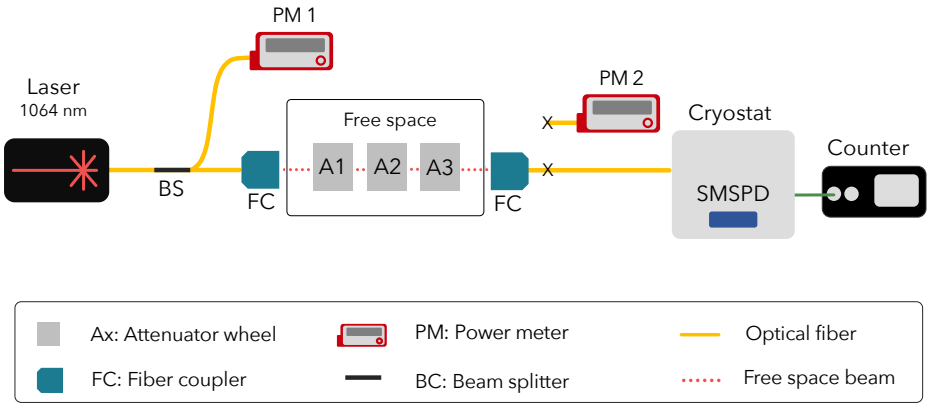


Figure 3.6: Efficiency measurement setup used to calibrate a source down to single-photon level output powers.

$$I(r) = I_0 \exp\left(-2\frac{r^2}{w_0^2}\right) \tag{3.1}$$

where w_0 is the beam waist (the radius at which the intensity drops to $1/e^2$ of its maximum value I_0). The area containing 100% of the power for a Gaussian beam is given by

$$A = \pi D^2 \tag{3.2}$$

where D is the beam diameter. We want to find the beam diameters such that the area A is between 0.7 mm^2 and 0.9 mm^2. This gives us the inequalities

$$0.7\,mm^2 \leq \pi D^2 \leq 0.9\,mm^2. \tag{3.3}$$

By isolating D^2, This can be expressed as

$$\frac{0.7\,mm^2}{\pi} \leq D^2 \leq \frac{0.9\,mm^2}{\pi}. \tag{3.4}$$

Taking the square root of each part provides the beam diameters:

$$\sqrt{\frac{0.7\,mm^2}{\pi}} \leq D \leq \sqrt{\frac{0.9\,mm^2}{\pi}}. \tag{3.5}$$

Now, calculating the specific values defines the optimal range

$$D_{\min} = \sqrt{\frac{0.7}{\pi}} \quad \text{and} \quad D_{\max} = \sqrt{\frac{0.9}{\pi}}. \tag{3.6}$$

$$D_{\min} \approx \sqrt{\frac{0.7}{3.14159}} \approx 471.4\,\mu\text{m}$$

and

$$D_{\max} \approx \sqrt{\frac{0.9}{3.14159}} \approx 537.1\,\mu\text{m}.$$

Thus, the beam diameters ensuring that 100% of the power is contained within the area range of 0.7 mm^2 to 0.9 mm^2 are approximately between 471.4 µm and 537.1 µm, and 500 µm is a convenient target within the range.

As shown in figure 3.7, the SDE reaches 4.2%. The uncertainty of the power meters was estimated by calculating the standard error of the mean of 10 consecutive measurements on 4 different power meter heads. This was determined to be $\sim 10\%$. The total SDE error is therefore $\pm 0.5\%$.

T_c Measurement

A resistance versus temperature measurement was performed on a Film 3 device, shown in figure 3.8. The T_c is defined as the inflection point, extracted by calculating the derivative of the curve, as illustrated. This is a robust method of defining the T_c, even with a narrow range of data. A T_c of 1.82 K was extracted from this measurement.

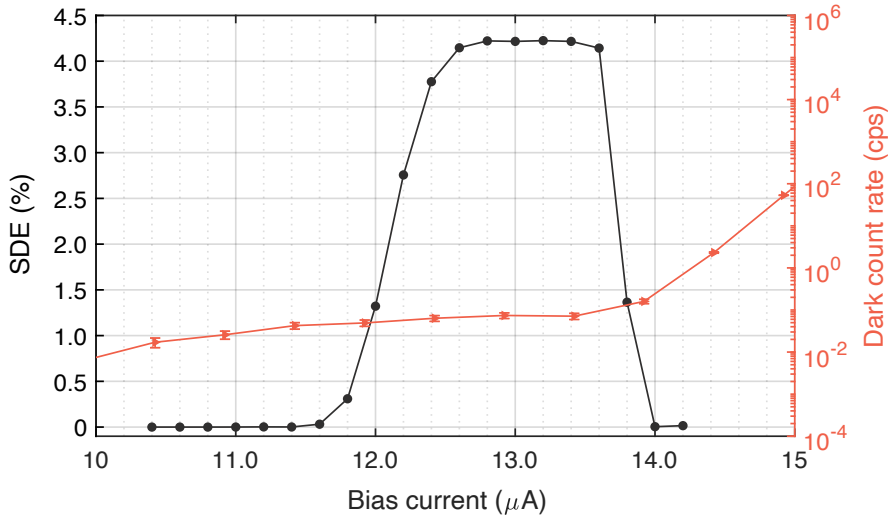


Figure 3.7: Left axis, black data: SDE_a vs. I_{bias} for the Film 3 device. Error bars of $\pm 0.5\%$ are not shown. Right axis, red data: system dark count rate vs. I_{bias} at 0.8 K.

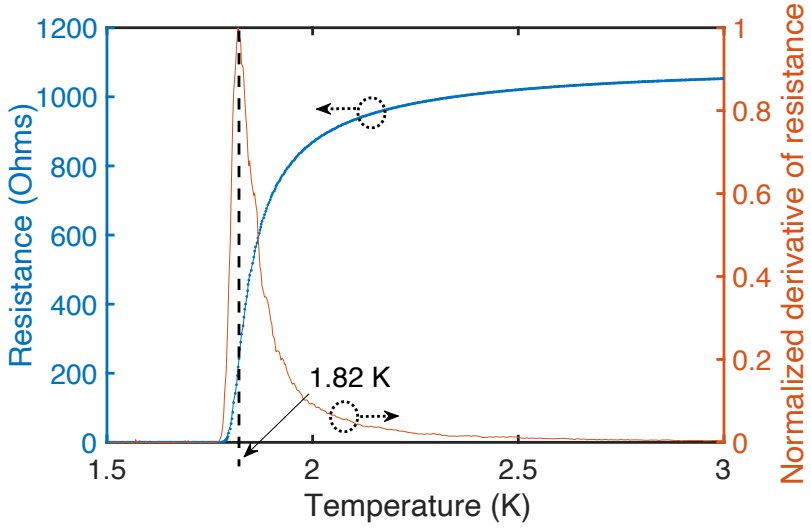


Figure 3.8: The resistance versus temperature curve for Film 3. The T_c at the inflection point of the curve is shown graphically at 1.82 K.

Timing Resolution Characterization

The timing resolution of single-photon detectors is an important detection metric, as it determines the precision with which a device can measure the arrival time of photons. Optimizing timing resolution is important for achieving the best performance in a given application. Among various types of single-photon detectors, SNSPDs offer exceptionally high timing resolution, surpassing that of most other detectors. Low jitter is essential applications in quantum information, classical and quantum optical communication, laser ranging, and measurement of short-lived signals such as fluorescence in biomedical imaging and ultra-fast transients in astronomy.

Fundamentally, the single-photon detection process in SNSPDs is not instantaneous and there is a finite period of time between the photon absorption event and the event registration in the readout electronics. This is referred to as detection latency. In addition, the latency will have some statistical variation across many events. Ultimately, this determines the timing resolution of an SNSPD. Because the absolute detection latency is not directly accessible experimentally, the standard method of characterizing the timing resolution of an SNSPD is to measure the instrument response function (IRF) which is measured by comparing the detector response to a reference. The width of this (usually the FWHM or similar metric) is referred to as the timing jitter.

Sources of jitter were once dominated by contributions from electrical and amplifier noise [117, 130]. There have been significant efforts in the community to reduce this through the development of low-noise cryogenic amplifiers [131]. Geometric contributions to jitter include longitudinal geometric jitter, which arises from the finite propagation speed of microwave signals along the length of the nanowire and transverse geometric jitter, which arises from the difference response times from various absorption sites along the width of the nanowire. Contributions from transverse geometric jitter (jitter from different

photon absorption sites along the width of the wire) are expected to be more pronounced in microwires than nanowires. In large active area devices, the largest contribution is the longitudinal geometric jitter which can be mitigated by using a double-ended readout scheme with a low noise cryogenic amplifier on each end and an impedance-matching taper to avoid reflections near the nanowire ends [132].

Large area detector elements also prone to inhomogeneity-induced jitter. Longer wires are more prone to geometric inhomogeneities along the nanowire (microwire) [133]. Inhomogeneities influence the electro-thermal evolution of the nanowire (microwire) during the detection process and create different local environments for hot-spots generated at different locations [134].

Given that the microwire arrays studied in this thesis are meander geometry with large active area (long microwire length), and made from thin film high kinetic inductance materials, the timing jitter is expected to be large compared to smaller devices made for fiber-coupled light detection, or detectors optimized for low timing jitter. This can be seen as an intrinsic trade-off of large SNSPDs.

In the target applications of microwire arrays in high energy physics and dark matter detection, the jitter requirements are not as stringent as those in the quantum information and quantum communication spaces. In low-mass dark matter detection experiments, the primary goal is to identify rare interactions between dark matter particles and ordinary matter, typically through low-energy recoils in a detector material. Unlike quantum information science applications, where ultra-high timing resolution is crucial, dark matter experiments do not necessarily require such precision for several reasons. First, low-mass dark matter interactions are expected to be extremely rare, necessitating long observation times to accumulate sufficient events for statistical significance. In this context, the maximum count rate can be relatively low and the timing resolution can be relatively coarse, as the events may be spaced out over longer timescales, allowing for effective signal discrimination from

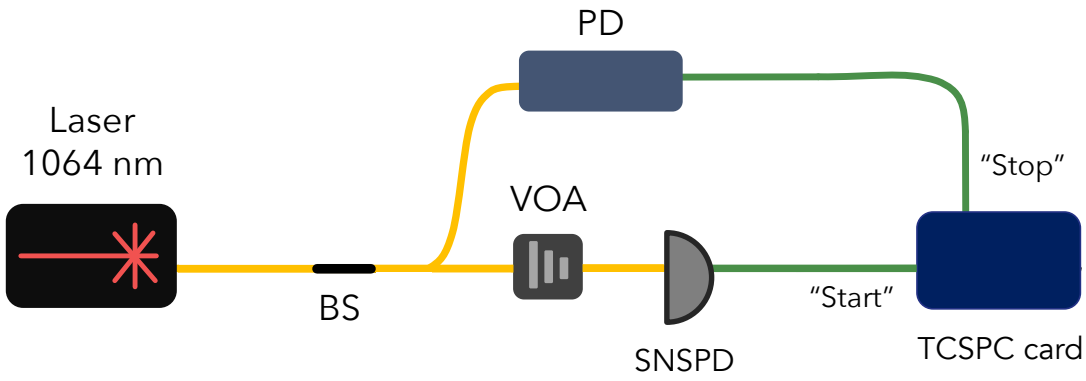


Figure 3.9: Jitter measurement setup using a 1064 nm mode-locked laser as a reference. The laser reference is split via a fiber beam splitter (BS) , where one port is diverted to a fast photodiode (PD) , and the other port is diverted to a variable optical attenuator (VOA) for illumination at the single-photon level of the SNSPD. The PD reference pulse and SNSPD output are connected to the Becker & Hickl TCSPC card.

noise. Additionally, the scintillation timescales of *n*-type GaAs are on the order of many microseconds [64]. Given this, the relatively high jitter expected from the mm^2 arrays will still be suitable for the application.

The timing jitter of the Film 3 array at $\lambda = 1064$ nm was characterized by measuring the IRF of the device with respect to a pulsed 1064 nm mode-locked laser. The output of the 1064 nm mode locked laser with 50 MHz repetition rate was attenuated to the single photon level by a fiber variable optical attenuator (VOA). Timing reference pulses were generated by a fast photodiode and sent to the "Stop" port of a commercial time-correlated single-photon counting (TCSPC) module (Becker-Hickl, SPC-150). The amplified voltage output pulses of the SNSPD were sent to the "Start" port of the SPC-150, which then builds a statistical distribution of the intervals between the "Start" and the "Stop" signals. This setup is depicted in figure 3.9.

The detector and illumination setup is shown in figure 3.10. A 1326 nm short pass filter

was implemented to reduce loading of background photons on the detector. An optical fiber was used to couple light via flood illumination onto the detector's active area.

The IRF (jitter histogram) of one pixel of the Film 3 array is shown in Figure 3.11 for bias currents of 10.4 µA, 11.4 µA, and 12.4 µA. Jitter is typically defined as the FWHM of the IRF and was measured, but as can be seen in Figure 3.11, the jitter is non-Gaussian and thus the observed trend with increasing bias current of operation isn't captured by the FWHM metric.

The observed FW1/10 max and FWHM for I_{bias} of 10.4 µA are 1.01 ns and 829.1 ps, 1.25 ns and 845.91 ps for I_{bias} of 11.4 µA, and 1.38 ns and 803.15 ps for I_{bias} of 12.4 µA. These widths are dominated by longitudinal geometric jitter. In a single-ended readout scheme, the differences in pulse propagation time from different absorption sites along the length of the nanowire contribute to the IRF. Figure 3.12 depicts this effect schematically.

The jitter histogram width is larger at lower bias currents. This feature is well-understood in terms of the intrinsic detection mechanism and SNR effects. In general, the amplitude of the detection response is proportional to the absolute bias current delivered to the device. When the jitter at different bias currents is measured with the same amplifier for each measurement, the same amplifier noise is present for each measurement. For higher bias currents, a higher output pulse amplitude results in a higher slope of the rising edge of the response pulse, and the amplitude noise from the amplifier leads to less temporal variation in crossing over a fixed threshold. This will result in less jitter [135]

3.3 Generation 2 Microwire Arrays

The second generation of the large-area microwire arrays features improvements in the photolithography process development, an increase in fill factor, overall active area, and individual pixel size. The film was sputtered using a compound 50:50 WSi target and

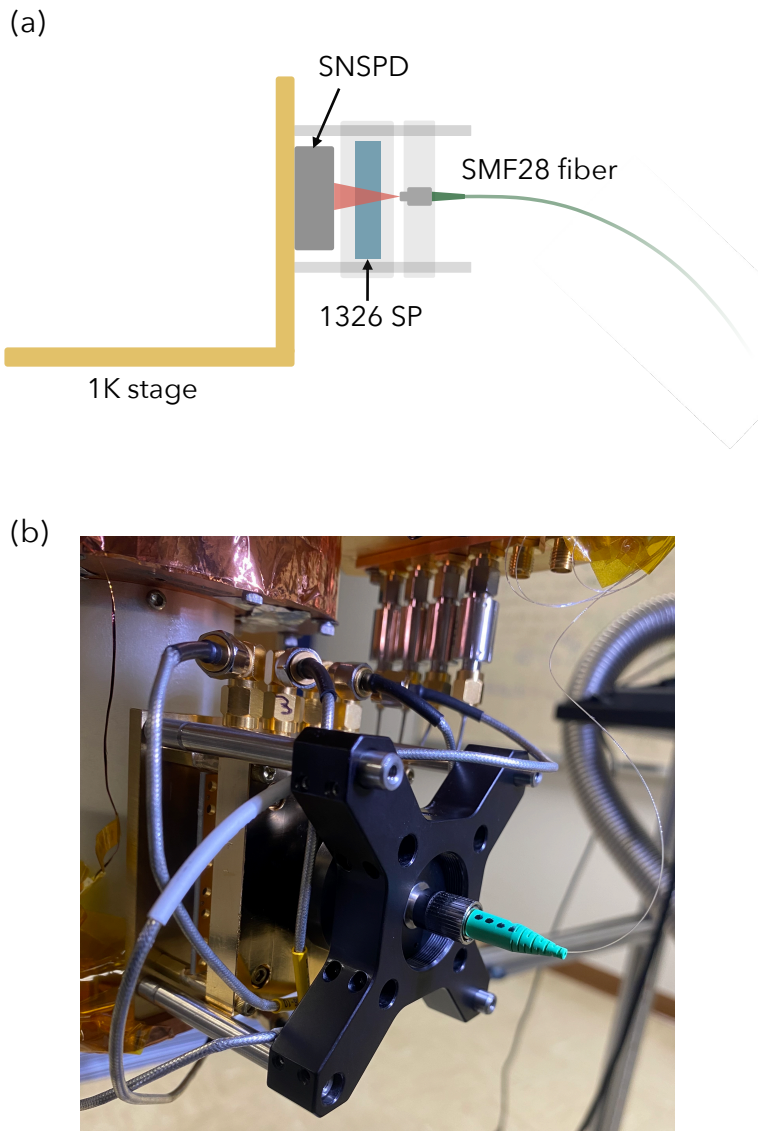


Figure 3.10: (a) shows an illustration of the flood illumination setup used for jitter measurements, where a single-mode fiber is incident on the SNSPD active area with a 1326 nm short pass filter to attenuate stay light from reaching the detector active area. (b) shows a photograph of the optical assembly mounted over the SNSPD packaging in the cryostat.

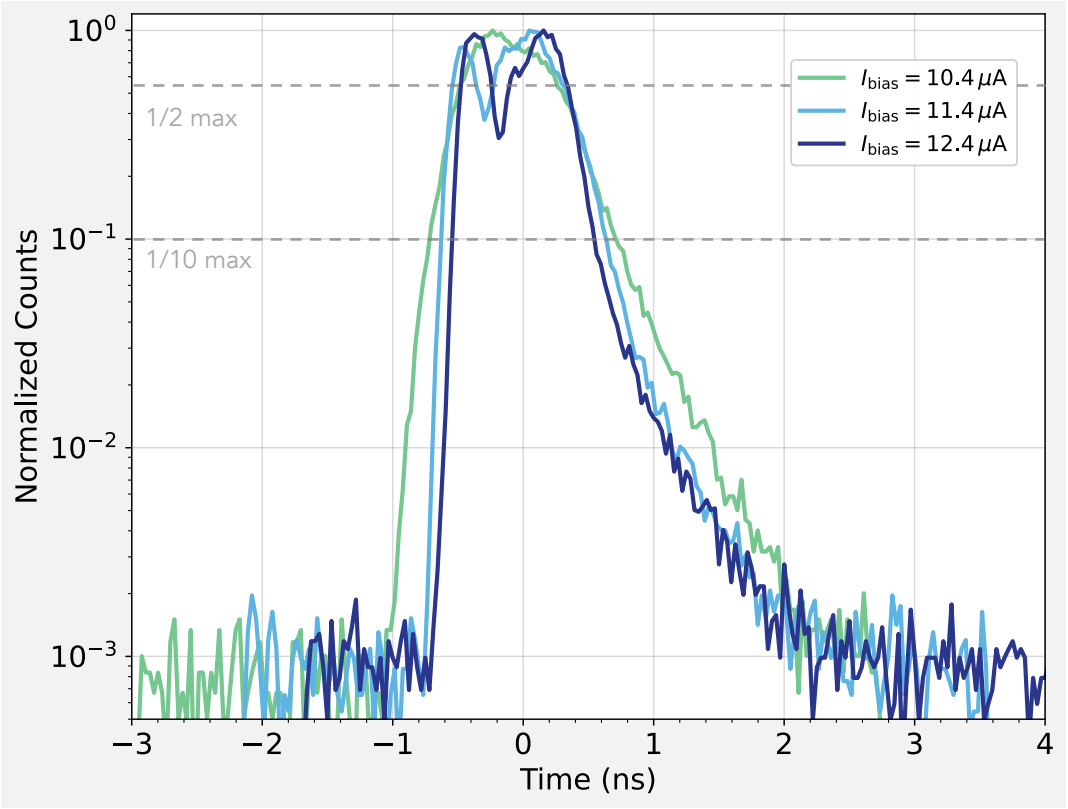


Figure 3.11: Jitter histogram for one channel of the Film 3 array at $\lambda = 1064\,\text{nm}$, measured at $I_{bias} = 10.4\,\mu\text{A}$, $I_{bias} = 11.4\,\mu\text{A}$, and $I_{bias} = 12.4\,\mu\text{A}$. The FWHM for $I_{bias} = 10.4\,\mu\text{A}$, $I_{bias} = 11.4\,\mu\text{A}$, and $I_{bias} = 12.4\,\mu\text{A}$ are 829.109 ps, 845.901 ps, and 803.15 ps respectively. The FW1/10M for the aforementioned I_{bias} are 1.01 ns, 1.25 ns, and 1.38 ns.

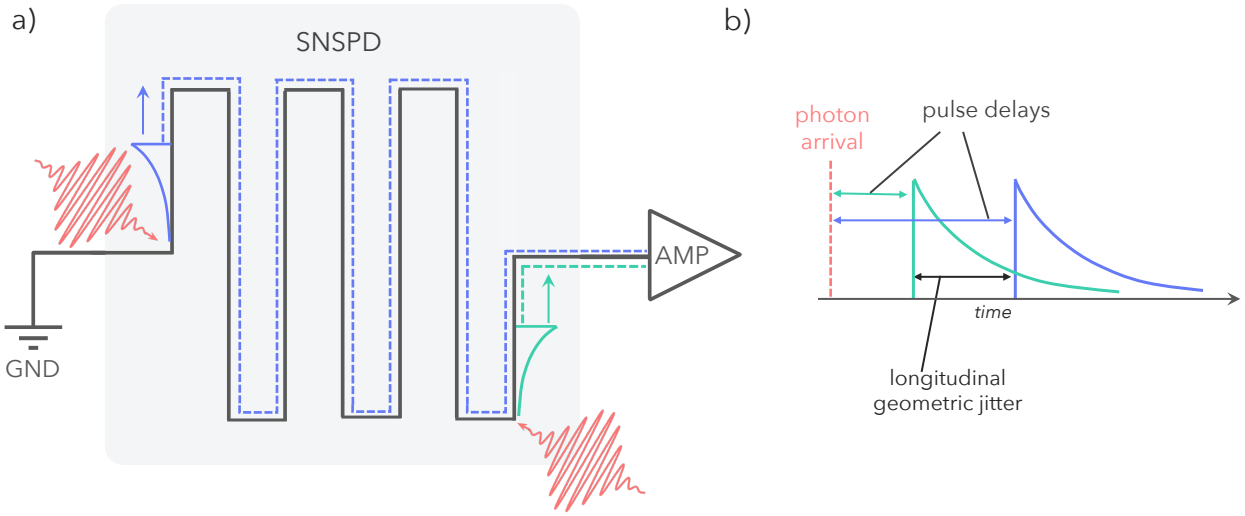


Figure 3.12: The origin of longitudinal geometric jitter is shown in (a), where the microwave signals associated with photon detection events along different segments of the nanowire have different lengths to travel. This leads to different delay times relative to the photon arrival, shown in (b).

deposited onto an oxidized silicon substrate with a 240 nm-thick oxide. The microwires have a width of 1.5 µm and were patterned on a 2.3 nm thick film using photolithography with the deep-UV stepper. After etching, the microwires were passivated with 40 nm of amorphous Si. Devices include 4-pixel, 8-pixel, and 16-pixel arrays with active areas of 1 mm^2, 4mm^2, and 16mm^2, respectively.

3.3.1 Detector Design

The second generation microwire arrays have a 1.6x increase in fill factor compared to the generation 1 microwire arrays (0.4 vs 0.25). SEM images of generation 1 and 2 microwire arrays are shown in figure 3.14. The bends are tapered out the outer radii in the generation 2 arrays to improve the lithography, as earlier attempts showed narrowing at the onset of the bends.

The perimeter of the SNSPD chip also has 5 µm- tall standoffs made from SU-8, a

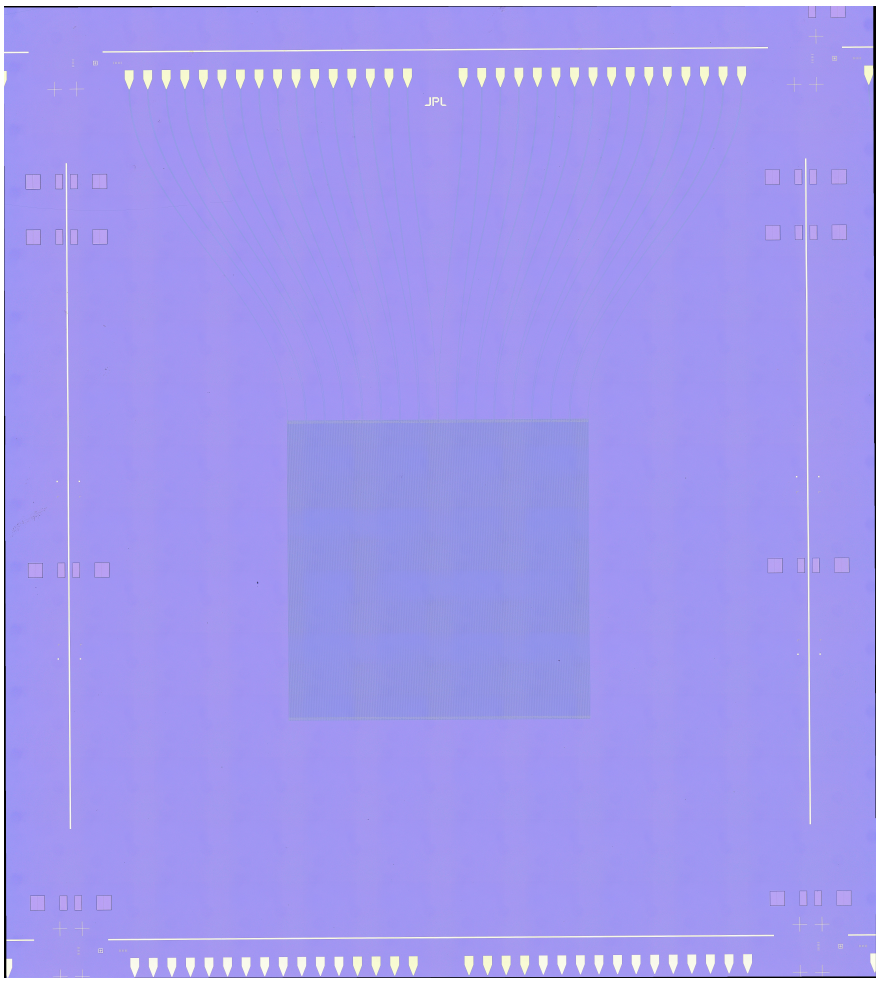


Figure 3.13: Full optical microscope image of the 4 mm x 4 mm generation 2 microwire array.

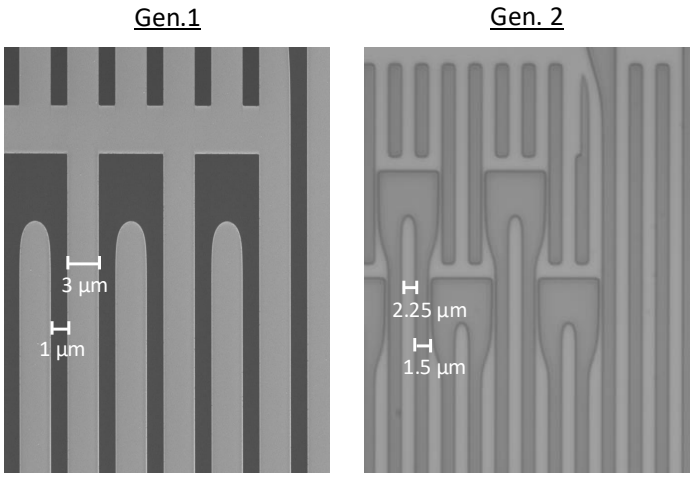


Figure 3.14: SEM images of a portion of the generation 1 microwire array (left) with a fill factor of 0.25 and 1 um wide wires and the generation 2 microwire (right) with a fill factor of 0.4 and 1.5 micron wide wires. The bends are widened in the generation 2 microwire design to improve photolithography.

high contrast, epoxy-based photo-resist, for mounting GaAs samples to the detector at a fixed distance for scintillation measurements. Figure 3.15 shows these in a zoomed-in microscope image. They can also be seen around the chip perimeter in the full micrograph of the 4 mm x 4 mm array shown in figure 3.13.

3.3.2 T_c Measurement

To measure T_c of the generation 2 microwire array, a resistance versus temperature measurement was performed, again taking T_c as the maximum in the inflection point of the derivative of resistance with respect to temperature. A T_c of 2.49 K was measured, shown in figure 3.16. There are advantages to a higher T_c compared to the generation 1 arrays (1.82 K). When operating a device, it is optimal to reach high fractions of the intrinsic depairing current [136], and it has been shown that the maximum achievable fraction of the depairing current (referred to as the constriction factor) is achieved when the operation temperature

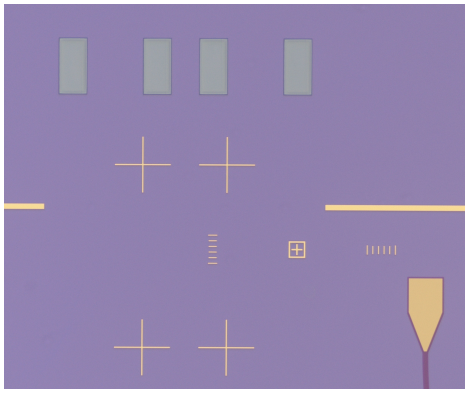


Figure 3.15: Optical microscope image of SU-8 standoffs on the corners of the SNSPD chip.

is $< 0.3T_c$ [136, 137]. Thus, for a fixed operating temperature of 800 mK, the optimal T_c is expected to be 2.4 K.

3.3.3 Optical Characterization

The response to UV, visible, and NIR single photons were measured in PCR curves. The various sources used for characterization are listed in table 3.2.

Wavelength	**Laser**
373 nm	Picoquant pulsed diode laser
660 nm	Newport Digital Modulated Laser Diode
1064 nm	Calmar Mendochino series mode locked laser
1310 nm	Diode laser

Table 3.2: Wavelength and Laser Specifications

These wavelengths were chosen to span the full width of scintillation light emitted from *n*-type GaAs. In addition to this, the response to higher energy photons (visible and UV) was measured for diagnostic purposes to assess the yield and quality of the array. Figure 3.17 shows the normalized PCR curves from a representative pixel of the array. Saturated internal detection efficiency is reached for all wavelengths measured. The plateau length is shorter for the longest wavelength measured (1310 nm), but the results indicate

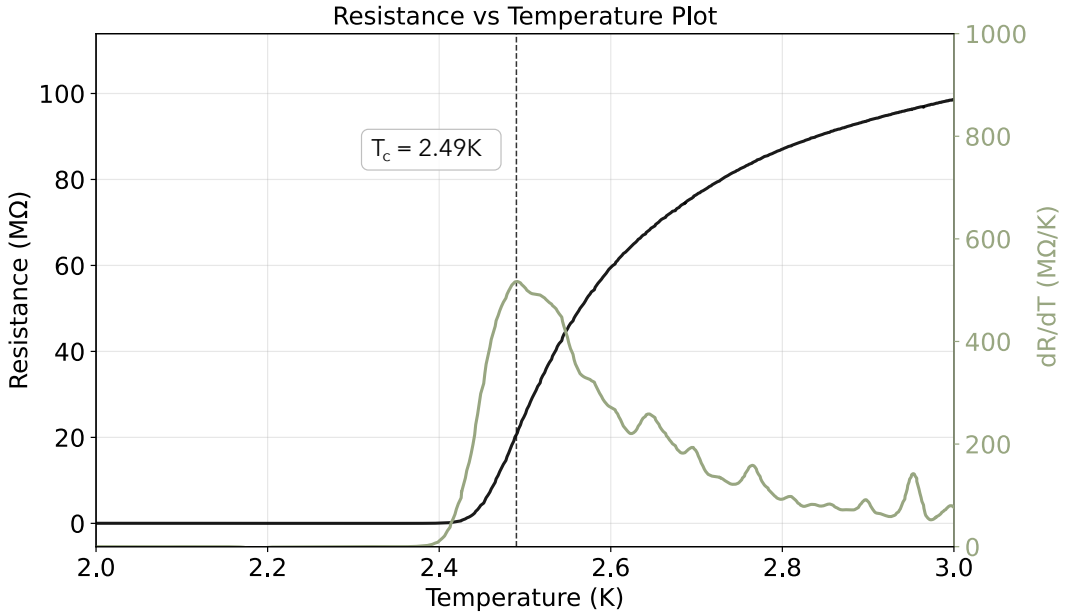


Figure 3.16: Resistance versus temperature measurement for one pixel of the 2mm x 2mm 8 pixel generation 2 microwire array showing a T_c of 2.49 K.

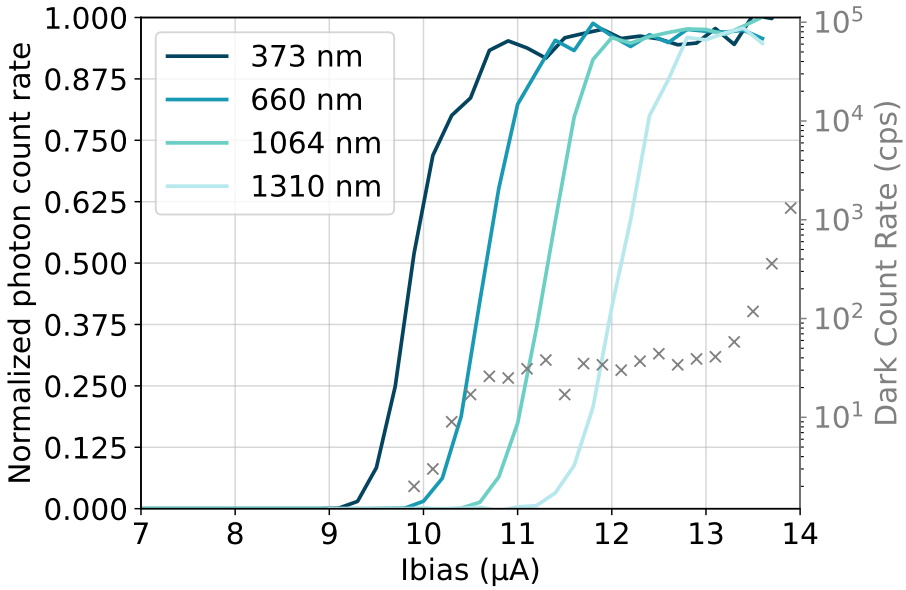


Figure 3.17: PCR curve for an 8 pixel generation 2 microwire array measured from UV to NIR wavelengths to characterize the dynamic range of the device. Saturated internal detection efficiency is reached for PCR curves out to 1310 nm, which is the longest emission wavelength of *n*-type GaAs.

that a bias current can be chosen such that the detector will be sensitive to even the longest wavelengths of emitted scintillation light from *n*-type GaAs.

3.3.4 Timing Resolution Characterization

The jitter in the generation 2 microwire array is expected to be higher than that of the generation 1 array measured for multiple reasons. The primary reason is that the microwire length is a more than a factor of 4 larger in the generation 2 array design, so longitudinal geometric contributions to jitter will scale accordingly. With a larger microwire width, there will also be some broadening from transverse geometric jitter, which arises from different photon absorption location along with width of the nanowire.

Previous work in the field has shown that longitudinal geometric jitter can be mitigated by using differential readout, where the positive and negative voltage pulses are read out

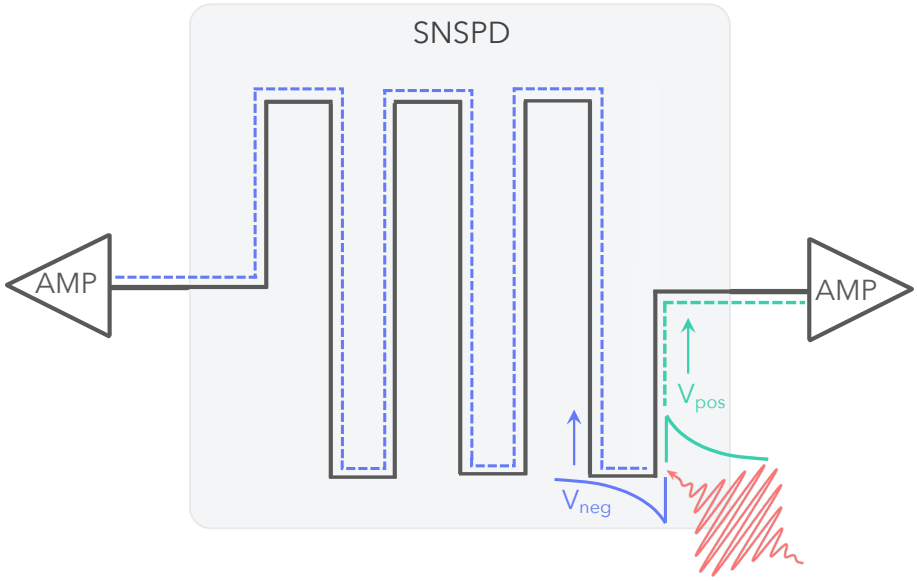


Figure 3.18: Illustration of double-ended readout of an SNSPD, where the positive and negative outgoing voltage pulses V_{pos} and $V_{neg}$are read out using two independent amplifier channels.

from each end of a nanowire [132] are collected. The pulses are subsequently processed and the differential signal has the geometric contribution to the jitter compensated for. This process relies on the transmission line behavior of a nanowire which is improved through ground plane coupling from the metal mirrors used as back-reflectors in optical stacks. Impedance-matching taper interfacing the nanowire to the readout line are also typically incorporated into devices intended for geometric jitter cancellation. These haven't been demonstrated for mm^2-scale arrays. Additionally, in the case of the large microwire arrays in this work which lack a metallic back-reflector and this are expected to exhibit more limited transmission line behavior , the extent to which the longitudinal geometric jitter can be canceled hasn't been measured.

To investigate this, the jitter of the 2mm x 2mm active area 8-pixel array was characterized using double-ended readout, which is illustrated in figure 3.18.

Here, signals from both ends are read out independently with two independent readout

channels of the DC-coupled cryogenic amplifiers that are a part of the measurement infrastructure of the cryostat used for measurements in this thesis (as opposed to a differential amplifier). The biasing scheme is shown in figure 3.19. The ends of a pixel were each wire bonded to separate signal pins, which were directed into different channel of the DC coupled cryoamps. When a detection event occurs along the microwire, both a positive and negative pulse will co-propagate into the readout electronics, and if both of these are timestamped, it can be inferred where on the microwire length the photon was detected and the effects from the propagation along the microwire to the readout can be canceled fully or partially. The goal of this measurement is to cancel out some or all of the effects from longitudinal geometric jitter.

In the DC-coupled cryogenic amplifier used in these experiments, there is an asymmetry between the negative and positive pulses which can be seen in figure 3.20 in the middle and bottom panels, where there is less SNR in the positive pulse than the negative output pulse. Given this asymmetry, it is unclear *a priori* which combination of thresholds will be the most amenable to the cancellation. Thus, to avoid having to pick sets of thresholds for a time-tagger, an oscilloscope was operated in segmented mode so that all waveforms could be recorded and different combinations of an arbitrary number of thresholds could be selected in post-processing to see which one is optimal.

To post-process the waveforms, a python script to process hdf5 output files was written to look for the crossing of a specified voltage threshold and via linear interpolation find the time of crossing for the positive and negative output pulses as well as the laser pulse signal from the fast photodiode. Arrays of the positive and negative pulse time-tags with respect to the sync as the reference were then constructed. This was done for a range of voltage thresholds. Waveforms from the photodiode and the negative and positive output pulses of the SNSPD are shown in figure 3.20

Now, with the positive voltage pulse arrival time τ_+ and the negative voltage pulse

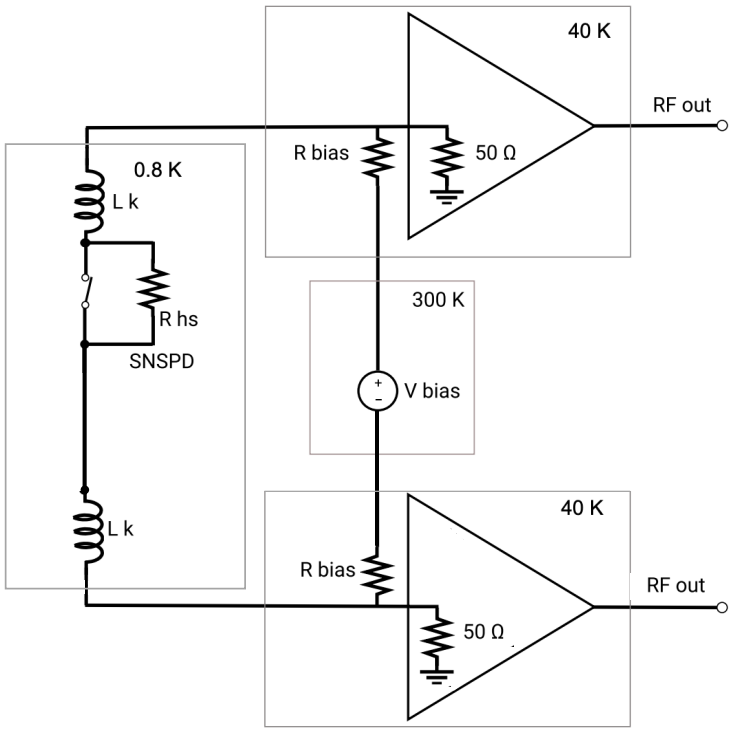


Figure 3.19: Double ended biasing and readout scheme employed for jitter measurements. Both ends of the SNSPD were connected to separate DC-coupled cryogenic amplifier channels where they receive I_{bias+} and I_{bias-}, respectively, and during the detection cycle, the negative and positive outgoing SNSPD pulses can both be directed into the readout electronics.

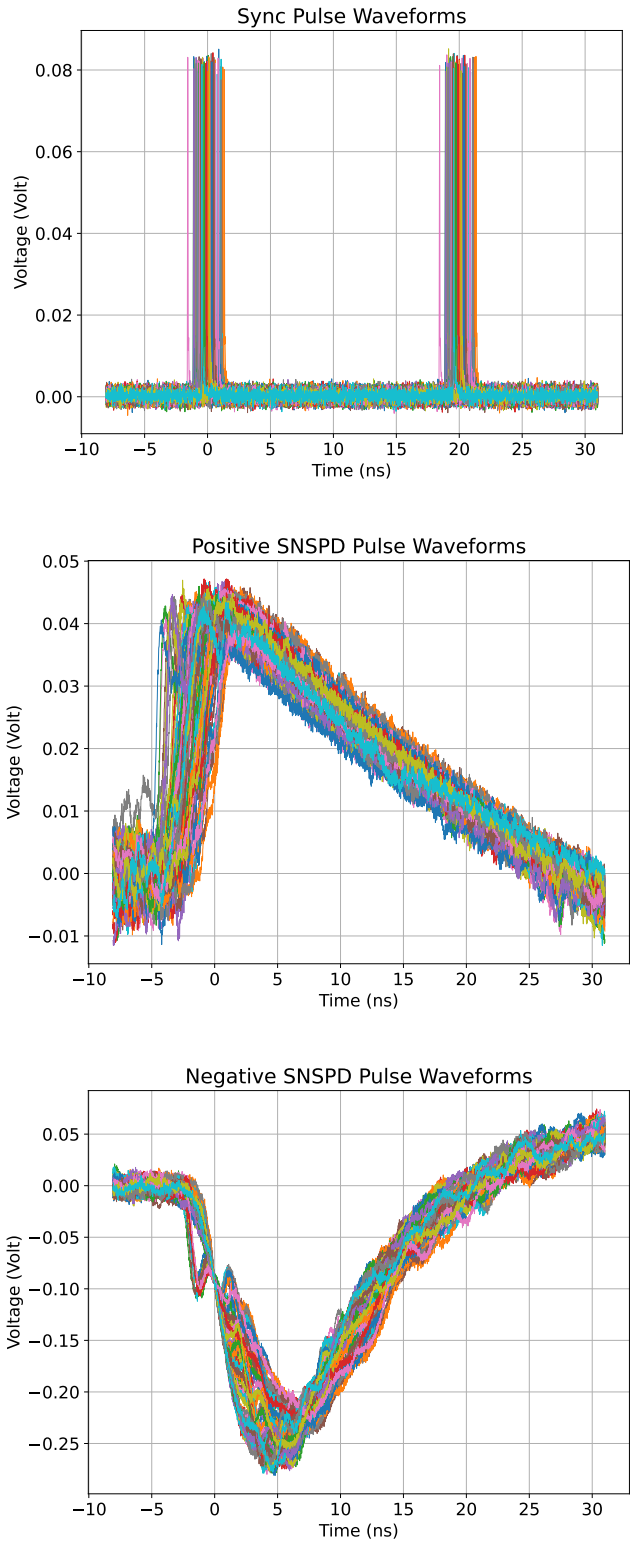


Figure 3.20: Waveforms for (top panel) fast photodiode reference pulses (middle) positive SNSPD output pulses, and (bottom) negative SNSPD output pulses.

arrival time τ_- both referenced to the sync pulses, the geometric jitter can be taken to be

$$Jitter_{geom} = (\tau_+ - \tau_-)/2, \tag{3.7}$$

and the system jitter with the geometric contributions subtracted is the average of the jitter from the negative and positive pulses

$$Jitter_{sub} = (\tau_+ + \tau_-)/2. \tag{3.8}$$

Figure 3.21 shows the jitter histograms for the negative and positive SNSPD pulses as well as the geometric subtracted jitter. The geometric subtracted jitter is narrower in FWHM and FW1/10M than the negative and positive SNSPD pulses histograms, which can be taken to be the single-ended jitter. The FWHM of the positive, negative, and geometric subtracted jitter histograms are 1.01, 0.91, and 0.79 ns, respectively, and the FW1/10M is 2.19, 1.99, and 1.60 ns, respectively.

The geometric jitter can be partially canceled with the detector in the current configuration to achieve sub-nanosecond timing resolution. This meets the jitter requirements to resolve the expected microsecond-scale scintillation timescales of *n*-type GaAs.

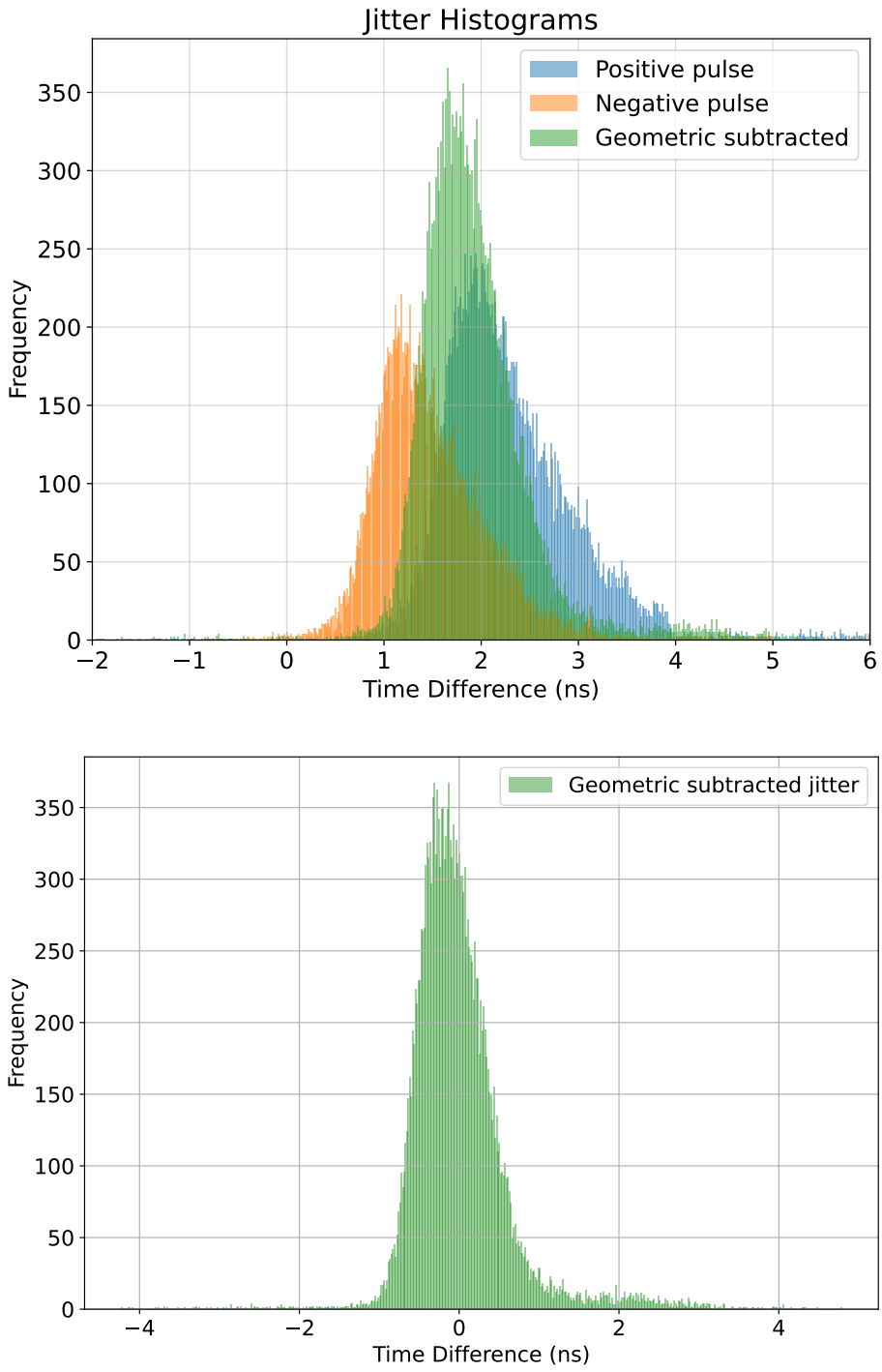


Figure 3.21: Top: IRFs of positive (blue) and negative (orange) SNSPD pulses with respect to the reference laser pulses, along with the average that gives the geometric subtracted jitter (green). The FWHM of the positive, negative, and geometric subtracted IRFs are 1.01, 0.91, and 0.79 ns, respectively, while the FW1/10 max values are 2.19, 1.99, and 1.60 ns. The bottom plot shows the geometric subtracted jitter histogram and the generation 2 microwire array jitter, both centered at a time difference of 0 ns for clarity.

Chapter 4: Backgrounds in Microwire Arrays

Each type of superconducting device has its own susceptibility to backgrounds that lead to spurious counts and lower the SNR. SNSPDs having single-photon sensitivity over a broad range of wavelengths for any given detector architecture means that stray photons coupling into the cryostat through windows or fibers have the potential to cause detection events. These can be mitigated by the implementation of spectral filtering to reduce incident blackbody photons on the detector system. In devices with free-space coupling with high-efficiency operation in the NIR, sub-0.1 Hz dark count rate have been demonstrated using optical filtering and external Peltier coolers for the fiber connectors usually sitting at room temperature [138]. The susceptibility of SNSPDs with large active areas to various backgrounds and intrinsic dark counts has not been systematically studied. This chapter details the study of the background and intrinsic dark counts of mm^2-scale SNSPDs as a function of pixel active area and temperature.

The SNSPDs studied in this chapter were fabricated by Ekkehart Schmidt, Sahil Patel, and Emanuel Knehr in the Microdevices Laboratory (MDL) clean room at JPL. The measurements described in Sections 4.1, 4.2, and 4.3 were independently performed and analyzed as part of this thesis research. The temperature dependent measurements described in Section 4.4 were conducted by Christina Wang at Fermilab on detectors that were pre-screened and characterized at 800 mK as part of this thesis research.

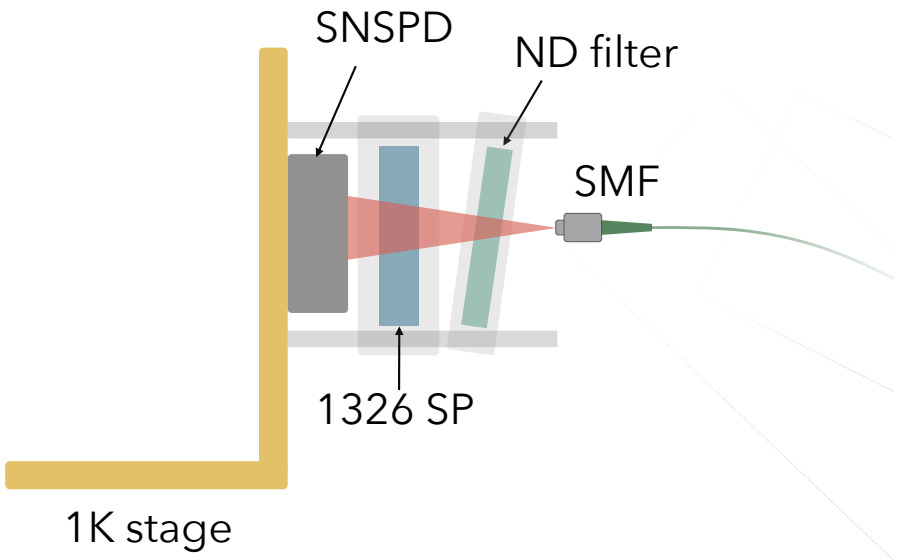


Figure 4.1: A typical filter stack for NIR illumination of a microwire array. Filters include a 1326 nm short pass filter (Semrock) and an OD 2 reflective NIR neutral density filter (Thorlabs NDUV20B). The ND filter is in an angled mount to prevent on-axis back scattering.

4.1 Extrinsic Background Mitigation

4.1.1 Filtering

The first thing to do is implement filtering to reduce background counts which decrease SNR and load the detector. Figure 4.1 shows a typical filter stack used with SMSPDs targeting NIR operation at GaAs scintillation wavelengths (850nm - 1300nm).

Dark Packaging

A dark packaging was designed to further mitigate background photons from accessing the detector active area. The first feature of this is a printed circuit board (PCB) mounted externally to the enclosed detector. Materials in PCBs can emit background photons through

mechanisms such as radioactivity and Cherenkov radiation, potentially interfering with sensitive detection systems. Materials like FR-4, commonly used in printed circuit boards (PCBs), may contain trace amounts of naturally occurring radioactive isotopes, including uranium, thorium, or potassium-40, which can decay and emit gamma rays, contributing to background photon levels. Cherenkov radiation can also be a concern in PCB dielectrics and insulators, where high-energy charged particles, such as those from cosmic rays or beta decay, pass through the material at speeds greater than the speed of light in that medium, producing photons in the visible or ultraviolet range. The design utilized interlocking grooves with small channels to enable air to be pumped out during cool-down. Glass-sealed hermetic pins were used to interface the detector housed on the interior of the packaging to the external PCB. The pins were sealed with Stycast 1285 epoxy to prevent stray light from leaking through. and then the device was wire-bonded directly to the pins. On the inside of the packaging, the SNSPD chip is mounted and bond pads are connected to pins through wire bonds. Two lids were designed for use in this packaging - one fully sealed for intrinsic dark count measurements and a version an aperture where 1/2" optics could be mounted.

The effect of the dark packaging on mitigating background photons can be demonstrated in figure 4.3. In a cool-down with the version of the packaging with the optical access aperture, a PCR curve was measured with a 940 nm source, as well as the background counts with the fiber in place but the source off. These are referred to as the background count rate (BCR). In a separate cool-down, the fully sealed lid was implemented to measure the dark counts, referred to as dark count rate (DCR). The lid reduces the dark count rate at low I_{bias} by 2 orders of magnitude and resolves the DCR into a plateau-regime at low I_{bias} and an exponential regime at high I_{bias}.

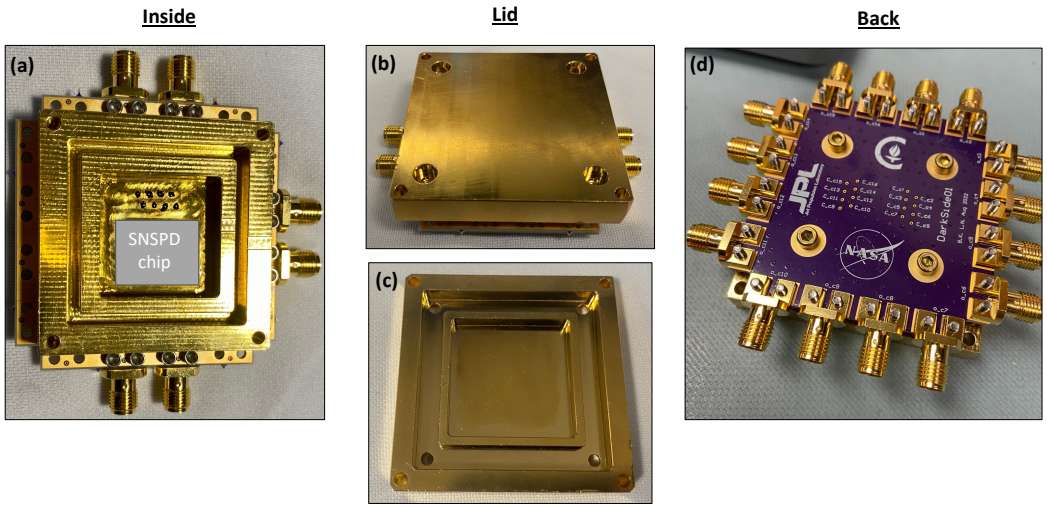


Figure 4.2: Photograph showing the dark box detector packaging. (a) is the inside of the packaging which houses the detector. (b) and (c) show the inside and outside of the lid, respectively. (d) shows the back of the packaging with the external PCB.

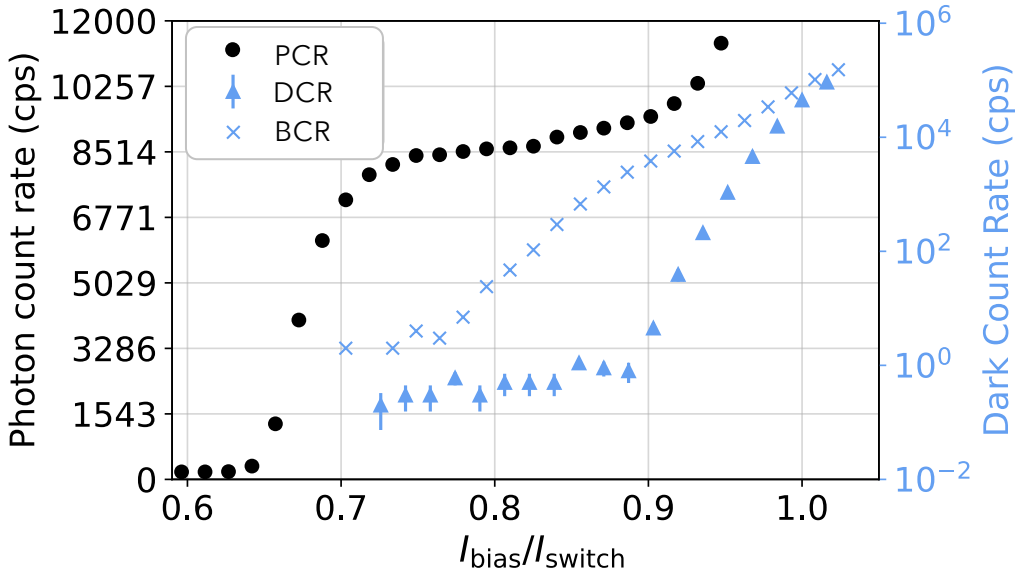


Figure 4.3: Dark count rate measured with closed lid (DCR) overlaid with background count rate measured with optical access lid and source turned off (BCR) and PCR curve measured with 660 nm diode laser.

4.2 Intrinsic Backgrounds in Microwire Arrays

4.3 Scaling with Active Area

To study the scaling of dark counts as a function of pixel area, the dark count rate (DCR) of the largest and smallest versions of the generation 2 microwire arrays were measured in the dark packaging described in the previous section with the fully enclosed lid. The top plot of Figure 4.4 shows the DCR as a function of normalized I_{bias} for one pixel of the 1 mm $\times$ 1 mm 4-pixel array and one pixel from the 4 mm $\times$ 4 mm 16-pixel version of the array. I_{bias} was normalized such that the transition between the plateau region of the DCR at low I_{bias} and the exponential portion at high I_{bias} was set to 1. This is shown in the dashed black vertical line. The pixel active areas are $0.25\,\text{mm}^2$ and $1\,\text{mm}^2$ for the small and large pixel, respectively. The bottom plot of Figure 4.4 shows the low I_{bias} portion of both DCRs. the As a visual guide, the DCR of the smaller pixel was multiplied by a factor of 4. The DCR of the larger pixel which is a factor of 4 larger area scales according to area at low I_{bias}.

The pixel from the 4-pixel array is four times smaller than the pixel from the 16-pixel array. As seen in Figure 4.4, there is slightly different scaling in the exponential portion of the dark count rate (DCR) at high bias currents. The smaller pixel (with an area of $0.25\,\text{mm}^2$) reaches roughly an order of magnitude lower dark counts at the lowest I_{bias} values, with dark counts of 10^{-2} cps for the 1 mm^2 pixel and 10^{-3} cps for the $0.25\,\text{mm}^2$ pixel, respectively. In terms of the measured dark counts, both devices feature sub-0.1 Hz at low I_{bias}.

Regarding the operational I_{bias} values on the plateau, the DCR curves from Figure 4.4 are shown in Figure 4.5, overlaid with 940 nm PCR curves. For operation at 940 nm with saturated internal detection efficiency, the $0.25\,\text{mm}^2$ pixel can be operated at $0.8I_{\text{bias}}$, where the DCR is 10^{-1} cps. The optimal I_{bias} for 930 nm operation with the $1\,\text{mm}^2$ pixel is closer

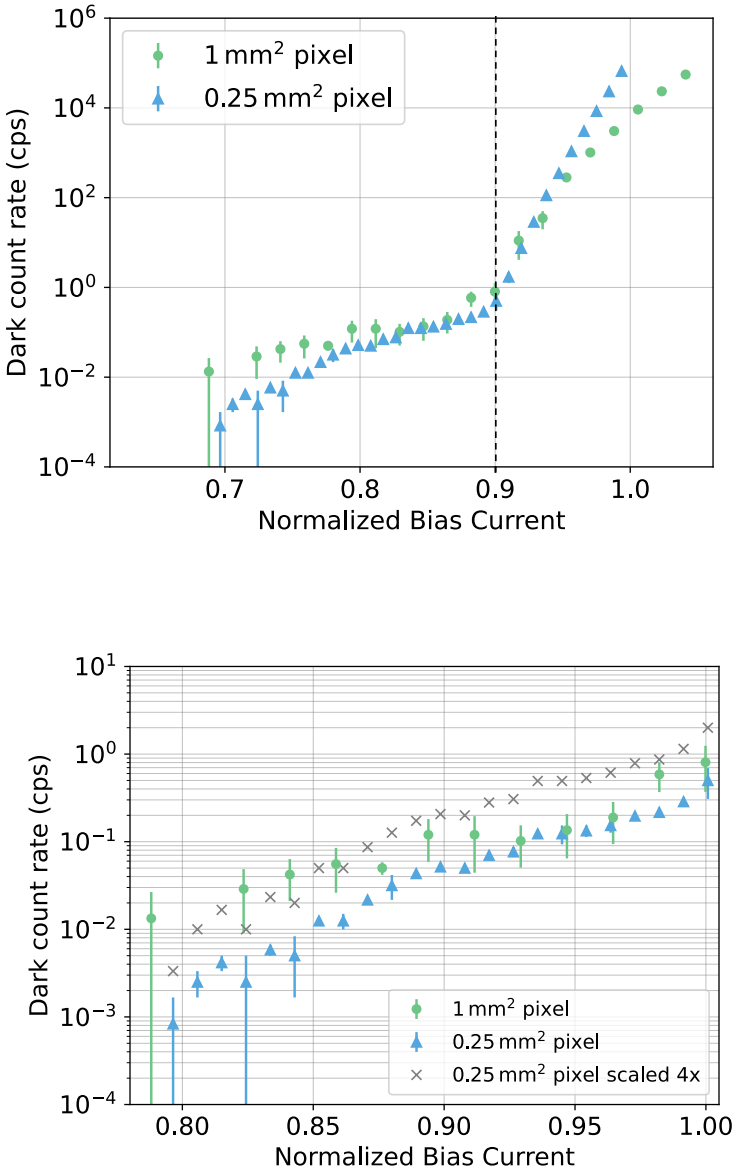


Figure 4.4: Top - The dark count rate as a function of normalized I_{bias} for the 0.25 mm^2 (blue triangles) and 1 mm^2 (green circles) SNSPD pixels, where I_{bias} is normalized such that the transition between the two regions of the DCR is set to 1, marked with the dashed vertical line. Bottom - The DCR of the larger and smaller pixel zoomed in on the low I_{bias} region. The grey x indicates the 0.25 mm^2 DCR scaled by a factor of 4. It can be seen that at low I_{bias}, the DCR scales with area as the 1 mm^2 DCR (green circles) overlaps with the gray x (scaled DCR by area).

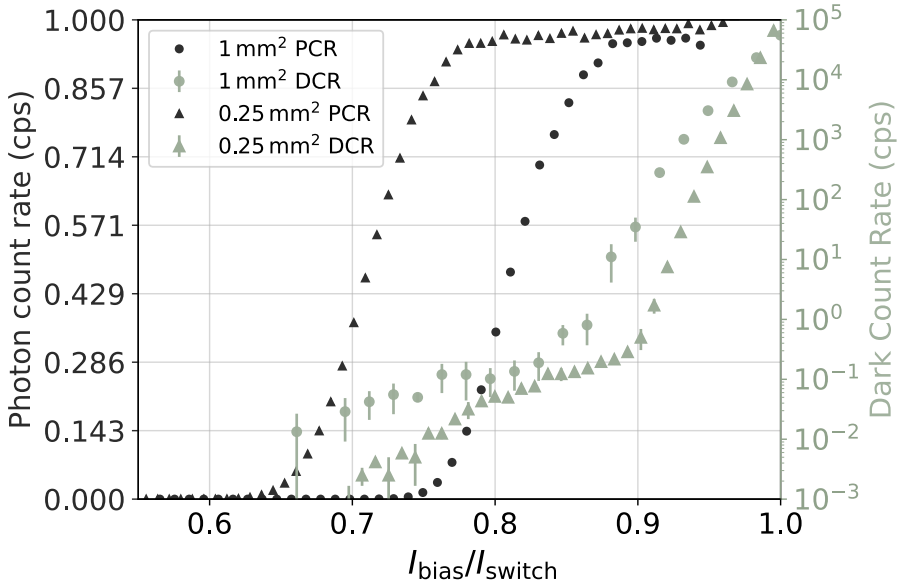


Figure 4.5: The PCR curves measured in a separate cool-down at 940 nm are overlaid with the 0.25 mm^2 pixel DCR (blue triangles) and the 1 mm^2 pixel (green circles) to demonstrate operational bias currents.

to $0.9I_{\text{bias}}$, where the DCR approaches tens of counts.

4.4 Temperature Dependence of Dark Counts

The dark count rate of an 8 pixel generation 1 microwire array was characterized in an adiabatic demagnetization refrigerator (ADR) in a collaborating facility at Fermilab. The open Rainer Model 103 ADR designed by High Precision Devices, Inc. is shown in a photograph in figure 4.6. The ADR has a base temperature of 50 mK and can be operated over a range of temperatures. The same DC-coupled cryogenic amplifier board used for all microwire measurements in this work was installed in the Fermilab ADR.

To prevent spurious photons from entering the fridge, light- tight radiation shields were added at 40 K and at room temperature. To further shield the detector active area from spurious photons, the lid designed for the generation 1 array packaging described in chapter

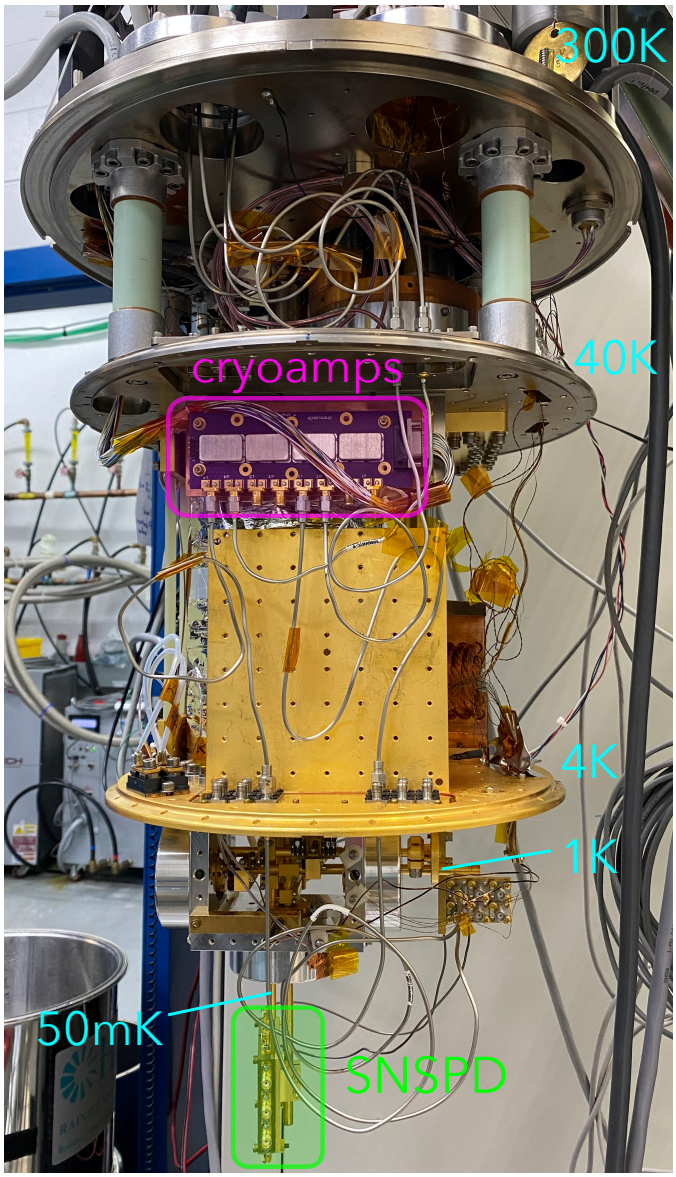


Figure 4.6: The opened ADR with SNSPD attached to the cold finger. The cryostat frame consists of three main stages (from top to bottom - 300 K, 40 K, and 4 K) connected by thermally isolating supports. Under the 4 K stage, the 1K stage is mounted and the 50 mK cold finger beneath has the SNSPD mounted.

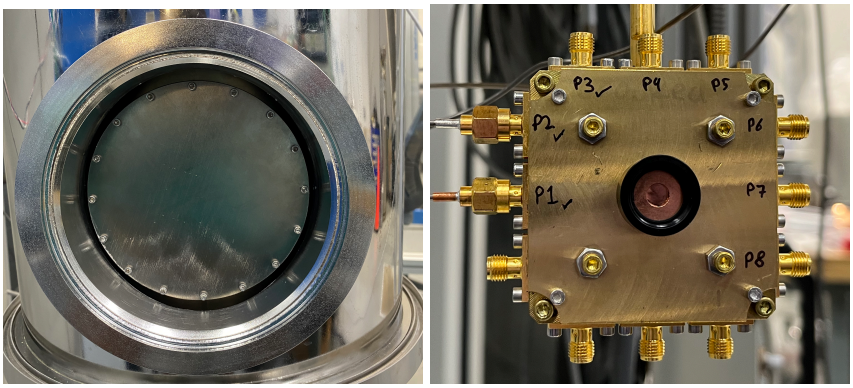


Figure 4.7: The 40K radiation shield (left) and the SNSPD packaging with lid (right).

3 was implemented. The radiation shield at 40 K and the SNSPD packaging with the lid installed are shown in figure 4.7

The use of ADR enables the operation of SNSPDs at lower temperatures and, for the first time, the observation of the temperature dependence of the DCR in large-area SNSPDs. Figure 4.8 illustrates the DCR as a function of bias current, measured at a range of temperatures from 0.2 K 0 1.2 K. The DCR shifts to the right as the operating temperature decreases. This indicates that, for the same bias current, operating at lower temperatures significantly reduces the dark count rate, highlighting the advantage of operating at the lowest possible temperatures for dark matter (DM) experiments. This observed temperature dependence aligns with previous studies conducted on traditional nanowire devices [108].

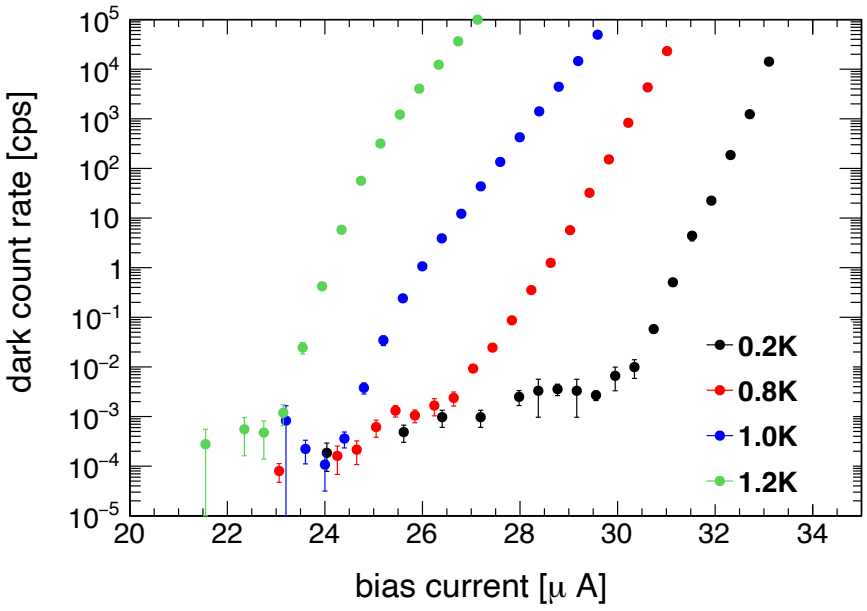


Figure 4.8: DCR curves for a generation 1 microwire array measured at different temperatures in the FNAL ADR. The DCR curves preserves its structure and shifts to higher I_{bias} with decreasing temperature. This points to a thermally mediated DCR mechanism and a better SNR can be achieved with lower operation temperature.

Chapter 5: Optically-excited Scintillation Measurements

N-type GaAs is a promising cryogenic scintillator for the detection of MeV-scale dark matter via electron recoils. This chapter describes efforts to demonstrate coupling of *n*-type GaAs to state-of-the-art large active area SNSPDs and characterize the hybridized system via optical excitation. Coupling a cryogenic scintillator to an SNSPD presents novel challenges. The well-established methods for achieving high system detection efficiency are primarily optimized for normally incident, fiber-coupled light, where the active area is matched to the diameter of a single-mode optical fiber. The optical stack is designed to enhance absorption through constructive interference of normally incident light at a specific wavelength over the fiber core's active area. Furthermore, nanofabrication techniques for standard NIR SNSPDs, intended for NIR fiber-coupled light detection, are well developed and even commercially available. Additionally, the timing resolution and background susceptibility of these systems are well-studied, making them suitable for advanced applications.

In a proof-of-concept hybridization of GaAs instrumented with SNSPD readout, two critical measurements characterize the system: the scintillation timescale and the light yield. It has been demonstrated that the scintillation timescale is highly dependent on the silicon and boron concentrations within the GaAs, as well as the proportions of scintillation light in each emission band [64]. While the scintillation timescale has been characterized at 10 K, it has yet to be investigated at even colder temperatures.

Previous characterization efforts have focused on optical excitation, with excitation-

emission spectra measured at 10 K using wavelengths ranging from ultraviolet to near-infrared [63]. This work aimed to probe the emission bands of GaAs, although timing information was not measured. The emission spectra and luminescence of GaAs have also been characterized at 10 K through X-ray excitation, alongside measurements of scintillation timescales using InGaAs photomultiplier tubes as the photosensor. However, the scintillation timescale remains understudied at sub-kelvin temperatures, particularly in response to lower energy excitations in GaAs.

To further investigate the scintillation response of *n*-type GaAs, two excitation sources were employed in this work. Measurements with a pulsed 660 nm source are detailed in this chapter, while those involving a cobalt-57 X-ray source are described in chapter 6. The 660 nm source excites the GaAs at the single electron-hole pair level, meaning that for each incident 600 nm photon, one electron-hole pair is created. In contrast, the X-ray source excites multiple electron-hole pairs, representing two distinct regimes of excitation.

5.1 Overview of systems measured

Scintillation measurements were performed with 2 different samples of *n*-type GaAs. These will be referred to as Sample A, and Sample B. Two different SNSPDs were used for Sample A and Sample B measurements, respectively.

The SNSPDs used in measurements in this chapter were fabricated by Ekkehart Schmidt, Sahil Patel, and Emanuel Knehr in the Microdevices Laboratory (MDL) clean-room at JPL. All measurement setups described in this chapter were constructed as a part of this thesis research with input from collaborator Steven Derenzo(LBNL). All of the described measurements were performed and analyzed as a part of this thesis research. Sample B of *n*-type GaAs was provided from LBNL.

5.1.1 GaAs Specifications and Analysis

N-type GaAs samples with high luminosity have free carrier concentrations from $2 \times 10^1\,\mathrm{cm}^{-3}$ to $6 \times 10^{17}\,\mathrm{cm}^{-3}$, with silicon and boron concentrations on the order of $10 \times 10^{17}\,\mathrm{cm}^{-3}$ [**?**]. Sample A was sourced from University Wafer, and sample B was sources from Freiberger. Table 5.1 lists the specifications of the two samples.

Sample	Dimensions (mm)	Carrier Concentration	N_{Boron}	$N_{Silicon}$
A	5 x 5 x 0.625	$2.99 \times 10^{17}\,\mathrm{cm}^{-3}$	$6.29 \times 10^{17}\,\mathrm{cm}^{-3}$	$1.14 \times 10^{19}\,\mathrm{cm}^{-3}$
B	10 x 10 x 4	$1 \times 10^{17}\,\mathrm{cm}^{-3}$ to $2 \times 10^{17}\,\mathrm{cm}^{-3}$	unknown	unknown

Table 5.1: Specifications of *n*-type GaAs samples. All information was obtained from the vendors, except for N_{Boron} and $N_{Silicon}$ which were obtained via SIMS analysis.

5.2 Detector and Sample Information

Two SNSPDs were used for measurements with the two *n*-type GaAs samples. The SNSPD used for sample A measurements was a WSi $1\,\mathrm{mm}^2$ active area 8 pixel array. Specifically, it was a generation 1 microwire array made from film 3 described in chapter 3. The SNSPD used for sample B measurements was a WSi $4\,\mathrm{mm}^2$ active area 8 pixel array from the generation 2 microwire wafer. More details on the device architecture and materials are listed in Table 5.2.

Device	Pixels	Material	Stoichiometry	Thickness	Wire Width	Fill Factor	Tc	Fabrication
A	8	WSi	42:58	4.7nm	1 µm	0.25	1.9K	e-beam lithography
B	8	WSi	50:50	2.3nm	1.5 µm	0.4	2K	photolithography

Table 5.2: Device Specifications

5.2.1 System A

System A consists of Sample A of GaAs coupled to device A.

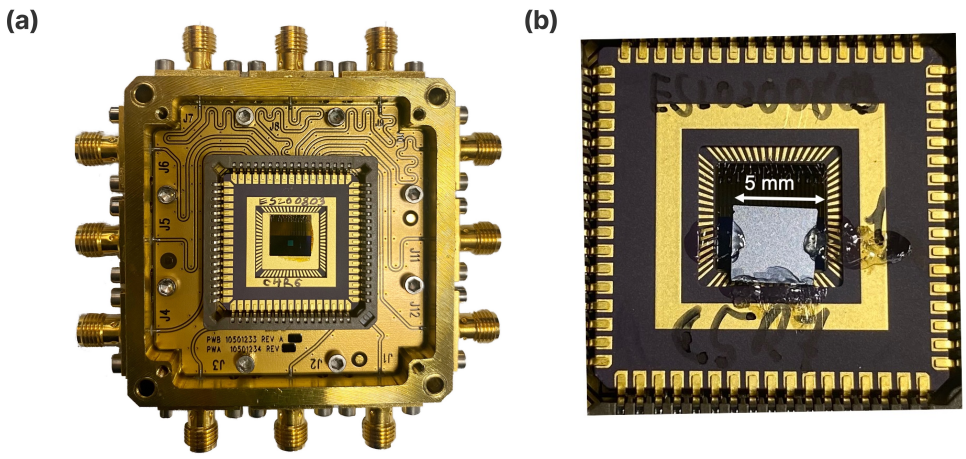


Figure 5.1: (a) the SNSPD and packaging used in system A (b) the SNSPD in the chip carrier with GaAs sample A

Device packaging and Hybridization

The device was placed in an LCC chip carrier in packaging with 8 SMA outputs. The GaAs sample was glued to the chip carrier using rubber cement. Figure 1a shows the SNSPD in the detector packaging, and Figure 1b shows the GaAs sample glued onto the active area of the SNSPD.

5.2.2 System B

System B consists of sample B of GaAs coupled to device B.

Device packaging and Hybridization

The packaging for system B was designed to be light-tight to reduce background counts. The PCB is external to the packaging to prevent any emitted Cherenkov radiation from

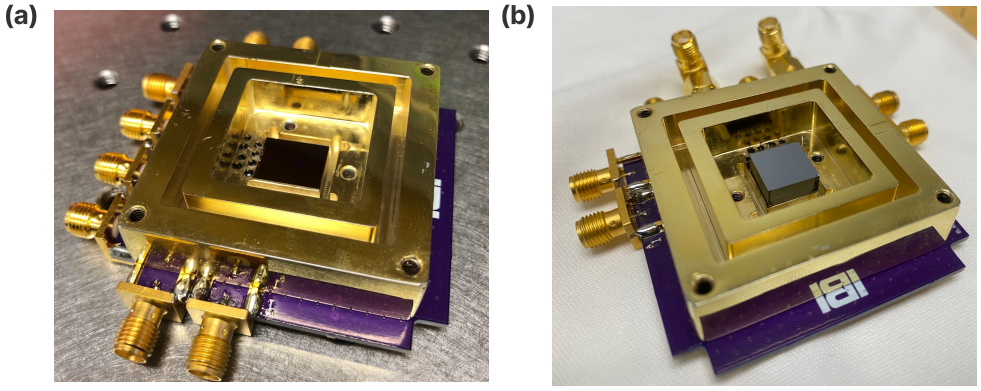


Figure 5.2: (a) the SNSPD and packaging used in system A (b) the SNSPD in the chip carrier with GaAs sample A

reaching the detector. The device is wire bonded to hermitic pins that are isolated from the exterior of the packaging and sealed in with Stycast 2850 ft epoxy. There are also barriers to prevent stray photons from accessing a path into the packaging. Figure 2 shows the dark box packaging. The lid with optical access was used for optical excitation measurements, and a sealed lid can also be implemented for a dark count rate measurement.

Device B has on-chip SU-8 standoffs for mounting the *n*-type GaAs sample at a fixed distance of 5 µm. Sample B of *n*-type GaAs was mounted over the active area and held in place with rubber cement glue, shown in figure 3.

5.3 Calibration of SNSPDs for Scintillation Light

As described in chapter 3, the near-infrared single-photon sensitivity of the SNSPDs was verified so it was expected that via visible pumping of the GaAs crystal hybridized to the SNSPD, a PCR curve could be measured. An example of this is shown in system A in figure 5.3, where the 660 nm laser was operated in CW mode while sweeping I_{bias}. PCR curves with different input powers of 660 nm excitation light were measured. This

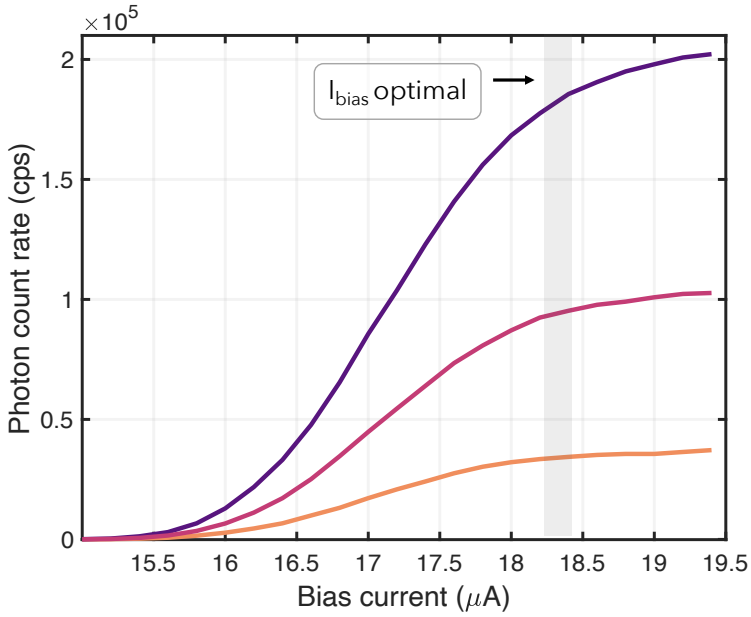


Figure 5.3: Scintillation light PCR curves shown for different levels of excitation beam power to show the dynamic range of the detector. A plateau indicating saturated internal detection efficiency is clear and allows for an optimal I_{bias} to be selected for operation.

procedure allowed an optimal I_{bias} to be determined for scintillation lifetime measurements, where as shown in this figure I_{bias} was selected to be within the plateau of the scintillation light PCR curve. We also observe a clear shift in the onset of the scintillation light PCR curve when it is compared to PCR curves on just the SNSPD (with no GaAs mounted) at wavelengths of 660 nm and 930 nm. This is shown in figure **??**, where the bias current was normalized to the switching current. The onset of the plateau of the scintillation PCR curve occurring at higher $I_{bias}$is due to the longer wavelength contributions from the 1100 nm and 1300 nm emission bands of *n*-type GaAs.

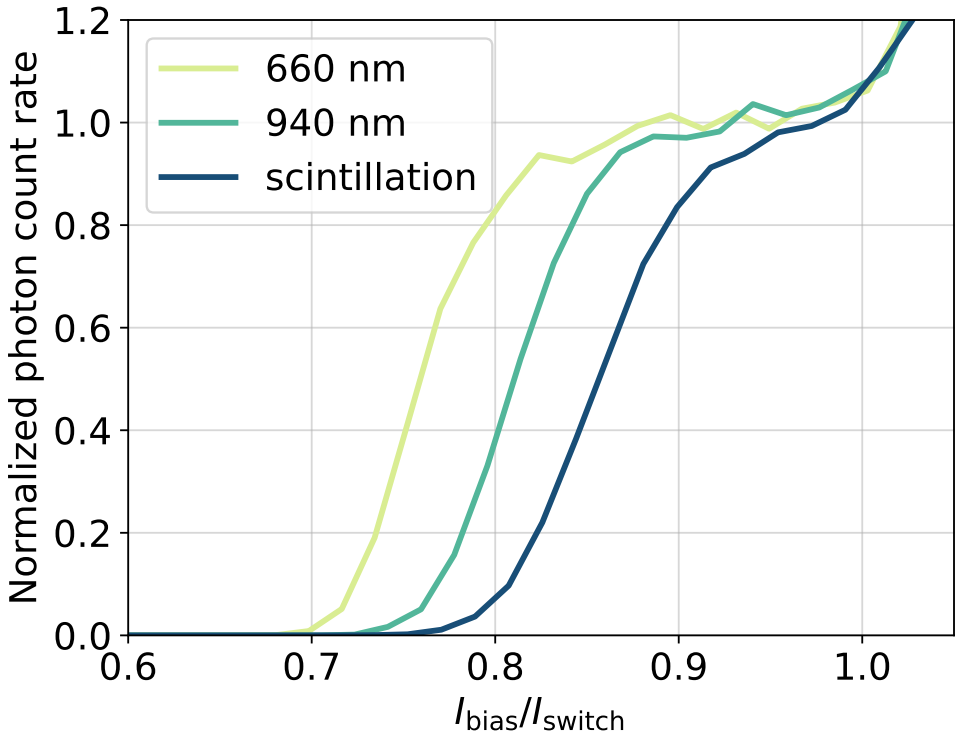


Figure 5.4: Normalized PCR curves for 660 nm and 930 nm incident on the SNSPD with no scintillator mounted and the PCR curve using the same detector of the NIR scintillation light generated from 660 nm excitation of the GaAs sample B. I_{bias} has been normalized to the I_{switch} measured since this image is a composite of two different cool-downs - one without the scintillator and one with the scintillator mounted.

5.4 Scintillation timescale measurements

Figure 5.7 shows the experimental setup used for scintillation timescale measurements using a pulsed 660 nm excitation beam. The 660 nm diode laser illuminating the *n*-type GaAs was driven via TTL control by a function generator to operate at a 10 kHz repetition rate. Another output of the function generator synced to the same pulse sequence was used as a reference for the Swabian Time Tagger. The SNSPD output was connected into an input channel on the Swabian Time Tagger, and the SNSPD output pulses correlated with the laser reference pulses were histogram. The SNSPD in system A was biased at the optimal I_{bias}. The count rate refers to the counts per second registered on the SNSPD with the GaAs under illumination.

This is shown on the GUI output in figure 5.5, where channel A is the SNSPD output, and input B is the reference pulse from the function generator driving the laser. The count rate on the SNSPD (channel A) is shown in the upper panel, and the histogram of correlated SNSPD output pulses with the laser reference is shown in the bottom panel.

To verify linearity of the decay curves and characterize the dynamic range of the detectors to scintillation light, a set of scintillation timescale histograms were measured using the setup described above at varying excitation beam powers. The scintillation decay curves measured for count rates of 10, 25, and 35 kcps on the detector are shown in figure 5.6 (a). The area under each curve was integrated, and the results are plotted in (b) for each count rate.

Single pixel measurement means that one pixel of the SMSPD array was biased, the GaAs was illuminated with 660 nm light, and the scintillation light was detected in the operating pixel. A sync pulse from the laser and the SMSPD output were directed to two different input channels of a Swabian Time Tagger Ultra run in standard resolution mode. A histogram of the time delay between the laser pulse and the SMSPD pulses was

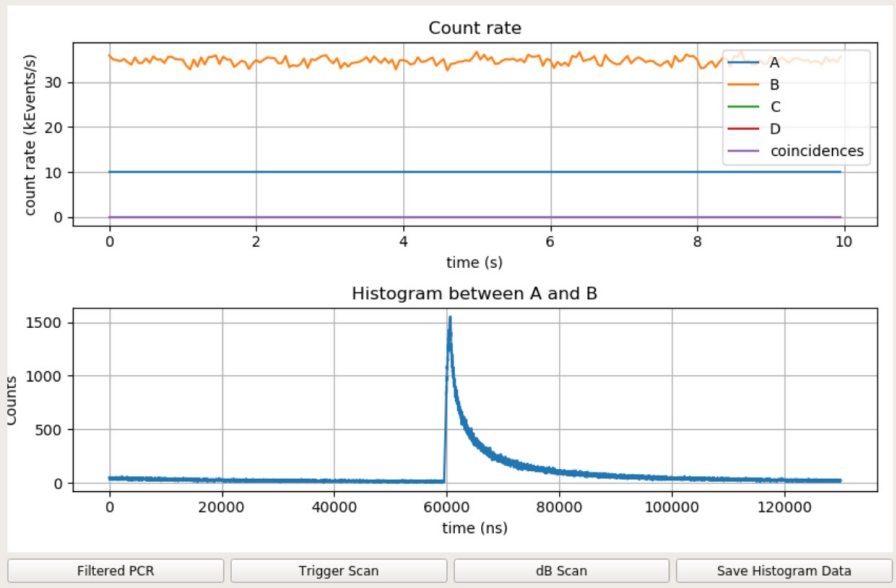


Figure 5.5: The Swabian Time Tagger GUI. Top panel showing the count rate on the SNSPD coupled to GaAs under 660 nm illumination (channel A), and the reference pulse from the function generator driving the laser (channel B). Bottom panel - histogram of the correlations between channel A and B is showing the SNSPD output pulses correlated with the laser sync pulses.

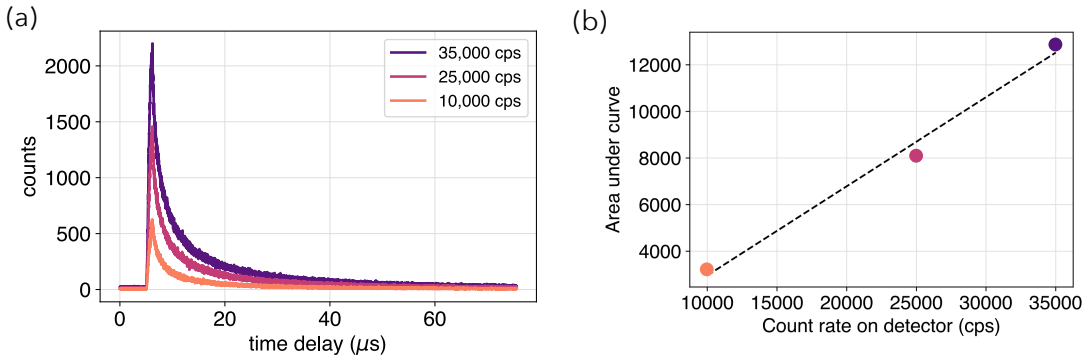


Figure 5.6: (a) The photoluminescence decay curves measured for different excitation beam powers, shown as different average count rates on the SNSPD.In (b) the area under each curve was calculated and plotted as a function of the average count rate on the SNSPD to verify linearity.

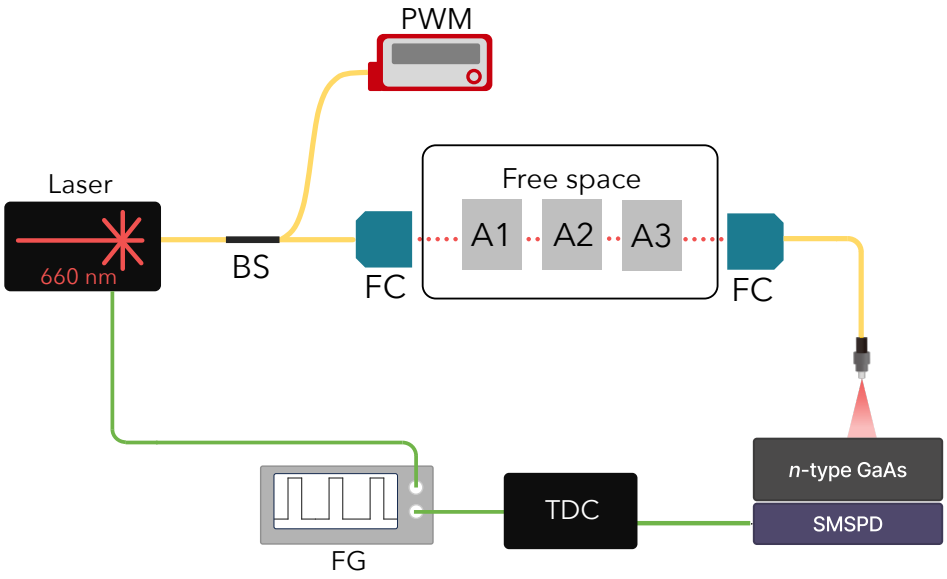


Figure 5.7: The 660 nm laser setup used for optically excited scintillation measurements. The pulse waveform parameters from function generator (FG) drive the laser repetition rate and a sync pulse into the Swabian Time Taggger . Light is coupled through a beam splitter (BS); one port is diverted to a power meter (PWM) to monitor power fluctuations in the laser. The signal path is attenuated by a series of ND filters (A1-A3) before it is coupled into a fiber that feeds into the fridge to illuminate the sample.

collected. These measurements were first done in the ICE fridge which had one readout line. The spot0 fridge has 8 readout and bias lines, and once the experiment was transferred to spot0 a set of single-pixel measurements were performed before scaling up to readout out multiple pixels at once. The System A SMSPD has a pixel size of 125 μm^2 and the the System B SMSPD has a pixel size of 500 μm^2.

5.4.1 Measurement setup

One pixel of System A was measured in the ICE fridge with the 660 nm laser running at a 10 kHz repetition rate. The light was directed into the fridge via a 660HP fiber.

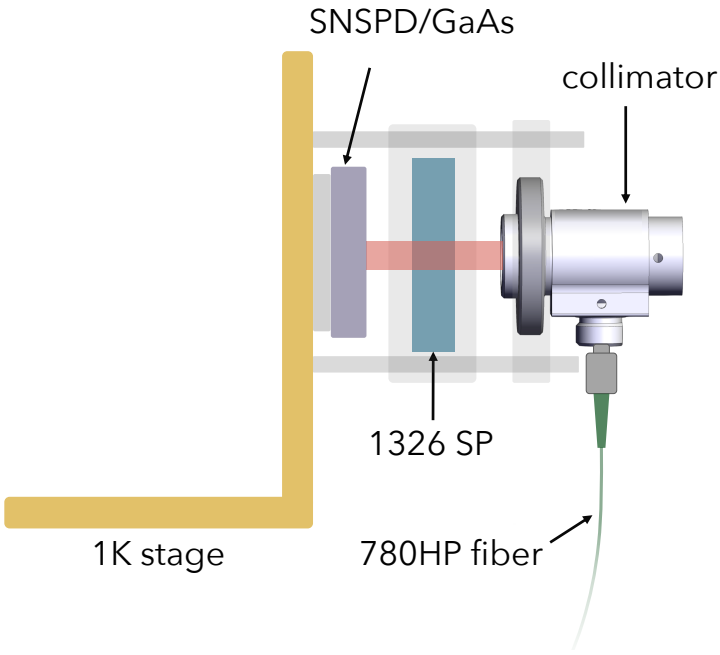


Figure 5.8: The optical assembly used for scintillation measurements. Via 780HP fiber, 660 nm light is coupled into reflective collimator, after which is passes through a 1326 nm short pass filter

A reflective collimator and focusing lens was added to the device packaging to deliver a small (15 µm) diameter spot on to the GaAs surface. Details of the optical assembly are shown in figure 5.8.

A single pixel measurement was done on System B in the spot0 cryostat. The same laser and optical setup was used, but to accommodate the longer timescale the laser repetition rate was slowed to 4 kHz.

5.4.2 Results and exponential fitting

Figure 5.9 shows the single-pixel scintillation timescale measurements; Figure A is from system A and figure B is from system B. An empirical 2-exponential fit to a function

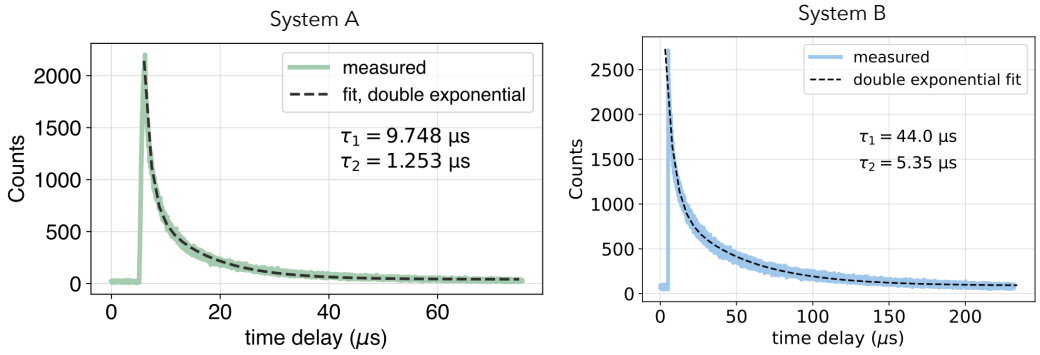


Figure 5.9: Scintillation timescale measurements from system A and system B.

of the form $A_1 e^{-\frac{t}{\tau_1}} + A_2 e^{-\frac{t}{\tau_2}} + B$.

System A decays on a shorter timescale with a ˜50 µs return to baseline. System B decays on a longer timescale with a ˜170 µs return to baseline. The larger geometry of the GaAs sample in System B will cause the scintillation light to bounce around more before exiting the face of the crystal adjacent to the SNSPD; this effect will cause broadening of the photoluminescence decay curve on the order of 100s of picoseconds per bounce. Given the very short timescales associated with this broadening, this is not sufficient to account for the longer time constants seen in System B compared to System A. The differences are likely due to System B having a significantly higher exiton lifetime, which is dependent on the dopant and free carrier concentrations of the GaAs sample [**?**].

5.5 Effective Light-yield Measurements

An estimate of the effective light yield Y_{meas} of the measurements of systems A and B was performed. This metric is defined by the following relationship:

$$Y_{meas} = Y_{abs} \cdot \eta_{det} \cdot \eta_{coll}, \tag{5.1}$$

where Y_{abs} is the absolute light yield of the n-type GaAs, an intrinsic property of the material, η_{det} is the system detection efficiency of the SNSPD over the range of wavelengths emitted by n-type GaAs, and η_{coll} is the light collection efficiency of the coupled scintillator and target which takes into account geometric losses, losses from absorption in materials other than the superconducting microwires, and scattering.

Measuring Y_{abs} directly is experimentally difficult due to the fact this it is difficult to quantify η_{coll} with a scintillator of known light yield [139]. Rather, in a system with a well-characterized high-efficiency detector, the effects of η_{coll} are usually calibrated out with a reference scintillator of known light yield. This is a future direction for a more efficient SNSPD and less system losses to achieve reasonable error bars.

In this work, Y_{meas} was estimated as a way to demonstrate the optical coupling between n-type GaAs instrumented with SNSPDs.

5.5.1 Measurement Setups

The quantity of light delivered to the n-type GaAs sample was calibrated using the same method described in chapter 3 for SNSPD efficiency measurements, where the 660 nm source was attenuated down to single-photon level using a series of calibrated ND filters. The losses through fiber and collimation optics were calibrated at 660 nm at room temperature. For Y_{meas} measurement on system A, one 1 SNSPD channel was biased and read out due to limitations in the cryostat readout lines at the time of measurement. The SNSPD output was directed to a Keysight counter. For system B, 5 SNSPD pixels were biased and readout simultaneously. The SNSPD outputs were directed to the Swabian Time Tagger. A measurement script and GUI was created to collect scintillation timescale histograms from all active channels out SNSPD output simultaneously, all using the laser sync pulse as the reference time.

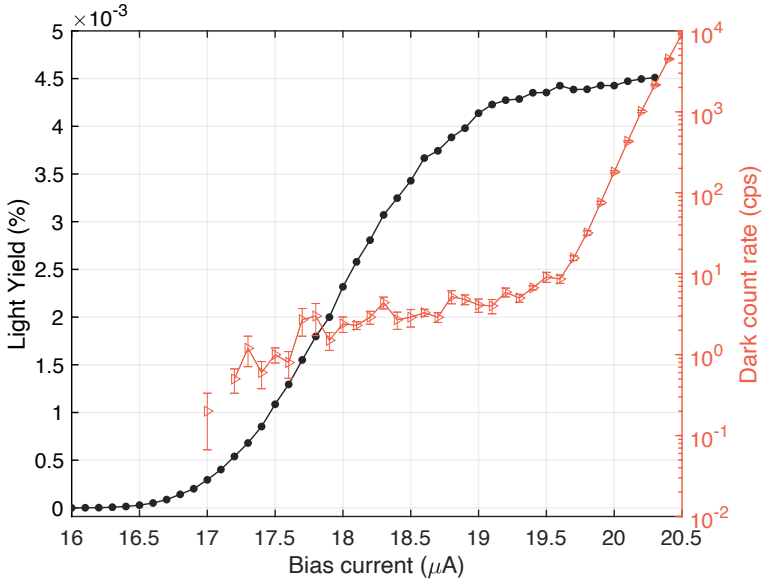


Figure 5.10: Light yield measurement performed on system A using the calibration setup shown in 3.6 to calibrate the 660 nm excitation source. The light yield is shown as a function of bias current with the dark count rate of the detector overlayed.

5.5.2 System A effective light yield

The effective light yield is shown in figure 5.10 as a function of I_{bias} of the SNSPD. The light yield on the y axis is the percentage of incident 660 nm excitation light that results in an NIR scintillation photon count on the SNSPD. A value of of 4e-3% is reached on the plateau.

5.5.3 System B Effective Light Yield

The scintillation timescales measured from the 5 operational SNSPD pixels are shown in figure 5.11 (raw data only, no fitting). The counts are relatively homogeneous across the array pixels.

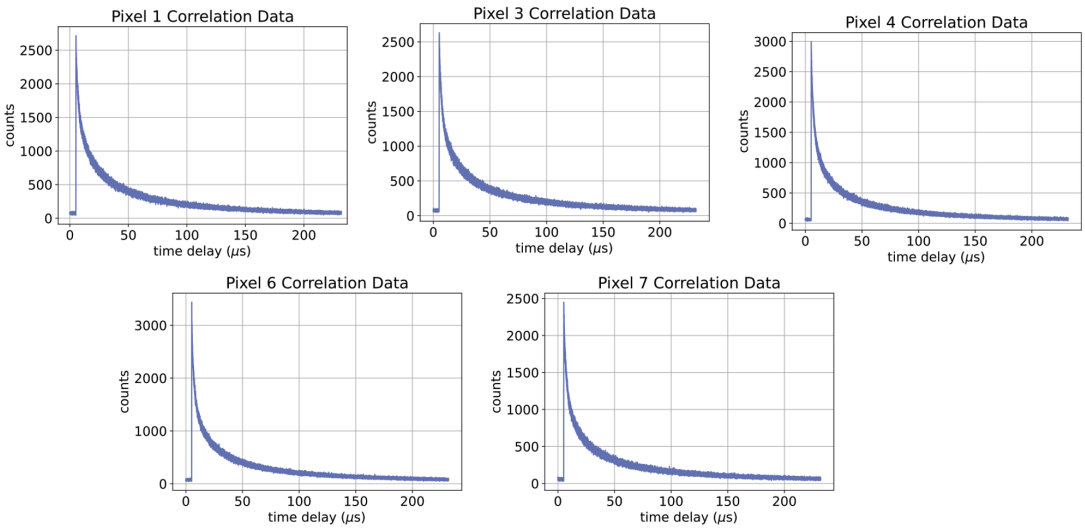


Figure 5.11: Multi-pixel scintillation timescale measurements system B.

The procedure to estimate the effective light yield in the configuration of system B utilizes a similar calibration setup shown in chapter 3.6. The version built for 660 nm is depicted schematically in figure **??**. Integrated into the measurement GUI controlling the Swabian Time Tagger is a feature that measures the cumulative power of the 660 nm laser and given the calibrated fiber losses, beam-splitter ratios, and a user input set of ND filters used, calculates the total power delivered to the scintillator during the measurement integration time. Then, the scintillation decay curves can be integrated to total a number of NIR photon counts collected during the measurement. Using this procedure, an effective light yield of $2.94 \times 10^{-4}\%$ was calculated. The order of magnitude of loss compared to the system A estimate is notes -¿ explanation will be added.

5.6 Future work towards Absolute Light Yield Measurements

The goal for a light yield measurement is to maximize the light collection efficiency of the scintillation light. To divert scintillation light that exits the GaAs crystal from faces that aren't adjacent to the SMSPD active area back into the crystal, external reflector will

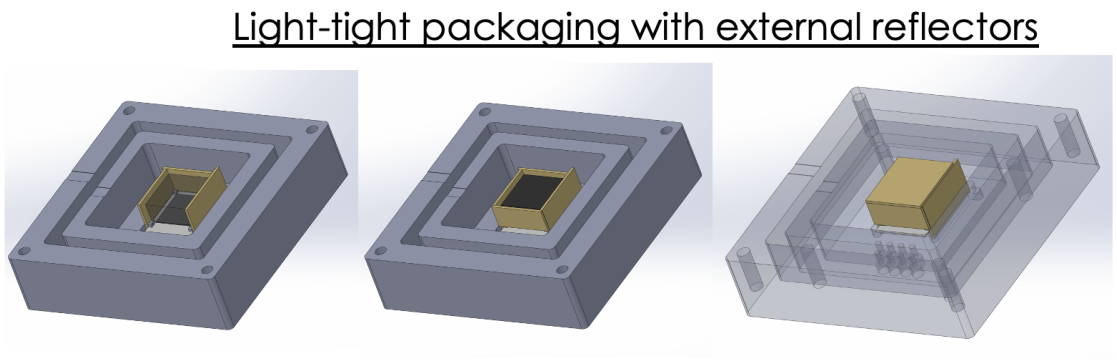


Figure 5.12: The light-tight packaging shown with machined slots for external reflectors to be inserted around the GaAs sample to improve light collection efficiency.

be places around the GaAs. This method was shown to be more efficient using monte carlo simulation methods in Ref. [**?**]. Once this light is redirected into the GaAs, it will bounce around in the sample and the scattering off of free carriers will change the angle of the photon's trajectory until it is within the solid angle that can couple out of the crystal (less than 16 degrees to avoid total internal reflection assuming an index of refraction of 3.6 for GaAs and a GaAs-air interface). Then the light will couple out of the GaAs on the detector-adjacent face. The packaging with these external reflector is shown in an illustration in figure 7.

With this implementation and an SNSPD in an optical stack with higher efficiency, the system losses can be calibrated with a scintillator of known light yield such as BGO in the same geometry is the *n*-type GaAs sample under investigation.

Chapter 6: X-ray Excited Scintillation Measurements

Chapter 5 detailed optically-excited scintillation measurements with *n*-type GaAs using microwire SNSPDs. This chapter describes X-ray excited scintillation measurement on the same system and implementation of energy-tagged X-ray excitation measurement infrastructure. The GaAs/SNSPD modules used in this chapter are system B as described in Chapter 5. The design and analysis of the mock-up energy-tagged X-ray excitation setup was lead by Christina Wang and Jason Trevor (Caltech) [140]. The extension of this to the GaAs/SNSPD and cryogenic system and analysis was carried out as a part of this thesis research.

The direct band gap of *n*-type GaAs is 1.42 eV, corresponding to a wavelength of approximately 870 nm. In chapter 5, the 660 nm excitation beam, which corresponds to 1.88 eV, is slightly above the band gap. The absorption coefficient α for GaAs at 660 nm is $\approx 10^4\,\mathrm{cm}^{-1}$. The penetration depth is given by $d = \frac{1}{\alpha}$. For a 660 nm photon, the penetration depth $d_{660\,\mathrm{nm}}$ is given by $d_{660\,\mathrm{nm}} \approx \frac{1}{10^4\,\mathrm{cm}^{-1}} = 0.1\,\mathrm{microns} \approx 100\,\mathrm{nm}$. So, the 660 nm photons that get absorbed in a 4 mm thick GaAs crystal will result in a near-surface excitation of approximately 1 electron-hole pair.

X-ray deposition in scintillators using a Compton scattering setup which will be outlines in the following section is a standard method of characterization in High Energy Physics. When X-rays pass through a material, they interact with the atoms primarily via processes like photoelectric absorption, Compton scattering, and pair production. These interactions cause the X-ray intensity to decrease exponentially with the thickness of the

material. The reduction in intensity I of X-rays as they travel through a material of thickness x is described by the equation:

$$I(x) = I_0\, e^{-\mu_l x} \tag{6.1}$$

where I_0 is the initial intensity of the X-ray beam, μ_l is the linear absorption coefficient, and x is the thickness of the material. The linear absorption coefficient μ_l represents the probability per unit length that an X-ray photon will be absorbed or scattered as it travels through a material. The linear absorption coefficient μ_{lin} is calculated from the mass absorption coefficient μ_m using the following formula:

$$\mu_{\text{lin}} = \mu_m \times \rho$$

For 5 keV X-rays:

$$\mu_{\text{lin}}(5\,\text{keV}) = 350\,\text{cm}^2/\text{g} \times 5.32\,\text{g/cm}^3 = 1862\,\text{cm}^{-1}$$

For 10 keV X-rays:

$$\mu_{\text{lin}}(10\,\text{keV}) = 50\,\text{cm}^2/\text{g} \times 5.32\,\text{g/cm}^3 = 266\,\text{cm}^{-1}$$

The penetration depth d is the inverse of the linear absorption coefficient μ_{lin}:

$$d = \frac{1}{\mu_{\text{lin}}}$$

For 5 keV X-rays:

$$d5\,\text{keV}) = \frac{1}{1862\,\text{cm}^{-1}} \approx 0.000537\,\text{cm} \approx 5.37\,\mu\text{m}$$

For 10 keV X-rays:

$$d(10\,\mathrm{keV}) = \frac{1}{266\,\mathrm{cm}^{-1}} \approx 0.00376\,\mathrm{cm} \approx 37.6\,\mu\mathrm{m}$$

In this regime, the penetration is greater by roughly an order of magnitude, and the number of electron-hole pairs created in GaAs upon excitation is approximately 1000–2000 for 5 keV and 10 keV energy depositions, respectively. The scintillation timescale and exciton interaction dynamics will be different in this regime.

This chapter details the energy-tagged X-ray excitation system designed to measure the light yield and detection efficiency of the GaAs/SNSPD prototype.

The SNSPDs used in the measurements of this chapter were fabricated by Emanuel Knehr in the Microdevices Laboratory (MDL) clean-room at JPL. The measurement setup described in Section 6.3 was designed and implemented by Christina Wang (FNAL) and Jason Trevor (Caltech). The X-ray measurements of the SNSPS/GaAs system in the cryostat and analysis were performed independently as a part of this thesis research.

6.1 Compton Scattering

When X-rays interact with GaAs, several processes can occur, including photoelectric absorption and Compton scattering. In photoelectric absorption, the X-ray photon transfers all its energy to an electron, ejecting it from the atom. In Compton scattering, the X-ray photon collides with an electron, transferring part of its energy and changing its direction. In the setup used for this work, an incoming high-energy photon will have some probability of undergoing Compton scattering with the target. In that case, it scatters off the GaAs, depositing some energy and leading to scintillation photons that the SNSPD will detect. This also produces an outgoing scattered photon at an angle θ with respect to the original photon's direction. The relationship between the energy of the incoming photon (E_{in}) and

the outgoing photon (E_{out}) is given by:

$$E_{\text{out}} = \frac{E_{\text{in}}}{1 + \frac{E_{\text{in}}}{m_e c^2}(1 - \cos\theta)} \tag{6.2}$$

where m_e is the electron mass, c is the speed of light, and θ is the scattering angle. A detector placed external to the cryostat can be used to capture the outgoing scattered photon. Coincidences between this external detector and the SNSPD detection events will indicate that Compton scattering events have been captured.

A detector placed external to the cryostat can be used to capture the outgoing scattered photon. Coincidences between this external detector and the SNSPD detection events will mean that the Compton scattering events are captured. A high-purity Germanium detector (HPGe) is used as the external detector due to its excellent energy resolution in the 3-300 keV range. In comparison, other scintillating detectors traditionally used in Compton-scattering setups such as Sodium Iodide (NaI) detectors with photomultiplier tubes (PMTs) can't resolve energies lower than 1000 keV. A schematic diagram of the experimental setup for the X-ray characterization is shown in Figure 6.1. In this setup, the GaAs and SNSPD are located inside of a cryostat. The radioactive source is at room temperature on a linear stage, and the HPGe detector requires cooling to cryogenic temperature with liquid nitrogen which can be accomplished using a dewar.

Cobalt-57 (^{57}Co) has gamma-ray emissions at 6.5 keV, 14.4 keV, 122.1 keV, and 136.5 keV. These energies are useful for both calibration and energy deposition in the scintillating GaAs. The relationship between the target energy (E_{out}) and the scattering angle θ from equation 6.2 is plotted in figure 6.2.

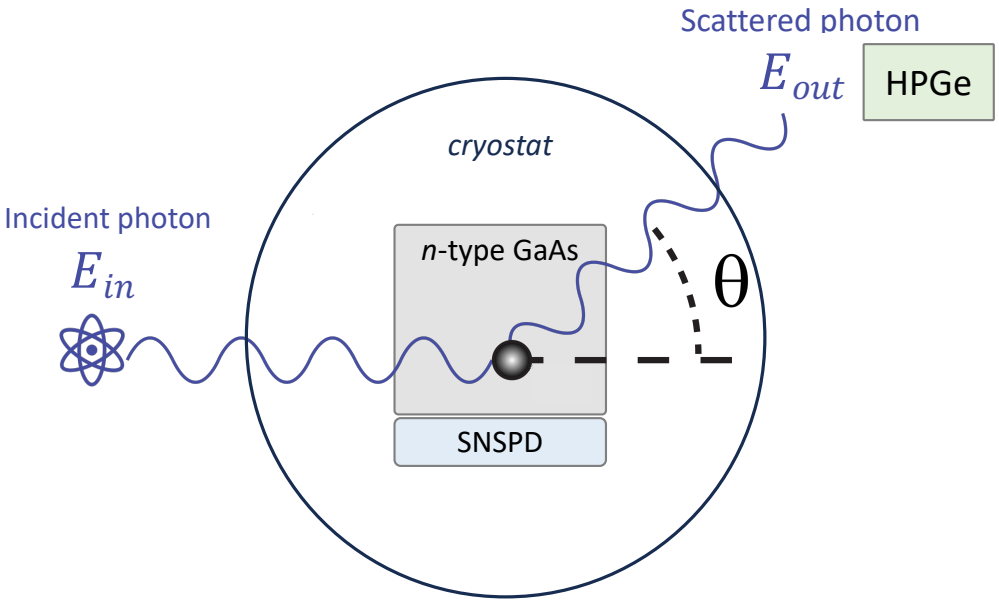


Figure 6.1: Schematic of the Compton scattering setup for the X-ray characterization. An incident X-ray with energy E_{in} travels through the cryostat to the n-type GaAs target, where it undergoes a Compton scattering interaction with an electron in the target. An outgoing X-ray with lower energy E_{out} exits the cryostat is is detected by an externally mounted HPGe detector.

6.2 X-ray Source

The X-ray source shown in a lead container in figure 6.1 is a 50 Mössbauer cobalt-57 sample. The activity in June 2018 was 50 mCi. The activity at the time of experiments (October 2024) can be calculated using the following formula for radioactive decay:

$$A(t) = A_0 \times e^{-\lambda t} \tag{6.3}$$

where $A(t)$ is the activity at time t,A_0 is the initial activity, λ is the decay constant, and t is the elapsed time .

The half life ($T_{1/2}$) of cobalt-57 is 271.82 days and can be related to the decay constant λ as $\lambda = \frac{ln(2)}{T_{1/2}}$. The elapsed time from June 2018 to October 2024 is 2,313 days. Plugging all of this in, the activity of the source at the time of measurement is

$$A(t) = 50\,\text{mCi} \times e^{-\left(\frac{\ln(2)}{271.8} \times 2313\right)} \approx 0.137\,\text{mCi} \tag{6.4}$$

For all experiments, the cobalt-57 source was placed in a tungsten collimator with a 3 mm diameter aperture. The rate of X-ray flux through the collimator aperture can be calculated as $\Gamma_x = \Phi * \eta_{co-57}$, where Φ is the flux through the collimator aperture, given by the activity of the source in Bequerels / aperture area, and η_{Co57} is the X-ray yield for cobalt-57. Plugging in the relevant values, we have

$$\Phi = \frac{(0.137 \times 10^{-3}) \times (3.7 \times 10^{10}\,\text{Bq}) \times 0.09}{\pi \times (1.5 \times 10^{-3}\,\text{m})^2} \approx 6.45 \times 10^{10}\,\text{Bq/m}^2 \tag{6.5}$$

$$\approx 6.45 \times 10^{10}\,\text{x rays/(s} \cdot \text{m}^2) \tag{6.6}$$

The portion of this rate corresponding to the 122 keV, 136 keV and lower energy emissions can be estimated from the branching ratios of cobalt-57 which provide the percentage of emissions corresponding to each energy. These are listed in table 6.1.

Gamma Energy (keV)	**Branching Ratio (%)**
122	85.5
136	11.4
Others	3.1

Table 6.1: Branching ratios for gamma emissions from Cobalt-57

6.3 Calibration of HPGe Detectors

To validate the setup, the cryogenic GaAs/SNSPD system was replaced by a second HPGe detector with the goal of measuring the energy deposited in both detectors. Each HPGe detector was calibrated by measuring and analyzing the energy spectrum of Co-57. The output signal from the HPGe detectors is processed through a shaping amplifier, which



Figure 6.2: A photograph of the Cobalt - 57 source in leaded housing used for X-ray characterization experiments.

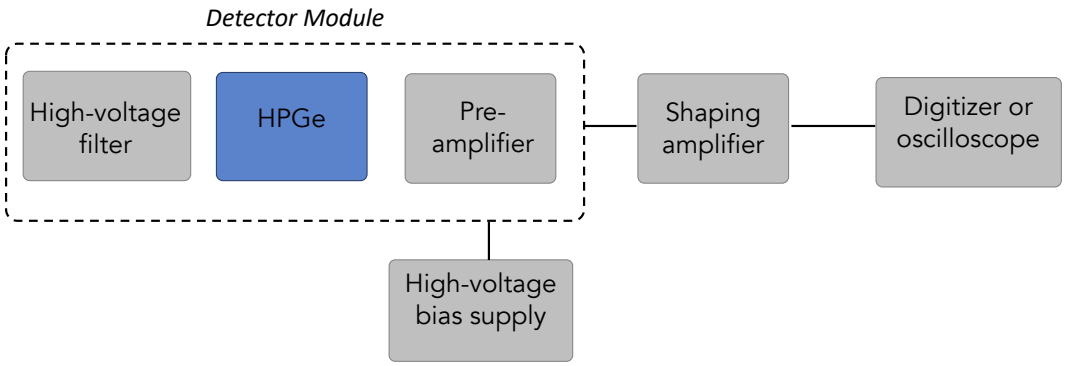


Figure 6.3: Connection of components in an HPGE Energy Spectroscopy System. The HPGe is biased with an Ortec 659 NIM module. Internal to the HPGe detector there is a high voltage filter implemented as well as a preamplifier before the detector output to a shaping amplifier.

generates Gaussian pulses with amplitudes proportional to the energy. These pulses are then displayed on an oscilloscope, producing a histogram of the pulse amplitudes. This is shown schematically in Figure 6.3. The amplitudes are converted to energy by correlating the peaks in the histogram with the known photon emissions of Co-57, specifically at 6.5, 14.4, 122.1, and 136.5 keV. Figure 6.4 shows the energy spectrum of Co-57 as measured by one of the HP-Ge detectors. The observed peaks are at 6.3, 14.2, 121.9, and 136.6 keV, with full widths at half maximum (FWHM) of 1.4, 1.9, 1.1, and 0.5 keV, respectively, which are consistent with the vendor's specifications.

A picture of the two-HPGe setup is shown in 6.5. Measurements were performed with angles 35^{o}, 70^{o}, and 120^{o}, corresponding to target detector energy deposits of 5, 16, and 32 keV, respectively. The measured energy at both detectors agrees with the expected energy, which was calculated based on the scattering angle between the two detectors for all angles.

The 2D energy distribution of the target and tag detectors for the 35^{o} experiment is shown in Figure 6.6 (left). A diagonal line with an energy sum of 122 keV is clearly visible, and another fainter diagonal line with a sum of 136 keV is also visible, corresponding to

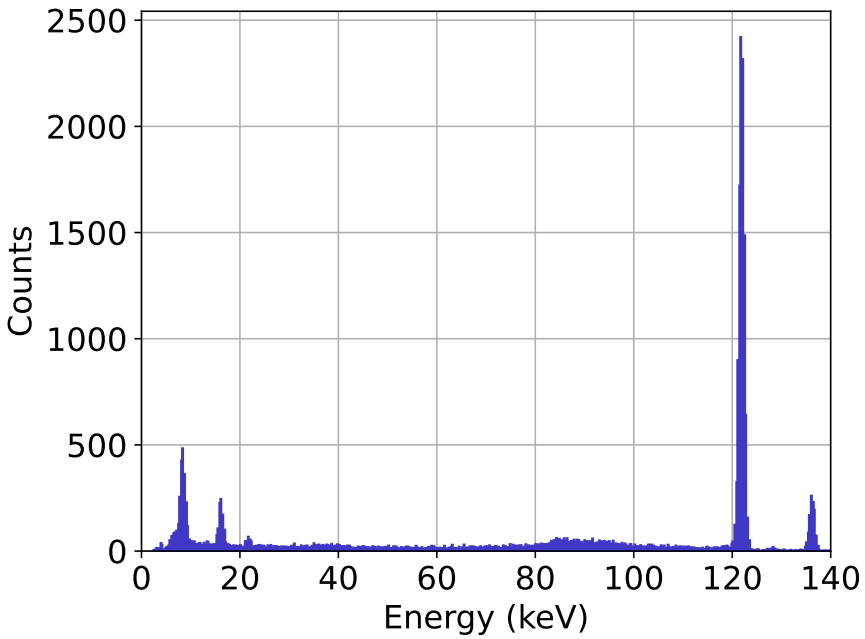


Figure 6.4: Energy spectrum of Co-57 measured by HPGe detector using an oscilloscope.

122 and 136 keV photons from Co-57. The energy distributions of the target and tag detectors after requiring the sum of the energy deposits at the detectors to be between 121 and 123 keV are shown in Figure 6.6 (right). Energy peaks of 5.3 ± 1.1 keV and 116.3 ± 1.3 keV are measured at the target and tag detectors, respectively, agreeing with the expected energies of 5 and 117 keV for a scattering angle of 35^{o}. Similar agreements were observed for scattering angles 70^{o} and 120^{o}. Therefore, it has been demonstrated that X-ray energy between 5 (= 35^{o}) and 32 keV (= 120^{o}) can be deposited in the GaAs.

6.4 Timescale Measurements

Before proceeding with measurements on the hybridized SNSPS-GaAs system, it was verified in a measurement with the SNSPD without the scintillator did not have direct sensitivity to the X-ray source. The detector was mounted with the lid that has optical

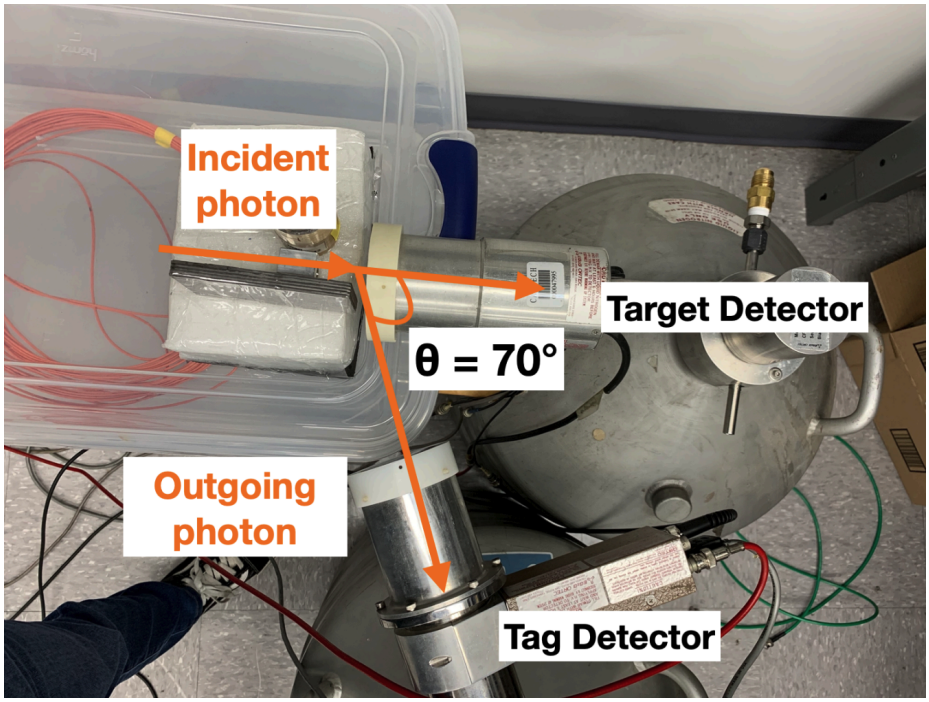


Figure 6.5: A picture of the setup to validate the Compton scattering experiment with two HPGe detectors is shown. The radioactive source is placed as close as possible to the target detector, where the Compton scattering occurs, to maximize the rate. Lead plates are placed next to the source to block any photons from Co-57 to directly reach the tag detector. The tag detector is placed at an angle of 70^{o} from the target detector.

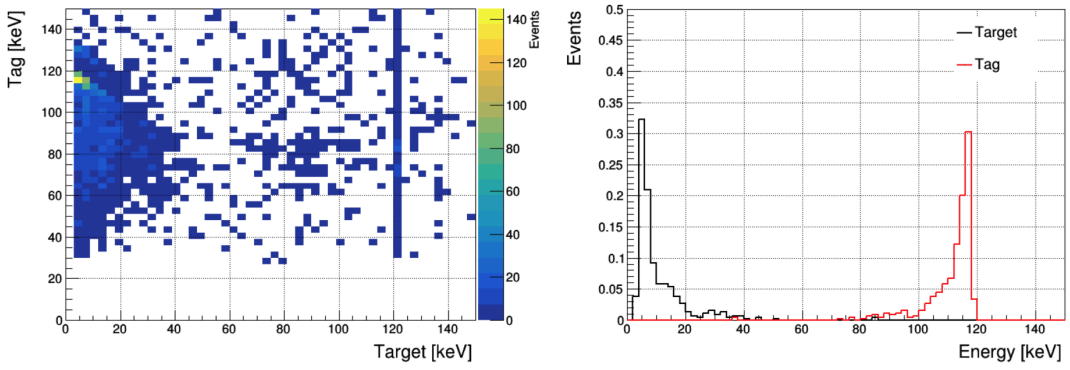


Figure 6.6: The 2D energy distribution (left) of the tag and target detector and the individual energy distributions (right) of the two detectors after requiring their energy sum to be between 121 and 123 keV. The energy distributions correspond to a scattering angle of 35^{o}.

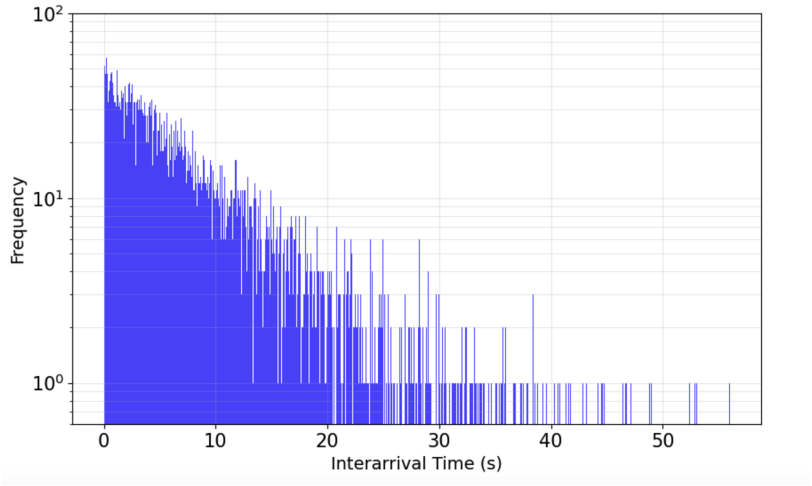


Figure 6.7: The inter-arrival time of the time-ordered SNSPD detection events measured with no X-ray source. The data approximately follows an exponential, indicating Poisson distributed noise.

access over the active area. A central pixel of the SNSPD was biased and the output was directed to a Keysight counter. The X-ray source was placed directly in front of the spot where the detector is mounted from outside of the cryostat in the collimator and with the top of the collimator open to increase the flux. In both situations, no change in the counts on the detector occurred. This procedure was repeated for all active channels across the array. Moving forward with analysis, the GaAs sample B was mounted for an 8 pixel 2 mm x 2 mm generation 2 microwire array (system B as described in chapter 5).

6.4.1 Background Measurements of GaAs-SNSPD System

System B was cooled to 800 mK and the SNSPD channels were biased with SRS voltage sources to 0.90 I_{switch} and outputs were connected to the Swabian Time tagger. Time tags corresponding to detection events on the SNSPD were collected for 1 hour. Figure 6.7 shows the inter-arrival times of these events across all measured SNSPD channels.



Figure 6.8: Photograph of a CAEN digitizer V1751 module in VME crate.

6.4.2 CAEN Digitizer Readout

The CAEN Mod.V1751, shown in figure 6.8, is a digitizer that records waveforms. It can also perform advanced algorithms for online digital pulse processing (DPP) of charge integration and pulse shape discrimination with constant fraction timing and zero-length encoding. Data is read by a Flash ADC with 10-bit resolution and 1 GS/s sampling rate, which is well suited for signals from common detectors used in High Energy Physics including organic, inorganic and liquid scintillators coupled to PMTs or Silicon Photomultipliers. For the Compton Scattering experiment of interest in this work, the HPGe detector's energy resolution is needed to infer the quantity of energy deposited into the scintillator. The ADC channels of the digitizer can be calibrated to the cobalt-57 emission spectrum. An example of this calibration is shown in figure blah blah.

To implement the full Compton-scattering experiment, it is necessary to also integrate the SNSPD output channels intro the digitizer readout. This readout for SNSPDs offers the advantages of waveform filtering to remove noise pulses from electrical pickup. An example of this is shown in figure 6.9

The digitizer stores data using ROOT, the open-source software and analysis framework

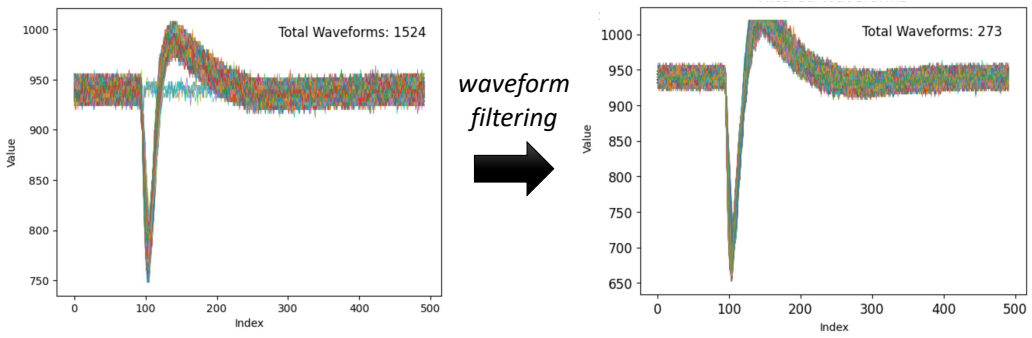


Figure 6.9: Waveform filtering capabilities enabled by the CAEN digitizer demonstrated, where the waveforms on the left include events that triggered on electronic noise. These are filtered out in the set of waveforms shown on the right.

developed by CERN. In the work contained within this chapter, the python library Uproot was used for reading and writing ROOT files in pure Python and NumPy to then perform analysis in python. In the ROOT data structure, the waveforms are time-stamped, so time tags corresponding to the detection events can be accessed and analyzed in a similar manner to the analysis performed using a Swabian Time tagger.

6.4.3 Source Effect on GaAs-SNSPD System

With the SNSPDs biased at this same I_{bias} as the measurement in Section 6.4.1, the cobalt-57 source was directed at the mounted GaAs from outside of the cryostat. The angle of the source relative to the cryostat was scanned to maximize the count rate across SNSPD pixels. This corresponds to approximately normally incident X-ray flux onto the GaAs sample. The GaAs sample was irradiated for 1.5 hours while the SNSPD time-stamped waveforms were collected on the CAEN digitizer. The inter-arrival times of the SNSPD detection events are plotted in Figure 6.10.

In the inter-arrival time data, there are two timescales evident - a prompt component and a slower component resembling the background distribution shown in figure 6.10. Figure

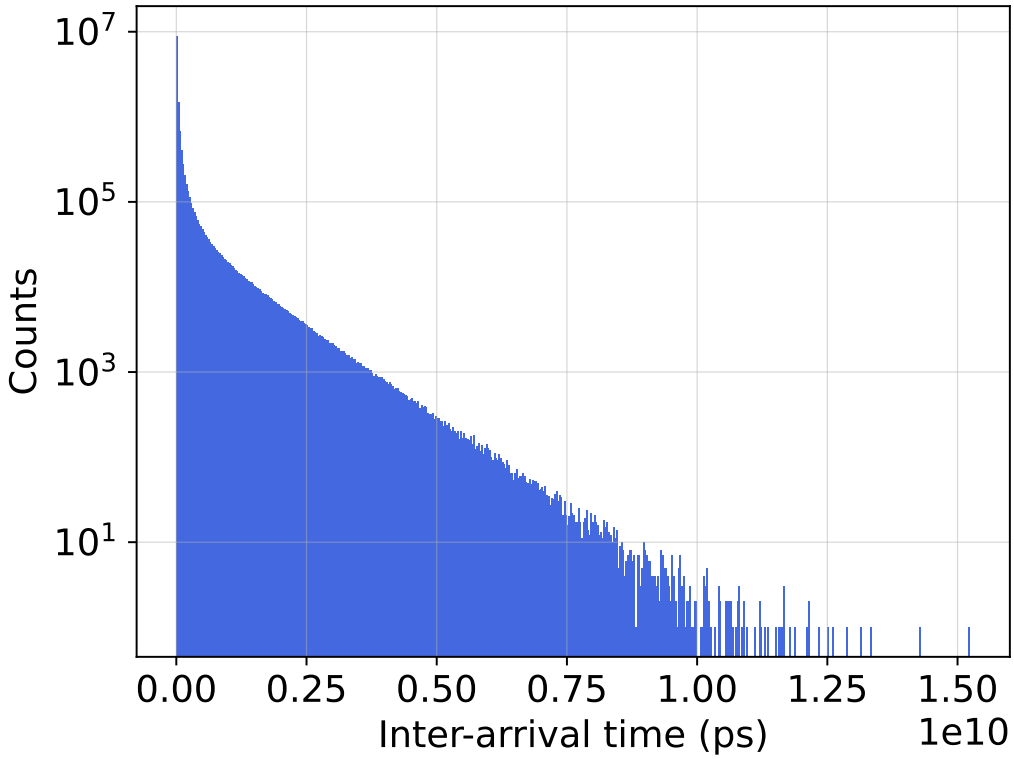


Figure 6.10: Inter-arrival times of SNSPD counts recorded on the CAEN digitizer during X-ray irradiation of the *n*-type GaAs through the cryostat.

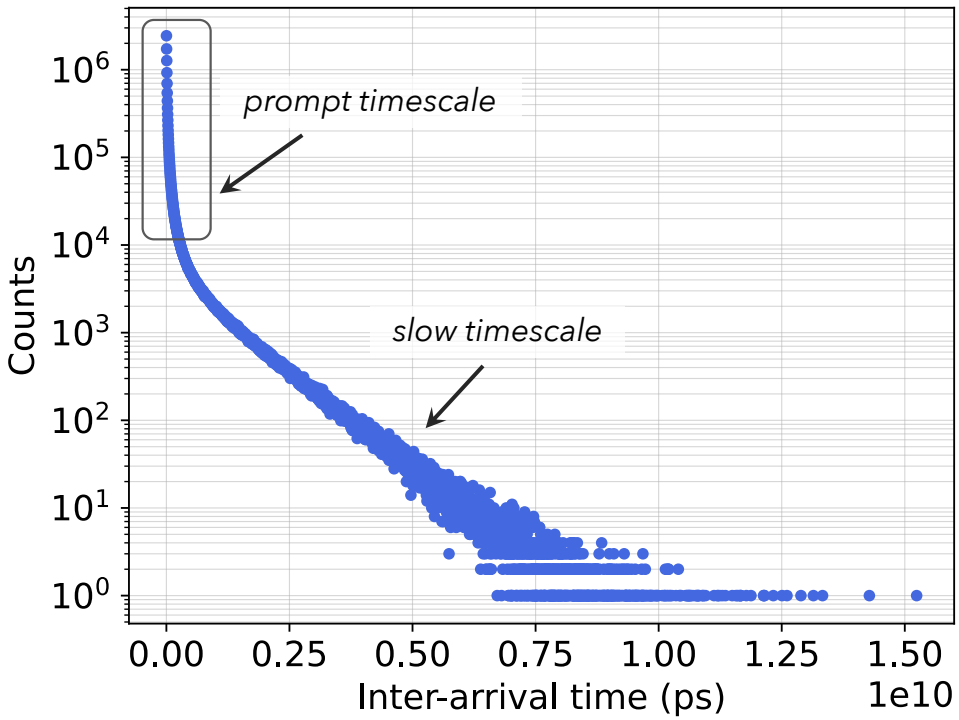


Figure 6.11: The inter-arrival time distribution for the SNSPD channels during irradiation of GaAs with the cobalt-57 source has a prompt decay component and a slow decay component.

shows these components.

Fitting the prompt component (0 - 100 µs) of the inter-arrival time distribution to a triple exponential of the form blah, the timescales associated with this decay are consistent with the scintillation decay times of *n*-type GaAs. The prompt component of the inter-arrival times and exponential fits are shown in figure 6.12 with (a) linear y-scale and (b) logarithmic log scale.

The scintillation decay curve measured via X-ray excitation is compared to the measurement obtained via optical excitation in Chapter 5 in Figure 6.13.

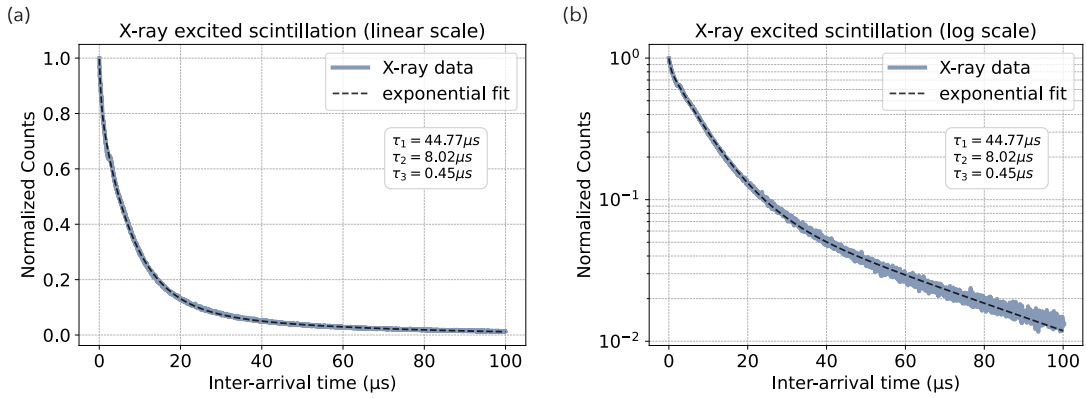


Figure 6.12: The prompt component of the inter-arrival time distribution (inter-arrival times up to 100 μs) is fit to a triple exponential. The normalized decay curve and exponential fits are plotted on a linear scale (a) and logarithmic scale (b).

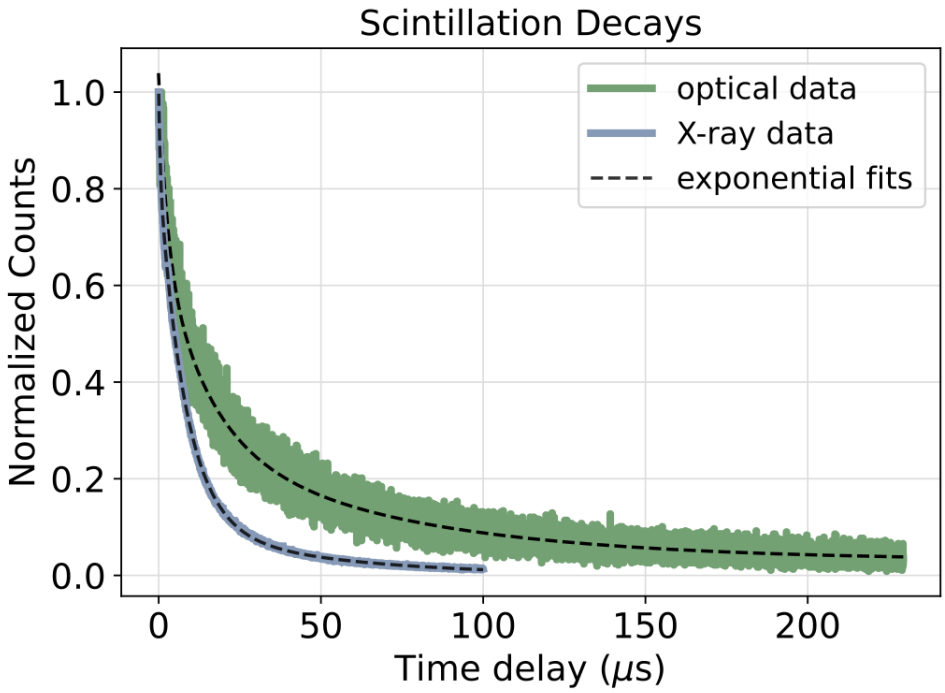


Figure 6.13: The scintillation decay measured via X-ray excitation (blue) and via optical excitation (green). The X-ray excited scintillation measurements feature a more prompt decay.

6.5 Compton Scattering Analysis and Challenges

In the ideal scenario of a Compton scattering experiment, the X-ray Compton scatters off of the *n*-type GaAs target, depositing some energy into the target. Then, the outgoing X-ray exits the cryostat and is detected by the HPGe detector at a set angle with respect to the irradiation axis, while the excited GaAs in the cryostat decays and begins emitting scintillation photons. There will be an expected burst of scintillation photons detected on the SNSPD in coincidence with the Compton-scattered X-ray detection in the external HPGe detector. The coincidence window is set by the scintillation decay timescale. Figure 6.14 demonstrates this schematically, taking this window to be 20 µs, where (a) shows the SNSPD pulse bursts centered around the HPGe pulses, (b) depicts the energy-resolved HPGe output pulses coming out of the shaping amplifier, and (c) demonstrates the expected proportionality between the HPGe pulse amplitude and the number of photons detected on the SNSPD. The higher amplitude HPGe pulses correspond to higher X-ray energies, meaning that less energy was deposited into the GaAs target, so fewer photons are expected to shower the SNSPD. The slope of (c) is the light yield in photons/keV of the system, accounting for all losses.

If the digitizer is operated to store all time-stamped waveforms on the SNSPD and HPGE output channels, it should therefore be possible to expose the target and collect time and energy-stamped waveforms from the SNSPD and HPGe output pulses, and in post-processing make an energy cut for a particular energy on the HPGe detector. Then, for a particular, the script can search for SNSPD pulses that occurred within the coincidence window around the HPGe event. These will correspond to SNSPD events from radiative decay of *n*-type GaAs after an X-ray deposited a known quantity of energy into it via Compton scattering.

For example, a dataset is collected with the HPGe set at an angle pf blah from the

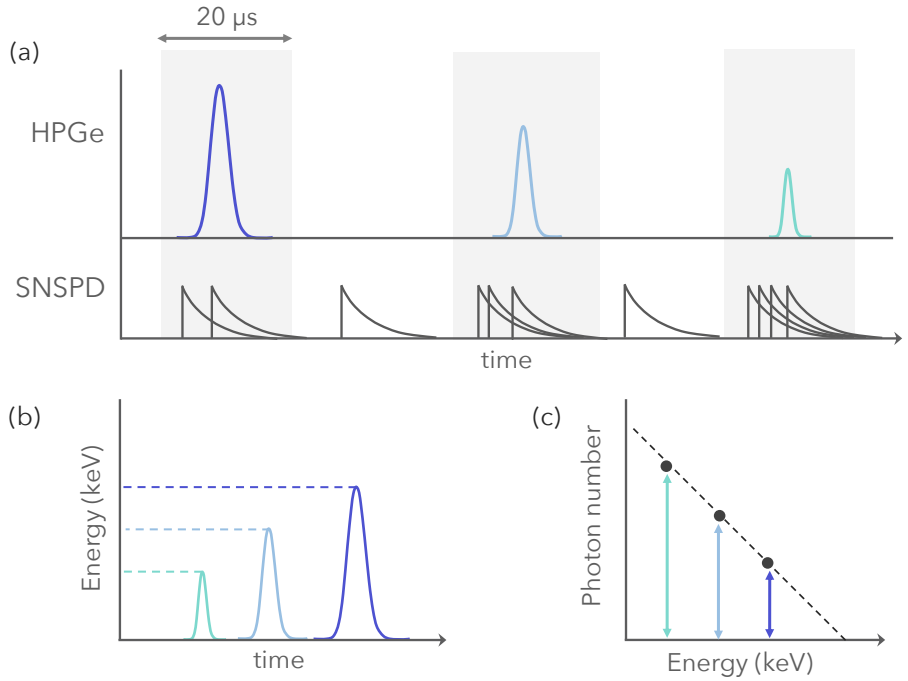


Figure 6.14: (a) The top panel shows HPGe events where the pulses are energy resolving, and the bottom panel shows bursts of SNSPD pulses correlated with the HPGe pulses in a 20 μs coincidence window. (b) depicts the energy proportionality of the HPGe output pulses, and (c) depicts the relationship between the HPGe pulse amplitude and the number of photons detected by the SNSPD.

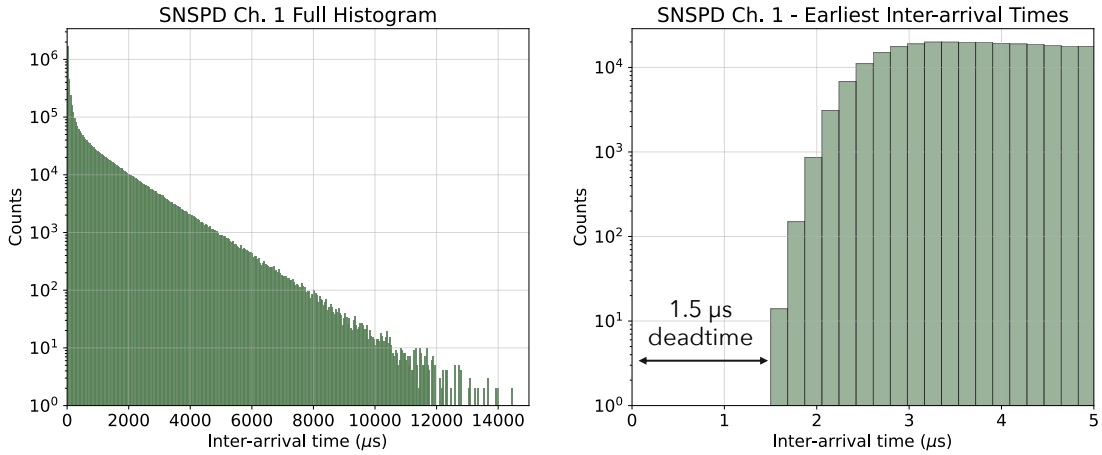


Figure 6.15: The dead time of the SNSPD can be extracted by looking at the early inter-arrival times in the histogram, shown in (a). (b) shows the histogram zoomed in to the earliest inter-arrival times, and where the counts drop to zero is the recovery time of the device.

irradiation axis to target a 7 keV energy deposition into the cryostat by the relationship in equation 6.2. After the run, a narrow energy cut is made around 115 keV ± 0.2 on the HPGe output pulses. This signal on the HPGe means that the 122 keV X-ray exited the co-57 source and deposited 7 keV of energy into the GaAs before exiting the cryostat. The coincident events on the SNSPD channels in a 20 µ window around the HPGe event are then counted.

The scintillation timescale of is in a regime where one SNSPD channel can go through the detection cycle and recover while the GaAs is still undergoing radiative decays. To verify this, the time tags from the dataset of section 6.4.3 measuring the source effect on the GaAs-SNSPD system were separated by SNSPD channel. In the single-channel inter-arrival time histograms, the dead-time of the SNSPD is the distance between 0 and the first bin of events. This is shown in figure 6.15 for one of the SNSPD channels where the dead-time was measured to be 1.5 µs.

6.5.1 Poisson Statistics and Mean Photon Number Fitting

In the full Compton scattering setup at this stage, there are system-level losses that complicate the ability to obtain an absolute photon number count with respect to a given HPGe energy cut. These losses include geometric losses due to the mismatch in the coupled surface area between the GaAs sample B (10×10 mm^2) and the SNSPD active area (4 mm^2), a low system detection efficiency of the SNSPD, and losses from photons exiting the face of the GaAs sample not adjacent to the detector. The logic for a modeling-based workaround is as follows:

In the post-processing analysis of the Compton scattering data, when a correlation search is performed around an energy-cut HPGe event to look for coincidence detection events on SNSPD channels, there will be some number of single-pixel SNSPD events correlated with the HPGe event, and a distribution of multifold SNSPD pixel coincidences. Given that the SNSPD channels are independent from each-other, and the excitation of the scintillator is driven by a radioactive decay process, the distribution of 1-fold, 2-fold, 3-fold, 4-fold, 5-fold, and 6-fold coincidences measured across the SNSPD channels should follow a Poisson distribution. Therefore, if the SNSPD events correlated with a HPGe event are histogrammed according to coincidence order, a Poisson distribution can be fit to the data and a mean photon number can be extracted. As discussed in the previous section, the lower energy events on the HPGe detector correspond to greater energy deposition into the GaAs target, so there should be a higher mean photon number for SNSPD events correlated with a lower energy HPGe event.

For clarity, the histograms will be organized in terms of the *energy deposited*, which corresponds to the energy deposited into the GaAs, given by 122 keV (the excitation energy) - the energy detected on the HPGe detector.

The coincidence order histograms for HPGe energies of 70keV, 80keV, 90keV, and

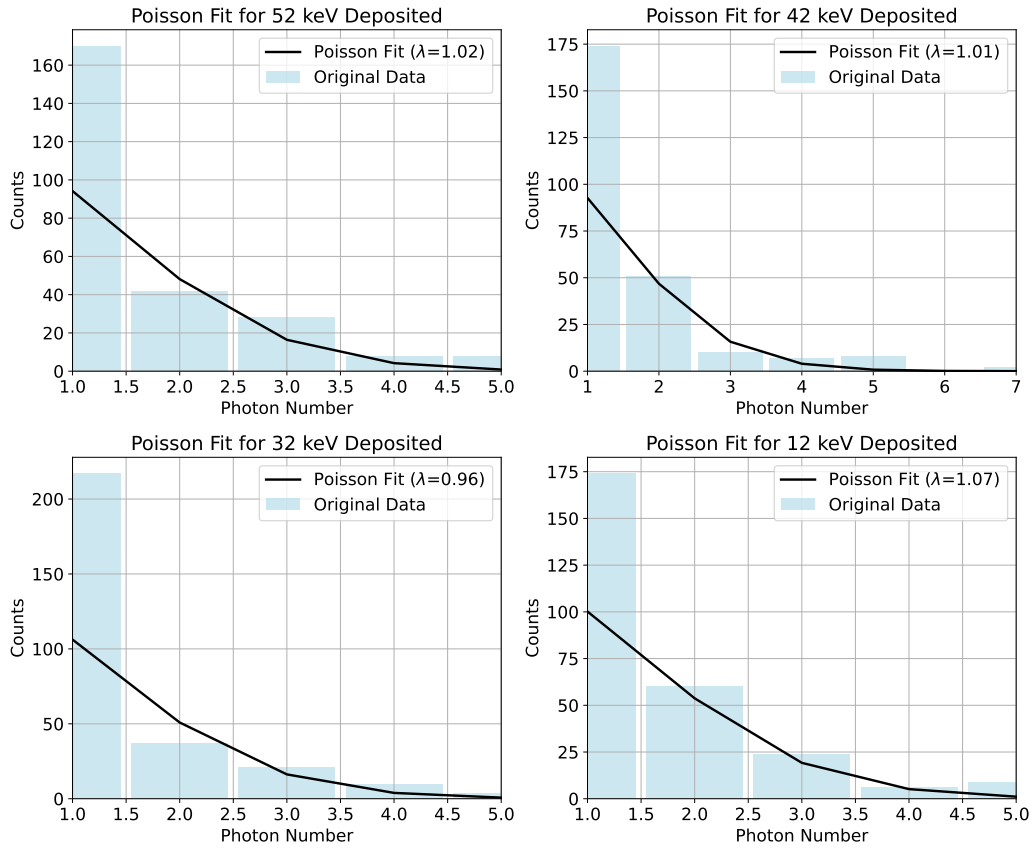


Figure 6.16: Histograms of 1-, 2-, and multifold coincidence events across SNSPD pixels correlated with an energy-cut HPGe event. The data is shown in light blue and the Poisson distribution fits are shown in black, with the mean photon number λ given in the legend. The Poisson distribution doesn't adequately describe the statistics

110keV, corresponding to deposited energies of 52 keV, 42 keV, 32 keV, and 12 keV, respectively are shown in figure 6.16

It can be seen from visual inspection of figure figure 6.16 that the Poisson distribution doesn't adequately fit the data. There is a clear excess of SNSPD events in the 1-fold coincidence bin, corresponding to single SNSPD pixel clicks. Making the assumption that there is some noise contribution inflating the count of that bin, the mean photon number also doesn't scale as expected. It is in the vicinity of a mean photon number of 1 for all deposited energies when the expectation is that it would be higher for higher deposited energies.

6.5.2 Understanding the Observed Distribution

Given the clear evidence of scintillation present from the inter-arrival times discussed in section 6.4.3, it is unlikely that the dark counts in SNSPD pixels can account for the observed non-Poissonian distributions shown in the previous section. This can be shown through modeling.

In a measurement time of 5 hours, 168,860 counts on the HPGe detector registered within the energy cut of 1500 - 2750 ADC units. Each SNSPD channel has a dark count rate and given these, the number of "false" coincidences arising due to dark counts on the SNSPDs can be estimated. To estimate the number of *n*-fold, where *n* SNSPD channels fire within a 20 microsecond window in coincidence with the HPGe detector, the following dark count rates were measured for each SNSPD channel:

Channel	**DCR (cps)**
1	3.5
2	3.3
4	1.5
5	2.8
7	12.8

Table 6.2: Dark Count Rates (DCR) for SNSPD channels

For a channel with dark count rate rate_i, the probability that it will have a count within a 20-microsecond window is:

$$\text{probability}_i = \text{rate}_i \times 20 \times 10^{-6} \tag{6.7}$$

Applying this to each channel:

$$\text{Channel 1: } 3.5\,\text{cps} \Rightarrow 3.5 \times 20 \times 10^{-6} = 7 \times 10^{-5}$$

$$\text{Channel 2: } 3.3\,\text{cps} \Rightarrow 3.3 \times 20 \times 10^{-6} = 6.6 \times 10^{-5}$$

$$\text{Channel 4: } 1.5\,\text{cps} \Rightarrow 1.5 \times 20 \times 10^{-6} = 3 \times 10^{-5}$$

$$\text{Channel 5: } 2.8\,\text{cps} \Rightarrow 2.8 \times 20 \times 10^{-6} = 5.6 \times 10^{-5}$$

$$\text{Channel 7: } 12.8\,\text{cps} \Rightarrow 12.8 \times 20 \times 10^{-6} = 2.56 \times 10^{-4}$$

The HPGe detector had 168,860 counts over 5 hours:

$$\text{HPGe rate} = \frac{168,860}{5 \times 3600} \approx 9.38\,\text{cps} \tag{6.8}$$

Since we are looking for coincidences in the 20-microsecond window, the number of coincidence windows per second with HPGe events is:

$$\text{HPGe coincidence windows per second} = 9.38 \tag{6.9}$$

So, over 5 hours, the total number of coincidence windows with an HPGe event is:

$$9.38 \times 5 \times 3600 \approx 168,860\,\text{windows} \tag{6.10}$$

For each possible n-fold coincidence, we'll calculate the probability of exactly n out of the 5 channels firing within the same 20-microsecond window as an HPGe event.

Let p_1, p_2, p_3, p_4, p_5 be the probabilities calculated in Step 1 for each of the SNSPD. Then the probability of an n-fold coincidence with HPGe is given by the binomial distribution:

$$P(n\text{-fold}) = \binom{5}{n} \times \left(\prod_{i=1}^{n} p_i \right) \times \left(\prod_{i=n+1}^{5} (1 - p_i) \right) \tag{6.11}$$

The expected number of n-fold coincidences for a total of 168,860 HPGe events over a 5-hour period is as follows: approximately 59 events for 1-fold coincidences, 0.008 events for 2-fold coincidences (negligible), about 2.3×10^{-7} events for 3-fold coincidences, roughly 6.6×10^{-12} events for 4-fold coincidences, and effectively zero, approximately 3.4×10^{-16} events, for 5-fold coincidences.

The justification for binomial distribution is as follows: For each SNSPD channel, there are only two possible outcomes within the coincidence window: it either fires (registers a dark count) or it doesn't. This binary outcome (fire or no fire) aligns with the binomial distribution's basic conditions. Each HPGe event is a trial during which we check if any subset of the 5 channels fires. Thus, for every HPGe coincidence window, we assess whether 1, 2, 3, or more channels fire. It is assumed that each channel has a fixed probability of firing within the 20-microsecond window, calculated based on its dark count rate and that the probabilities remain constant throughout the measurement duration. Finally, it is assumed that the dark counts in each channel are independent, so the probability of multiple channels firing is based on the independent probabilities of each channel firing within the given window.

One feature not incorporated into this model thus far is that the coincidence window is long compared to the detector reset time. Taking the dead time of the detector to be 1.5 microseconds as it was measured in Figure 6.15, any of the SNSPD channels can fire multiple times within a 20-microsecond coincidence window. To account for this, the probability calculation for each channel must be adjusted to reflect that it could fire multiple times within the 20-microsecond coincidence window. Taking this into account, First, the number of sub-windows within each 20-microsecond coincidence window can be determined by dividing the total window duration by the reset (dead-time) interval. This gives each channel approximately 13.33 effective sub-windows, meaning it could potentially reset and fire again around 13 times within the 20-microsecond span.

$$N_{\text{effective}} = \frac{20\,\mu s}{1.5\,\mu s} \approx 13.33 \tag{6.12}$$

Now, the probability that each channel will have at least one count in a sub-window based on its dark count rate. For a channel with dark count rate rate_i, the mean number of expected counts within a single 20-microsecond window is given by

$$\lambda_i = \text{rate}_i \times 20 \times 10^{-6}. \tag{6.13}$$

To factor in the multiple sub-windows, we adjust the expected counts using

$$\lambda_i = N_{\text{effective}} \times \text{rate}_i \times 20 \times 10^{-6}, \tag{6.14}$$

where $N_{\text{effective}}$ is the number of effective sub-windows. The cumulative probability that each channel will fire at least once within the 20-microsecond window is then calculated as

$$P(\text{firing}) = 1 - e^{-N_{\text{effective}} \times p_i}, \tag{6.15}$$

using the exponential model to reflect a Poisson process.

The binomial distribution can then be used to calculate the probability of exactly n-fold coincidences occurring among the channels. The expected number of n-fold coincidences with the HPGe detector over the 5-hour measurement period is obtained by multiplying the probability of each n-fold coincidence with the total number of coincidence windows in this time-frame. The number of coincidence windows with HPGe events is estimated as

$$N_{\text{HPGe windows}} = 168,860, \tag{6.16}$$

based on an HPGe rate of 9.38 counts per second.

After adjusting for the channels' reset times, the expected counts is calculated for each level of n-fold coincidences over the 5-hour measurement period. The results are as follows: for 1-fold coincidences, approximately 783 events are expected; for 2-fold coincidences, around 1.38 events; for 3-fold coincidences, approximately 5.5×10^{-4} events ; for 4-fold coincidences, 2.1×10^{-7} ; and for 5-fold coincidences, 1.4×10^{-10} events, which is effectively negligible. This doesn't explain the statistics observed.

6.5.3 Understanding System Losses and Secondary X-ray Generation

The energy-tagged X-ray excitation setup, in principle, is designed to deliver an incident photon with well-defined energy E_{in}, as shown in Figure 6.1) through the cryostat and onto the GaAs target. Upon reaching the target, this X-ray undergoes Compton scattering within the GaAs, depositing some energy in the target. The outgoing scattered X-ray E_{out} is then expected to exit the cryostat and reach the HPGe detector. Then, using conservation of energy, the quantity of energy deposited into the GaAs target via Compton scattering, E_{dep}, can be calculated as $E_{dep} = E_{in} - E_{out}$. Figure 6.17 a) demonstrates this ideal scenario schematically in the cryostat, where an incident X-ray penetrates the cryostat outer can and radiation shields without interaction before Compton scattering in the GaAs, and then the outgoing X-ray transits the detector packaging, radiation shields, and outer can once again without interaction before hitting the HPGe. In practice, however, the materials in the cryostat introduce significant attenuation losses and secondary beam generation mechanisms that are not considered in the ideal scenario explained above and shown in figure 6.17 a). A major source of these effects arises from X-ray interactions with the copper components inside the cryostat. These include the detector packaging, the bracket that connects the detector packaging to the 1K stage, and the surrounding radiation shields. Together, these components add more than 10 mm of copper interaction path for any given

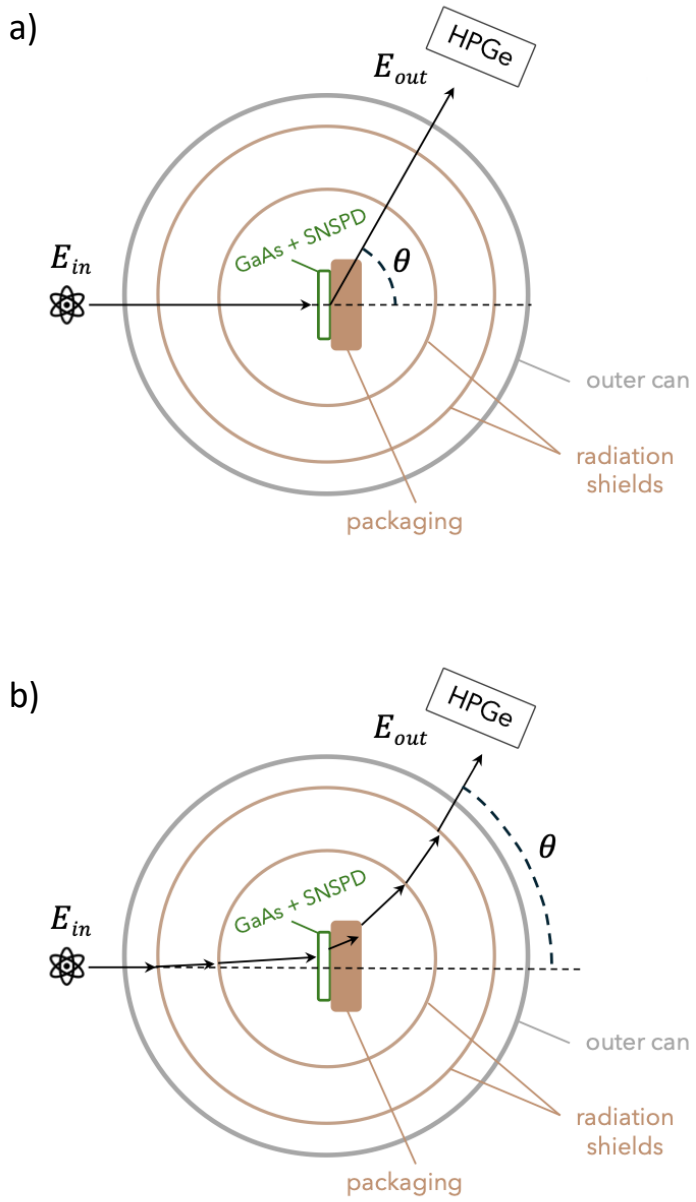


Figure 6.17: The cryostat consists of an aluminum outer can shown in silver. The radiation shields and copper detector packaging and brackets are shown in a copper color. The GaAs/SNSPD module is shown in green. The ideal scenario in the energy-tagged X-ray excitation experiment is depicted in a), where the incident X-ray of energy E_{in} doesn't interact with any of the cryostat metal, it Compton scatters in the GaAs depositing some energy, and the outgoing X-ray of energy E_{out} passes through the cryostat metal without interaction and is detected in the externally mounted HPGe detector. A more realistic scenario is shown in b), where at every copper interface, the X-ray Compton scatters off of electrons in the copper, leading to unmeasured losses and beam deflection.

X-ray.

Copper's high density and atomic number (Z) significantly increase its interaction probability with X-rays compared to a material like aluminum. The linear attenuation coefficient (μ) scales with both density (ρ) and atomic number (Z), as $\mu \propto \rho Z$. This has the effect of signal loss of both the excitation beam and the outgoing scattered X-rays, reducing the SNR. In addition to attenuation, Compton scattering in the copper of the cryostat generates secondary X-rays. The Compton scattering cross-section (σ_C) also scales with Z, so the rates are significant in Copper. In the ideal scenario, the X-rays only Compton scatter off of the GaAs target. In practice, the unwanted X-ray - copper Compton scattering events cause any given incident X-ray to deposit unknown amounts of energy into the surrounding copper before it reaches the GaAs. The outgoing X-rays leaving the GaAs target also undergo these spurious Compton scattering interactions with surrounding copper in the transit out of the cryostat. This process is depicted schematically in figure 6.17 b), where each time an X-ray interacts with a copper component in the cryostat, an unwanted Compton scattering interaction occurs, depositing energy into the Copper, and the outgoing scattered X-ray has lost some energy and deflected by an angle θ proportional to the energy loss. This creates uncertainty in the energy deposited into the actual GaAs target. Notably, in figure 6.17, the HPGe detects a scattered X-ray out of the cryostat of the same energy in a) and b) (the angle with respect to the original incident X-ray is θ in both cases); however, in a) there were no losses due to spurious Compton scattering in Copper, and in b) there are losses due to Compton scattering at every Copper interface. Since the Compton scatters in Copper aren't read out by a detector, the energy that is actually deposited in the Copper versus GaAs can't be determined. Ultimately, these loss mechanisms have the effect of decoupling the incident X-ray beam from the detected HPGe signal, complicating the interpretation of the measured energy spectra on the HPGe detector and preventing the expected proportionality in the effective light yield.

Copper also exhibits a high K-shell fluorescence yield of 41%, compared to only 3.5% for aluminum. From this, a low energy background of a few keV arises, further degrading the correlation between the SNSPD events and HPGe events. This, in combination with the low SNSPD efficiency and the low light collection efficiency of the GaAs - SNSPD system, can also qualitatively explain the excess of single events and deviation from Poissonian behavior seen in figure 6.16.

Element	ρ (g/cm^3)	Z	**K-shell fluorescence yield**
Cu (Copper)	8.96	29	41%
Al (Aluminum)	2.70	13	3.5%

Table 6.3: Comparison of material properties affecting X-ray attenuation and scattering.

Given the properties listed in 6.3, aluminum emerges as a superior choice for detector packaging and for components surrounding the detector area within the cryostat. Its lower density, atomic number, and fluorescence yield significantly reduce X-ray attenuation, Compton scattering, and secondary X-ray emissions. To effectively minimize unwanted interactions with copper components, a cryostat dedicated to energy-tagged X-ray excitation could be designed or retrofitted with clear and direct entrance and exit pathways for X-rays, ensuring that the excitation and scattered beams traverse minimal copper. By combining aluminum-based packaging with strategic cryostat design, the correlation between SNSPD events and HPGe detector measurements can be preserved, enabling a cleaner, more interpretable signal and enhancing the overall performance of the experimental setup.

Chapter 7: Designs and Challenges of Improved Microwire Arrays

The next steps in improving large-area microwire arrays focus on enhancing yield, performance, and detector efficiency. One key development for performance enhancement is the implementation of bend thickening to alleviate current crowding. This is illustrated in Figure 7.1, where (a) shows a meander geometry with thicker bending regions, and (b) displays a standard uniform thickness meander. The out-of-plane thickening alleviates current crowding, which suppresses switched current and lowers the energy barrier for vortex entry—a mechanism that contributes to dark counts. This modification improves detection efficiency, reduces timing jitter, and lowers the dark count rate compared to uniform thickness devices of the same geometry and film quality [114]. Figure B.1 demonstrates the reduction of current crowding in the inner radius of the variably thickened bend (b) compared to the uniform thickness bend (a). Additionally, (c) and (d) show how the lower vortex-entry barrier in uniform thickness bends contributes to dark counts.

In addition to bend thickening, the integration of an optical stack is being explored. A significant challenge for large-area devices is ensuring the reflector's homogeneity over a large area, as surface inhomogeneities, such as spurious particle counts, can limit the material homogeneity of the thin-film superconductor deposited above. This issue is less pronounced in UV SNSPDs, which are made with thicker superconducting films due to higher photon energies. However, NIR SNSPDs typically have thicknesses in the range of 2-4 nm, where this effect is more noticeable. Furthermore, commercial distributed Bragg reflector (DBR) mirrors are often used as back reflectors in UV SNSPDs due to gold's poor

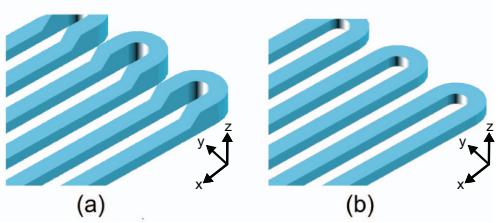


Figure 7.1: Illustration of (a) variable thickness between the straight nanowire segments and the bends in the superconducting film, where the bends are thickened to suppress current crowding effects compared to the (b) conventional device with uniform thickness. Figure taken from [113].

reflectivity in the UV range. These DBR mirrors can be engineered for the wavelength range of GaAs scintillation output.

The simulation results discussed in this chapter and the IV curve measurements were performed independently as a part of this thesis research on devices fabricated by Emanuel Knehr in the MDL clean room at JPL.

7.1 Optical Stack Design for Microwire Arrays

The canonical optical stack for SNSPDs is shown in Figure 7.3. It consists of a mirror layer, a quarter-wave dielectric spacer, the sensor layer, and one or more layers of anti-reflection coatings deposited on top. Using Rigorous Coupled-Wave Analysis (RCWA), the thicknesses of the anti-reflection coating layers and the spacer layer between the back reflector and the nanowire layer can be optimized for a specific wavelength, incident angle, and, if desired, polarization.

Extending this approach to large-area microwire arrays introduces additional challenges. One key issue is the large capacitance of a gold back reflector over large active areas (mm^2-scale), which can cause pulse distortion. This issue is less significant in smaller devices.

For any back reflector, it is crucial to ensure high homogeneity over a large area. Surface inhomogeneities, such as spurious particle counts, can degrade the material homogeneity

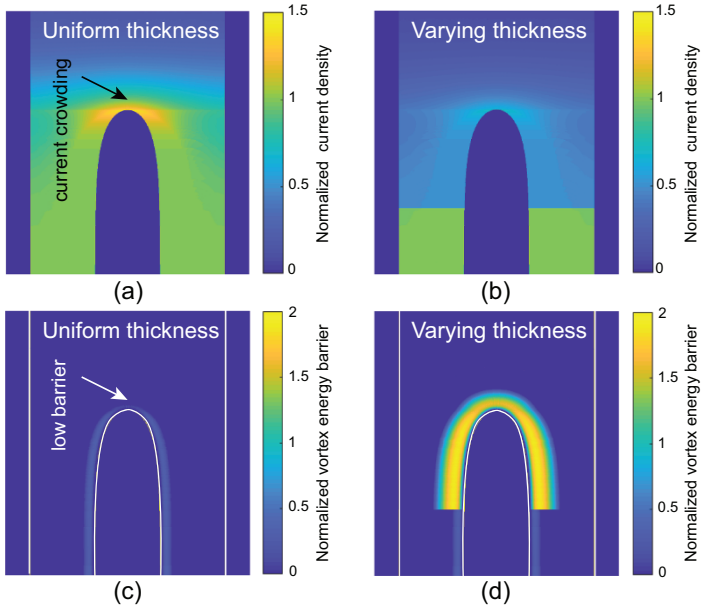


Figure 7.2: The bias current density in the bend region of the SNSPD, normalized to the current density in the straight segment, for (a) uniform and (b) variable thickness NbN SNSPDs with 100 nm-wide wires. Current crowding can be seen in (a) at the inner bend radius, which is alleviated in (b) through bend thickening, thereby reducing the current density. (c) and (d) show the vortex potential barriers, normalized to the characteristic vortex energy, ε_0, within the fully etched region for (c) uniform and (d) variable thickness SNSPDs, where the uniform thickness bend in (c) has a lower potential barrier than the varying thickness bend in (d) in the inner bend radius. Figure taken from [113].

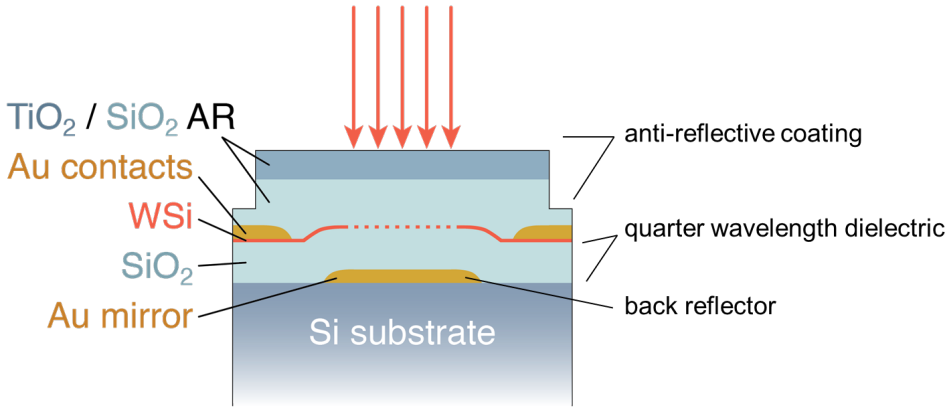


Figure 7.3: Conventional optical stack design for SNSPDs, where the nanowire is embedded in a cavity with a back reflector underneath a quarter-wavelength dielectric spacer, and layers of AR coating are deposited on top. The back reflector is a gold-coated mirror which is typical for NIR devices.

of the thin-film superconductor deposited above. This problem is less pronounced in UV SNSPDs, which use thicker superconducting films, allowing higher photon energies to penetrate. In contrast, NIR SNSPDs typically have thinner films (around 3-4 nm), making them more sensitive to surface irregularities.

In terms of optimizing an optical stack for a particular wavelength, RCWA can be used to generate broadband or narrowband optical stacks. Gold remains a suitable choice for broadband optical stacks across the visible and mid-infrared wavelengths, although it is less effective in the UV range. For detecting scintillation light with an isotropic emission pattern, implementing an optical stack based on constructive interference is not ideal. Antireflection (AR) coating layers are sensitive to incident angles, so a more effective design is the use of a *half stack*, which incorporates a DBR back reflector at an optimized distance, tailored to a broad range of incident angles.

7.1.1 Rigorous Coupled Wave Analysis

The thin-film nature of the superconducting materials used in SNSPDs limits the amount of light absorbed in a single transmissive pass. To enhance absorption, nanowires (or microwires) are integrated into an optical stack. Since SNSPDs are typically meandered over an active area, they can be modeled as periodic structures, and Rigorous Coupled-Wave Analysis (RCWA) can be applied to solve Maxwell's equations in the Fourier basis for incident plane waves. Using this semi-analytical approach, the amount of light absorbed in the nanowire layer and the electric field profile can be numerically computed. This allows for the efficient design of optical stack structures that maximize constructive interference in the sensor layer, leading to high detection efficiency. This method has been successfully employed in many SNSPDs.

In RCWA simulations, the device is divided into layers, each uniform in the z-direction. Electromagnetic modes are calculated and analytically propagated through these layers, with boundary conditions matched at the interfaces between them. The electromagnetic modes of the incident plane wave are computed by expanding the partial differential form of Maxwell's equations and applying the boundary conditions using Floquet functions in Fourier space.

The geometry and conventions of a standard RCWA simulation is shown in Figure 7.4.

7.1.2 Angled-Incidence RCWA Simulations

An RCWA simulation was performed on the Generation 2 microwire array with a fixed geometry (0.4 FF, 1.5um-wide wires, 3-nm thick WSi with an amorphous Si passivation-layer on top) to understand the detector's response to light at various incident angles. The detection efficiency for different wavelengths at different incident angles is shown in Figure 7.5. In these results, each curve has been polarization-averaged and averaged over all

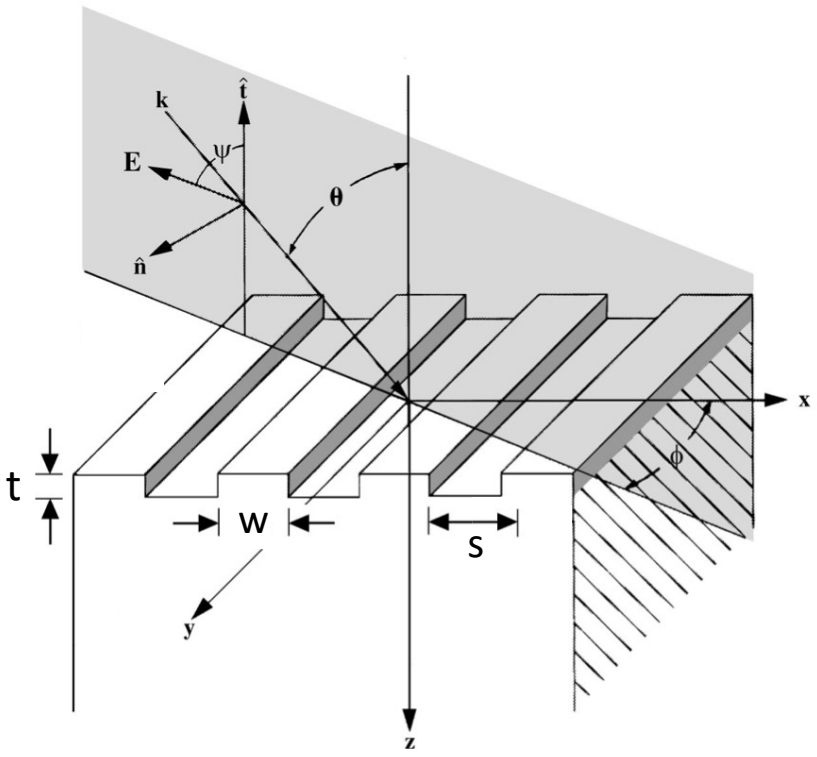


Figure 7.4: The geometry of a RCWA simulation of an SNSPD modelled as a periodic structure is shown. The angle theta is the angle from the vertical, phi is the polar angle, and psy is the electric field orientation denoting the polarization of the light. T is the thickness of layer, w is the wire width, and s is the spacing between nanowires.

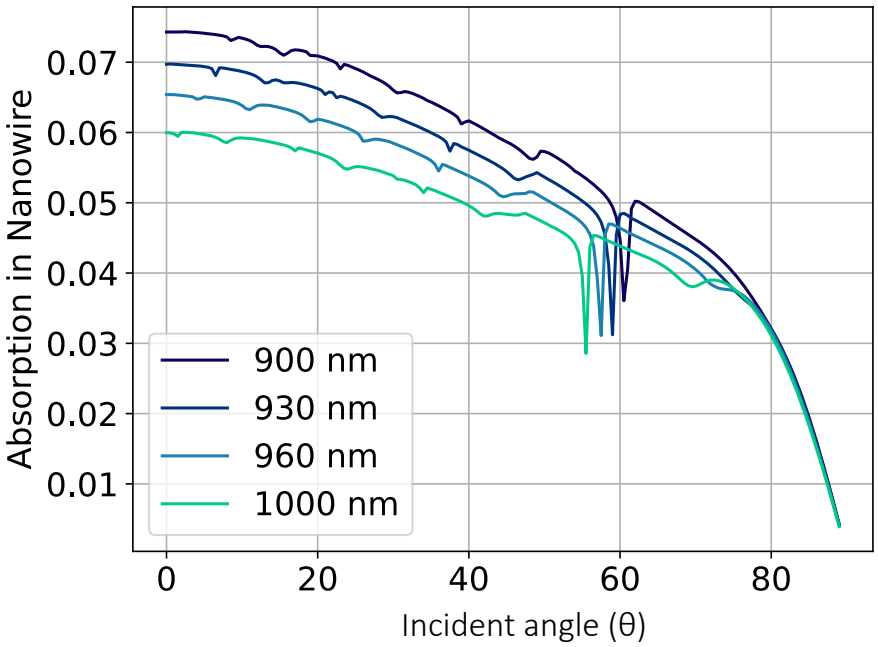


Figure 7.5: The detection efficiency of a generation 2 microwire array is simulated for a range of incident angles and a range of wavelengths centered around 950 nm.

polar angles.

From the results, we can observe that the detection efficiency drops as θ increases, and some resonances appear due to interference effects. Averaging over all angles and polarizations yields an overall efficiency of 5.1%. The goal of the next section is to design an optical stack configuration that can significantly improve the detection efficiency over these target wavelengths.

7.1.3 DBR Optical Stack Design for Broad-Angle Efficiency

A key challenge in the detection of scintillation light is the need to design an optical stack that achieves high efficiency over a broad range of incident angles. This is particularly important for many dark matter (DM) experiments, where the target emits isotropic

light or light over a broader range of angles than what is typically encountered in fiber-coupled SNSPD experiments. To date, this aspect of optical stack design has not been well-developed.

The development of efficient optical stacks, including DBR stacks, will be beneficial for microwire arrays in general. Improving the system detection efficiency of large-area microwire arrays is still a topic of study in the SNSPD field, and for this, the application of gold reflectors is not a straightforward solution.

In this context, commercial broadband SiO_2/Ta_2O_5 DBR mirrors optimized for absorption in the wavelength range from 850 nm to 1300 nm were obtained from Spectrum Thin Films. These were implemented into the RCWA simulation using structural information and n and k data from the vendor

For designing an optical stack for the Generation 2 microwire array, the thickness of the superconducting layer, the amorphous silicon capping layer, and the DBR configuration were held constant, while the SiO_2 spacer layer was varied to optimize the design for enhanced absorption.

The difference between a DBR mirror and a gold mirror as the back reflector for 930 nm light at various incidence angles, polarization-averaged and averaged over all polar angles, is shown in Figure B.1. A DBR mirror consists of alternating layers of materials with different refractive indices, designed to reflect light through constructive interference. When light hits these layers, it is partially reflected and transmitted at each boundary. For specific wavelengths, the reflections from multiple layers interfere constructively, enhancing the reflection.

DBR mirrors are sensitive to the angle of incidence because the phase relationship between reflected waves changes with angle. At normal incidence, the light waves align perfectly for constructive interference. However, as the angle increases, the optical path length changes, which affects the phase and alters the range of wavelengths that can be reflected

efficiently. This makes DBR mirrors highly effective at specific angles and wavelengths, but less so as the angle deviates from normal.

As shown in Figure 7.6, the optical stack with a DBR back-reflector exhibits a drop in efficiency at smaller incident angles compared to the gold back-reflector device. This limitation is inherent to the use of DBR reflectors. The gold back-reflector device also experiences a drop in efficiency, but at larger incident angles, as the stack becomes less effective. In Figure 7.6, the absorption as a function of incident angle is shown for two devices, both with 5 nm-thick WSi of 1.5 μm width, a fill factor of 0.6, and an amorphous silicon capping layer. The data in blue represents the simulated nanowire absorption for the DBR back-reflector device, while the data in gold represents the simulated nanowire absorption for the gold back-reflector device.

Angular Distribution of Light from GaAs

The light incident on an SNSPD to instrument GaAs has a distribution of angles that can be modeled as the distribution of light leaving a GaAs-air interface using the fresnel equations. To analyze the angular distribution of light exiting a GaAs-air interface, the refractive indices for GaAs and air are defined as

$$n_i = 3.6 \quad \text{(GaAs)}, \quad n_t = 1.0 \quad \text{(air)} \tag{7.1}$$

The critical angle for total internal reflection at the GaAs-air interface is calculated as:

$$\theta_c = \arcsin\left(\frac{n_t}{n_i}\right) \tag{7.2}$$

This critical angle, θ_c, represents the maximum angle of incidence within GaAs beyond which light undergoes total internal reflection instead of transmission. Now, using Snell's

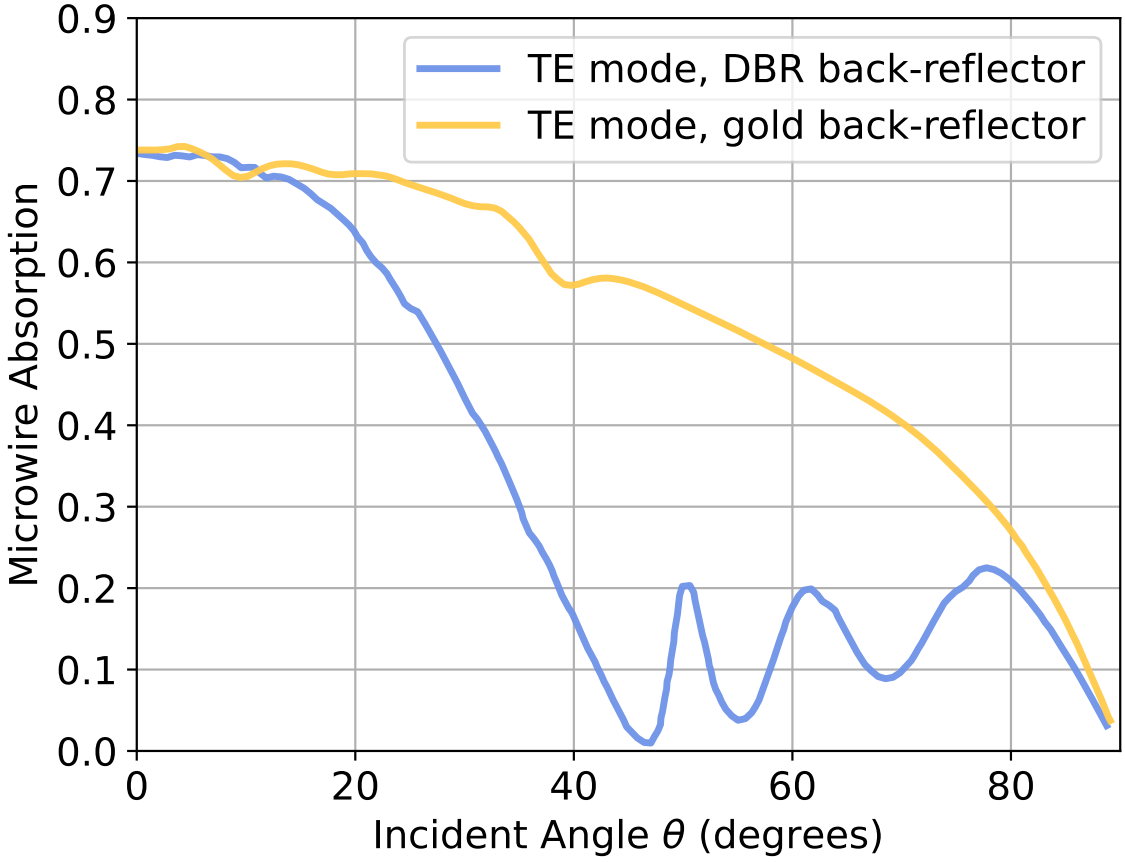


Figure 7.6: Simulated absorption as a function of incident angle θ in a device with a DBR-back-reflector (blue data) and a device with a gold back-reflector (gold data). Both configurations experience a decrease in efficiency at larger incident angles, but the DBR device drops off in efficiency at smaller incident angles.

Law, we calculate the transmission angle θ_t in air for each incident angle θ_i in GaAs:

$$n_i \sin(\theta_i) = n_t \sin(\theta_t) \tag{7.3}$$

Solving for θ_t, we have:

$$\theta_t = \arcsin\left(\frac{n_i}{n_t}\sin(\theta_i)\right) \tag{7.4}$$

This equation is applied over a range of incident angles, from 0° up to the critical angle θ_c.

The Fresnel equations give the reflection (r) and transmission (t) coefficients for light at the GaAs-air interface. These coefficients depend on the polarization of the incident light. For s-polarized light where the electric field is perpendicular to the plane of incidence, the reflection coefficient r_s and transmission coefficient t_s are given by:

$$r_s = \frac{n_i \cos(\theta_i) - n_t \cos(\theta_t)}{n_i \cos(\theta_i) + n_t \cos(\theta_t)} \tag{7.5}$$

The transmission coefficient for s-polarized light is then:

$$t_s = 1 - r_s^2 \tag{7.6}$$

This expression for t_s represents the fraction of incident s-polarized light that is transmitted into the air.

For p-polarized light where the electric field is parallel to the plane of incidence, the reflection coefficient r_p and transmission coefficient t_p are:

$$r_p = \frac{n_t \cos(\theta_i) - n_i \cos(\theta_t)}{n_t \cos(\theta_i) + n_i \cos(\theta_t)} \tag{7.7}$$

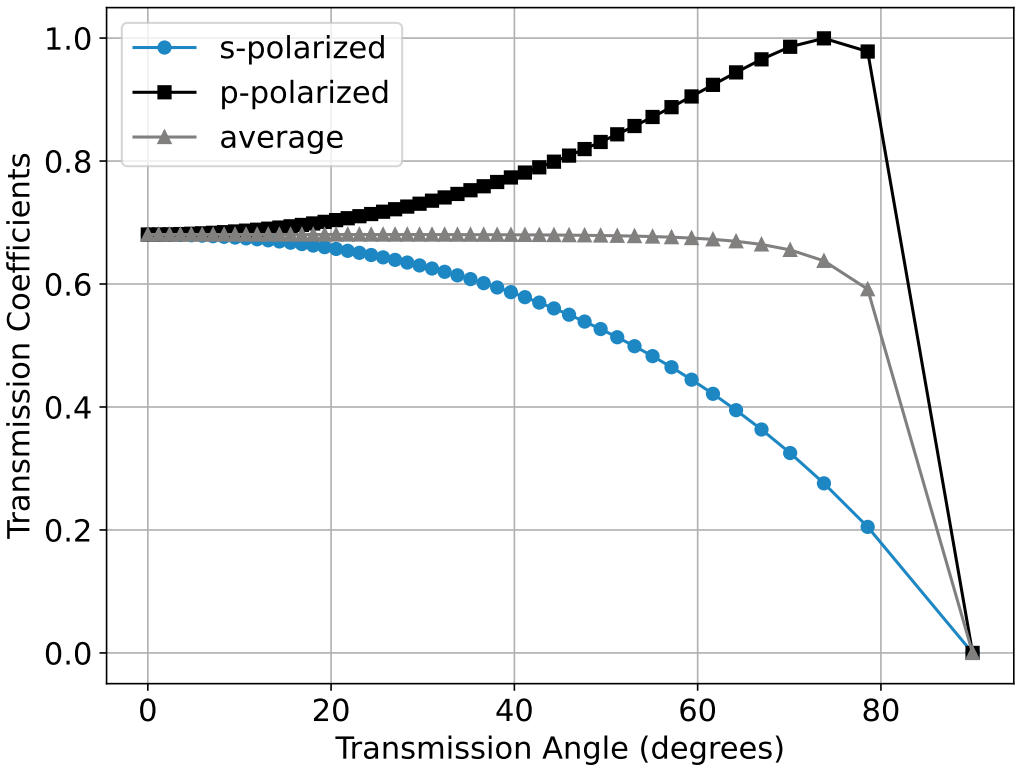


Figure 7.7: The transmission coefficients are shown for s-polarized, p-polarized, and the average of s- and p-polarization, calculated for a GaAs-air interface using the Fresnel equations.

And the transmission coefficient for p-polarized light is:

$$t_p = 1 - r_p^2 \tag{7.8}$$

Here, t_p represents the fraction of incident p-polarized light transmitted through the interface.

The transmission probabilities for both s-polarized and p-polarized light can be calculated across the range of incident angles. These in addition to the average of both polarizations are plotted with respect to incident angle in figure 7.7:

To accurately represent the angular distribution of light exiting the GaAs-air interface, we need to account for both the transmission probability and the spatial distribution of the

transmitted light. The transmission coefficients t_s and t_p (for s-polarized and p-polarized light, respectively) give the fraction of light intensity transmitted through the interface at each angle. However, they do not capture how this transmitted light spreads out in physical space at each angle. The solid angle factor $2\pi\sin(\theta_t)$ describes the angular spread of the transmitted light as a function of the transmission angle θ_t. Specifically,

$$d\Omega = 2\pi\sin(\theta_t) \tag{7.9}$$

where Ω is the solid angle. This factor quantifies the spatial distribution of light exiting the interface. By multiplying the transmission coefficients t_s and t_p by the solid angle factor $2\pi\sin(\theta_t)$, we obtain an effective transmission intensity that considers both the likelihood of transmission and the angular spread of light. This yields:

$$\text{Effective Transmission}_s = t_s \cdot 2\pi\sin(\theta_t) \tag{7.10}$$

$$\text{Effective Transmission}_p = t_p \cdot 2\pi\sin(\theta_t) \tag{7.11}$$

For the average transmission (assuming no preferred polarization), we can define:

$$\text{Effective Average Transmission} = \frac{t_s + t_p}{2} \cdot 2\pi\sin(\theta_t) \tag{7.12}$$

Thus, the product $t_s \cdot 2\pi\sin(\theta_t)$ (or $t_p \cdot 2\pi\sin(\theta_t)$) gives the effective transmission intensity. This quantity is proportional to both the transmission probability and the spatial area over which the light exits, providing a more comprehensive representation of the transmitted light's angular distribution at the GaAs-air interface. The effective transmission intensity is shown in figure 7.8 as a function of transmission angle.

After incorporating the solid angle weighting factor $2\pi\sin(\theta_t)$ into the transmission co-

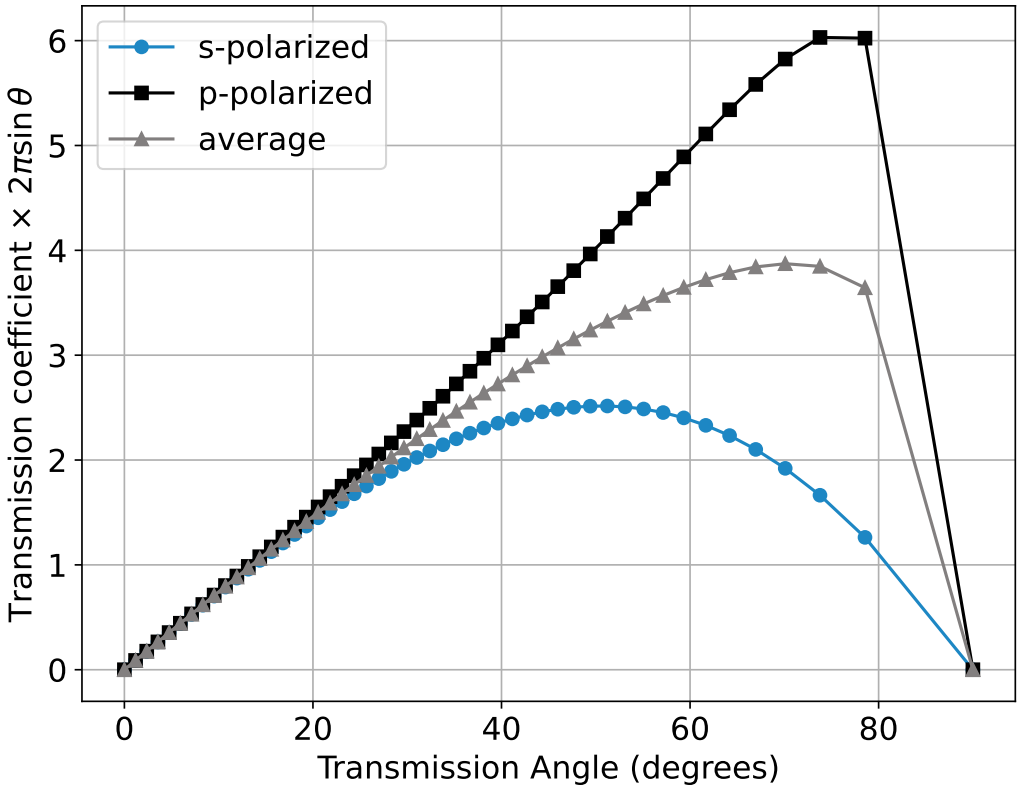


Figure 7.8: The effective transmission coefficients (transmission coefficients $\times$ solid angle weighting factor $2\pi \sin\theta$) are shown for s-polarized, p-polarized, and the average of s- and p-polarization.

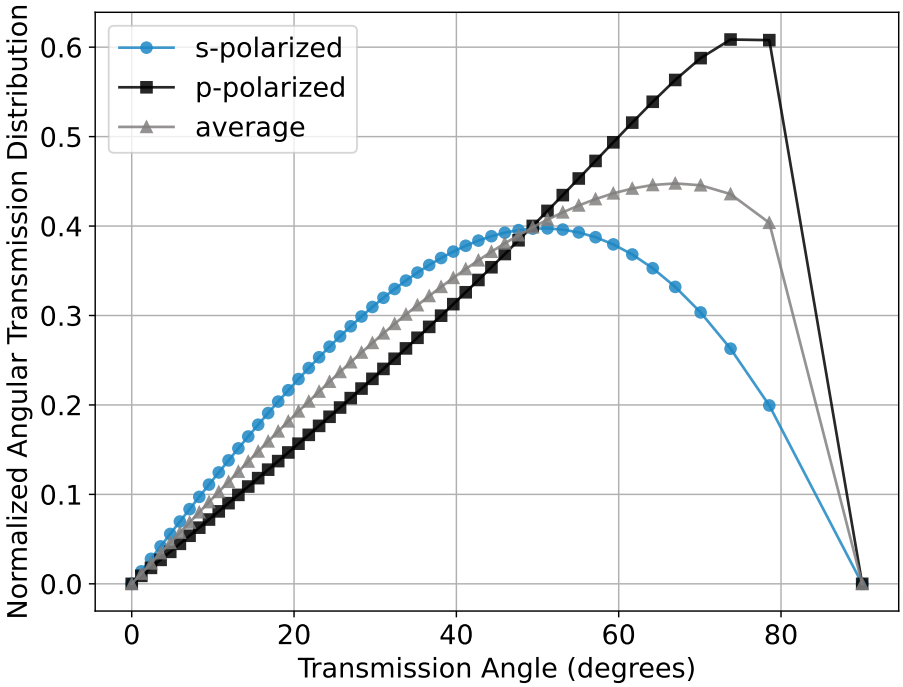


Figure 7.9: Normalized transmission probability for s-polarized, p-polarized, and the average of s- and p-polarization.

efficients, we introduce a normalization condition to ensure that the angular distribution of transmitted light sums to the total solid angle, 4π steradians. To achieve this normalization, we first calculate the sum of all effective transmission values over the range of transmission angles. We then divide each effective transmission value by this sum and multiply by 4π to maintain the total solid angle. This ensures that the distribution reflects the true angular spread of the transmitted light while conserving the total intensity within a 4π steradian solid angle. The normalized transmission probability distribution is shown as a function of transmission angle in figure 7.9.

The transmission angles at this interface become the incident angles on the SNSPD. It can be seen when looking at the polarization-averaged angular transmission probability distribution that it is skewed to be maximized at larger incident angles. The distribution

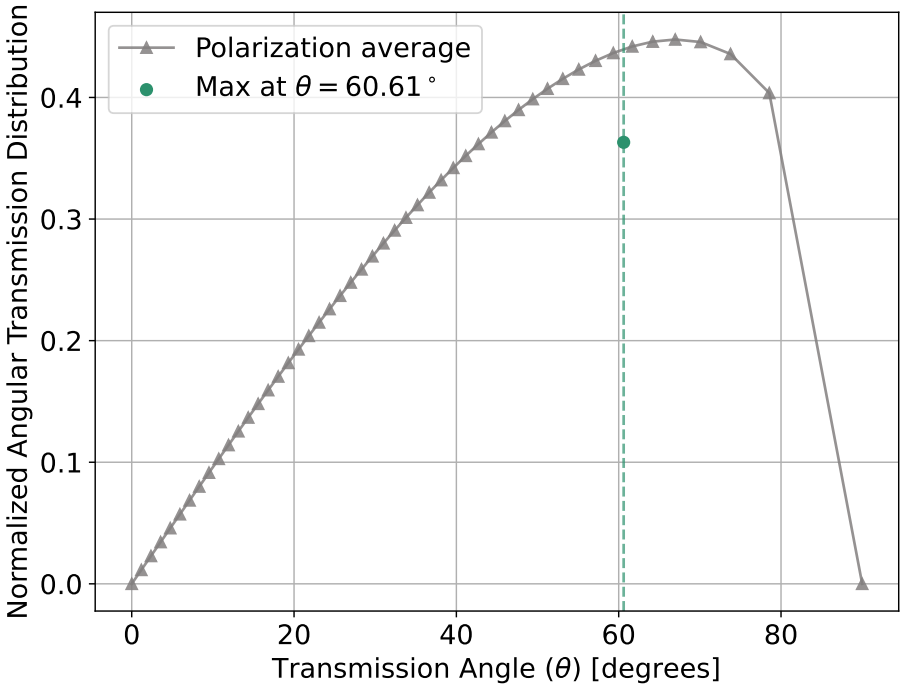


Figure 7.10: The normalized transmission probability for the average of s- and p-polarizations is maximized at $\theta = 60.1^\circ$.

maximum calculated through the gradient method is 60.1 degrees as shown in figure 7.10. This is in contrast to the common situation in SNSPDs designed for single-mode fiber-coupled light in which nearly all of the incident light is normal incidence (0 degrees in the convention used in this chapter).

It is possible to designate 60° as the incident angle in the RCWA optimizer instead of running the RCWA optimizer to optimize the stack configuration for normally incident light. A more robust approach is to expand the capabilities of the RCWA optimizer to optimize for a weighted distribution of incident angles.

In MATLAB a multi-objective wrapper for the RCWA optimizer was created for optimizing an optical stack design. The wrapper function allows for inputting a range or distribution of incident angles rather than a single designated angle. Within the wrapper,

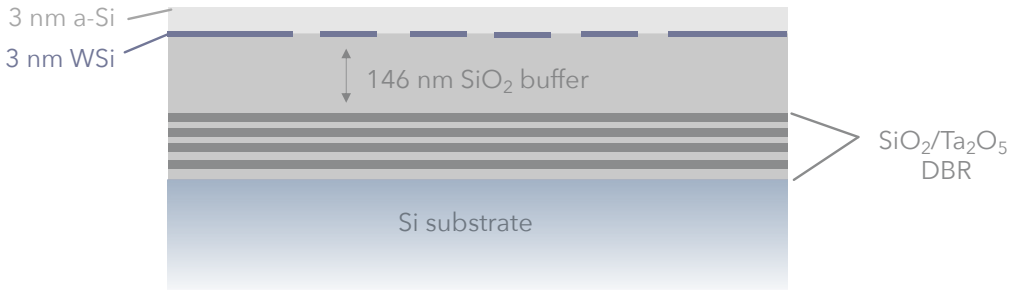


Figure 7.11: The SNSPD on a Si substrate with a DBR back-reflector, SiO_2 spacer layer, and amorphous silicon capping layer.

a loop iterates over the specified angles, calculating and summing the objective function values for each angle. By accumulating the results across multiple angles, the optimization process aims to improve the optical stack's performance over a broader range of incident angles. This approach is particularly useful in applications where light arrives at varying angles, ensuring the design is robust and efficient across different incidence conditions.

DBR Design

The detector model in the DBR cavity for input into the RCWA optimization script is shown in figure 7.11. The value of the SiO_2 layer thickness between the microwire and top of the DBR mirror was varied in the optimization. The figure shows the optimal value of 146 nm for the SiO_2 spacing layer thickness. The optimization was performed with the weighted distribution given in figure 7.10 for a wavelength of 930 nm. The fill factor for the device was chosen to be 0.4 and WSi thickness was set to 2.3 nm to be consistent with the set of generation 2 microwire arrays used in chapters 5 and 6. The absorption will be higher if the thickness of the WSi is increased.

The response of this configuration to angled incident light at 930 nm, as well as the

detection efficiency for light at different wavelengths near the optimized value, is shown in Figure 7.12 (a) and (b), respectively. The results reveal that the response is primarily dominated by the angular and wavelength dependence of the DBR mirror.

The increasing the fill factor of the device in future iterations will increase the overall optical absorption. The polarization-averaged response to angled incident 930 nm light is shown for fill factor 0.4 (the current iteration of the design), as well as fill factors of 0.5, 0.6, and 0.65.

7.2 Fabrication Challenges and Steps Forward

The SNSPD design from the previous section was fabricated, and the reflectance was measured for the bare DBR mirror, the DBR mirror on the Si substrate, and the mirror integrated into the optical stack in the SNSPD array using a Filmetrics F40-UV for reflectometry. The results, shown in figure 7.14 are consistent with the expected behavior and specifications from the vendor, within the quoted bandwidth of 800 nm - 1350 nm, as well as the RCWA simulations.

Along with the DBR optical stack, bi-layer NbTiN bends were implemented for enhanced performance and current crowding suppression. The full design of the array in the optical stack is shown in Figure 7.15. The wafer was fabricated with 4, 8, and 16 pixel arrays, each with a 0.4 fill factor, 1.5 μm wide wires, and active areas of 1 mm^2, 4 mm^2, and 16 mm^2.

The attempt at nanofabrication showed suppressed switching currents and degraded pixels, with none of them being photosensitive. The suppressed switching currents can be seen in the IV curves from two devices that are representative of the wafer. There is a combination of open channels and channels with degraded switching currents that are asymmetric across the array.

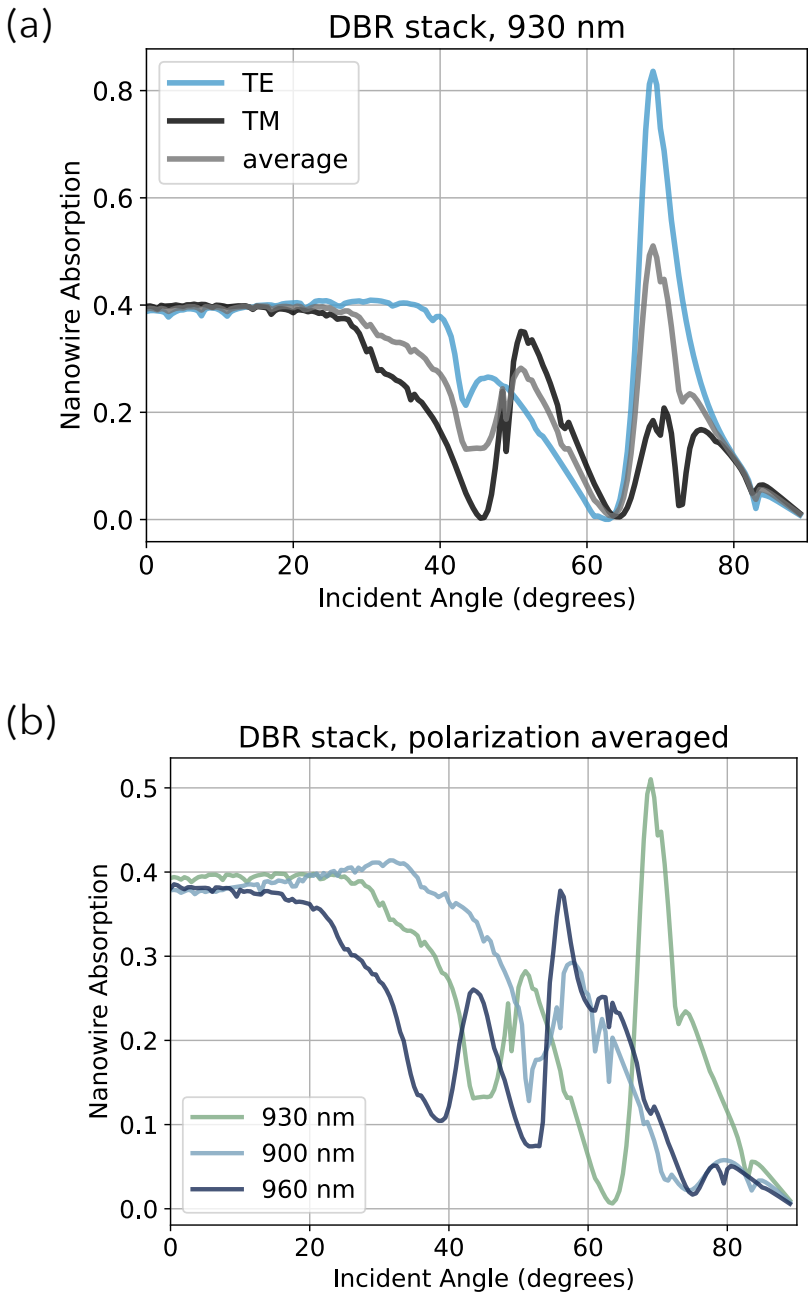


Figure 7.12: For the 0.4 fill factor version of the detector shown in figure 7.11(a) RCWA-simulated nanowire absorption as a function of incident angle in the optimized DBR optical stack for TE, TM, and polarization-averaged light. (b) RCWA-simulated nanowire absorption at wavelengths of 900 nm, 930 nm, and 960 nm for polarization-averaged light.

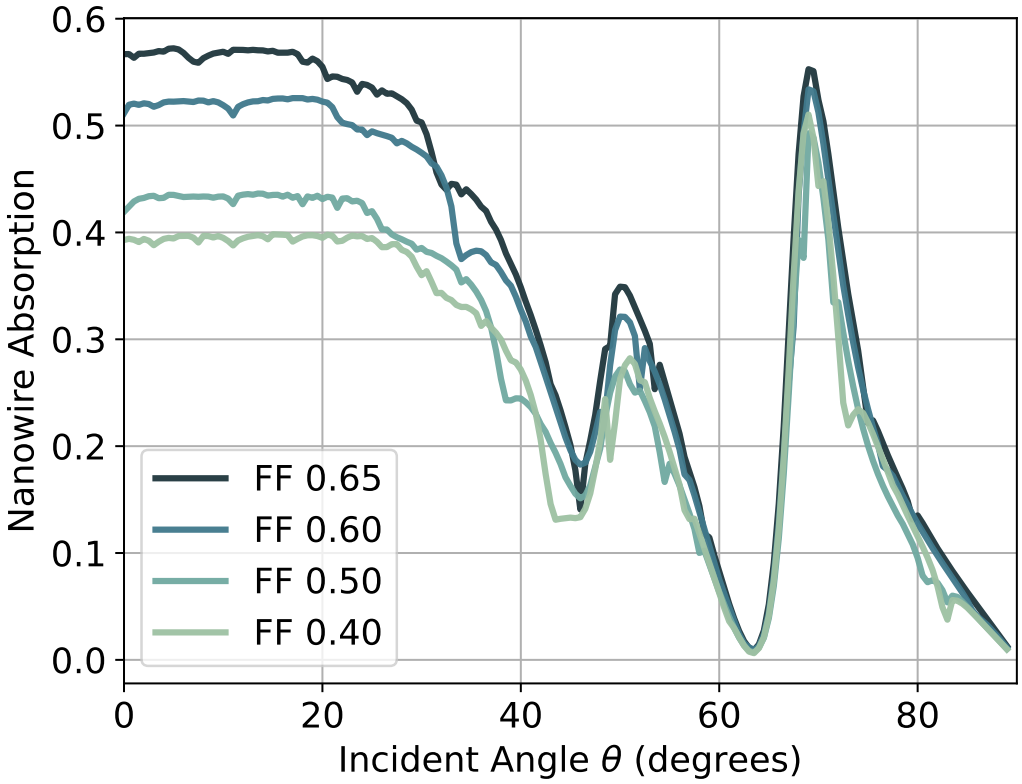


Figure 7.13: The response to angled incident 930 nm light for RCWA-optimized optical stacks with DBR mirror back reflectors, an SiO2 spacer, and 3 nm-thick WSi patterned with various fill factors.

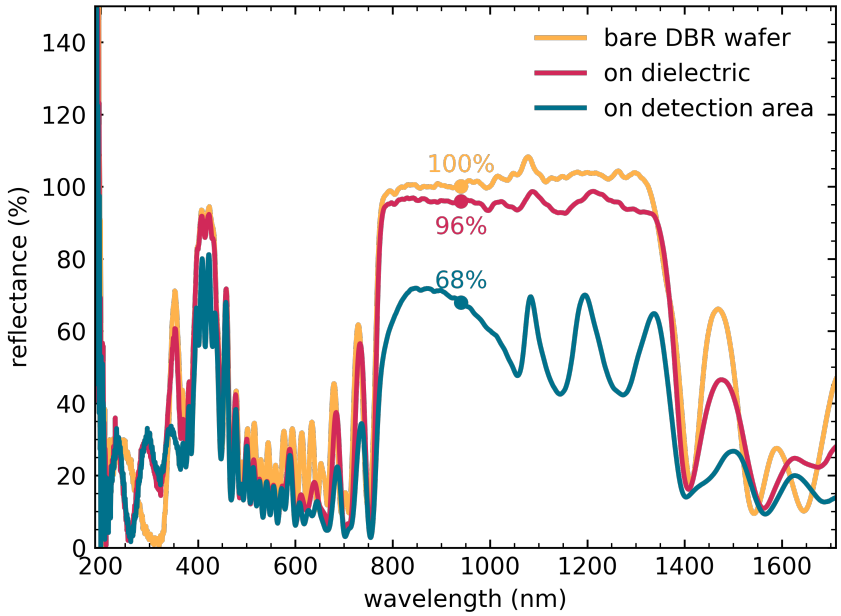


Figure 7.14: Measured reflectance of the bare DBR mirror (yellow), the DBR mirror on the dielectric (red), and in the detection area of the SNSPD (blue) as a function of wavelength.

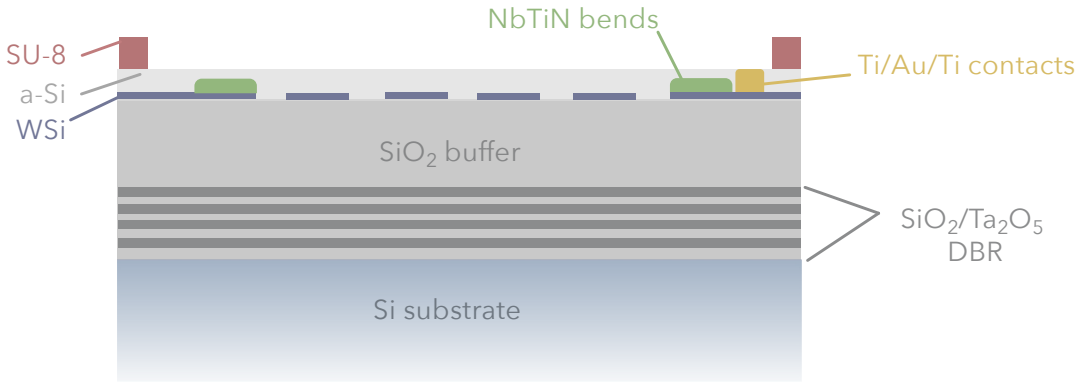


Figure 7.15: A schematic of the SNSPD design with the DBR optical stack and bi-layer bends.

As mentioned previously, particle contamination on the DBR mirror can disrupt the uniformity of the superconducting layer deposited above, potentially leading to inhomogeneities that affect the device's performance. This likely impacted the yield. Future work will focus on systematically exploring solutions and further optimizing the nanofabrication processes. For example, planarization processes used for arrays with stacked photosensitive layers, such as the thermal row-column architecture [97], could potentially be optimized to planarize the surface above the DBR layer. Additionally, *First Contact*, a proprietary blend of solvents designed to clean mirrors, diffraction gratings, and diffractive optics to the molecular level, could be incorporated into the process. To improve robustness to inhomogeneities, the WSi layer can be thickened. To maintain sensitivity while thickening the WSi layer, a more tungsten-rich stiochiometry can be used. This approach would allow for thicker films while maintaining sensitivity, as these films will ultimately have a lower T_c.

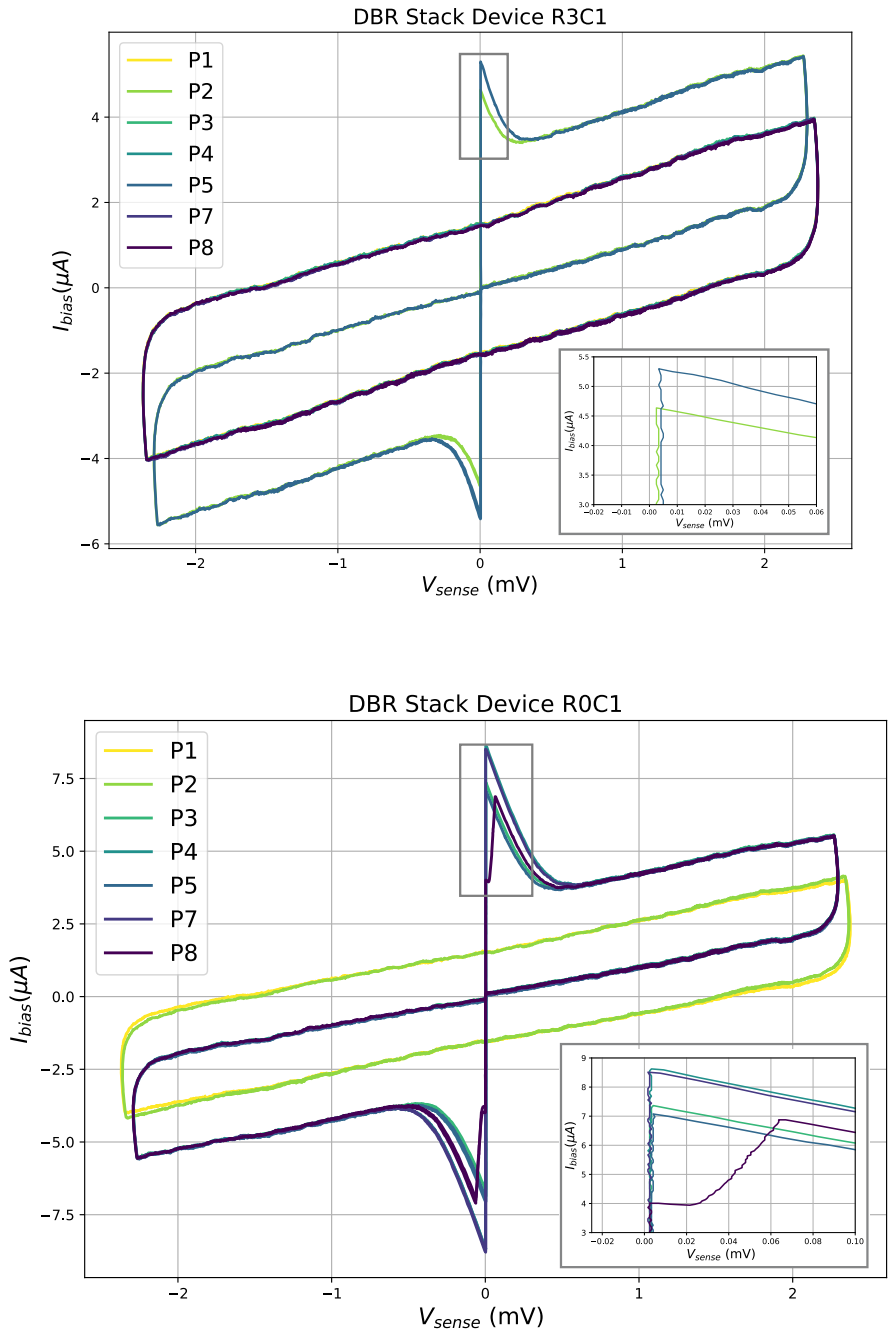


Figure 7.16: IV curves for two different devices from the wafer with the DBR mirror integrated into the microwire array. The low yield and suppressed switching currents are evident in devices from two locations on the wafer: R3C1 (top), where only two pixels switch with degraded switching currents, and R0C1 (bottom), where there is a spread of switching currents across the pixels.

Chapter 8: Microwire Arrays in Other Experiments

This chapter discusses additional experiments that have integrated the microwire arrays developed in this work. The first section details the study of a Generation 2 microwire array in the GeV-scale beam line at Fermilab and its response to high-energy proton, electron, and pions. This work is part of efforts to integrate large-area SNSPDs into future accelerator experiments. The second section describes a pilot-phase broadband axion and dark photon search, where a large-area SNSPDs will serve as the photosensor coupled to a reflector-based haloscope target.

The detectors described in this chapter were fabricated by Emanuel Knehr, Sahil Patel, and Ekkehart Schmidt in the MDL cleanroom t JPL. The detectors were screened and characterized as a part of this thesis research. The RCWA simulations discussed in SEction 8.2 were performed independently as a part of this thesis research. The beam line measurements described in Section 8.1 were performed by collaborators at FNAL on detectors that were pre-screened and characterized as a part of this thesis research. The results follow the work discussed in reference [127].

8.1 Detection of High Energy Particles with Large Area SNSPDs

Until recently, SNSPDs have had limited use cases in high energy physics (HEP) experiments due to their small active areas (approximately 100 μm^2) compared to, for example, Silicon Photomultipliers (SiPMs), which can have active areas ranging from tens to hun-

dreds of cm^2 and are commonly used in accelerator experiments. The mm^2-scale microwire arrays developed and characterized as part of this thesis work represent an advancement in the state of the art for the active area of SNSPDs, opening up the detector technology for future accelerator-based experiments. With future collider experiments in mind as potential applications for large active area SNSPD arrays, the response of a Generation 2 microwire array to GeV-energy particles from the Fermilab Test Beam Facility (FTBF) was studied.

8.1.1 Detector Design and Measurement Infrastructure

The detector implemented in the FTBF beam line is a WSi generation 2 microwire array with 2 mm x 2 mm total active area and 8 pixels. The device was pre-screened before deployment. It was packaged in the dark packaging described in Chapter 4, and each pixel was wire bonded so that it could be biased and read out single-ended. The dark box and detector were mounted in a Helium Sorption Fridge with a base temperature of 0.9K. The DC-coupled cryoamps described in previous chapters were mounted on the 40K stage. More information on the measurement setup of the beam line can be found in ref. [127].

8.1.2 Results

The beams available for testing included a 120 GeV proton beam and 8 GeV secondary electron and pion beams consisting of about 35% of pions and 65% of electrons. The FTBF is equipped with a silicon tracking telescope to measure the position of each incident particle and a 240 micro-channel plate (MCP-PMT) which provides reference timestamp with 10 ps resolution.

Future work will focus on optimizing SNSPDs for high-energy particle detection, offering high spatial and temporal resolution with larger active areas. This will enable the exploration of the feasibility of using superconducting wire detector arrays in upcoming

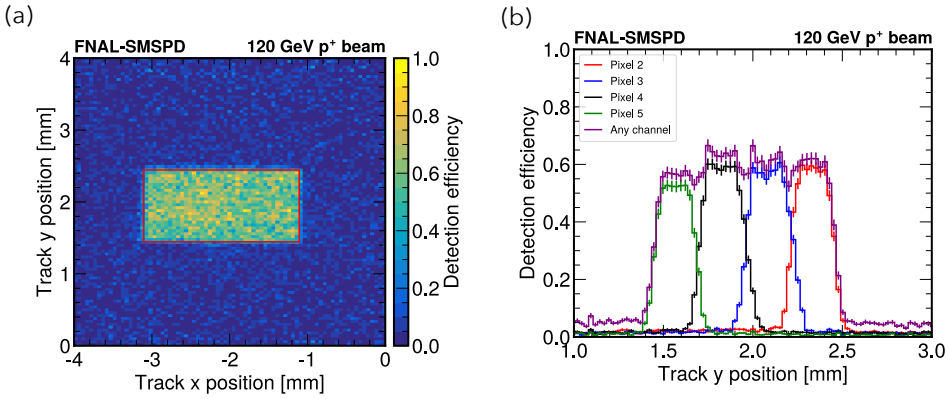


Figure 8.1: The detection efficiency, normalized to the fill factor (40%), of four SNSPD pixels is shown as a function of the incident proton track position in both the x and y directions (left) and in the y direction only (right).

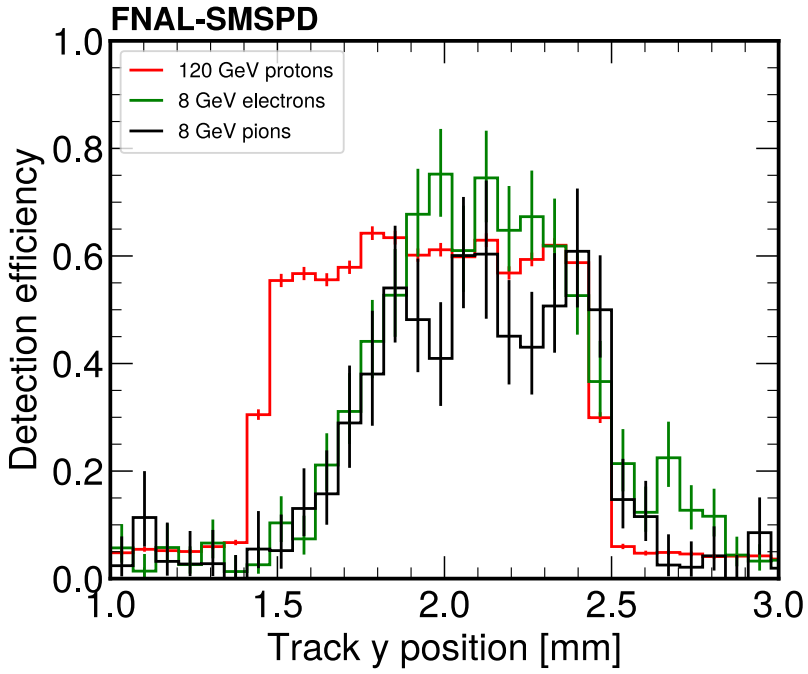


Figure 8.2: The detection efficiency normalized to the detector fill factor (40%) of four SMSPD pixels as a function of the track position in the y direction for 120 GeV protons (red), 8 GeV electrons (green), and 8 GeV pions (black).

collider and beam-target experiments.

8.2 Broadband Reflector Experiment for Axion Detection

The Broadband Reflector Experiment for Axion Detection (BREAD) science program based out of the University of Chicago and Fermilab is developing haloscope-based dark matter experiment with two pilot experiments.

8.2.1 Detection Concept and Experiment Design

Traditional radio-frequency resonant-cavity axion searches have several disadvantages. Narrow-band tuning is intrinsically limiting for unknown dark matter (DM) mass, and these searches scale poorly to high masses. The axion-to-photon conversion power is proportional to the volume, $\lambda^3 \propto \frac{1}{m_a^3}$, meaning that large numbers of small cavities are needed to maintain signal power as the mass increases. There are significant sensitivity gaps in the $[10^{-4} - 1\ \text{eV}]$ mass regime, which motivates the development of new broadband approaches.

BREAD realizes a new dish-antenna haloscope approach using a cylindrical metal barrel for broadband DM-to-photon conversion with a coaxial parabolic reflector that focuses signal photons onto a sensor. The performance and sensitivity of the photosensor ultimately govern the final discovery reach.

The geometry of the experiment was optimized around the magnetic field profile of high-field solenoids for the axion search component of the pilot experiment. Additionally, there is also a dark-photon search, which does not require the external magnetic field to run. There are two ongoing pilot experiment in the BREAD program. GigaBREAD operates in the 10-20 GHz range and uses a coaxial horn antenna as the sensor. InfraBREAD operates at 300 THz (1 micron) and uses superconducting nanowire detectors (SNSPDs) as the

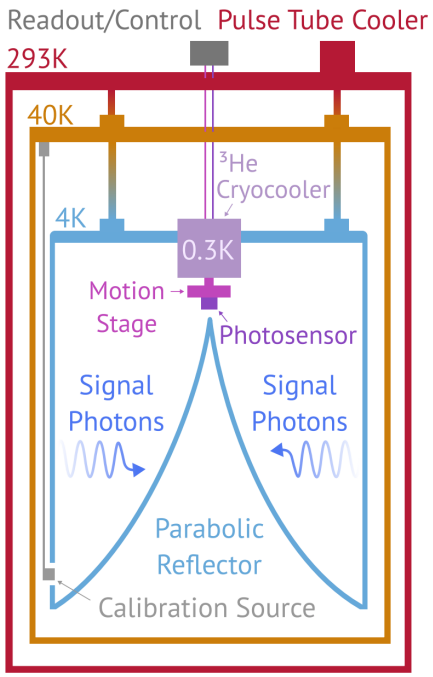


Figure 8.3: Schematic setup in the cryostat for the BREAD pilot dark photon searches. Figure taken from [125].

sensor. A Generation 1 microwire array is currently deployed in the BREAD cryostat for characterization.

The InfraBREAD experimental setup is shown in figure 8.3. The signal photons are focused onto the SNSPD. The current area of the reflector is 0.7 cm^2, but it is expected to scale to 10 m^2 over time. The 1 mm^2 SNSPD is suitable for the current pilot experiment.

The light focused by the parabolic reflector requires the SNSPD to have a broad range of acceptance angles over its active area. Additionally, the broadband nature of the experiment necessitates that the sensor have sensitivity over a range of wavelengths. Given these requirements, coupled with the cryogenic operating temperature and low dark count rate, the SNSPD is an ideal choice for the sensor. Moreover, the Generation 1 microwire array does not require an optical stack, which is acceptable. As mentioned in the previous chapter, conventional optical stacks can limit the efficiency of light at large incident an-

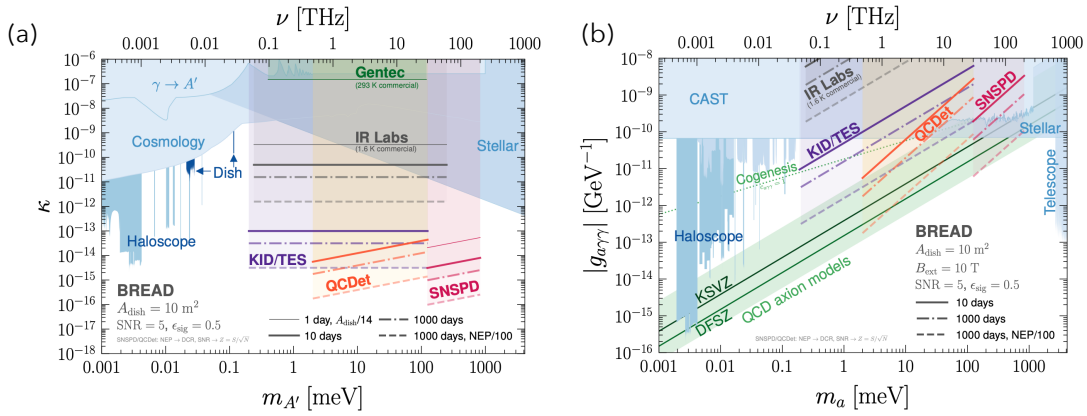


Figure 8.4: Projected BREAD sensitivity for different sensor technologies: (a) dark photons (A') and (b) axions (a). In (a), κ is the strength of the kinetic mixing term coupling dark photons to SM photons (this was ε in the notation in Chapter 1). In (b), $g_{a\gamma\gamma}$ is the axion-photon coupling constant. Figure taken from [125].

gles, enhancing efficiency at a target wavelength but narrowing the sensitivity to different wavelengths.

The projected sensitivity with a a dish area of 10 m^2using different sensor technologies including KIS/TES-based sensors, quantum capacitance detectors, and SNSPDs are shown in figure 8.4 for (a) dark photon searches and (b) axion searches.

8.2.2 RCWA Efficiency Simulations

RCWA simulations were performed to provide collaborators at Fermilab with estimates of the SNSPD detection efficiency for different wavelengths across a range of angles, consistent with the numerical apertures of the experiment design. In the simulations, following the convention of Chapter 7, the incident angle is denoted as θ, the azimuthal angle as ϕ, and the polarization as ψ. The SNSPD modeled has a fill factor of 0.25, a WSi thickness of 5.1 nm, and a 40 nm a-Si capping layer. This was chosen to match the parameters for the film 2 array described in [119], as the device is from that wafer.

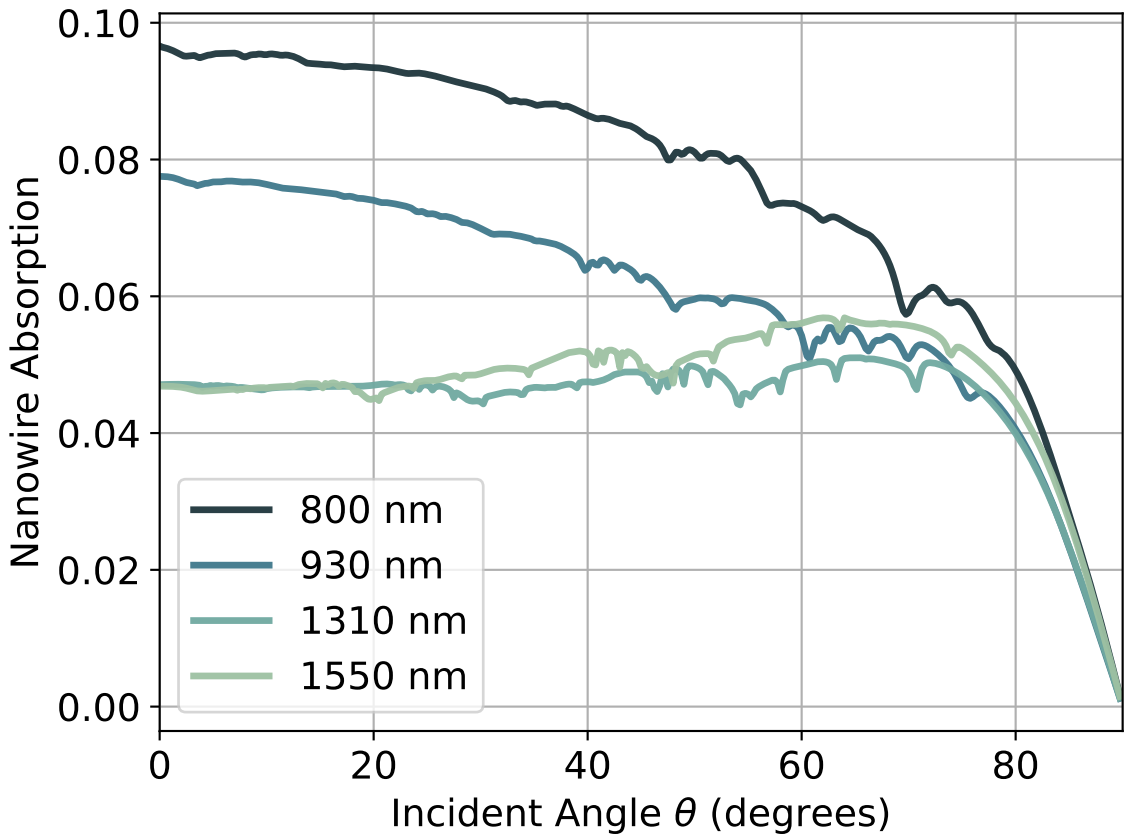


Figure 8.5: Simulated nanowire absorption as a function of incident angle θ for the Film 2, Generation 1 microwire array deployed at FNAL for the BREAD pilot experiment. The results are polarization-averaged and averaged over the azimuthal angle ϕ from 0 to 180 degrees.

Numerical apertures (NA) of 0.643, 0.766, and 0.866, corresponding to to incident angles θ in the ranges:

$$0^\circ \leq \theta \leq 40^\circ, \quad 0^\circ \leq \theta \leq 50^\circ, \quad 0^\circ \leq \theta \leq 60^\circ,$$

respectively.

The simulation results in figure 8.5 show the nanowire absorption as a function of incident angle for the average of the TE and TM polarization modes, averaged over ϕ 0 to 180 degrees for wavelengths of 930 nm, 1064 nm, 1310 nm, and 1550 nm. These results integrated over the different NAs are tabulated in table 8.1.

Wavelength (nm)	**Nanowire Absorption**		
	NA 0.643	**NA 0.766**	**NA 0.866**
800	9.25%	9.08%	8.85%
930	7.29%	7.09%	6.88%
1310	4.66%	4.69%	4.70%
1550	4.77%	4.82%	4.92%

Table 8.1: Simulated nanowire absorption at different wavelengths, averaged over incident angles $0^\circ \leq \theta \leq 40^\circ$ (NA 0.643), $0^\circ \leq \theta \leq 50^\circ$ (NA 0.766), and $0^\circ \leq \theta \leq 60^\circ$ (NA 0.866).

It can be observed that the detector maintains most of its efficiency across the different numerical apertures (NAs) considered. Although the absolute efficiency is relatively low, this robustness to incident angles arises because the array in an optical stack, which typically increases a detector's sensitivity to varying incident angles. Additionally, the efficiency of a detector in an optical stack would be enhanced for a narrow-band target wavelength, but this enhancement would drop off for wavelengths outside of the range optimized for. Therefore, the device without the optical stack serves as a suitable sensor for this experiment which requires a broadband photosensor with a wide range of acceptance angles.

8.2.3 Future Work

Future work will involve validating the above simulation results with calibrated efficiency measurements over a range of different numerical apertures. This can be done using similar methods as those depicted in reference [118]. In addition to this, the susceptibility of large active SNSPDs to backgrounds from muons is under investigation.

Traditional SNSPDs do not have a large enough area to interact significantly with muons, given the known event rates of muons from cosmic ray origins. However, large-area SNSPDs in the mm^2 regime may be sufficiently large for this effect to become significant. The underlying mechanism involves energy deposition into the substrate, energy deposi-

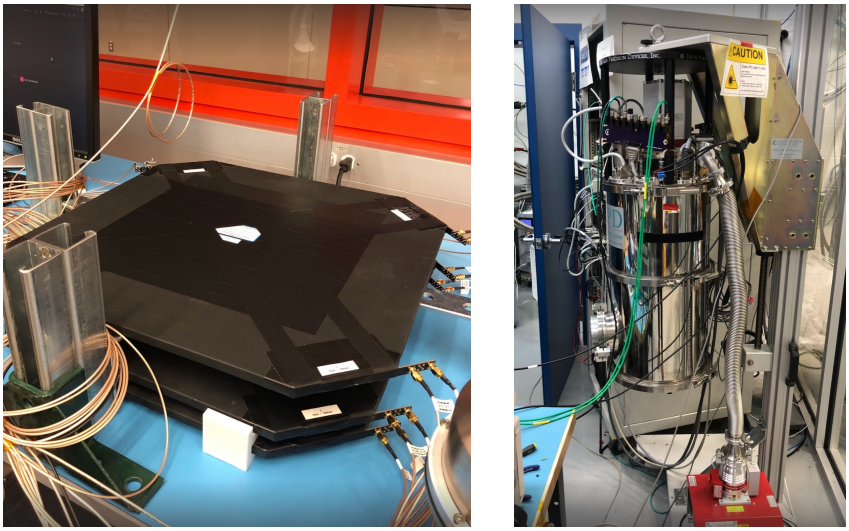


Figure 8.6: Muon telescope infrastructure at FNAL including (left) plastic scintillator paddles wrapped in reflective coatings and black shielding and (right) the skipper CCD group ADR which will house the muon coincidence search.

tion into the substrate which can then down-convert into high energy phonons and trigger a detection event in the active area. A system to study the SNSPD dark count rate using a muon telescope is currently under development. This system consists of plastic scintillator paddles mounted at the top and bottom of the cryostat, coupled to photomultiplier tubes (PMTs). When a muon shower occurs, it will cause a coincidence event between the two scintillator paddles. This event can then be investigated to determine if one or more SNSPD pixels within the cryostat have events that are correlated with the muon detectors mounted externally to the cryostat. This effort to understand susceptibility of large-area SNSPDs to high energy backgrounds is important for applications in HEP and also for the understanding of the DCR performance limitations of large-area SNSPD.

Chapter 9: Conclusions

9.1 Summary

This thesis presents the development, characterization, and study of large-area superconducting nanowire single-photon detectors (SNSPDs). The successful operation of SNSPDs with sub-0.1 Hz dark count rates at the mm^2-scale with near-infrared (NIR) sensitivity has been demonstrated. This combination of results is promising for the application of SNSPDs to low mass dark matter searches.

This work also highlights the pathways towards SNSPDs with active areas on the cm^2 scale. This can be accomplished by combining high-resistivity amorphous superconducting materials with multiplexing techniques to scalably increase pixel number while limiting the number of readout lines and the heat load on system cryogenics.

Additionally, this thesis explores the coupling of state-of-the-art large-area SNSPDs with cryogenic scintillating targets, which are under development for low-mass dark matter detection applications. The measurement infrastructure developed for this work merges high-energy physics instrumentation with single-photon counting instrumentation to enable novel characterization capabilities. This work lays a foundation for future advancements in DM detection technologies using SNSPDs.

9.2 Future Work and Outlook

Future work in detector development includes several key directions. First, improvements in large-area SNSPD nanofabrication processes, particularly the use of DBR mirrors, will enable high system detection efficiency in microwire arrays. Techniques such as bend thickening to reduce current crowding and He ion irradiation to reduce constrictions in microwires can further enhance their performance. Furthermore, new device architectures that incorporate multiple offset sensor layers can enable devices with a higher effective fill factor and higher efficiency.

Another future direction to explore for *n*-type GaAs as a cryogenic scintillating target is hybridization with other classes of superconducting detectors such as microwave kinetic inductance detectors (MKIDs), which can offer energy resolution capabilities. Furthermore, developing methods to index-match high-index scintillators to the materials commonly used in SNSPD optical stacks will improve the light extraction efficiency of hybridized systems and behavior at interfaces.

Additionally, the development of a cryostat specifically designed for energy-tagged X-ray excitation via Compton scattering is a promising direction for a robust test-bed facility. This system would feature aluminum windows in the radiation shields, minimizing the attenuation of X-rays and production of secondary X-rays that degrade SNR.

Appendix A: Procedure for IV Curve Analysis with DC Coupled Cryogenic Amplifiers

The DC-coupled cryogenic amplifiers used for all measurements have both an unknown DC offset and series resistance that can vary between cool-downs and thus must be measured and adjusted for each time an IV curve is taken. The IV curve is obtained by measuring the voltage across the SNSPD (V_{sense}) as the bias voltage (V_{bias}) varies.

The DC offset can be found through symmetrizing the measured IV curve. The IV curve first acquired will be asymmetric with respect to zero I_{bias}. This is shown in Figure A.1, where an offset between the positive and negative switching currents, $I_{\text{switch +}}$ and $I_{\text{switch -}}$, respectively, is demonstrated on the raw IV curve data.

After obtaining $I_{\text{switch +}}$ and $I_{\text{switch -}}$ from the raw data, the DC offset can be calculated as

$$I_{\text{offset}} = \frac{I_{\text{switch +}} - |I_{\text{switch -}}|}{2}. \tag{A.1}$$

In this example, we have

$$I_{\text{offset}} = \frac{24.23 - |-18.80|}{2} = 2.715\,\mu\text{A}. \tag{A.2}$$

Now, subtracting this offset from all I_{bias} values in the IV curve and re-plotting, the switching currents are symmetrized with respect to zero I_{bias}. This is shown in Figure A.2.

The next feature to correct for is the unknown parasitic resistance that we assume to

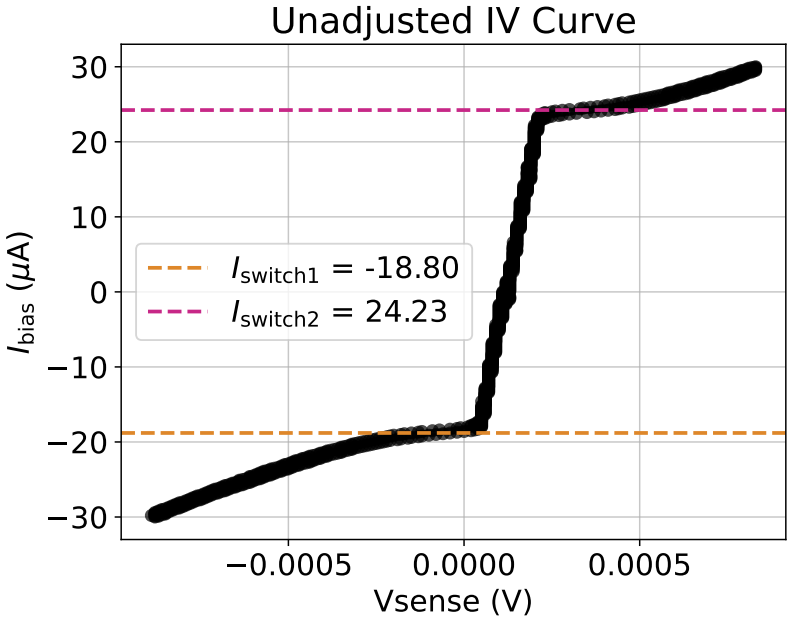


Figure A.1: The raw IV curve of an SNSPD pixel with asymmetric switching currents for negative and positive bias currents.

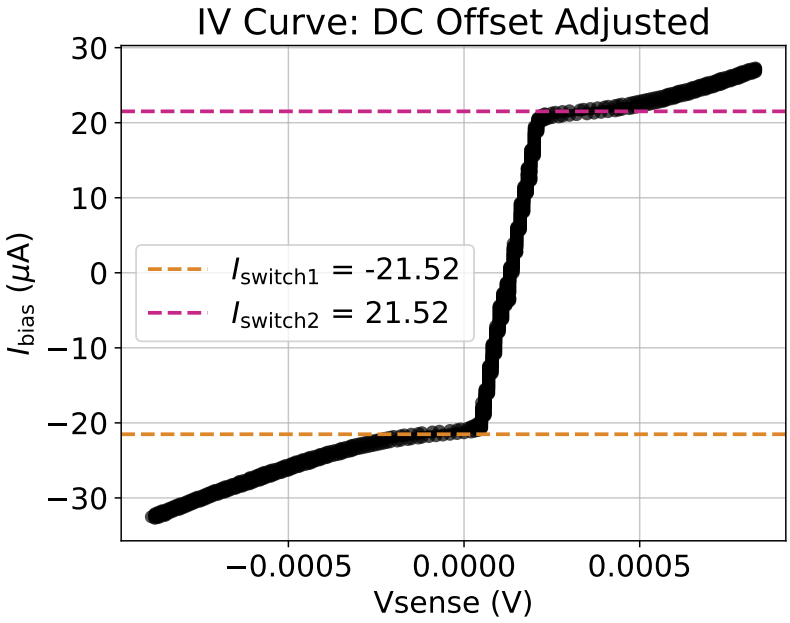


Figure A.2: The IV curve has had the calculated DC offset subtracted from all I_{bias} values, and the positive and negative switching currents are now symmetric.

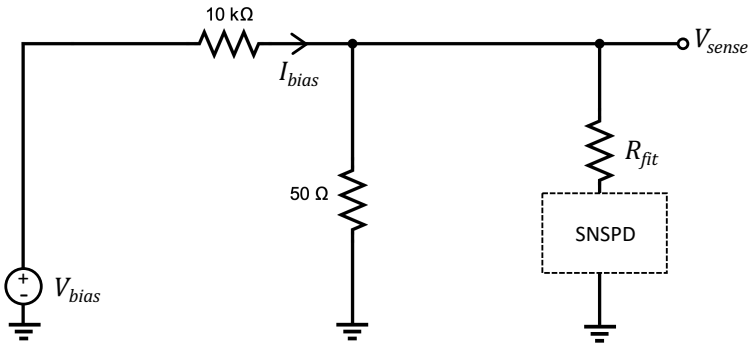


Figure A.3: The IV curve has had the calculated DC offset subtracted from all I_{bias} values, and the positive and negative switching currents are now symmetric.

be in series with the SNSPD from the cabling. Figure A.3 shows a simplified diagram depicting the biasing scheme. Governed by the equation

$$V_{\text{bias}} = V_{\text{sense}} \left[1 + 10\,\text{k}\Omega \times \left(\frac{1}{50\Omega} + \frac{1}{R_{\text{fit}}} \right) \right], \tag{A.3}$$

the parasitic resistance R_{fit} can be extracted from the superconducting portion of the offset-corrected IV curve as the inverse of the slope. Using this extracted series resistance, the actual bias current delivered to the SNSPD, $I_{\text{bias, SNSPD}}$, can be calculated as

$$I_{\text{bias, SNSPD}} = \frac{V_{\text{bias}}}{10\,\text{k}\Omega} + \frac{50\,\Omega \times R_{\text{hs}}}{50\,\Omega + R_{\text{fit}}}. \tag{A.4}$$

The final value of $I_{\text{bias, SNSPD}}$ after this correction procedure is thus

$$I_{\text{bias, SNSPD}} = (I_{\text{bias}} - \text{offset}) \times \frac{50}{50 + R_{\text{fit}}}, \tag{A.5}$$

where $\frac{50}{50+R_{\text{fit}}}$ is the scale factor accounting for the parasitic series resistance.

This linear fit, superimposed onto the superconducting portion of the offset-corrected IV curve, is shown in Figure A.3.

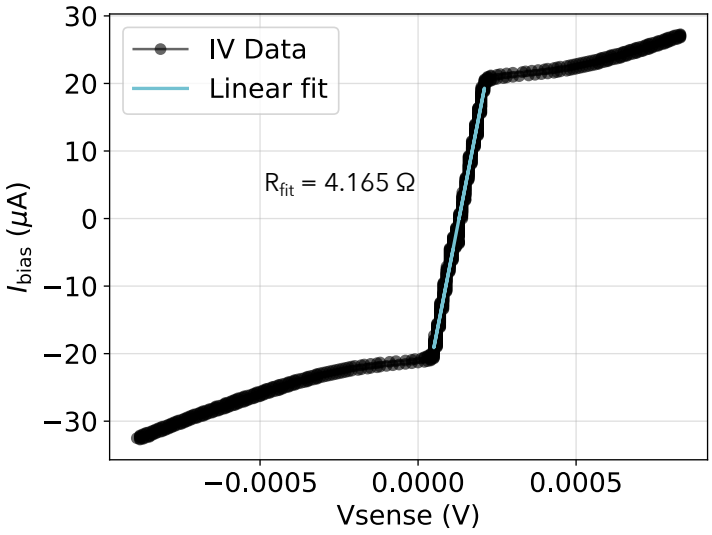


Figure A.4: The superconducting branch of the IV curve, adjusted for the DC offset, with the superimposed linear fit to extract the unknown series resistance. A value of 4.164 Ω was found in the fit, which is within the expected range for the cabling used.

In this example, it can be seen from inspection of the IV curve plot that the slope has units of $\frac{\text{current}\,[\mu\text{A}]}{\text{voltage}\,[\text{V}]}$. The inverse of this gives R_{fit} in units of MΩ. The extracted slope is $240072.22\,\mu$A/V or $240072.22\,\text{M}\Omega^{-1}$. Taking the inverse of the slope, we get a value of:

$$R_{\text{fit}} = \frac{1}{\text{slope}} = \frac{1}{240072.22} = 4.165 \times 10^{-6}\,\text{M}\Omega = 4.165\,\Omega. \tag{A.6}$$

The scale factor from this would be:

$$\frac{50\,\Omega}{50\,\Omega + R_{\text{fit}}} = \frac{50\,\Omega}{50\,\Omega + 4.165\,\Omega} = 0.9231061005169963. \tag{A.7}$$

Now, all of the I_{bias} values for measurements (PCR curves, etc.) can be adjusted as:

$$I_{\text{bias, SNSPD}} = (I_{\text{bias}} - \text{offset}) \times \text{Scale factor} = (I_{\text{bias}} - 2.715) \times 0.9231061005169963. \tag{A.8}$$

Appendix B: *n*-type GaAs Sample Information

Two samples of *n*-type GaAs were obtained for experiments in this thesis. Sample A was sourced from University Wafer, and Sample B was sources from Freiberger. Table B.1 lists the specifications of the two samples.

Sample	Dimensions (mm)	Carrier Concentration	N_{Boron}	$N_{Silicon}$
A	5 x 5 x 0.625	2.99×10^{17} cm^{-3}	6.29×10^{17} cm^{-3}	1.14×10^{19} cm^{-3}
B	10 x 10 x 4	1×10^{17} cm^{-3} to 2×10^{17} cm^{-3}	unknown	unknown

Table B.1: Specifications of *n*-type GaAs samples. All information was obtained from the vendors, except for N_{Boron} and $N_{Silicon}$ which were obtained via SIMS analysis.

B.1 Sample A - More Information

Table A.2 shows more information on Sample A from the vendor.

Item	1F1058
Diameter (mm)	100 ± 0.1
Diameter (inch)	4
Thickness (µm)	625
EPD (cm^{-2})	4869
Mobility (cm^2/V.s)	3185
CC (cm^{-2})	2.99×10^{17}
Resistivity (ohm-cm)	6.55×10^3
Orientation	(100)
Surface	Polished

Table B.2: Sample Properties and Characteristics

SIMS analysis on a piece of the wafer was carried out by Eurofins, Inc. to determine the

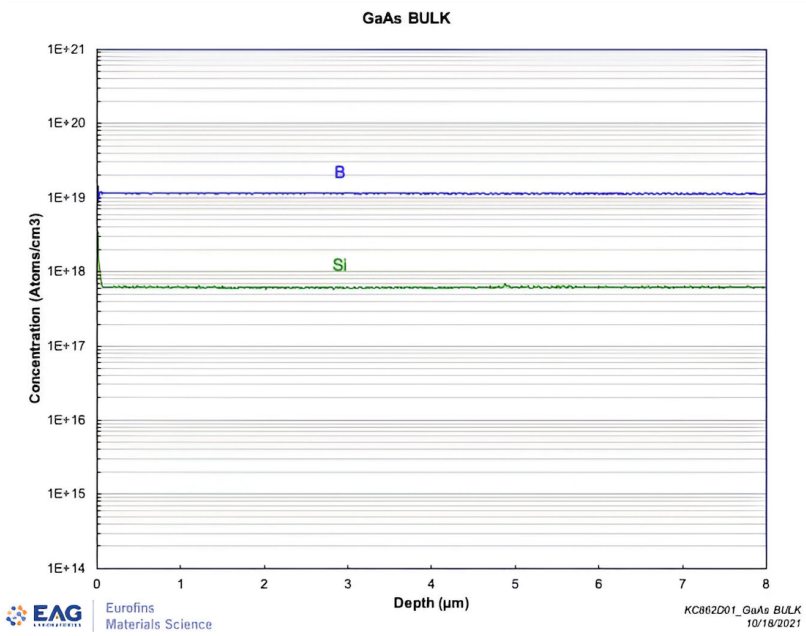


Figure B.1: Measured concentrations of Silicon and Boron in the sample analyzed via SIMS analysis as a function of depth.

Si and B concentrations. The lower detection limits of this analysis are $N_B = 2 \times 10^{14}\,\mathrm{cm}^{-3}$, and $N_{Si} = 5 \times 10^{14}\,\mathrm{cm}^{-3}$. The measured values, $N_B = 6.29 \times 10^{17}\,\mathrm{cm}^{-3}$ and $N_{Si} = 1.14 \times 10^{19}\,\mathrm{cm}^{-3}$, are well above the detection limits. Figure A.1 shows the analysis plot.

B.2 Sample B - More Information

The following table contains information on the wafer that sample B was cut from. This was supplied by Freiberger.

Property	Value
Crystal Growth Method	VGF
Font Side	Pre-polished
Back Side	Pre-polished
Roughness Front Side (Ra)	≤ 10 nm
Roughness Back Side (Ra)	≤ 10 nm
Conduction Type	N-Type, semi-conducting
Dopant	Si
Carrier concentration (cm^{-3})	$(1.0-2.0)\times 10^{17}$
EPD (Average over wafer) (cm^{-2})	≤ 5000
Diameter (mm)	150.0 ± 0.5
Notch	$[010] \pm 2^{\circ}$
Surface Orientation	(100)
Off-Orientation Degree	6 ± 0.5 tow. (11-1)
Edge Rounding	facet manually ground, facet can vary in width, $\leq$ 3mm edge exclusion, notch is not beveled

Table B.3: Sample Properties and Characteristics. Notes: (1) Roughness Front Side (Ra) ≤ 10 nm. (2) Roughness Back Side (Ra) ≤ 10 nm.

Appendix C: Publications

Luskin, J., Schmidt, E., Korzh, B., Beyer, A., Bumble, B., Allmaras, J., Walter, A., Wollman, E., Narváez, L., Verma, V., Nam, S., Charaev, I., Colangelo, M., Berggren, K., Peña, C., Spiropulu, M., Garcia-Sciveres, M., Derenzo, S., Shaw, M. (2023). Large Active-area Superconducting Microwire Detector Array with Single-photon Sensitivity in the Near-infrared. *Applied Physics Letters*, 122(24), 243506.

Peña, C., Wang, C., Xie, S., Bornheim, A., Barría, M., San Martín, C., Vega, V., Apresyan, A., Knehr, E., Korzh, B., **Luskin, J.**, Narváez, L., Patel, S., Shaw, M., Spiropulu, M. (2024). High Energy Particle Detection with Large Area Superconducting Microwire Array.

Bibliography

[1] F. Zwicky. Republication of: The redshift of extragalactic nebulae. *General Relativity and Gravitation*, 41(1):207–224, Jan 2009. ISSN 1572-9532. doi: 10.1007/s10714-008-0707-4. URL https://doi.org/10.1007/s10714-008-0707-4.

[2] Vera C. Rubin and Jr. Ford, W. Kent. Rotation of the Andromeda Nebula from a Spectroscopic Survey of Emission Regions. , 159:379, February 1970. doi: 10.1086/150317.

[3] V. C. Rubin, Jr. Ford, W. K., and N. Thonnard. Rotational properties of 21 SC galaxies with a large range of luminosities and radii, from NGC 4605 (R=4kpc) to UGC 2885 (R=122kpc). , 238:471–487, June 1980. doi: 10.1086/158003.

[4] Julio F. Navarro, Carlos S. Frenk, and Simon D. M. White. The Structure of Cold Dark Matter Halos. , 462:563, May 1996. doi: 10.1086/177173.

[5] M. Milgrom. A modification of the Newtonian dynamics as a possible alternative to the hidden mass hypothesis. , 270:365–370, July 1983. doi: 10.1086/161130.

[6] S. Mendoza, T. Bernal, J. C. Hidalgo, and S. Capozziello. Mond as the weak-field limit of an extended metric theory of gravity. *AIP Conference Proceedings*, 1458 (1):483–486, 07 2012. ISSN 0094-243X. doi: 10.1063/1.4734465. URL https://doi.org/10.1063/1.4734465.

[7] E. Margaret Burbidge, G. R. Burbidge, D. J. Crampin, V. C. Rubin, and K. H. Prendergast. The Rotation and Mass of NGC 6503. , 139:539, February 1964. doi: 10.1086/147782.

[8] Ethan Siegel. How the planck satellite forever changed our view of the universe, Jul 2018. URL https://www.forbes.com/sites/startswithabang/2018/07/19/how-the-planck-satellite-changed-our-view-of-the-universe/?sh=5eef97e07ad2.

[9] Wayne Hu. Cmb temperature and polarization anisotropy fundamentals. *Annals of Physics*, 303(1):203–225, 2003. ISSN 0003-4916. doi: https://doi.org/10.1016/S0003-4916(02)00022-2. URL https://www.sciencedirect.com/science/article/pii/S0003491602000222.

[10] George F. Smoot. COBE observations and results. *AIP Conference Proceedings*, 476(1):1–10, 05 1999.

[11] G. Hinshaw, D. Larson, E. Komatsu, D. N. Spergel, C. L. Bennett, J. Dunkley, M. R. Nolta, M. Halpern, R. S. Hill, N. Odegard, L. Page, K. M. Smith, J. L. Weiland, B. Gold, N. Jarosik, A. Kogut, M. Limon, S. S. Meyer, G. S. Tucker, E. Wollack, and E. L. Wright. Nine-year wilkinson microwave anisotropy probe (wmap) observations: Cosmological parameter results. *The Astrophysical Journal Supplement Series*, 208(2):19, sep 2013. doi: 10.1088/0067-0049/208/2/19. URL https://dx.doi.org/10.1088/0067-0049/208/2/19.

[12] N. Aghanim, Y. Akrami, M. Ashdown, J. Aumont, C. Baccigalupi, M. Ballardini, A. J. Banday, R. B. Barreiro, N. Bartolo, S. Basak, R. Battye, K. Benabed, J.-P. Bernard, M. Bersanelli, P. Bielewicz, J. J. Bock, J. R. Bond, J. Borrill, F. R. Bouchet, F. Boulanger, M. Bucher, C. Burigana, R. C. Butler, E. Calabrese, J.-F. Cardoso, J. Carron, A. Challinor, H. C. Chiang, J. Chluba, L. P. L. Colombo, C. Combet, D. Contreras, B. P. Crill, F. Cuttaia, P. de Bernardis, G. de Zotti, J. Delabrouille, J.-M. Delouis, E. Di Valentino, J. M. Diego, O. Doré, M. Douspis, A. Ducout, X. Dupac, S. Dusini, G. Efstathiou, F. Elsner, T. A. Enßlin, H. K. Eriksen, Y. Fantaye, M. Farhang, J. Fergusson, R. Fernandez-Cobos, F. Finelli, F. Forastieri, M. Frailis, A. A. Fraisse, E. Franceschi, A. Frolov, S. Galeotta, S. Galli, K. Ganga, R. T. Génova-Santos, M. Gerbino, T. Ghosh, J. González-Nuevo, K. M. Górski, S. Gratton, A. Gruppuso, J. E. Gudmundsson, J. Hamann, W. Handley, F. K. Hansen, D. Herranz, S. R. Hildebrandt, E. Hivon, Z. Huang, A. H. Jaffe, W. C. Jones, A. Karakci, E. Keihänen, R. Keskitalo, K. Kiiveri, J. Kim, T. S. Kisner, L. Knox, N. Krachmalnicoff, M. Kunz, H. Kurki-Suonio, G. Lagache, J.-M. Lamarre, A. Lasenby, M. Lattanzi, C. R. Lawrence, M. Le Jeune, P. Lemos, J. Lesgourgues, F. Levrier, A. Lewis, M. Liguori, P. B. Lilje, M. Lilley, V. Lindholm, M. López-Caniego, P. M. Lubin, Y.-Z. Ma, J. F. Macías-Pérez, G. Maggio, D. Maino, N. Mandolesi, A. Mangilli, A. Marcos-Caballero, M. Maris, P. G. Martin, M. Martinelli, E. Martínez-González, S. Matarrese, N. Mauri, J. D. McEwen, P. R. Meinhold, A. Melchiorri, A. Mennella, M. Migliaccio, M. Millea, S. Mitra, M.-A. Miville-Deschênes, D. Molinari, L. Montier, G. Morgante, A. Moss, P. Natoli, H. U. Nørgaard-Nielsen, L. Pagano, D. Paoletti, B. Partridge, G. Patanchon, H. V. Peiris, F. Perrotta, V. Pettorino, F. Piacentini, L. Polastri, G. Polenta, J.-L. Puget, J. P. Rachen, M. Reinecke, M. Remazeilles, A. Renzi, G. Rocha, C. Rosset, G. Roudier, J. A. Rubiño-Martín, B. Ruiz-Granados, L. Salvati, M. Sandri, M. Savelainen, D. Scott, E. P. S. Shellard, C. Sirignano, G. Sirri, L. D. Spencer, R. Sunyaev,

A.-S. Suur-Uski, J. A. Tauber, D. Tavagnacco, M. Tenti, L. Toffolatti, M. Tomasi, T. Trombetti, L. Valenziano, J. Valiviita, B. Van Tent, L. Vibert, P. Vielva, F. Villa, N. Vittorio, B. D. Wandelt, I. K. Wehus, M. White, S. D. M. White, A. Zacchei, and A. Zonca. Planck2018 results: Vi. cosmological parameters. *Astronomy amp; Astrophysics*, 641:A6, September 2020. ISSN 1432-0746. doi: 10.1051/0004-6361/201833910. URL http://dx.doi.org/10.1051/0004-6361/201833910.

[13] J. R. Brownstein and J. W. Moffat. The bullet cluster 1e0657-558 evidence shows modified gravity in the absence of dark matter. *Monthly Notices of the Royal Astronomical Society*, 382(1):29–47, 10 2007. ISSN 0035-8711. doi: 10.1111/j.1365-2966.2007.12275.x. URL https://doi.org/10.1111/j.1365-2966.2007.12275.x.

[14] Matthew D A Orkney, Ethan Taylor, Justin I Read, Martin P Rey, A Pontzen, Oscar Agertz, Stacy Y Kim, and Maxime Delorme. EDGE: the shape of dark matter haloes in the faintest galaxies. *Monthly Notices of the Royal Astronomical Society*, 525 (3):3516–3532, 08 2023. ISSN 0035-8711. doi: 10.1093/mnras/stad2516. URL https://doi.org/10.1093/mnras/stad2516.

[15] P. J. E. Peebles. Large-scale background temperature and mass fluctuations due to scale-invariant primeval perturbations. , 263:L1–L5, December 1982. doi: 10.1086/183911.

[16] George R. Blumenthal, S. M. Faber, Joel R. Primack, and Martin J. Rees. Formation of galaxies and large-scale structure with cold dark matter. *Nature*, 311(5986):517–525, Oct 1984. ISSN 1476-4687. doi: 10.1038/311517a0. URL https://doi.org/10.1038/311517a0.

[17] Elisa G. M. Ferreira. Ultra-light dark matter. *The Astronomy and Astrophysics Review*, 29(1):7, Sep 2021. ISSN 1432-0754. doi: 10.1007/s00159-021-00135-6. URL https://doi.org/10.1007/s00159-021-00135-6.

[18] Julien Billard, Mark Boulay, Susana Cebrián, Laura Covi, Giuliana Fiorillo, Anne Green, Joachim Kopp, Béla Majorovits, Kimberly Palladino, Federica Petricca, Leszek Roszkowski (chair), and Marc Schumann. Direct detection of dark matter—appec committee report*. *Reports on Progress in Physics*, 85(5):056201, April 2022. ISSN 1361-6633. doi: 10.1088/1361-6633/ac5754. URL http://dx.doi.org/10.1088/1361-6633/ac5754.

[19] Kathryn M. Zurek. Dark matter candidates of a very low mass. *Annual Review of Nuclear and Particle Science*, 2024. ISSN 0163-8998. doi: https://doi.org/10.1146/annurev-nucl-101918-023542. URL https://www.annualreviews.org/content/journals/10.1146/annurev-nucl-101918-023542.

[20] L. Bergström. Dark matter evidence, particle physics candidates and detection methods. *Annalen der Physik*, 524(9-10):479–496. doi: https://doi.org/10.1002/andp.201200116. URL https://onlinelibrary.wiley.com/doi/abs/10.1002/andp.201200116.

[21] Lam Hui. Wave dark matter. *Annual Review of Astronomy and Astrophysics*, 59(Volume 59, 2021):247–289, 2021. ISSN 1545-4282. doi: https://doi.org/10.1146/annurev-astro-120920-010024. URL https://www.annualreviews.org/content/journals/10.1146/annurev-astro-120920-010024.

[22] David J.E. Marsh. Axion cosmology. *Physics Reports*, 643:1–79, 2016. ISSN 0370-1573. doi: https://doi.org/10.1016/j.physrep.2016.06.005. URL https://www.sciencedirect.com/science/article/pii/S0370157316301557. Axion cosmology.

[23] R. Khatiwada, D. Bowring, A. S. Chou, A. Sonnenschein, W. Wester, D. V. Mitchell, T. Braine, C. Bartram, R. Cervantes, N. Crisosto, N. Du, L. J. Rosenberg, G. Rybka, J. Yang, D. Will, S. Kimes, G. Carosi, N. Woollett, S. Durham, L. D. Duffy, R. Bradley, C. Boutan, M. Jones, B. H. LaRoque, N. S. Oblath, M. S. Taubman, J. Tedeschi, John Clarke, A. Dove, A. Hashim, I. Siddiqi, N. Stevenson, A. Eddins, S. R. O'Kelley, S. Nawaz, A. Agrawal, A. V. Dixit, J. R. Gleason, S. Jois, P. Sikivie, N. S. Sullivan, D. B. Tanner, J. A. Solomon, E. Lentz, E. J. Daw, M. G. Perry, J. H. Buckley, P. M. Harrington, E. A. Henriksen, K. W. Murch, and G. C. Hilton. Axion Dark Matter Experiment: Detailed design and operations. *Review of Scientific Instruments*, 92(12):124502, 12 2021. ISSN 0034-6748. doi: 10.1063/5.0037857. URL https://doi.org/10.1063/5.0037857.

[24] Deniz Aybas, Janos Adam, Emmy Blumenthal, Alexander V. Gramolin, Dorian Johnson, Annalies Kleyheeg, Samer Afach, John W. Blanchard, Gary P. Centers, Antoine Garcon, Martin Engler, Nataniel L. Figueroa, Marina Gil Sendra, Arne Wickenbrock, Matthew Lawson, Tao Wang, Teng Wu, Haosu Luo, Hamdi Mani, Philip Mauskopf, Peter W. Graham, Surjeet Rajendran, Derek F. Jackson Kimball, Dmitry Budker, and Alexander O. Sushkov. Search for axionlike dark matter using solid-state nuclear magnetic resonance. *Phys. Rev. Lett.*, 126:141802, Apr 2021. doi: 10.1103/PhysRevLett.126.141802. URL https://link.aps.org/doi/10.1103/PhysRevLett.126.141802.

[25] Dennis M. Nenno, Christina A. C. Garcia, Johannes Gooth, Claudia Felser, and Prineha Narang. Axion physics in condensed-matter systems. *Nature Reviews Physics*, 2(12):682–696, Dec 2020. ISSN 2522-5820. doi: 10.1038/s42254-020-0240-2. URL https://doi.org/10.1038/s42254-020-0240-2.

[26] M. Raggi and V. Kozhuharov. Results and perspectives in dark photon physics. *La Rivista del Nuovo Cimento*, 38(10):449–505, Oct 2015. ISSN 1826-

9850. doi: 10.1393/ncr/i2015-10117-9. URL https://doi.org/10.1393/ncr/i2015-10117-9.

[27] Alessandra Filippi and M. De Napoli. Searching in the dark: the hunt for the dark photon. *Reviews in Physics*, 5:100042, 2020. ISSN 2405-4283. doi: https://doi.org/10.1016/j.revip.2020.100042. URL https://www.sciencedirect.com/science/article/pii/S2405428320300058.

[28] Basudeb Dasgupta and Joachim Kopp. Sterile neutrinos. *Physics Reports*, 928:1–63, 2021. ISSN 0370-1573. doi: https://doi.org/10.1016/j.physrep.2021.06.002. URL https://www.sciencedirect.com/science/article/pii/S0370157321002696. Sterile neutrinos.

[29] CMS Collaboration. Dark sector searches with the cms experiment, 2024. URL https://arxiv.org/abs/2405.13778.

[30] Brian Batell, Nikita Blinov, Christopher Hearty, and Robert McGehee. Exploring dark sector portals with high intensity experiments, 2022. URL https://arxiv.org/abs/2207.06905.

[31] Giorgio Arcadi, Glauber C. Dorsch, Jacinto P. Neto, Farinaldo S. Queiroz, and Y.M. Oviedo-Torres. Probing a dark sector with collider physics, direct detection, and gravitational waves. *Physics Letters B*, 848:138382, 2024. ISSN 0370-2693. doi: https://doi.org/10.1016/j.physletb.2023.138382. URL https://www.sciencedirect.com/science/article/pii/S0370269323007165.

[32] S. Asztalos, E. Daw, H. Peng, L. J Rosenberg, C. Hagmann, D. Kinion, W. Stoeffl, K. van Bibber, P. Sikivie, N. S. Sullivan, D. B. Tanner, F. Nezrick, M. S. Turner, D. M. Moltz, J. Powell, M.-O. André, J. Clarke, M. Mück, and Richard F. Bradley. Large-scale microwave cavity search for dark-matter axions. *Phys. Rev. D*, 64:092003, Oct 2001. doi: 10.1103/PhysRevD.64.092003. URL https://link.aps.org/doi/10.1103/PhysRevD.64.092003.

[33] A. Wagner, G. Rybka, M. Hotz, L. J Rosenberg, S. J. Asztalos, G. Carosi, C. Hagmann, D. Kinion, K. van Bibber, J. Hoskins, C. Martin, P. Sikivie, D. B. Tanner, R. Bradley, and J. Clarke. Search for hidden sector photons with the admx detector. *Phys. Rev. Lett.*, 105:171801, Oct 2010. doi: 10.1103/PhysRevLett.105.171801. URL https://link.aps.org/doi/10.1103/PhysRevLett.105.171801.

[34] N. Du, N. Force, R. Khatiwada, E. Lentz, R. Ottens, L. J Rosenberg, G. Rybka, G. Carosi, N. Woollett, D. Bowring, A. S. Chou, A. Sonnenschein, W. Wester, C. Boutan, N. S. Oblath, R. Bradley, E. J. Daw, A. V. Dixit, J. Clarke, S. R. O'Kelley, N. Crisosto, J. R. Gleason, S. Jois, P. Sikivie, I. Stern, N. S. Sullivan, D. B Tanner, and G. C. Hilton. Search for invisible axion dark matter with the axion dark matter experiment. *Phys. Rev. Lett.*, 120:151301, Apr 2018. doi:

10.1103/PhysRevLett.120.151301. URL https://link.aps.org/doi/10.1103/PhysRevLett.120.151301.

[35] C. Bartram, T. Braine, E. Burns, R. Cervantes, N. Crisosto, N. Du, H. Korandla, G. Leum, P. Mohapatra, T. Nitta, L. J Rosenberg, G. Rybka, J. Yang, John Clarke, I. Siddiqi, A. Agrawal, A. V. Dixit, M. H. Awida, A. S. Chou, M. Hollister, S. Knirck, A. Sonnenschein, W. Wester, J. R. Gleason, A. T. Hipp, S. Jois, P. Sikivie, N. S. Sullivan, D. B. Tanner, E. Lentz, R. Khatiwada, G. Carosi, N. Robertson, N. Woollett, L. D. Duffy, C. Boutan, M. Jones, B. H. LaRoque, N. S. Oblath, M. S. Taubman, E. J. Daw, M. G. Perry, J. H. Buckley, C. Gaikwad, J. Hoffman, K. W. Murch, M. Goryachev, B. T. McAllister, A. Quiskamp, C. Thomson, and M. E. Tobar. Search for invisible axion dark matter in the $3.3 - -4.2$ μeV mass range. *Phys. Rev. Lett.*, 127:261803, Dec 2021. doi: 10.1103/PhysRevLett.127.261803. URL https://link.aps.org/doi/10.1103/PhysRevLett.127.261803.

[36] T. Braine, R. Cervantes, N. Crisosto, N. Du, S. Kimes, L. J. Rosenberg, G. Rybka, J. Yang, D. Bowring, A. S. Chou, R. Khatiwada, A. Sonnenschein, W. Wester, G. Carosi, N. Woollett, L. D. Duffy, R. Bradley, C. Boutan, M. Jones, B. H. LaRoque, N. S. Oblath, M. S. Taubman, J. Clarke, A. Dove, A. Eddins, S. R. O'Kelley, S. Nawaz, I. Siddiqi, N. Stevenson, A. Agrawal, A. V. Dixit, J. R. Gleason, S. Jois, P. Sikivie, J. A. Solomon, N. S. Sullivan, D. B. Tanner, E. Lentz, E. J. Daw, J. H. Buckley, P. M. Harrington, E. A. Henriksen, and K. W. Murch. Extended search for the invisible axion with the axion dark matter experiment. *Phys. Rev. Lett.*, 124:101303, Mar 2020. doi: 10.1103/PhysRevLett.124.101303. URL https://link.aps.org/doi/10.1103/PhysRevLett.124.101303.

[37] L. Zhong, S. Al Kenany, K. M. Backes, B. M. Brubaker, S. B. Cahn, G. Carosi, Y. V. Gurevich, W. F. Kindel, S. K. Lamoreaux, K. W. Lehnert, S. M. Lewis, M. Malnou, R. H. Maruyama, D. A. Palken, N. M. Rapidis, J. R. Root, M. Simanovskaia, T. M. Shokair, D. H. Speller, I. Urdinaran, and K. A. van Bibber. Results from phase 1 of the haystac microwave cavity axion experiment. *Phys. Rev. D*, 97:092001, May 2018. doi: 10.1103/PhysRevD.97.092001. URL https://link.aps.org/doi/10.1103/PhysRevD.97.092001.

[38] M. J. Jewell, A. F. Leder, K. M. Backes, Xiran Bai, K. van Bibber, B. M. Brubaker, S. B. Cahn, A. Droster, Maryam H. Esmat, Sumita Ghosh, Eleanor Graham, Gene C. Hilton, H. Jackson, Claire Laffan, S. K. Lamoreaux, K. W. Lehnert, S. M. Lewis, M. Malnou, R. H. Maruyama, D. A. Palken, N. M. Rapidis, E. P. Ruddy, M. Simanovskaia, Sukhman Singh, D. H. Speller, Leila R. Vale, H. Wang, and Yuqi Zhu. New results from haystac's phase ii operation with a squeezed state receiver. *Phys. Rev. D*, 107:072007, Apr 2023. doi: 10.1103/PhysRevD.107.072007. URL https://link.aps.org/doi/10.1103/PhysRevD.107.072007.

[39] Marco Battaglieri et. al. Us cosmic visions: New ideas in dark matter 2017: Community report. *arXiv*, High Energy Physics - Phenomenology (hep-ph), 2017. URL https://doi.org/10.48550/arXiv.1707.04591.

[40] Rouven Essig, Marivi Fernández-Serra, Jeremy Mardon, Adrián Soto, Tomer Volansky, and Tien-Tien Yu. Direct detection of sub-gev dark matter with semiconductor targets. *Journal of High Energy Physics*, 2016(5):46, May 2016. ISSN 1029-8479. doi: 10.1007/JHEP05(2016)046. URL https://doi.org/10.1007/JHEP05(2016)046.

[41] E. Aprile, F. Agostini, M. Alfonsi, K. Arisaka, F. Arneodo, M. Auger, C. Balan, P. Barrow, L. Baudis, B. Bauermeister, A. Behrens, P. Beltrame, K. Bokeloh, A. Brown, E. Brown, S. Bruenner, G. Bruno, R. Budnik, J. M. R. Cardoso, A. P. Colijn, H. Contreras, J. P. Cussonneau, M. P. Decowski, E. Duchovni, S. Fattori, A. D. Ferella, W. Fulgione, F. Gao, M. Garbini, C. Geis, L. W. Goetzke, C. Grignon, E. Gross, W. Hampel, R. Itay, F. Kaether, G. Kessler, A. Kish, H. Landsman, R. F. Lang, M. Le Calloch, D. Lellouch, C. Levy, S. Lindemann, M. Lindner, J. A. M. Lopes, K. Lung, A. Lyashenko, S. MacMullin, T. Marrodán Undagoitia, J. Masbou, F. V. Massoli, D. Mayani Paras, A. J. Melgarejo Fernandez, Y. Meng, M. Messina, B. Miguez, A. Molinario, M. Murra, J. Naganoma, K. Ni, U. Oberlack, S. E. A. Orrigo, E. Pantic, R. Persiani, F. Piastra, J. Pienaar, G. Plante, N. Priel, S. Reichard, C. Reuter, A. Rizzo, S. Rosendahl, J. M. F. dos Santos, G. Sartorelli, S. Schindler, J. Schreiner, M. Schumann, L. Scotto Lavina, M. Selvi, P. Shagin, H. Simgen, A. Teymourian, D. Thers, A. Tiseni, G. Trinchero, O. Vitells, H. Wang, M. Weber, and C. Weinheimer. First axion results from the xenon100 experiment. *Phys. Rev. D*, 90:062009, Sep 2014. doi: 10.1103/PhysRevD.90.062009. URL https://link.aps.org/doi/10.1103/PhysRevD.90.062009.

[42] E. Aprile, J. Aalbers, F. Agostini, M. Alfonsi, F. D. Amaro, M. Anthony, F. Arneodo, P. Barrow, L. Baudis, B. Bauermeister, M. L. Benabderrahmane, T. Berger, P. A. Breur, A. Brown, E. Brown, S. Bruenner, G. Bruno, R. Budnik, A. Buss, L. Bütikofer, J. M. R. Cardoso, M. Cervantes, D. Cichon, D. Coderre, A. P. Colijn, J. Conrad, J. P. Cussonneau, M. P. Decowski, P. de Perio, P. Di Gangi, A. Di Giovanni, E. Duchovni, A. D. Ferella, A. Fieguth, D. Franco, W. Fulgione, M. Galloway, M. Garbini, C. Geis, L. W. Goetzke, Z. Greene, C. Grignon, E. Gross, C. Hasterok, E. Hogenbirk, R. Itay, B. Kaminsky, G. Kessler, A. Kish, H. Landsman, R. F. Lang, L. Levinson, M. Le Calloch, C. Levy, F. Linde, S. Lindemann, M. Lindner, J. A. M. Lopes, A. Lyashenko, A. Manfredini, T. Marrodán Undagoitia, J. Masbou, F. V. Massoli, D. Masson, D. Mayani, A. J. Melgarejo Fernandez, Y. Meng, M. Messina, K. Micheneau, B. Miguez, A. Molinario, M. Murra, J. Naganoma, U. Oberlack, S. E. A. Orrigo, P. Pakarha, B. Pelssers, R. Persiani, F. Piastra, J. Pienaar, G. Plante, N. Priel, L. Rauch, S. Reichard, C. Reuter, A. Rizzo, S. Rosendahl, N. Rupp, J. M. F. dos Santos, G. Sartorelli,

M. Scheibelhut, S. Schindler, J. Schreiner, M. Schumann, L. Scotto Lavina, M. Selvi, P. Shagin, H. Simgen, A. Stein, D. Thers, A. Tiseni, G. Trinchero, C. D. Tunnell, M. von Sivers, R. Wall, H. Wang, M. Weber, Y. Wei, C. Weinheimer, J. Wulf, and Y. Zhang. Low-mass dark matter search using ionization signals in xenon100. *Phys. Rev. D*, 94:092001, Nov 2016. doi: 10.1103/PhysRevD.94.092001. URL `https://link.aps.org/doi/10.1103/PhysRevD.94.092001`.

[43] E. Aprile, J. Aalbers, F. Agostini, M. Alfonsi, F. D. Amaro, M. Anthony, F. Arneodo, P. Barrow, L. Baudis, B. Bauermeister, M. L. Benabderrahmane, T. Berger, P. A. Breur, A. Brown, E. Brown, S. Bruenner, G. Bruno, R. Budnik, L. Bütikofer, J. Calvén, J. M. R. Cardoso, M. Cervantes, D. Cichon, D. Coderre, A. P. Colijn, J. Conrad, J. P. Cussonneau, M. P. Decowski, P. de Perio, P. Di Gangi, A. Di Giovanni, S. Diglio, E. Duchovni, J. Fei, A. D. Ferella, A. Fieguth, D. Franco, W. Fulgione, A. Gallo Rosso, M. Galloway, F. Gao, M. Garbini, C. Geis, L. W. Goetzke, Z. Greene, C. Grignon, C. Hasterok, E. Hogenbirk, R. Itay, B. Kaminsky, G. Kessler, A. Kish, H. Landsman, R. F. Lang, D. Lellouch, L. Levinson, M. Le Calloch, C. Levy, Q. Lin, S. Lindemann, M. Lindner, J. A. M. Lopes, A. Manfredini, T. Marrodán Undagoitia, J. Masbou, F. V. Massoli, D. Masson, D. Mayani, Y. Meng, M. Messina, K. Micheneau, B. Miguez, A. Molinario, M. Murra, J. Naganoma, K. Ni, U. Oberlack, S. E. A. Orrigo, P. Pakarha, B. Pelssers, R. Persiani, F. Piastra, J. Pienaar, M.-C. Piro, G. Plante, N. Priel, L. Rauch, S. Reichard, C. Reuter, A. Rizzo, S. Rosendahl, N. Rupp, J. M. F. dos Santos, G. Sartorelli, M. Scheibelhut, S. Schindler, J. Schreiner, M. Schumann, L. Scotto Lavina, M. Selvi, P. Shagin, M. Silva, H. Simgen, M. v. Sivers, A. Stein, D. Thers, A. Tiseni, G. Trinchero, C. D. Tunnell, R. Wall, H. Wang, M. Weber, Y. Wei, C. Weinheimer, J. Wulf, and Y. Zhang. Xenon100 dark matter results from a combination of 477 live days. *Phys. Rev. D*, 94:122001, Dec 2016. doi: 10.1103/PhysRevD.94.122001. URL `https://link.aps.org/doi/10.1103/PhysRevD.94.122001`.

[44] R. Agnese, A. J. Anderson, T. Aralis, T. Aramaki, I. J. Arnquist, W. Baker, D. Balakishiyeva, D. Barker, R. Basu Thakur, D. A. Bauer, T. Binder, M. A. Bowles, P. L. Brink, R. Bunker, B. Cabrera, D. O. Caldwell, R. Calkins, C. Cartaro, D. G. Cerdeño, Y. Chang, H. Chagani, Y. Chen, J. Cooley, B. Cornell, P. Cushman, M. Daal, P. C. F. Di Stefano, T. Doughty, L. Esteban, E. Fascione, E. Figueroa-Feliciano, M. Fritts, G. Gerbier, M. Ghaith, G. L. Godfrey, S. R. Golwala, J. Hall, H. R. Harris, Z. Hong, E. W. Hoppe, L. Hsu, M. E. Huber, V. Iyer, D. Jardin, A. Jastram, C. Jena, M. H. Kelsey, A. Kennedy, A. Kubik, N. A. Kurinsky, A. Leder, B. Loer, E. Lopez Asamar, P. Lukens, D. MacDonell, R. Mahapatra, V. Mandic, N. Mast, E. H. Miller, N. Mirabolfathi, R. A. Moffatt, B. Mohanty, J. D. Morales Mendoza, J. Nelson, J. L. Orrell, S. M. Oser, K. Page, W. A. Page, R. Partridge, M. Pepin, M. Peñalver Martinez, A. Phipps, S. Poudel, M. Pyle, H. Qiu, W. Rau, P. Redl, A. Reisetter, T. Reynolds, A. Roberts, A. E. Robinson, H. E. Rogers, T. Saab, B. Sadoulet, J. Sander, K. Schneck, R. W. Schnee, S. Scorza, K. Senapati, B. Serfass,

D. Speller, M. Stein, J. Street, H. A. Tanaka, D. Toback, R. Underwood, A. N. Villano, B. von Krosigk, B. Welliver, J. S. Wilson, M. J. Wilson, D. H. Wright, S. Yellin, J. J. Yen, B. A. Young, X. Zhang, and X. Zhao. Low-mass dark matter search with cdmslite. *Phys. Rev. D*, 97:022002, Jan 2018. doi: 10.1103/PhysRevD.97.022002. URL https://link.aps.org/doi/10.1103/PhysRevD.97.022002.

[45] I. Alkhatib, D. W. P. Amaral, T. Aralis, T. Aramaki, I. J. Arnquist, I. Ataee Langroudy, E. Azadbakht, S. Banik, D. Barker, C. Bathurst, D. A. Bauer, L. V. S. Bezerra, R. Bhattacharyya, T. Binder, M. A. Bowles, P. L. Brink, R. Bunker, B. Cabrera, R. Calkins, R. A. Cameron, C. Cartaro, D. G. Cerdeño, Y.-Y. Chang, M. Chaudhuri, R. Chen, N. Chott, J. Cooley, H. Coombes, J. Corbett, P. Cushman, F. De Brienne, M. L. di Vacri, M. D. Diamond, E. Fascione, E. Figueroa-Feliciano, C. W. Fink, K. Fouts, M. Fritts, G. Gerbier, R. Germond, M. Ghaith, S. R. Golwala, H. R. Harris, N. Herbert, B. A. Hines, M. I. Hollister, Z. Hong, E. W. Hoppe, L. Hsu, M. E. Huber, V. Iyer, D. Jardin, A. Jastram, V. K. S. Kashyap, M. H. Kelsey, A. Kubik, N. A. Kurinsky, R. E. Lawrence, A. Li, B. Loer, E. Lopez Asamar, P. Lukens, D. MacDonell, D. B. MacFarlane, R. Mahapatra, V. Mandic, N. Mast, A. J. Mayer, H. Meyer zu Theenhausen, É. M. Michaud, E. Michielin, N. Mirabolfathi, B. Mohanty, J. D. Morales Mendoza, S. Nagorny, J. Nelson, H. Neog, V. Novati, J. L. Orrell, S. M. Oser, W. A. Page, P. Pakarha, R. Partridge, R. Podviianiuk, F. Ponce, S. Poudel, M. Pyle, W. Rau, E. Reid, R. Ren, T. Reynolds, A. Roberts, A. E. Robinson, T. Saab, B. Sadoulet, J. Sander, A. Sattari, R. W. Schnee, S. Scorza, B. Serfass, D. J. Sincavage, C. Stanford, J. Street, D. Toback, R. Underwood, S. Verma, A. N. Villano, B. von Krosigk, S. L. Watkins, L. Wills, J. S. Wilson, M. J. Wilson, J. Winchell, D. H. Wright, S. Yellin, B. A. Young, T. C. Yu, E. Zhang, H. G. Zhang, X. Zhao, L. Zheng, J. Camilleri, Yu. G. Kolomensky, and S. Zuber. Light dark matter search with a high-resolution athermal phonon detector operated above ground. *Phys. Rev. Lett.*, 127:061801, Aug 2021. doi: 10.1103/PhysRevLett.127.061801. URL https://link.aps.org/doi/10.1103/PhysRevLett.127.061801.

[46] M. F. Albakry, I. Alkhatib, D. Alonso, D. W. P. Amaral, T. Aralis, T. Aramaki, I. J. Arnquist, I. Ataee Langroudy, E. Azadbakht, S. Banik, C. Bathurst, R. Bhattacharyya, P. L. Brink, R. Bunker, B. Cabrera, R. Calkins, R. A. Cameron, C. Cartaro, D. G. Cerdeño, Y.-Y. Chang, M. Chaudhuri, R. Chen, N. Chott, J. Cooley, H. Coombes, J. Corbett, P. Cushman, S. Das, F. De Brienne, M. Rios, S. Dharani, M. L. di Vacri, M. D. Diamond, M. Elwan, E. Fascione, E. Figueroa-Feliciano, C. W. Fink, K. Fouts, M. Fritts, G. Gerbier, R. Germond, M. Ghaith, S. R. Golwala, J. Hall, S. A. S. Harms, N. Hassan, B. A. Hines, Z. Hong, E. W. Hoppe, L. Hsu, M. E. Huber, V. Iyer, V. K. S. Kashyap, M. H. Kelsey, A. Kubik, N. A. Kurinsky, M. Lee, M. Litke, J. Liu, Y. Liu, B. Loer, E. Lopez Asamar, P. Lukens, D. B. MacFarlane, R. Mahapatra, N. Mast, A. J. Mayer, H. Meyer zu Theenhausen, É. Michaud, E. Michielin, N. Mirabolfathi, B. Mohanty, B. Nebolsky, J. Nelson, H. Neog, V. Novati, J. L. Orrell, M. D. Osborne, S. M. Oser, W. A. Page, L. Pandey, S. Pandey, R. Par-

tridge, D. S. Pedreros, L. Perna, R. Podviianiuk, F. Ponce, S. Poudel, A. Pradeep, M. Pyle, W. Rau, E. Reid, R. Ren, T. Reynolds, E. Tanner, A. Roberts, A. E. Robinson, T. Saab, D. Sadek, B. Sadoulet, S. P. Sahoo, I. Saikia, J. Sander, A. Sattari, B. Schmidt, R. W. Schnee, S. Scorza, B. Serfass, S. S. Poudel, D. J. Sincavage, P. Sinervo, Z. Speaks, J. Street, H. Sun, G. D. Terry, F. K. Thasrawala, D. Toback, R. Underwood, S. Verma, A. N. Villano, B. von Krosigk, S. L. Watkins, O. Wen, Z. Williams, M. J. Wilson, J. Winchell, K. Wykoff, S. Yellin, B. A. Young, T. C. Yu, B. Zatschler, S. Zatschler, A. Zaytsev, A. Zeolla, E. Zhang, L. Zheng, Y. Zheng, A. Zuniga, P. An, P. S. Barbeau, S. C. Hedges, L. Li, and J. Runge. First measurement of the nuclear-recoil ionization yield in silicon at 100 ev. *Phys. Rev. Lett.*, 131:091801, Aug 2023. doi: 10.1103/PhysRevLett.131.091801. URL `https://link.aps.org/doi/10.1103/PhysRevLett.131.091801`.

[47] M. F. Albakry, I. Alkhatib, D. Alonso-González, D. W. P. Amaral, T. Aralis, T. Aramaki, I. J. Arnquist, I. Ataee Langroudy, E. Azadbakht, S. Banik, C. Bathurst, R. Bhattacharyya, P. L. Brink, R. Bunker, B. Cabrera, R. Calkins, R. A. Cameron, C. Cartaro, D. G. Cerdeño, Y.-Y. Chang, M. Chaudhuri, R. Chen, N. Chott, J. Cooley, H. Coombes, J. Corbett, P. Cushman, S. Das, F. De Brienne, M. Rios, S. Dharani, M. L. di Vacri, M. D. Diamond, M. Elwan, E. Fascione, E. Figueroa-Feliciano, C. W. Fink, K. Fouts, M. Fritts, G. Gerbier, R. Germond, M. Ghaith, S. R. Golwala, J. Hall, N. Hassan, B. A. Hines, Z. Hong, E. W. Hoppe, L. Hsu, M. E. Huber, V. Iyer, D. Jardin, V. K. S. Kashyap, M. H. Kelsey, A. Kubik, N. A. Kurinsky, M. Lee, A. Li, M. Litke, J. Liu, Y. Liu, B. Loer, E. Lopez Asamar, P. Lukens, D. B. MacFarlane, R. Mahapatra, J. S. Mammo, N. Mast, A. J. Mayer, H. Meyer zu Theenhausen, É. Michaud, E. Michielin, N. Mirabolfathi, B. Mohanty, J. Nelson, H. Neog, V. Novati, J. L. Orrell, M. D. Osborne, S. M. Oser, W. A. Page, L. Pandey, S. Pandey, R. Partridge, D. S. Pedreros, L. Perna, R. Podviianiuk, F. Ponce, S. Poudel, A. Pradeep, M. Pyle, W. Rau, E. Reid, R. Ren, T. Reynolds, A. Roberts, A. E. Robinson, T. Saab, D. Sadek, B. Sadoulet, I. Saikia, J. Sander, A. Sattari, B. Schmidt, R. W. Schnee, S. Scorza, B. Serfass, S. S. Poudel, D. J. Sincavage, P. Sinervo, J. Street, H. Sun, G. D. Terry, F. K. Thasrawala, D. Toback, R. Underwood, S. Verma, A. N. Villano, B. von Krosigk, S. L. Watkins, O. Wen, Z. Williams, M. J. Wilson, J. Winchell, C.-P. Wu, K. Wykoff, S. Yellin, B. A. Young, T. C. Yu, B. Zatschler, S. Zatschler, A. Zaytsev, E. Zhang, L. Zheng, and A. Zuniga. Search for low-mass dark matter via bremsstrahlung radiation and the migdal effect in supercdms. *Phys. Rev. D*, 107:112013, Jun 2023. doi: 10.1103/PhysRevD.107.112013. URL `https://link.aps.org/doi/10.1103/PhysRevD.107.112013`.

[48] Itay M. Bloch, Rouven Essig, Kohsaku Tobioka, Tomer Volansky, and Tien-Tien Yu. Searching for dark absorption with direct detection experiments. *Journal of High Energy Physics*, 2017(6):87, Jun 2017. ISSN 1029-8479. doi: 10.1007/JHEP06(2017)087. URL `https://doi.org/10.1007/JHEP06(2017)087`.

[49] Andrea Mitridate, Tanner Trickle, Zhengkang Zhang, and Kathryn M. Zurek. Dark matter absorption via electronic excitations. *Journal of High Energy Physics*, 2021 (9):123, Sep 2021. ISSN 1029-8479. doi: 10.1007/JHEP09(2021)123. URL https://doi.org/10.1007/JHEP09(2021)123.

[50] Francis Froborg and Alan R Duffy. Annual modulation in direct dark matter searches. *Journal of Physics G: Nuclear and Particle Physics*, 47(9):094002, jul 2020. doi: 10.1088/1361-6471/ab8e93. URL https://dx.doi.org/10.1088/1361-6471/ab8e93.

[51] Chris Kouvaris and Niklas G. Nielsen. Daily modulation and gravitational focusing in direct dark matter search experiments. *Phys. Rev. D*, 92:075016, Oct 2015. doi: 10.1103/PhysRevD.92.075016. URL https://link.aps.org/doi/10.1103/PhysRevD.92.075016.

[52] Y. Hochberg, M. Pyle, and et al Y. Zhao. Detecting superlight dark matter with fermi-degenerate materials. *Journal of High Energy Physics*, 57, 2016. URL https://doi.org/10.1007/JHEP08(2016)057.

[53] Rouven Essig, Jesús Pérez-Ríos, Harikrishnan Ramani, and Oren Slone. Direct detection of nuclear scattering of sub-gev dark matter using molecular excitations. *Phys. Rev. Research*, 1, 2019. URL https://link.aps.org/doi/10.1103/PhysRevResearch.1.033105.

[54] G. Cavoto, F. Luchetta, and A.D. Polosa. Sub-gev dark matter detection with electron recoils in carbon nanotubes. *Physics Letters B*, 776:338–344, 2018. URL https://www.sciencedirect.com/science/article/pii/S0370269317309565.

[55] Yonit Hochberg, Yonatan Kahn, Mariangela Lisanti, Christopher G. Tully, and Kathryn M. Zurek. Directional detection of dark matter with two-dimensional targets. *Physics Letters B*, 772:239–246, 2017. URL https://www.sciencedirect.com/science/article/pii/S0370269317305270.

[56] Ilya Charaev Jeff Chiles Marco Colangelo Sae Woo Nam Karl K. Berggren Yonit Hochberg, Benjamin V. Lehmann. New constraints on dark matter from superconducting nanowires. *arXiv*, High Energy Physics - Phenomenology, 2021. URL https://doi.org/10.48550/arXiv.2110.01586.

[57] Carlos Blanco, Rouven Essig, Marivi Fernandez-Serra, Harikrishnan Ramani, and Oren Slone. Dark matter direct detection with quantum dots. *Phys. Rev. D*, 107:095035, May 2023. doi: 10.1103/PhysRevD.107.095035. URL https://link.aps.org/doi/10.1103/PhysRevD.107.095035.

[58] R. Essig. The low-mass dark matter frontier. *Physics*, 13, 2020. URL https://physics.aps.org/articles/v13/172.

[59] Stephen Derenzo, Rouven Essig, Andrea Massari, Adrián Soto, and Tien-Tien Yu. Direct detection of sub-gev dark matter with scintillating targets. *Phys. Rev. D*, 96: 016026, Jul 2017. doi: 10.1103/PhysRevD.96.016026. URL https://link.aps.org/doi/10.1103/PhysRevD.96.016026.

[60] S. Derenzo, E. Bourret, S. Hanrahan, , and G. Bizarri. Cryogenic scintillation properties of n-type gaas for the direct detection of mev/c2 dark matter. *Journal of Applied Physics*, 123, 2018. URL https://doi.org/10.1063/1.5018343.

[61] Stephen Derenzo, Rouven Essig, Andrea Massari, Adrián Soto, and Tien-Tien Yu. Direct detection of sub-gev dark matter with scintillating targets. *Phys. Rev. D*, 96, 2017. URL https://link.aps.org/doi/10.1103/PhysRevD.96.016026.

[62] S. Vasiukov, F. Chiossi, C. Braggio, G. Carugno, F. Moretti, E. Bourret, and S. Derenzo. Gaas as a bright cryogenic scintillator for the detection of low-energy electron recoils from mev/c2 dark matter. *IEEE Transactions on Nuclear Science*, 66(11):2333–2337, 2019. doi: 10.1109/TNS.2019.2946725.

[63] S. Derenzo, E. Bourret, S. Hanrahan, , and G. Bizarri. Cryogenic scintillation properties of n-type gaas for the direct detection of mev/c^2 dark matter. *Journal of Applied Physics*, 123(114501), 2018. doi: 10.1063/1.5018343.

[64] S. Derenzo, E. Bourret, C. Frank-Rotsch, S. Hanrahan, and M. Garcia-Sciveres. How silicon and boron dopants govern the cryogenic scintillation properties of n-type gaas. *Nuclear Instruments and Methods in Physics Research Section A: Accelerators, Spectrometers, Detectors and Associated Equipment*, 989:164957, 2021. ISSN 0168-9002. doi: https://doi.org/10.1016/j.nima.2020.164957. URL http://www.sciencedirect.com/science/article/pii/S0168900220313541.

[65] M. Benzaquen, D. Walsh, and K. Mazuruk. Conductivity of n-type gaas near the mott transition. *Phys. Rev. B*, 36:4748–4753, 1987. doi: 10.1103/PhysRevB.36.4748. URL https://link.aps.org/doi/10.1103/PhysRevB.36.4748.

[66] Rouven Essig, Aaron Manalaysay, Jeremy Mardon, Peter Sorensen, and Tomer Volansky. First Direct Detection Limits on Sub-Gev Dark Matter from Xenon10. *Phys. Rev. Lett.*, 109:021301, 2012. doi: 10.1103/PhysRevLett.109.021301.

[67] Rouven Essig, Tomer Volansky, and Tien-Tien Yu. New Constraints and Prospects for Sub-Gev Dark Matter Scattering Off Electrons in Xenon. *Phys. Rev.*, D96(4): 043017, 2017. doi: 10.1103/PhysRevD.96.043017.

[68] J. Angle et al. A Search for Light Dark Matter in Xenon10 Data. *Phys. Rev. Lett.*, 107:051301, 2011. doi: 10.1103/PhysRevLett.110.249901,10.1103/PhysRevLett.107.051301. [Erratum: Phys. Rev. Lett.110,249901(2013)].

[69] E. Aprile et al. Low-Mass Dark Matter Search Using Ionization Signals in Xenon100. *Phys. Rev.*, D94(9):092001, 2016. doi: 10.1103/PhysRevD.94.092001, 10.1103/PhysRevD.95.059901. [Erratum: Phys. Rev.D95,no.5,059901(2017)].

[70] P. Agnes et al. Constraints on Sub-GeV Dark-Matter Electron Scattering from the DarkSide-50 Experiment. *Phys. Rev. Lett.*, 121(11):111303, 2018. doi: 10.1103/PhysRevLett.121.111303.

[71] R. Agnese et al. First Dark Matter Constraints from a Supercdms Single-Charge Sensitive Detector. *Phys. Rev. Lett.*, 121(5):051301, 2018. doi: 10.1103/PhysRevLett.121.051301.

[72] Michael Crisler, Rouven Essig, Juan Estrada, Guillermo Fernandez, Javier Tiffenberg, Miguel Sofo haro, Tomer Volansky, and Tien-Tien Yu. Sensei: First Direct-Detection Constraints on Sub-Gev Dark Matter from a Surface Run. *Phys. Rev. Lett.*, 121(6):061803, 2018. doi: 10.1103/PhysRevLett.121.061803.

[73] Liron Barak, Itay M. Bloch, Mariano Cababie, Gustavo Cancelo, Luke Chaplinsky, Fernando Chierchie, Michael Crisler, Alex Drlica-Wagner, Rouven Essig, Juan Estrada, Erez Etzion, Guillermo Fernandez Moroni, Daniel Gift, Sravan Munagavalasa, Aviv Orly, Dario Rodrigues, Aman Singal, Miguel Sofo Haro, Leandro Stefanazzi, Javier Tiffenberg, Sho Uemura, Tomer Volansky, and Tien-Tien Yu. Sensei: Direct-detection results on sub-gev dark matter from a new skipper ccd. *Phys. Rev. Lett.*, 125:171802, Oct 2020. doi: 10.1103/PhysRevLett.125.171802. URL `https://link.aps.org/doi/10.1103/PhysRevLett.125.171802`.

[74] Q. Arnaud, E. Armengaud, C. Augier, A. Benoît, L. Bergé, J. Billard, A. Broniatowski, P. Camus, A. Cazes, M. Chapellier, F. Charlieux, M. De Jésus, L. Dumoulin, K. Eitel, E. Elkhoury, J.-B. Fillipini, D. Filosofov, J. Gascon, A. Giuliani, M. Gros, Y. Jin, A. Juillard, M. Kleifges, H. Lattaud, S. Marnieros, D. Misiak, X.-F. Navick, C. Nones, E. Olivieri, C. Oriol, P. Pari, B. Paul, D. Poda, S. Rozov, T. Salagnac, V. Sanglard, B. Siebenborn, L. Vagneron, M. Weber, E. Yakushev, and A. Zolotarova. First germanium-based constraints on sub-mev dark matter with the edelweiss experiment. *Phys. Rev. Lett.*, 125:141301, Oct 2020. doi: 10.1103/PhysRevLett.125.141301. URL `https://link.aps.org/doi/10.1103/PhysRevLett.125.141301`.

[75] D. W. Amaral, T. Aralis, T. Aramaki, I. J. Arnquist, E. Azadbakht, S. Banik, D. Barker, C. Bathurst, D. A. Bauer, L. V. S. Bezerra, R. Bhattacharyya, T. Binder, M. A. Bowles, P. L. Brink, R. Bunker, B. Cabrera, R. Calkins, R. A. Cameron, C. Cartaro, D. G. Cerdeño, Y.-Y. Chang, R. Chen, N. Chott, J. Cooley, H. Coombes, J. Corbett, P. Cushman, F. De Brienne, M. L. di Vacri, M. D. Diamond, E. Fascione, E. Figueroa-Feliciano, C. W. Fink, K. Fouts, M. Fritts, G. Gerbier, R. Germond, M. Ghaith, S. R. Golwala, H. R. Harris, N. Herbert, B. A. Hines, M. I. Hollister,

Z. Hong, E. W. Hoppe, L. Hsu, M. E. Huber, V. Iyer, D. Jardin, A. Jastram, M. H. Kelsey, A. Kubik, N. A. Kurinsky, R. E. Lawrence, A. Li, B. Loer, E. Lopez Asamar, P. Lukens, D. MacDonell, D. B. MacFarlane, R. Mahapatra, V. Mandic, N. Mast, A. J. Mayer, É. M. Michaud, E. Michielin, N. Mirabolfathi, B. Mohanty, J. D. Morales Mendoza, S. Nagorny, J. Nelson, H. Neog, V. Novati, J. L. Orrell, S. M. Oser, W. A. Page, P. Pakarha, R. Partridge, R. Podviianiuk, F. Ponce, S. Poudel, M. Pyle, W. Rau, E. Reid, R. Ren, T. Reynolds, A. Roberts, A. E. Robinson, H. E. Rogers, T. Saab, B. Sadoulet, J. Sander, A. Sattari, R. W. Schnee, S. Scorza, B. Serfass, D. J. Sincavage, C. Stanford, M. Stein, J. Street, D. Toback, R. Underwood, S. Verma, A. N. Villano, B. von Krosigk, S. L. Watkins, L. Wills, J. S. Wilson, M. J. Wilson, J. Winchell, D. H. Wright, S. Yellin, B. A. Young, T. C. Yu, E. Zhang, H. G. Zhang, X. Zhao, and L. Zheng. Constraints on low-mass, relic dark matter candidates from a surface-operated supercdms single-charge sensitive detector. *Phys. Rev. D*, 102:091101, Nov 2020. doi: 10.1103/PhysRevD.102.091101. URL https://link.aps.org/doi/10.1103/PhysRevD.102.091101.

[76] Report of the Workshop "Basic Research Needs for Dark Matter Small Projects New Initiatives" (October 2018) is available online at: https://science.osti.gov/-/media/hep/pdf/Reports/Dark_Matter_New_Initiatives_rpt.pdf.

[77] J. Billard, J. Gascon, S. Marnieros, and S. Scorza. Transition edge sensors with sub-ev resolution and cryogenic targets (tesseract) at the underground laboratory of modane (lsm). *Nuclear Physics B*, 1003:116465, 2024. ISSN 0550-3213. doi: https://doi.org/10.1016/j.nuclphysb.2024.116465. URL https://www.sciencedirect.com/science/article/pii/S0550321324000312. Special Issue of Nobel Symposium 182 on Dark Matter.

[78] Matti Heikinheimo, Sebastian Sassi, Kai Nordlund, Kimmo Tuominen, and Nader Mirabolfathi. Identification of the low-energy excess in dark matter searches with crystal defects. *Phys. Rev. D*, 106:083009, Oct 2022. doi: 10.1103/PhysRevD.106.083009. URL https://link.aps.org/doi/10.1103/PhysRevD.106.083009.

[79] G. Angloher, S. Banik, G. Benato, A. Bento, A. Bertolini, R. Breier, C. Bucci, L. Canonica, A. D'Addabbo, S. Di Lorenzo, L. Einfalt, A. Erb, F. von Feilitzsch, N. Ferreiro Iachellini, S. Fichtinger, D. Fuchs, A. Fuss, A. Garai, V. M. Ghete, S. Gerster, P. Gorla, P. V. Guillaumon, S. Gupta, D. Hauff, M. Ješkovský, J. Jochum, M. Kaznacheeva, A. Kinast, H. Kluck, H. Kraus, A. Langenkämper, M. Mancuso, L. Marini, L. Meyer, V. Mokina, A. Nilima, M. Olmi, T. Ortmann, C. Pagliarone, L. Pattavina, F. Petricca, W. Potzel, P. Povinec, F. Pröbst, F. Pucci, F. Reindl, J. Rothe, K. Schäffner, J. Schieck, D. Schmiedmayer, S. Schönert, C. Schwertner, M. Stahlberg, L. Stodolsky, C. Strandhagen, R. Strauss, I. Usherov, F. Wagner, M. Willers, and V. Zema. Latest observations on the low energy excess in CRESST-III. *SciPost Phys. Proc.*, page 013, 2023. doi: 10.21468/SciPostPhysProc.12.013. URL https://scipost.org/10.21468/SciPostPhysProc.12.013.

[80] P. Adari, A. Aguilar-Arevalo, D. Amidei, G. Angloher, E. Armengaud, C. Augier, L. Balogh, S. Banik, D. Baxter, C. Beaufort, G. Beaulieu, V. Belov, Y. Ben Gal, G. Benato, A. Benoît, A. Bento, L. Bergé, A. Bertolini, R. Bhattacharyya, J. Billard, I.M. Bloch, A. Botti, R. Breier, G. Bres, J-.L. Bret, A. Broniatowski, A. Brossard, C. Bucci, R. Bunker, M. Cababie, M. Calvo, P. Camus, G. Cancelo, L. Canonica, F. Cappella, L. Cardani, J.-F. Caron, N. Casali, G.del Castello, A. Cazes, R. Cerulli, B.A. Cervantes Vergara, D. Chaize, M. Chapellier, L. Chaplinsky, F. Charlieux, M. Chaudhuri, A.E. Chavarria, G. Chemin, R. Chen, H. Chen, F. Chierchie, I. Colantoni, J. Colas, J. Cooley, J.-M. Coquillat, E.C. Corcoran, S. Crawford, M. Crisler, A. Cruciani, P. Cushman, A. D'Addabbo, J.C. D'Olivo, A. Dastgheibi-Fard, M. De Jésus, Y. Deng, J.B. Dent, E.L. Depaoli, K. Dering, S. Dharani, S. Di Lorenzo, A. Drlica-Wagner, L. Dumoulin, D. Durnford, B. Dutta, L. Einfalt, A. Erb, A. Erhart, R. Essig, J. Estrada, E. Etzion, O. Exshaw, F. Favela-Perez, F. v. Feilitzsch, G. Fernandez Moroni, N. Ferreiro Iachellini, S. Ferriol, S. Fichtinger, E. Figueroa-Feliciano, J.-B. Filippini, D. Filosofov, J. A. Formaggio, M. Friedl, S. Fuard, D. Fuchs, A. Fuss, R. Gaïor, A. Garai, C. Garrah, J. Gascon, G. Gerbier, M. Ghaith, V.M. Ghete, D. Gift, I. Giomataris, G. Giroux, A. Giuliani, P. Gorel, P. Gorla, C. Goupy, J. Goupy, C. Goy, M. Gros, P. Gros, Y. Guardincerri, C. Guerin, V. Guidi, O. Guillaudin, S. Gupta, E. Guy, P. Harrington, D. Hauff, S. T. Heine, S. A. Hertel, S.E. Holland, Z. Hong, E.W. Hoppe, T.W. Hossbach, J.-C. Ianigro, V. Iyer, A. Jastram, M. Ješkovský, Y. Jin, J. Jochum, J. P. Johnston, A. Juillard, D. Karaivanov, V. Kashyap, I. Katsioulas, S. Kazarcev, M. Kaznacheeva, F. Kelly, B. Kilminster, A. Kinast, L. Klinkenberg, H. Kluck, P. Knights, Y. Korn, H. Kraus, B. von Krosigk, A. Kubik, N.A. Kurinsky, J. Lamblin, A. Langenkämper, S. Langrock, T. Lasserre, H. Lattaud, P. Lautridou, I. Lawson, S.J. Lee, M. Lee, A. Letessier-Selvon, D. Lhuillier, M. Li, Y.-T. Lin, A. Lubashevskiy, R. Mahapatra, S. Maludze, M. Mancuso, I. Manthos, L. Marini, S. Marnieros, R.D. Martin, A. Matalon, J. Matthews, B. Mauri, D. W. Mayer, A. Mazzolari, E. Mazzucato, H. Meyer zu Theenhausen, E. Michielin, J. Minet, N. Mirabolfathi, K. v. Mirbach, D. Misiak, P. Mitra, J-.L. Mocellin, B. Mohanty, V. Mokina, J.-P. Mols, A. Monfardini, F. Mounier, S. Munagavalasa, J.-F. Muraz, X.-F. Navick, T. Neep, H. Neog, H. Neyrial, K. Nikolopoulos, A. Nilima, C. Nones, V. Novati, P. O'Brien, L. Oberauer, E. Olivieri, M. Olmi, A. Onillon, C. Oriol, A. Orly, J.L. Orrell, T. Ortmann, C.T. Overman, C. Pagliarone, V. Palušová, P. Pari, P. K. Patel, L. Pattavina, F. Petricca, A. Piers, H. D. Pinckney, M.-C. Piro, M. Platt, D. Poda, D. Ponomarev, W. Potzel, P. Povinec, F. Pröbst, P. Privitera, F. Pucci, K. Ramanathan, J.-S. Real, T. Redon, F. Reindl, R. Ren, A. Robert, J.Da Rocha, D. Rodrigues, R. Rogly, J. Rothe, N. Rowe, S. Rozov, I. Rozova, T. Saab, N. Saffold, T. Salagnac, J. Sander, V. Sanglard, D. Santos, Y. Sarkis, V. Savu, G. Savvidis, I. Savvidis, S. Schönert, K. Schäffner, N. Schermer, J. Schieck, B. Schmidt, D. Schmiedmayer, C. Schwertner, L. Scola, M. Settimo, Ye. Shevchik, V. Sibille, I. Sidelnik, A. Singal, R. Smida, M. Sofo Haro, T. Soldner, J. Stachurska, M. Stahlberg, L. Stefanazzi, L. Stodolsky, C. Strandhagen, R. Strauss,

A. Stutz, R. Thomas, A. Thompson, J. Tiffenberg, C. Tomei, M. Traina, S. Uemura, I. Usherov, L. Vagneron, W. Van De Pontseele, F.A. Vazquez de Sola Fernandez, M. Vidal, M. Vignati, A.L. Virto, M. Vivier, T. Volansky, V. Wagner, F. Wagner, J. Walker, R. Ward, S.L. Watkins, A. Wex, M. Willers, M.J. Wilson, L. Winslow, E. Yakushev, T.-T. Yu, M. Zampaolo, A. Zaytsev, V. Zema, D. Zinatulina, and A. Zolotarova. EXCESS workshop: Descriptions of rising low-energy spectra. *SciPost Phys. Proc.*, page 001, 2022. doi: 10.21468/SciPostPhysProc.9.001. URL https://scipost.org/10.21468/SciPostPhysProc.9.001.

[81] Roger K. Romani. Aluminum relaxation as the source of excess low energy events in low threshold calorimeters. *Journal of Applied Physics*, 136(12):124502, 09 2024. ISSN 0021-8979. doi: 10.1063/5.0222654. URL https://doi.org/10.1063/5.0222654.

[82] Robin Anthony-Petersen, Clarence L. Chang, Yen-Yung Chang, Luke Chaplinsky, Caleb W. Fink, Maurice Garcia-Sciveres, Wei Guo, Scott A. Hertel, Xinran Li, Junsong Lin, Marharyta Lisovenko, Rupak Mahapatra, William Matava, Daniel N. McKinsey, David Z. Osterman, Pratyush K. Patel, Bjoern Penning, Mark Platt, Matt Pyle, Yinghe Qi, Maggie Reed, Ivar Rydstrom, Roger K. Romani, Bernard Sadoulet, Bruno Serfass, Peter Sorensen, Burkhant Suerfu, Vetri Velan, Gensheng Wang, Yue Wang, Samuel L. Watkins, and Michael R. Williams. Low energy backgrounds and excess noise in a two-channel low-threshold calorimeter. *arXiv preprint arXiv:2410.16510*, 2024. URL https://arxiv.org/abs/2410.16510.

[83] O. Okunev G. N. Gol'tsman, G. Chulkova, A. Lipatov, A. Semenov, K.Smirnov, B. Voronov, A. Dzardanov, C. Williams, and R. Sobolewski. Picosecond superconducting single-photon optical detector. *Applied Physics Letters*, 79(6), 2001. doi: 10.1063/1.1388868. URL https://doi.org/10.1063/1.1388868.

[84] Dileep V. Reddy, Robert R. Nerem, Sae Woo Nam, Richard P. Mirin, and Varun B. Verma. Superconducting nanowire single-photon detectors with 98% system detection efficiency at 1550 nm. *Optica*, 7(12):1649–1653, 2020. doi: 10.1364/OPTICA.400751. URL https://doi.org/10.1364/OPTICA.400751.

[85] Boris Korzh, Qing-Yuan Zhao, Jason P. Allmaras, Simone Frasca, Travis M. Autry, Eric A. Bersin, Andrew D. Beyer, Ryan M. Briggs, Bruce Bumble, Marco Colangelo, Garrison M. Crouch, Andrew E. Dane, Thomas Gerrits, Adriana E. Lita, Francesco Marsili, Galan Moody, Cristián Peña, Edward Ramirez, Jake D. Rezac, Neil Sinclair, Martin J. Stevens, Angel E. Velasco, Varun B. Verma, Emma E. Wollman, Si Xie, Di Zhu, Paul D. Hale, Maria Spiropulu, Kevin L. Silverman, Richard P. Mirin, Sae Woo Nam, Alexander G. Kozorezov, Matthew D. Shaw, and Karl K. Berggren. Demonstration of sub-3 ps temporal resolution with a superconducting nanowire single-photon detector. *Nature Photonics*, 14:250–255, 2020. doi: 10.1109/TNS.2019.2946725.

[86] Jeff Chiles, Ilya Charaev, Robert Lasenby, Masha Baryakhtar, Alexana Roshko Junwu Huang, George Burton, Marco Colangelo, Ken Van Tilburg, Asimina Arvanitaki, Sae Woo Nam, and Karl K. Berggren. New constraints on dark photon dark matter with superconducting nanowire detectors in an optical haloscope. *arXiv*, High Energy Physics - Experiment:1145411, 2020. URL https://doi.org/10.48550/arXiv.2110.01582.

[87] Gregor G. Taylor, Alexander B. Walter, Boris Korzh, Bruce Bumble, Sahil R. Patel, Jason P. Allmaras, Andrew D. Beyer, Roger O'Brient, Matthew D. Shaw, and Emma E. Wollman. Low-noise single-photon counting superconducting nanowire detectors at infrared wavelengths up to 29 μm. *Optica*, 10(12):1672–1678, Dec 2023. doi: 10.1364/OPTICA.509337. URL https://opg.optica.org/optica/abstract.cfm?URI=optica-10-12-1672.

[88] S. Khasminskaya, F. Pyatkov, K. Słowik, S. Ferrari, O. Kahl, V. Kovalyuk, P. Rath, A. Vetter, F. Hennrich, M. M. Kappes, G. Gol'tsman, A. Korneev, C. Rockstuhl, R. Krupke, and W. H. P. Pernice. Fully integrated quantum photonic circuit with an electrically driven light source. *Nature Photonics*, 10:727–732, 2016. doi: 10.1038/nphoton.2016.178. URL https://www.nature.com/articles/nphoton.2016.178.

[89] L. Elsinger, R. Gourgues, I. E. Zadeh, J. Maes, A. Guardiani, G. Bulgarini, S. F. Pereira, S. N. Dorenbos, V. Zwiller, Z. Hens, and D. Van Thourhout. Integration of colloidal pbs/cds quantum dots with plasmonic antennas and superconducting detectors on a silicon nitride photonic platform. *Nature Photonics*, 19:5452–5458, 2019. doi: 10.1021/acs.nanolett.9b01948. URL https://doi.org/10.1021/acs.nanolett.9b01948.

[90] Alberto Boaron, Gianluca Boso, Davide Rusca, Cédric Vulliez, Claire Autebert, Misael Caloz, Matthieu Perrenoud, Gaëtan Gras, Félix Bussières, Ming-Jun Li, Daniel Nolan, Anthony Martin, and Hugo Zbinden. Secure quantum key distribution over 421 km of optical fiber. *Phys. Rev. Lett.*, 121, 2018. doi: 10.1103/PhysRevLett.121.190502. URL https://link.aps.org/doi/10.1103/PhysRevLett.121.190502.

[91] Y. Yu, Ma F., and Luo XY et al. Entanglement of two quantum memories via fibres over dozens of kilometres. *Nature*, 578:240–245, 2020. doi: 10.1038/s41586-020-1976-7. URL https://doi.org/10.1038/s41586-020-1976-7.

[92] Jiu-Peng Chen, Chi Zhang, Yang Liu, Cong Jiang, Weijun Zhang, Xiao-Long Hu, Jian-Yu Guan, Zong-Wen Yu, Hai Xu, Jin Lin, Ming-Jun Li, Hao Chen, Hao Li, Lixing You, Zhen Wang, Xiang-Bin Wang, Qiang Zhang, and Jian-Wei Pan. Sending-or-not-sending with independent lasers: Secure twin-field quantum key distribution over 509 km. *Phys. Rev. Lett.*, 124:070501, Feb 2020. doi:

10.1103/PhysRevLett.124.070501. URL https://link.aps.org/doi/10.1103/PhysRevLett.124.070501.

[93] Raju Valivarthi, Samantha I. Davis, Cristián Peña, Si Xie, Nikolai Lauk, Lautaro Narváez, Jason P. Allmaras, Andrew D. Beyer, Yewon Gim, Meraj Hussein, George Iskander, Hyunseong Linus Kim, Boris Korzh, Andrew Mueller, Mandy Rominsky, Matthew Shaw, Dawn Tang, Emma E. Wollman, Christoph Simon, Panagiotis Spentzouris, Daniel Oblak, Neil Sinclair, and Maria Spiropulu. Teleportation systems toward a quantum internet. *PRX Quantum*, 1:020317, Dec 2020. doi: 10.1103/PRXQuantum.1.020317. URL https://link.aps.org/doi/10.1103/PRXQuantum.1.020317.

[94] Lynden K. Shalm, Evan Meyer-Scott, Bradley G. Christensen, Peter Bierhorst, Michael A. Wayne, Martin J. Stevens, Thomas Gerrits, Scott Glancy, Deny R. Hamel, Michael S. Allman, Kevin J. Coakley, Shellee D. Dyer, Carson Hodge, Adriana E. Lita, Varun B. Verma, Camilla Lambrocco, Edward Tortorici, Alan L. Migdall, Yanbao Zhang, Daniel R. Kumor, William H. Farr, Francesco Marsili, Matthew D. Shaw, Jeffrey A. Stern, Carlos Abellán, Waldimar Amaya, Valerio Pruneri, Thomas Jennewein, Morgan W. Mitchell, Paul G. Kwiat, Joshua C. Bienfang, Richard P. Mirin, Emanuel Knill, and Sae Woo Nam. Strong loophole-free test of local realism. *Phys. Rev. Lett.*, 115:250402, Dec 2015. doi: 10.1103/PhysRevLett.115.250402. URL https://link.aps.org/doi/10.1103/PhysRevLett.115.250402.

[95] Lixing You. Superconducting nanowire single-photon detectors for quantum information. *Nanophotonics*, 9(9):2673–2692, 2020. doi: doi:10.1515/nanoph-2020-0186. URL https://doi.org/10.1515/nanoph-2020-0186.

[96] A. N. McCaughan, Y. Zhai, B. Korzh, J. P. Allmaras, B. G. Oripov, M. D. Shaw, and S. W. Nam. The thermally coupled imager: A scalable readout architecture for superconducting nanowire single photon detectors. *Applied Physics Letters*, 121 (10):102602, 09 2022. ISSN 0003-6951. doi: 10.1063/5.0102154. URL https://doi.org/10.1063/5.0102154.

[97] Jason P. Allmaras, Emma E. Wollman, Andrew D. Beyer, Ryan M. Briggs, Boris A. Korzh, Bruce Bumble, and Matthew D. Shaw. Demonstration of a thermally coupled row-column snspd imaging array. *Nano Letters*, 20(3):2163–2168, Mar 2020. ISSN 1530-6984. doi: 10.1021/acs.nanolett.0c00246. URL https://doi.org/10.1021/acs.nanolett.0c00246.

[98] Matthew Shaw. Superconducting nanowire single photon detectors for optical communication and astronomy. *Proc. SPIE 11454, X-Ray, Optical, and Infrared Detectors for Astronomy*, IX:1145411, 2020. doi: 10.1117/12.2563483. URL https://doi.org/10.1117/12.2563483.

[99] Emma E. Wollman, Varun B. Verma, Alexander B. Walter, Jeff Chiles, Boris Korzh, Jason P. Allmaras, Yao Zhai, Adriana E. Lita, Adam N. McCaughan, Ekkehart Schmidt, Simone Frasca, Richard P. Mirin, Sae-Woo Nam, and Matthew D. Shaw. Recent advances in superconducting nanowire single-photon detector technology for exoplanet transit spectroscopy in the mid-infrared. *Journal of Astronomical Telescopes, Instruments, and Systems*, 7, 2021. URL https://doi.org/10.1117/1.JATIS.7.1.011004.

[100] Iman Esmaeil Zadeh, J. Chang, Johannes W. N. Los, Samuel Gyger, Ali W. Elshaari, Stephan Steinhauer, Sander N. Dorenbos, and Val Zwiller. Superconducting nanowire single-photon detectors: A perspective on evolution, state-of-the-art, future developments, and applications. *Applied Physics Letters*, 118(19):056101, 2021. doi: 10.1063/5.0045990. URL https://doi.org/10.1063/5.0045990.

[101] Emma E. Wollman, Varun B. Verma, Adriana E. Lita, William H. Farr, Matthew D. Shaw, Richard P. Mirin, and Sae Woo Nam. Kilopixel array of superconducting nanowire single-photon detectors. *Optics Express*, 27(24), 2019. URL http://opg.optica.org/oe/abstract.cfm?URI=oe-27-24-35279.

[102] B. G. Oripov, D. S. Rampini, J. Allmaras, M. D. Shaw, S. W. Nam, B. Korzh, and A. N. McCaughan. A superconducting nanowire single-photon camera with 400,000 pixels. *Nature*, 622(7984):730–734, Oct 2023. ISSN 1476-4687. doi: 10.1038/s41586-023-06550-2. URL https://doi.org/10.1038/s41586-023-06550-2.

[103] M. S. Allman, V. B. Verma, M. Stevens, T. Gerrits, R. D. Horansky, A. E. Lita, F. Marsili, A. Beyer, M. D. Shaw, D. Kumor, R. Mirin, and S. W. Nam. A near-infrared 64-pixel superconducting nanowire single photon detector array with integrated multiplexed readout. *Applied Physics Letters*, 106(19):192601, 05 2015. ISSN 0003-6951. doi: 10.1063/1.4921318. URL https://doi.org/10.1063/1.4921318.

[104] Jason P. Allmaras, Emma E. Wollman, Andrew D. Beyer, Ryan M. Briggs, Boris A. Korzh, Bruce Bumble, and Matthew D. Shaw. Demonstration of a thermally coupled row-column snspd imaging array. *Nano Letters*, 20(3), 2020. URL https://doi.org/10.1021/acs.nanolett.0c00246.

[105] Jason Paul Allmaras. Modeling and development of superconducting nanowire single-photon detectors. *Dissertation (Ph.D.)*, California Institute of Technology (2020):2020, 2020. doi: 0.7907/wgak-vs11. URL https://resolver.caltech.edu/CaltechTHESIS:05312020-201105584.

[106] Chandra M Natarajan, Michael G Tanner, and Robert H Hadfield. Superconducting nanowire single-photon detectors: physics and applications. *Superconductor Science and Technology*, 25(063001), 2012. URL https://doi.org/10.1088/0953-2048/25/6/063001.

[107] Faraz Najafi, Francesco Marsili, Varun B. Verma, Qingyuan Zhao, Matthew D. Shaw, Karl K. Berggren, and Sae Woo Nam. *Superconducting Nanowire Architectures for Single Photon Detection*, pages 3–30. Springer International Publishing, Cham, 2016. ISBN 978-3-319-24091-6. doi: 10.1007/978-3-319-24091-6_1. URL https://doi.org/10.1007/978-3-319-24091-6_1.

[108] T. Yamashita, S. Miki, K.f Makise, W. Qiu, H. Terai, M. Fujiwara, M. Sasaki, and Z. Wang. Origin of intrinsic dark count in superconducting nanowire single-photon detectors. *Applied Physics Letters*, 99(16):161105, 10 2011. ISSN 0003-6951. doi: 10.1063/1.3652908. URL https://doi.org/10.1063/1.3652908.

[109] Mohsen K. Akhlaghi, Haig Atikian, Amin Eftekharian, Marko Loncar, and A. Hamed Majedi. Reduced dark counts in optimized geometries for superconducting nanowire single photon detectors. *Opt. Express*, 20(21):23610–23616, Oct 2012. doi: 10.1364/OE.20.023610. URL https://opg.optica.org/oe/abstract.cfm?URI=oe-20-21-23610.

[110] Xingyu Zhang, Xiaofu Zhang, Jia Huang, Can Yang, Lixing You, Xiaoyu Liu, Peng Hu, You Xiao, Wenying Zhang, Yongliang Wang, Lingyun Li, Zhen Wang, and Hao Li. Geometric origin of intrinsic dark counts in superconducting nanowire single-photon detectors. *Superconductivity*, 1:100006, 2022. ISSN 2772-8307. doi: https://doi.org/10.1016/j.supcon.2022.100006. URL https://www.sciencedirect.com/science/article/pii/S2772830722000059.

[111] John R. Clem and Karl K. Berggren. Geometry-dependent critical currents in superconducting nanocircuits. *Phys. Rev. B*, 84, 2011. URL https://link.aps.org/doi/10.1103/PhysRevB.84.174510.

[112] D. Henrich, P. Reichensperger, M. Hofherr, J. M. Meckbach, K. Il'in, M. Siegel, A. Semenov, A. Zotova, and D. Yu. Vodolazov. Geometry-induced reduction of the critical current in superconducting nanowires. *Phys. Rev. B*, 86, 2012. URL https://link.aps.org/doi/10.1103/PhysRevB.86.144504.

[113] Reza Baghdadi, Ekkehart Schmidt, Saman Jahani, Ilya Charaev, Michael G. W. Mueller, Di Zhu, Marco Colangelo, Konstantin Il'in, A Semenov, Zubin Jacob, Michael Siegel, and Karl K Berggren. Enhancing the performance of superconducting nanowire-based detectors with high-filling factor by using variable thickness. *Superconductor Science and Technology*, 2021. URL http://iopscience.iop.org/article/10.1088/1361-6668/abdba6.

[114] Jia-Min Xiong, Wei-Jun Zhang, Guang-Zhao Xu, Li-Xing You, Xing-Yu Zhang, Lu Zhang, Cheng-Jun Zhang, Dong-Hui Fan, Yu-Ze Wang, Hao Li, and Zhen Wang. Reducing current crowding in meander superconducting strip single-photon detectors by thickening bends. *Superconductor Science and Technology*, 35(5):055015,

apr 2022. doi: 10.1088/1361-6668/ac5fe4. URL https://dx.doi.org/10.1088/1361-6668/ac5fe4.

[115] Jeff Chiles, Ilya Charaev, Robert Lasenby, Masha Baryakhtar, Junwu Huang, Alexana Roshko, George Burton, Marco Colangelo, Ken Van Tilburg, Asimina Arvanitaki, Sae Woo Nam, and Karl K. Berggren. New constraints on dark photon dark matter with superconducting nanowire detectors in an optical haloscope. *Phys. Rev. Lett.*, 128:231802, Jun 2022. doi: 10.1103/PhysRevLett.128.231802. URL https://link.aps.org/doi/10.1103/PhysRevLett.128.231802.

[116] Q. Zhao, L. Zhang, T. Jia, L. Kang, W. Xu, J. Chen, and P. Wu. Intrinsic timing jitter of superconducting nanowire single-photon detectors. *Applied Physics B*, 104 (3):673–678, Sep 2011. ISSN 1432-0649. doi: 10.1007/s00340-011-4574-4. URL https://doi.org/10.1007/s00340-011-4574-4.

[117] Junjie Wu, Lixing You, Sijing Chen, Hao Li, Yuhao He, Chaolin Lv, Zhen Wang, and Xiaoming Xie. Improving the timing jitter of a superconducting nanowire single-photon detection system. *Appl. Opt.*, 56(8):2195–2200, Mar 2017. doi: 10.1364/AO.56.002195. URL https://opg.optica.org/ao/abstract.cfm?URI=ao-56-8-2195.

[118] Emma E. Wollman, Jason P. Allmaras, Andrew D. Beyer, Boris Korzh, Marcus C. Runyan, Lautaro Narváez, William H. Farr, Francesco Marsili, Ryan M. Briggs, Gregory J. Miles, and Matthew D. Shaw. An snspd-based detector system for nasa's deep space optical communications project, 2024. URL https://arxiv.org/abs/2409.02356.

[119] Jamie S. Luskin, Ekkehart Schmidt, Boris Korzh, Andrew D. Beyer, Bruce Bumble, Jason P. Allmaras, Alexander B. Walter, Emma E. Wollman, Lautaro Narváez, Varun B. Verma, Sae Woo Nam, Ilya Charaev, Marco Colangelo, Karl K. Berggren, Cristián Peña, Maria Spiropulu, Maurice Garcia-Sciveres, Stephen Derenzo, and Matthew D. Shaw. Large active-area superconducting microwire detector array with single-photon sensitivity in the near-infrared. *Applied Physics Letters*, 122 (24):243506, 06 2023. ISSN 0003-6951. doi: 10.1063/5.0150282. URL https://doi.org/10.1063/5.0150282.

[120] M. Erbe, R. Berrazouane, S. Geyer, L. Stasi, F. van der Brugge, G. Gras, M. Schmidt, A.D. Wieck, A. Ludwig, F. Bussières, and R.J. Warburton. Mo-Si superconducting nanowire single-photon detectors on GaAs. *Phys. Rev. Appl.*, 22:014072, Jul 2024. doi: 10.1103/PhysRevApplied.22.014072. URL https://link.aps.org/doi/10.1103/PhysRevApplied.22.014072.

[121] Stefan Strohauer, Fabian Wietschorke, Christian Schmid, Stefanie Grotowski, Lucio Zugliani, Björn Jonas, Kai Müller, and Jonathan J. Finley. Current-crowding-free

superconducting nanowire single-photon detectors, 2024. URL https://arxiv.org/abs/2407.14171.

[122] Yu. P. Korneeva, N.N. Manova, I.N. Florya, M. Yu. Mikhailov, O.V. Dobrovolskiy, A.A. Korneev, and D. Yu. Vodolazov. Different single-photon response of wide and narrow superconducting mo_xsi_{1-x} strips. *Phys. Rev. Applied*, 13:024011, Feb 2020. doi: 10.1103/PhysRevApplied.13.024011. URL https://link.aps.org/doi/10.1103/PhysRevApplied.13.024011.

[123] J. Chiles1, S. M. Buckley, A. Lita, V. B. Verma, J. Allmaras, B. Korzh, M. D. Shaw, J. M. Shainline, R. P. Mirin, and S. W. Nam. Superconducting microwire detectors based on wsi with single-photon sensitivity in the near-infrared. *Applied Physics Letters*, 116(24):242602, 2020. URL https://doi.org/10.1063/5.0006221.

[124] D.Yu. Vodolazov, N.N. Manova, Yu.P. Korneeva, and A.A. Korneev. Timing jitter in nbn superconducting microstrip single-photon detector. *Phys. Rev. Applied*, 14:044041, Oct 2020. doi: 10.1103/PhysRevApplied.14.044041. URL https://link.aps.org/doi/10.1103/PhysRevApplied.14.044041.

[125] Jesse Liu, Kristin Dona, Gabe Hoshino, Stefan Knirck, Noah Kurinsky, Matthew Malaker, David W. Miller, Andrew Sonnenschein, Mohamed H. Awida, Peter S. Barry, Karl K. Berggren, Daniel Bowring, Gianpaolo Carosi, Clarence Chang, Aaron Chou, Rakshya Khatiwada, Samantha Lewis, Juliang Li, Sae Woo Nam, Omid Noroozian, and Tony X. Zhou. Broadband solenoidal haloscope for terahertz axion detection. *Phys. Rev. Lett.*, 128:131801, Mar 2022. doi: 10.1103/PhysRevLett.128.131801. URL https://link.aps.org/doi/10.1103/PhysRevLett.128.131801.

[126] Stefan Knirck, Gabe Hoshino, Mohamed H. Awida, Gustavo I. Cancelo, Martin Di Federico, Benjamin Knepper, Alex Lapuente, Mira Littmann, David W. Miller, Donald V. Mitchell, Derrick Rodriguez, Mark K. Ruschman, Matthew A. Sawtell, Leandro Stefanazzi, Andrew Sonnenschein, Gary W. Teafoe, Daniel Bowring, G. Carosi, Aaron Chou, Clarence L. Chang, Kristin Dona, Rakshya Khatiwada, Noah A. Kurinsky, Jesse Liu, Cristián Pena, Chiara P. Salemi, Christina W. Wang, and Jialin Yu. First results from a broadband search for dark photon dark matter in the 44 to 52 ¯eV range with a coaxial dish antenna. *Phys. Rev. Lett.*, 132:131004, Mar 2024. doi: 10.1103/PhysRevLett.132.131004. URL https://link.aps.org/doi/10.1103/PhysRevLett.132.131004.

[127] Cristián Peña, Christina Wang, Si Xie, Adolf Bornheim, Matías Barría, Claudio San Martín, Valentina Vega, Artur Apresyan, Emanuel Knehr, Boris Korzh, Jamie Luskin, Lautaro Narváez, Sahil Patel, Matthew Shaw, and Maria Spiropulu. High Energy Particle Detection with Large Area Superconducting Microwire Array, 2024. URL https://arxiv.org/abs/2410.00251.

[128] Dileep V. Reddy, Negar Otrooshi, Sae Woo Nam, Richard P. Mirin, and Varun B. Verma. Broadband polarization insensitivity and high detection efficiency in high-fill-factor superconducting microwire single-photon detectors. *APL Photonics*, 7(5), 2022. URL https://doi.org/10.1063/5.0088007.

[129] E. E. Wollman, V. B. Verma, A. D. Beyer, R. M. Briggs, B. Korzh, J. P. Allmaras, F. Marsili, A. E. Lita, R. P. Mirin, S. W. Nam, and M. D. Shaw. Uv superconducting nanowire single-photon detectors with high efficiency, low noise, and 4 k operating temperature. *Opt. Express*, 25:26792–26801, 2017. URL http://opg.optica.org/oe/abstract.cfm?URI=oe-25-22-26792.

[130] Q. Zhao, L. Zhang, T. Jia, L. Kang, W. Xu, J. Chen, and P. Wu. Intrinsic timing jitter of superconducting nanowire single-photon detectors. *Applied Physics B*, 104 (3):673–678, Sep 2011. ISSN 1432-0649. doi: 10.1007/s00340-011-4574-4. URL https://doi.org/10.1007/s00340-011-4574-4.

[131] Junjie Wu, Lixing You, Sijing Chen, Hao Li, Yuhao He, Chaolin Lv, Zhen Wang, and Xiaoming Xie. Improving the timing jitter of a superconducting nanowire single-photon detection system. *Appl. Opt.*, 56(8):2195–2200, Mar 2017. doi: 10.1364/AO.56.002195. URL https://opg.optica.org/ao/abstract.cfm?URI=ao-56-8-2195.

[132] Marco Colangelo, Boris Korzh, Jason P. Allmaras, Andrew D. Beyer, Andrew S. Mueller, Ryan M. Briggs, Bruce Bumble, Marcus Runyan, Martin J. Stevens, Adam N. McCaughan, Di Zhu, Stephen Smith, Wolfgang Becker, Lautaro Narváez, Joshua C. Bienfang, Simone Frasca, Angel E. Velasco, Edward E. Ramirez, Alexander B. Walter, Ekkehart Schmidt, Emma E. Wollman, Maria Spiropulu, Richard Mirin, Sae Woo Nam, Karl K. Berggren, and Matthew D. Shaw. Impedance-matched differential superconducting nanowire detectors. *Phys. Rev. Appl.*, 19:044093, Apr 2023. doi: 10.1103/PhysRevApplied.19.044093. URL https://link.aps.org/doi/10.1103/PhysRevApplied.19.044093.

[133] Mariia Sidorova, Alexej Semenov, Heinz-Wilhelm Hübers, Ilya Charaev, Artem Kuzmin, Steffen Doerner, and Michael Siegel. Physical mechanisms of timing jitter in photon detection by current-carrying superconducting nanowires. *Phys. Rev. B*, 96:184504, Nov 2017. doi: 10.1103/PhysRevB.96.184504. URL https://link.aps.org/doi/10.1103/PhysRevB.96.184504.

[134] Yuhao Cheng, Chao Gu, and Xiaolong Hu. Inhomogeneity-induced timing jitter of superconducting nanowire single-photon detectors. *Applied Physics Letters*, 111 (6):062604, 08 2017. ISSN 0003-6951. doi: 10.1063/1.4985226. URL https://doi.org/10.1063/1.4985226.

[135] Lixing You, Xiaoyan Yang, Yuhao He, Wenxing Zhang, Dengkuan Liu, Weijun Zhang, Lu Zhang, Ling Zhang, Xiaoyu Liu, Sijing Chen, Zhen Wang, and Xiaom-

ing Xie. Jitter analysis of a superconducting nanowire single photon detector. *AIP Advances*, 3(7):072135, 07 2013. ISSN 2158-3226. doi: 10.1063/1.4817581. URL https://doi.org/10.1063/1.4817581.

[136] S Frasca, B Korzh, M Colangelo, D Zhu, A E Lita, J P Allmaras, E E Wollman, V B Verma, A E Dane, E Ramirez, A D Beyer, S W Nam, A G Kozorezov, M D Shaw, and K K Berggren. Determining the depairing current in superconducting nanowire single-photon detectors. *Phys. Rev. B*, 100:054520, 2019.

[137] Marco Colangelo, Alexander B Walter, Boris A Korzh, Ekkehart Schmidt, Bruce Bumble, Adriana E Lita, Andrew D Beyer, Jason P Allmaras, Ryan M Briggs, Alexander G Kozorezov, Emma E Wollman, Matthew D Shaw, and Karl K Berggren. Large-area superconducting nanowire single-photon detectors for operation at wavelengths up to 7.4 μm. *Nano Lett.*, 22:5667, 2022.

[138] Andrew S. Mueller, Boris Korzh, Marcus Runyan, Emma E. Wollman, Andrew D. Beyer, Jason P. Allmaras, Angel E. Velasco, Ioana Craiciu, Bruce Bumble, Ryan M. Briggs, Lautaro Narvaez, Cristián Pe na, Maria Spiropulu, and Matthew D. Shaw. Free-space coupled superconducting nanowire single-photon detector with low dark counts. *Optica*, 8(12):1586–1587, Dec 2021. doi: 10.1364/OPTICA.444108. URL https://opg.optica.org/optica/abstract.cfm?URI=optica-8-12-1586.

[139] J.T.M. de Haas, P. Dorenbos, and C.W.E. van Eijk. Measuring the absolute light yield of scintillators. *Nuclear Instruments and Methods in Physics Research Section A: Accelerators, Spectrometers, Detectors and Associated Equipment*, 537(1):97–100, 2005. ISSN 0168-9002. doi: https://doi.org/10.1016/j.nima.2004.07.243. URL https://www.sciencedirect.com/science/article/pii/S0168900204017917. Proceedings of the 7th International Conference on Inorganic Scintillators and their Use in Scientific adn Industrial Applications.

[140] Christina Wenlu Wang. *Search for New Physics with the Compact Muon Solenoid Experiment and QIS-enabled Technology*. Dissertation (ph.d.), California Institute of Technology, 2024. URL https://resolver.caltech.edu/CaltechTHESIS:03072024-065323362.